

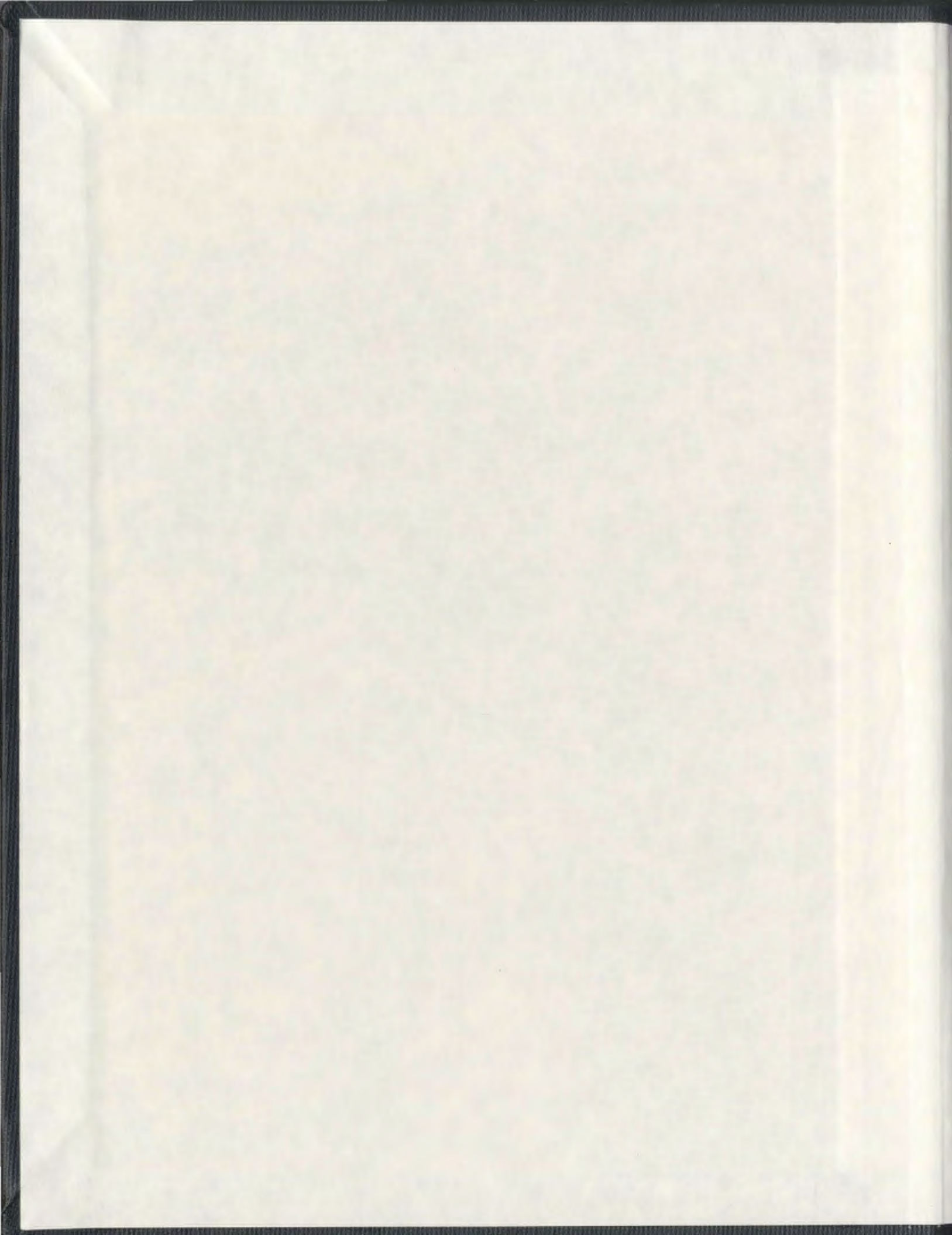
RAMAN SPECTROSCOPIC STUDIES OF
MANGANESE CHLORIDE-ALKALI
METAL CHLORIDE SYSTEMS

CENTRE FOR NEWFOUNDLAND STUDIES

TOTAL OF 10 PAGES ONLY
MAY BE XEROXED

(Without Author's Permission)

AHMED AMIN ALY
AHMED SHABANA



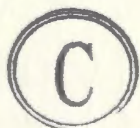
CONFERENCE

CENTRE FOR Nfld. STUDIES
NOV 8 1986
MEMORIAL UNIVERSITY
OF NEWFOUNDLAND

MEMORIAL UNIVERSITY
PERIODICALS
NOV 6 1986
DIVISION
OF NEWFOUNDLAND

RAMAN SPECTROSCOPIC STUDIES OF MANGANESE
CHLORIDE-ALKALI METAL CHLORIDE SYSTEMS

by



Ahmed Amin Aly Ahmed Shabana, B.Sc., M.Sc.

A thesis submitted in partial fulfillment of the requirements
for the degree of Doctor of Philosophy.

Department of Chemistry
Memorial University of Newfoundland

July 1985

St. John's

Newfoundland

Canada

Abstract

The Raman and visible spectra of $\text{MnCl}_2 - \text{ACl}$ systems (A = Li, Na, K, Rb and Cs) were investigated in the solid and the molten phases to identify possible species formation. The many solid compounds precipitated from the melts were identified by their characteristic spectra. The agreement with reported phase diagrams was good. The results indicated that the MnCl_4^{2-} ions were present in solid Cs_2MnCl_4 and Cs_3MnCl_5 but in the other compounds the manganese was octahedrally coordinated with bridged chlorides.

The Raman spectra of the solids were discussed in terms of factor group analysis. The data for the melts suggested that a discrete MnCl_4^{2-} species was the predominant species in the molten phase of composition $\text{MnCl}_2 \cdot n\text{ACl}$ ($n \geq 2$). For melts of composition $\text{MnCl}_2 \cdot n\text{ACl}$ ($n < 2$) a tetrahedral species with corner sharing was proposed but no new peaks due to new discrete species could be identified. Melts of high MnCl_2 content appeared to have a very rapid equilibrium of ions with most Mn retaining tetrahedral coordination but some octahedral coordination was also suggested from assessment of visible spectra. A rapidly fluctuating local structure around the Mn^{2+} with lifetime of the aggregate on the time scale of 10^{-12} seconds would be consistent with the composition and temperature studies of the bandshape of the Mn-Cl stretching region.

The Raman spectra of $\text{MgCl}_2 - \text{CsCl}$ and $\text{MgCl}_2 - \text{KCl}$ systems were investigated in the molten phase for comparison. The results confirm the presence of discrete MgCl_4^{2-} ions as the predominant species in melts even of low MgCl_2 concentration, but a distinct polynuclear species $\text{Mg}_2\text{Cl}_7^{3-}$ was also formed when the MgCl_2 concentration was

increased. In contrast to the manganese system the equilibrium species present in the magnesium system have lifetimes greater than 10^{-12} seconds. The results also indicated that by increasing the temperature the polynuclear species was broken down and more MgCl_4^{2-} ions were formed.

ACKNOWLEDGEMENTS

I would like to express my warmest gratitude to my research supervisor Professor Murray Brooker for his friendly guidance, assistance and enthusiastic interest throughout the course of this work. His encouragement and supervision have been extremely valuable. Special thanks to B. Rice for his generous computer help. Special thanks to Teresa Barker for typing this thesis.

I would like to thank Memorial University for financial support which made this work possible.

TABLE OF CONTENTS

	page
LIST OF TABLES	vii
LIST OF FIGURES	x
1. Introduction	1
1.1 Previous Work	6
2. Theory	16
3. Experimental Procedures	19
3.1 Samples Preparation	19
3.2 Characterization of solids	21
3.3 Raman Spectroscopic Measurements	21
3.3.1 Molten Phase	21
3.3.2 Solid Phase	24
3.4 Visible Spectroscopic Measurements	25
4. Results and Discussion	
4.1 Raman studies of $MnCl_2 \cdot nACl$: Solid state	29
4.1.1 $MnCl_2$	29
4.1.2 $MnCl_2 \cdot CsCl$ System	29
(i) Cs_2MnCl_4	29
(ii) Cs_3MnCl_5	46
(iii) $CsMnCl_3$	47
(iv) $CsMn_4Cl_9$	55
4.1.3 $MnCl_2 \cdot RbCl$ System	60
(i) $RbMnCl_3$	60
(ii) Rb_2MnCl_4	61
(iii) $Rb_3Mn_2Cl_7$	63
4.1.4 $MnCl_2 \cdot KCl$ System	68
4.1.5 $MnCl_2 \cdot NaCl$ System	69
4.1.6 $MnCl_2 \cdot LiCl$ System	78

	page
4.2 Raman Studies of $\text{MnCl}_2 \cdot n\text{ACl}$: Molten state	82
4.2.1 MnCl_2 and $\text{MnCl}_2 \cdot \text{CsCl}$ Melts	82
4.2.2 $\text{MnCl}_2 \cdot \text{RbCl}$ Melts	111
4.2.3 $\text{MnCl}_2 \cdot \text{KCl}$ Melts	111
4.2.4 $\text{MnCl}_2 \cdot \text{NaCl}$ Melts	129
4.2.5 $\text{MnCl}_2 \cdot \text{LiCl}$ Melts	176
4.2.6 Half band width of ν_1 mode for $\text{ACl} \cdot \text{MnCl}_2$ melts .	176
4.3 Raman Studies of $\text{MgCl}_2 \cdot n\text{ACl}$: Molten state	191
4.3.1 MgCl_2 and $\text{MgCl}_2 \cdot \text{CsCl}$ Melts	191
4.3.2 $\text{MgCl}_2 \cdot \text{KCl}$ Melts	193
4.3.3 Effect of temperature on the spectra of CsMgCl_3 and K_2MgCl_4 Melts	219
4.3.4 Comparison of Results for MgCl_2 and MnCl_2 systems	248
4.4 Visible Spectra of $\text{MnCl}_2 \cdot n\text{ACl}$	249
4.4.1 Solid State	255
(i) Cs_2MnCl_4 and Cs_3MnCl_5	255
(ii) MnCl_2 , NaMn_4Cl_9 and $\text{Na}_2\text{Mn}_3\text{Cl}_8$	257
(iii) CsMnCl_3 and CsMn_4Cl_9	274
(iv) RbMnCl_3 , Rb_2MnCl_4 and $\text{Rb}_3\text{Mn}_2\text{Cl}_7$	274
(v) KMnCl_3 , K_4MnCl_6 and $\text{K}_3\text{Mn}_2\text{Cl}_7$	274
(vi) NaMnCl_3 , Na_2MnCl_4 and Na_6MnCl_8	291
4.4.2 Molten State	306
(i) Cs_2MnCl_4 , Cs_3MnCl_5 , K_4MnCl_6 and Na_6MnCl_8 . . .	306
(ii) $\text{Rb}_3\text{Mn}_2\text{Cl}_7$, $\text{K}_3\text{Mn}_2\text{Cl}_7$, Na_2MnCl_4 and Rb_2MnCl_4 . .	307
(iii) CsMnCl_3 , NaMnCl_3 , KMnCl_3 and RbMnCl_3	307
(iv) MnCl_2 , CsMn_4Cl_9 , NaMn_4Cl_9 and $\text{Na}_2\text{Mn}_3\text{Cl}_8$. . .	307
5. Conclusion	345
6. References	346

LIST OF TABLES

	page
1. Peak frequencies in cm^{-1} and assignments for solid MnCl_2 .	30
2. Determination of Γ_{red} for MnCl_4^{2-} ion.	35
3. Internal modes of MnCl_4^{2-} ion	38
4. Lattice modes of MnCl_4^{2-} ion (Translation).	39
5. Lattice modes of MnCl_4^{2-} ion (Rotation)	40
6. Lattice modes of Cs^{+1} ions.	41
7. Assignments and peak positions in cm^{-1} for solid Cs_2MnCl_4 .	43
8. Internal modes of MnCl_4^{2-} ion.	48
9. Lattice modes of MnCl_4^{2-} ion (Translation).	49
10. Lattice modes of MnCl_4^{2-} ion (Rotation)	50
11. Assignments and frequencies in cm^{-1} for solid Cs_3MnCl_5 . .	51
12. Assignments and peak frequencies in cm^{-1} for CsMnCl_3 and $(\text{CH}_3)_4\text{NMnCl}_3$	56
13. Peak frequencies in cm^{-1} and assignments for the solid compounds formed in CsCl-MnCl_2 mixture	57
14. Assignments and frequencies in cm^{-1} for solid RbMnCl_3 . . .	62
15. Peak frequencies in cm^{-1} and assignments for the solid compounds formed in RbCl-MnCl_2 mixtures	64
16. Assignments and peak frequencies in cm^{-1} for solid $\text{Rb}_3\text{Mn}_2\text{Cl}_7$	65
17. Assignments and peak frequencies in cm^{-1} for the solid compounds formed in KCl-MnCl_2 system	70
18. Assignments and frequencies in cm^{-1} for the solid compounds formed in $\text{MnCl}_2\text{-NaCl}$ system	75
19. Peak frequencies in cm^{-1} and assignments for the solid compounds formed in LiCl-MnCl_2 system	79
20. Summary of results of curve resolution analysis for MnCl_2 and $\text{MnCl}_2\text{-CsCl}$ Melts	84

	page
21. Summary of results of curve resolution analysis for MnCl ₂ -RbCl Melts	112
22. Summary of results of curve resolution analysis for MnCl ₂ -KCl Melts	130
23. Summary of results of curve resolution analysis for MnCl ₂ -NaCl Melts	151
24. Summary of results of curve resolution analysis for MnCl ₂ -LiCl Melts	177
25. Half band width for AlCl-MnCl ₂ melts	190
26. Summary of results of curve resolution analysis for MgCl ₂ and MgCl ₂ -CsCl Melts	194
27. Summary of results of curve resolution analysis for MgCl ₂ -KCl Melts	220
28. Summary of results of curve resolution analysis for CsMgCl ₃ and K ₂ MgCl ₄ Melts	237
29. Splitting of the sextet and quartet terms of a d ⁵ ion in octahedral field	250
30. Absorption spectrum of Mn(H ₂ O) ₆ ²⁺	251
31. Absorption spectra of [MnBr ₄] ²⁻ and [MnCl ₄] ²⁻	253
32. Electronic spectra of MnCl ₂	256
33. Band positions in cm ⁻¹ and assignments for solid Cs ₂ MnCl ₄ and Cs ₃ MnCl ₅	266
34. Peak frequencies in cm ⁻¹ and assignments for solid MnCl ₂ , NaMn ₄ Cl ₉ and Na ₂ Mn ₃ Cl ₈ at room temperature.	273
35. Peak positions in cm ⁻¹ and assignments for solid CsMnCl ₃ , CsMn ₄ Cl ₉ and (CH ₃) ₄ NMnCl ₃	283
36. Peak frequencies in cm ⁻¹ and assignments for solid RbMnCl ₃ , Rb ₂ MnCl ₄ and Rb ₃ Mn ₂ Cl ₇ at room temperature.	290
37. Peak positions in cm ⁻¹ and assignments for solid KMnCl ₃ K ₄ MnCl ₆ and K ₃ Mn ₂ Cl ₇ at room temperature.	298

	page
38. Assignments and peak positions in cm^{-1} for solid NaMnCl_3 , Na_2MnCl_4 and Na_6MnCl_8 at room temperature	305
39. Assignments and peak positions in cm^{-1} for Cs_2MnCl_4 , Cs_3MnCl_5 , K_4MnCl_6 , Na_6MnCl_8 and MnCl_2 - CsCl melts.	316
40. Peak positions in cm^{-1} and assignments for $\text{Rb}_3\text{Mn}_2\text{Cl}_7$, $\text{K}_3\text{Mn}_2\text{Cl}_7$, Na_2MnCl_4 , Rb_2MnCl_4 melts and $[\text{MnCl}_4]^{2-}$ solution.	325
41. Assignments and peak positions in cm^{-1} for CsMnCl_3 NaMnCl_3 , KMnCl_3 , RbMnCl_3 and MnCl_2 - CsCl melts	334
42. Assignments and peak positions in cm^{-1} for MnCl_2 , CsMn_4Cl_9 , NaMn_4Cl_9 , $\text{Na}_2\text{Mn}_3\text{Cl}_8$ and MnCl_2 - CsCl melts.	344

LIST OF FIGURES

	page
Fig. 1. Sample furnace.	28
Fig. 2. Raman spectrum of solid $MnCl_2$ at room temperature. The stars indicate ghost peaks. The dots indicate plasma lines.	32
Fig. 3. Normal vibrations of a tetrahedral molecule.	37
Fig. 4. Raman spectra of solid Cs_2MnCl_4 at 77, 298 and 800 K.	45
Fig. 5. Raman spectra of solid Cs_3MnCl_5 at 77, 298 and 760 K.	53
Fig. 6. Raman spectra of solids formed from the $CsCl-MnCl_2$ system. The stars indicate ghost peaks. The dots indicate plasma lines.	59
Fig. 7. Raman spectra of solids formed from the $RbCl-MnCl_2$ system. The stars indicate ghost peaks.	67
Fig. 8. Raman spectra of solids formed from the $KCl-MnCl_2$ system. The stars indicate ghost peaks.	72
Fig. 9. Raman spectra of solids formed from the $NaCl-MnCl_2$ system. The stars indicate ghost peaks. The dots indicate plasma lines.	77
Fig. 10. Raman spectra of solids formed from the $LiCl-MnCl_2$ system. The stars indicate ghost peaks. The dots indicate plasma lines.	81
Fig. 11. Raman spectra of molten $MnCl_2$ at 942 K, $I_{ }$ and I_{\perp}	86
Fig. 12. Raman spectra of molten Cs_2MnCl_4 at 844 K, $I_{ }$ and I_{\perp}	88
Fig. 13. Raman spectra of molten Cs_3MnCl_5 at 844 K, $I_{ }$ and I_{\perp}	90
Fig. 14. Raman spectra of molten $CsMnCl_3$ at 916 K, $I_{ }$ and I_{\perp}	92
Fig. 15. Raman spectra of molten $CsMn_4Cl_9$ at 865 K, $I_{ }$ and I_{\perp}	94

	page
Fig. 16. Effect of temperature on ν_1 mode of Cs_2MnCl_4	96
A. Plot of band position (cm^{-1}) vs temperature.	96
B. Plot of half band width (cm^{-1}) vs temperature.	96
Fig. 17. Effect of temperature on ν_1 mode of Cs_3MnCl_5	98
A. Plot of band position (cm^{-1}) vs temperature.	98
B. Plot of half band width (cm^{-1}) vs temperature.	98
Fig. 18. Isotropic Raman spectra of molten MnCl_2 . The smooth line is the best-fit curve calculated with a single Gaussian*Lorentzian functions.	100
Fig. 19. Isotropic Raman spectra of Molten Cs_2MnCl_4 . The smooth line is the best-fit curve calculated with a single Lorentzian function.	102
Fig. 20. Isotropic Raman spectra of molten Cs_3MnCl_5 . The smooth line is the best-fit curve calculated with a single Lorentzian function.	104
Fig. 21. Isotropic Raman spectra of molten CsMnCl_3 . The smooth line is the best-fit curve calculated with a single Gaussian*Lorentzian function.	106
Fig. 22. Isotropic Raman spectra of molten CsMnCl_3 . The smooth line is the best-fit curve calculated with a single Lorentzian function.	108
Fig. 23. Isotropic Raman spectra of molten CsMn_4Cl_9 . The smooth line is the best-fit curve calculated with a single Gaussian*Lorentzian function.	110
Fig. 24. Raman spectra of molten RbMnCl_3 at 878 K, $I_{ }$ and I_{\perp}	114
Fig. 25. Raman spectra of molten Rb_2MnCl_4 at 753 K, $I_{ }$ and I_{\perp}	116
Fig. 26. Raman spectra of molten $\text{RbCl}:\text{MnCl}_2(3:1)$ at 882 K, $I_{ }$ and I_{\perp}	118
Fig. 27. Raman spectra of molten $\text{Rb}_3\text{Mn}_2\text{Cl}_7$ at 889 K, $I_{ }$ and I_{\perp}	120

	page
Fig. 28. Isotropic Raman spectra of molten RbMnCl_3 . The smooth line is the best-fit curve calculated with a single Gaussian*Lorentzian function	122
Fig. 29. Isotropic Raman spectra of molten Rb_2MnCl_4 . The smooth line is the best-fit curve calculated with a single Lorentzian function	124
Fig. 30. Isotropic Raman spectra of molten RbCl:MnCl_2 (3:1). The smooth line is the best-fit curve calculated with a single Lorentzian function	126
Fig. 31. Isotropic Raman spectra of molten $\text{Rb}_3\text{Mn}_2\text{Cl}_7$. The smooth line is the best-fit curve calculated with a single Lorentzian function :	128
Fig. 32. Raman spectra of molten KMnCl_3 at 816 K, $I_{ }$ and I_{\perp}	132
Fig. 33. Raman spectra of molten KCl:MnCl_2 (2:1) at 882 K, $I_{ }$ and I_{\perp}	134
Fig. 34. Raman spectra of molten KCl:MnCl_2 (3:1) at 882 K, $I_{ }$ and I_{\perp}	136
Fig. 35. Raman spectra of molten $\text{K}_3\text{Mn}_2\text{Cl}_7$ at 794 K, $I_{ }$ and I_{\perp}	138
Fig. 36. Raman spectra of molten K_4MnCl_6 at 816 K, $I_{ }$ and I_{\perp}	140
Fig. 37. Isotropic Raman spectra of molten KMnCl_3 . The smooth line is the best-fit curve calculated with a single Gaussian*Lorentzian function	142
Fig. 38. Isotropic Raman spectra of molten KCl:MnCl_2 (2:1). The smooth line is the best-fit curve calculated with a single Lorentzian function	144
Fig. 39. Isotropic Raman spectra of molten KCl:MnCl_2 (3:1). The smooth line is the best-fit curve calculated with a single Lorentzian function	146
Fig. 40. Isotropic Raman spectra of molten $\text{K}_3\text{Mn}_2\text{Cl}_7$. The smooth line is the best-fit curve calculated with a single Lorentzian function	148

	page
Fig. 41. Isotropic Raman spectra of molten K_4MnCl_6 . The smooth line is the best-fit curve calculated with a single Lorentzian function	150
Fig. 42. Raman spectra of molten $NaMnCl_3$ at 773 K, $I_{ }$ and I_{\perp}	153
Fig. 43. Raman spectra of molten Na_2MnCl_4 at 794 K, $I_{ }$ and I_{\perp}	155
Fig. 44. Raman spectra of molten $NaCl:MnCl_2$ (3:1) at 973 K, $I_{ }$ and I_{\perp}	157
Fig. 45. Raman spectra of molten $Na_2Mn_3Cl_8$ at 816 K, $I_{ }$ and I_{\perp}	159
Fig. 46. Raman spectra of molten $NaMn_4Cl_9$ at 937 K, $I_{ }$ and I_{\perp}	161
Fig. 47. Raman spectra of molten Na_6MnCl_8 at 988 K, $I_{ }$ and I_{\perp}	163
Fig. 48. Isotropic Raman spectra of molten $NaMnCl_3$. The smooth line is the best-fit curve calculated as a sum of two Gaussian*Lorentzian functions. The second low frequency peak has only been added to improve the base line.	165
Fig. 49. Isotropic Raman spectra of molten Na_2MnCl_4 . The smooth line is the best-fit curve calculated as a sum of two Gaussian*Lorentzian functions. The second low frequency peak has only been added to improve the base line.	167
Fig. 50. Isotropic Raman spectra of molten $NaCl:MnCl_2$ (3:1). The smooth line is the best-fit curve calculated as a sum of two Gaussian*Lorentzian functions. The second low frequency peak has only been added to improve the base line.	169
Fig. 51. Isotropic Raman spectra of molten $Na_2Mn_3Cl_8$. The smooth line is the best-fit curve calculated with a single Gaussian*Lorentzian function.	171
Fig. 52. Isotropic Raman spectra of molten $NaMn_4Cl_9$. The smooth line is the best-fit curve calculated with a single Gaussian*Lorentzian function.	173

Fig. 53.	Isotropic Raman spectra of molten Na_6MnCl_8 . The smooth line is the best-fit curve calculated as a sum of two Gaussian*Lorentzian functions. The second low frequency peak has only been added to improve the base line.	175
Fig. 54.	Raman spectra of molten $\text{LiCl}:\text{MnCl}_2$ (1:1) at 945 K, $I_{ }$ and I_{\perp}	179
Fig. 55.	Raman spectra of molten $\text{LiCl}:\text{MnCl}_2$ (2:1) at 953 K, $I_{ }$ and I_{\perp}	181
Fig. 56.	Raman spectra of molten $\text{LiCl}:\text{MnCl}_2$ (3:1) at 973 K, $I_{ }$ and I_{\perp}	183
Fig. 57.	Isotropic Raman spectra of molten $\text{LiCl}:\text{MnCl}_2$ (1:1). The smooth line is the best-fit curve calculated with a single Gaussian*Lorentzian function.	185
Fig. 58.	Isotropic Raman spectra of molten $\text{LiCl}:\text{MnCl}_2$ (2:1). The smooth line is the best-fit curve calculated with a single Gaussian*Lorentzian function.	187
Fig. 59.	Isotropic Raman spectra of molten $\text{LiCl}:\text{MnCl}_2$ (3:1). The smooth line is the best-fit curve calculated with a single Gaussian*Lorentzian function.	189
Fig. 60.	Raman spectra of molten $\text{CsCl}:\text{MgCl}_2$ (4:1) at 840 K, $I_{ }$ and I_{\perp}	196
Fig. 61.	Raman spectra of molten Cs_2MgCl_4 at 896 K, $I_{ }$ and I_{\perp}	198
Fig. 62.	Raman spectra of molten $\text{CsCl}:\text{MgCl}_2$ (1.5:1) at 915 K, $I_{ }$ and I_{\perp}	200
Fig. 63.	Raman spectra of molten CsMgCl_3 at 896 K, $I_{ }$ and I_{\perp}	202
Fig. 64.	Raman spectra of molten $\text{CsCl}:\text{MgCl}_2$ (0.5:1) at 915 K, $I_{ }$ and I_{\perp}	204
Fig. 65.	Raman spectra of molten MgCl_2 at 1056 K, $I_{ }$ and I_{\perp}	206
Fig. 66.	Isotropic Raman spectra of molten $\text{CsCl}:\text{MgCl}_2$ (4:1). The smooth line is the best-fit curve calculated with a single Lorentzian function.	208

	page
Fig. 67. Isotropic Raman spectra of molten Cs_2MgCl_4 . The smooth line is the best-fit curve calculated as a sum of three Lorentzian functions.	210
Fig. 68. Isotropic Raman spectra of molten CsCl:MgCl_2 (1.5:1). The smooth line is the best-fit curve calculated as a sum of three Lorentzian functions. . .	212
Fig. 69. Isotropic Raman spectra of molten CsMgCl_3 . The smooth line is the best-fit curve calculated as a sum of three Lorentzian functions.	214
Fig. 70. Isotropic Raman spectra of molten CsCl:MgCl_2 (0.5:1). The smooth line is the best-fit curve calculated as a sum of four Lorentzian functions. . .	216
Fig. 71. Isotropic Raman spectra of molten MgCl_2 . The smooth line is the best-fit curve calculated as a sum of three Gaussian*Lorentzian functions.	218
Fig. 72. Raman spectra of molten K_2MgCl_4 at 1049 K, $I_{ }$ and I_{\perp}	222
Fig. 73. Raman spectra of molten KCl:MgCl_2 (1.5:1) at 1049 K, $I_{ }$ and I_{\perp}	224
Fig. 74. Raman spectra of molten KMgCl_3 at 1049 K, $I_{ }$ and I_{\perp}	226
Fig. 75. Raman spectra of molten KCl:MgCl_2 (0.5:1) at 1049 K, $I_{ }$ and I_{\perp}	228
Fig. 76. Isotropic Raman spectra of molten K_2MgCl_4 . The smooth line is the best-fit curve calculated as a sum of three Lorentzian functions.	230
Fig. 77. Isotropic Raman spectra of molten KCl:MgCl_2 (1.5:1). The smooth line is the best-fit curve calculated as a sum of three Lorentzian functions. . .	232
Fig. 78. Isotropic Raman spectra of molten KMgCl_3 . The smooth line is the best-fit curve calculated as a sum of three Lorentzian functions.	234
Fig. 79. Isotropic Raman spectra of molten KCl:MgCl_2 (0.5:1). The smooth line is the best-fit curve calculated as a sum of four Lorentzian functions. . .	236

	page
Fig. 80. Isotropic Raman spectra of molten CsMgCl_3 at 899 K. The smooth line is the best-fit curve calculated as a sum of three Lorentzian functions. . .	239
Fig. 81. Isotropic Raman spectra of molten CsMgCl_3 at 1054 K. The smooth line is the best-fit curve calculated as a sum of three Lorentzian functions. . .	241
Fig. 82. Isotropic Raman spectra of molten CsMgCl_3 at 1153 K. The smooth line is the best-fit curve calculated as a sum of three Lorentzian functions. . .	243
Fig. 83. Isotropic Raman spectra of molten K_2MgCl_4 at 973 K. The smooth line is the best-fit curve calculated as a sum of three Lorentzian functions. . .	245
Fig. 84. Isotropic Raman spectra of molten K_2MgCl_4 at 1143 K. The smooth line is the best-fit curve calculated as a sum of three Lorentzian functions. . .	247
Fig. 85. A. Upper spectrum is the projection lamp section. Lower spectrum is the projection lamp plus sample spectrum. B. The subtracted spectrum represents the visible spectrum of Cs_2MnCl_4 at room temperature	259
Fig. 86. Visible spectrum of Cs_2MnCl_4 at 681 K.	261
Fig. 87. Visible spectrum of Cs_3MnCl_5 at room temperature. . .	263
Fig. 88. Visible spectrum of Cs_3MnCl_5 at 681 K.	265
Fig. 89. Visible spectrum of MnCl_2 at room temperature. . . .	268
Fig. 90. Visible spectrum of NaMn_4Cl_9 at room temperature. . .	270
Fig. 91. Visible spectrum of $\text{Na}_2\text{Mn}_3\text{Cl}_8$ at room temperature. . .	272
Fig. 92. Visible spectrum of CsMnCl_3 at room temperature. . .	276
Fig. 93. Visible spectrum of CsMnCl_3 at 681 K.	278
Fig. 94. Visible spectrum of CsMn_4Cl_9 at room temperature. . .	280
Fig. 95. Visible spectrum of CsMn_4Cl_9 at 681 K.	282
Fig. 96. Visible spectrum of RbMnCl_3 at room temperature. . .	285
Fig. 97. Visible spectrum of Rb_2MnCl_4 at room temperature. . .	287

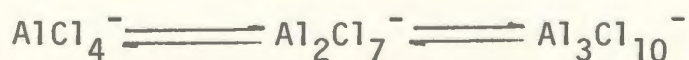
	page
Fig. 98. Visible spectrum of $\text{Rb}_3\text{Mn}_2\text{Cl}_7$ at room temperature. . . .	289
Fig. 99. Visible spectrum of KMnCl_3 at room temperature. . . .	293
Fig. 100. Visible spectrum of K_4MnCl_6 at room temperature. . . .	295
Fig. 101. Visible spectrum of $\text{K}_3\text{Mn}_2\text{Cl}_7$ at room temperature. . . .	297
Fig. 102. Visible spectrum of NaMnCl_3 at room temperature. . . .	300
Fig. 103. Visible spectrum of Na_2MnCl_4 at room temperature. . . .	302
Fig. 104. Visible spectrum of Na_6MnCl_8 at room temperature. . . .	304
Fig. 105. Visible spectrum of molten Cs_2MnCl_4 at 906 K.	309
Fig. 106. Visible spectrum of molten Cs_3MnCl_5 at 906 K.	311
Fig. 107. Visible spectrum of molten K_4MnCl_6 at 906 K.	313
Fig. 108. Visible spectrum of molten Na_6MnCl_8 at 922 K.	315
Fig. 109. Visible spectrum of molten $\text{Rb}_3\text{Mn}_2\text{Cl}_7$ at 900 K.	318
Fig. 110. Visible spectrum of molten $\text{K}_3\text{Mn}_2\text{Cl}_7$ at 900 K.	320
Fig. 111. Visible spectrum of molten Na_2MnCl_4 at 900 K.	322
Fig. 112. Visible spectrum of molten Rb_2MnCl_4 at 915 K.	324
Fig. 113. Visible spectrum of molten CsMnCl_3 at 906 K.	327
Fig. 114. Visible spectrum of molten NaMnCl_3 at 900 K.	329
Fig. 115. Visible spectrum of molten KMnCl_3 at 906 K.	331
Fig. 116. Visible spectrum of molten RbMnCl_3 at 906 K.	333
Fig. 117. Visible spectrum of molten MnCl_2 at 974 K.	337
Fig. 118. Visible spectrum of molten CsMn_4Cl_9 at 925 K.	339
Fig. 119. Visible spectrum of molten NaMn_4Cl_9 at 916 K.	341
Fig. 120. Visible spectrum of molten $\text{Na}_2\text{Mn}_3\text{Cl}_8$ at 901 K.	343

1. Introduction

Raman spectroscopy can be used to study, identify and characterize discrete species and ions that exist in melts and to monitor changes that accompany changes in temperature and composition. For instance the Raman study¹ of molten aluminium fluoride-alkali metal fluoride mixtures, indicated an equilibrium between the tetrahedral species AlF_4^- and the octahedral species AlF_6^{3-} . The spectra of mixtures of AlF_3 with 53.8, 59.4, 62.5, and 75 mole % of alkali fluoride were obtained. The Raman spectrum of the melt of composition 53.8 - 46.2 mole % AlF_3 -AF contain one strong polarized peak at 623 cm^{-1} and three depolarized peaks at 760, 322, and 210 cm^{-1} . These peaks were attributed to the AlF_4^- tetrahedral species. However another two peaks were detected, one polarized located at 555 cm^{-1} and the other one a weak shoulder located around 345 cm^{-1} . It was observed that the intensity of these two peaks increased at the same rate by increasing the concentration of alkali metal fluoride. These two peaks were attributed to the species AlF_6^{3-} . The spectrum of the melt of 25 mole % AlF_3 contained three peaks one polarized located at 555 cm^{-1} and two depolarized peaks located at 390 and 345 cm^{-1} . These three peaks were attributed to the octahedral AlF_6^{3-} species the most likely species at this composition. The results indicated that a melt of composition close to 50-50 mole % AlF_3 -AF contained almost only AlF_4^- ions, but the AlF_4^- ions were replaced by AlF_6^{3-} ions upon decreasing AlF_3 concentration. For the melt of 25 mole % AlF_3 no AlF_4^- could be detected spectroscopically and the melt contain almost pure AlF_6^{3-} ions. Thus the Raman study established the equilibrium between AlF_4^- and AlF_6^{3-} ions in the molten state i.e.,



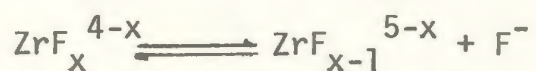
Another example of the application of Raman spectroscopy to the identification and characterization of discrete species was the Raman study² of Aluminium chloride-Alkali metal chloride melts. In this case the geometry remained tetrahedral but a polynuclear species was formed. The results suggested the formation of AlCl_4^- , Al_2Cl_7^- , and $\text{Al}_3\text{Cl}_{10}^-$ species in the melts. Four peaks were observed for the melt of 50 mole % AlCl_3 , one polarized and three depolarized and attributed to the presence of AlCl_4^- tetrahedral species. The relative intensities of these four peaks decreased by increasing AlCl_3 content. When the AlCl_3 concentration was increased from 50 to 66.7 mole %, new peaks were observed to increase in relative intensity. These peaks were attributed to the formation of Al_2Cl_7^- species which possibly has two distorted AlCl_4^- tetrahedra sharing one bridging Cl^- . Upon increasing the AlCl_3 content from 66.7 to 75.0 mole %, four peaks were detected and increased relative to the Al_2Cl_7^- peaks. These four peaks were attributed to the formation of $\text{Al}_3\text{Cl}_{10}^-$ species. Thus the Raman study established the existence of the equilibrium in the molten state i.e.,



The above Raman studies gave information about the presence and the coordination of new complex species which have lifetimes greater than 10^{-12} sec. which is the limit for Raman studies. In fact NMR studies of AlCl_4^- suggest that this species has a lifetime $\sim 10^{-5}$ sec.³

The interpretation of Raman measurements are not always as straightforward. Rapid equilibrium between species and severe band overlap may preclude the identification of peaks due to discrete species.

An interesting example of a Raman study of this type was the study⁴ of LiF-NaF-ThF₄ molten salt system. In this case severe band overlap prevented the separation of peaks due to specific species. This study established the coordination behaviour of Th(IV) in these melts. Two peaks were observed for the melt of 14 mole % ThF₄ in LiF-NaF (40-46 mole %) at 650°, one polarized band at 474 cm⁻¹ attributed to the symmetric stretching of ThF_x^{4-x} species and another depolarized peak centered at 250 cm⁻¹. It was noted that the position of the polarized peak remained unchanged for composition changes from 14 to 20 mole % ThF₄, the frequency increased to 478 cm⁻¹ when the concentration of ThF₄ was changed from 20 to 25 mole %, and no further frequency shift was observed by increasing ThF₄ content more than 25 mole %. The formation of ThF₈⁴⁻ species was proposed for melt of 14-20% mole ThF₄, while for melts of 20-25% ThF₄ the presence of ThF₇³⁻ species was suggested. Similar melts have been investigated by Raman spectroscopy⁵. Raman spectra of molten LiF-NaF-ZrF₄ mixtures at 650° have been studied to monitor the coordination of Zr(IV) in alkali metal fluoride melts. The formation of eight-, seven-, six-, and five coordinated zirconium in molten fluoride was inferred from frequency shifts upon changing ZrF₄ content. An equilibrium of several ZrF_x^{4-x} species (where X = 8, 7, 6, and possibly 5 or 4) was proposed in molten fluorides and is dependent on the fluoride ion concentration i.e.,



No new Raman lines were observed for Th(IV) and Zr(IV) melts upon changing the concentration, but equilibrium species were suggested from frequency shifts of the polarized peak. This suggests that the lifetime of these species is $\sim 10^{-12}$ sec. and the fluoride exchange rate is too fast to detect equilibrium species. It is also possible that the peak frequencies for the different species are similar and environmental broadening prevents band separation.

Studies of molten salts are important because of their use in electrowinning of metals from melts; for instance the production of Aluminium⁶ by electrolysis of Alumina (Al_2O_3) dissolved in molten cryolite (Na_3AlF_6). Aluminium is deposited as a liquid at the cathode, it is heavier than the electrolyte so it remains at the bottom of the cell. Pure cryolite has a melting point of 1009°C but cryolite-alumina eutectic melts at 962°C . Additives (such as LiF , NaCl , and CaF_2) can be used to decrease the melting point, viscosity, vapour pressure and density of the melt. Also Magnesium⁶ has been produced by electro-winning process from MgF_2 melt containing MgO as an additive to lower the melting temperature of the electrolyte bath.

Knowledge of the species present in the melts is important for process improvements. In the present study MnCl_2 was studied for comparison with MgCl_2 since discrete polynuclear species have been observed for MgCl_2 but preliminary results indicated that the MnCl_2 system did not reveal new polynuclear species. This was surprising since the ionic radii of Mg^{2+} and Mn^{2+} are quite close and they have the same charge.

Phase equilibrium studies along the solid metal equilibrium line also provides information about the solids which crystallize from melts. New salts of useful properties such as Li_2MnCl_4 , a solid state conductor have now been detected from Raman studies. A previous phase diagram study failed to reveal this compound.

Visible spectroscopy has also been used to characterize the coordination of the manganese salts. In an octahedral environment Mn^{2+} absorbs the 21000-16000 cm^{-1} region and the samples are red however in a tetrahedral environment Mn^{2+} absorbs in the 23000-19000 cm^{-1} region and the samples are yellow. In the present study the $\text{MnCl}_2 \cdot n\text{ACl}$ samples were studied by visible absorption spectroscopy in an effort to establish the Mn^{2+} coordination in the various samples.

1.1 Previous Work

In addition to the related studies mentioned in the introduction there have been a number of related studies of $ACl-MCl_2$ systems which will be reviewed below.

Early Raman measurements on molten $MgCl_2$ and $MgCl_2-KCl$ by Balasubrahmanyam⁷ were interpreted in terms of $MgCl_6^{4-}$ in pure $MgCl_2$ and $MgCl_3^-$ in $KMgCl_3$ but these results were shown to be flawed by peaks due to instrumental artifacts⁸.

Maroni et. al.⁸ studied Raman spectra of MgX_2-KX ($X = Cl, Br, \text{ and } I$) over a range of X^-/Mg^{2+} mole ratios in the molten state. The results for $MgCl_2-KCl$ and $MgBr_2-KBr$ systems were interpreted in terms of discrete MgX_4^{2-} complex ion in equilibrium with a residual ionic lattice at high $MgCl_2$ concentration, i.e., a polynuclear complex $[MgX_2]_p$, similar in structure to solid $MgCl_2$ and solid $MgBr_2$. Polynuclear aggregates have also been proposed for $SnCl_2-KCl$ and $ZnCl_2-AlCl_3$ melts^{11,12}. It was found that the concentration of $[MgX_2]_p$ species decrease by increasing the X^-/Mg^{2+} mole ratio from 2.5 to 4.0. The Raman spectra of MgI_2-KI system of I^-/Mg^{2+} mole ratio 3.0 and 3.5 indicated the presence of a single highly symmetric species, and the observation of two depolarized peaks in the low frequency region for this species is consistent with the existence of MgI_4^{2-} of tetrahedral structure. The experimental data suggested that at X^-/Mg^{2+} mole ratio near 4.0, the MgX_4^{2-} ions of tetrahedral geometry are the predominant species in all three systems.

The Raman spectra of MgX_2-KX ($X = Cl, Br, \text{ and } I$) with X^-/Mg^{2+} mole ratios near 4.0 have been studied in the molten state⁹. One polarized peak and three depolarized peaks were observed for each halide melt.

For MX_4 molecules⁷ of T_d symmetry, four vibrations are expected as follows:

$$\Gamma_{T_d} = \begin{matrix} A_1 & + & E & + & 2T_2 \\ R & & R & & \text{IR/R} \end{matrix} \quad (1)$$

The A_1 and E modes are Raman active and the T_2 modes are IR and Raman active. The Raman spectra and normal coordinate analysis calculations strongly indicated the existence of tetrahedral complexes MgX_4^{2-} .

The Raman spectra of single crystal and molten MgCl_2 have been studied by Capwell¹⁰. The existence of discrete complex ions was not supported. Two peaks were observed at 243 and 157 cm^{-1} in the spectrum of the crystal and assigned to the totally symmetric A_{1g} mode and the E_g mode respectively. Two peaks at 195 and 102 cm^{-1} in the melt were assigned to residual lattice modes by analogy to the spectrum of the crystal. He concluded that the melt was structurally similar to the layered solid.

The IR and Raman spectra of $(\text{NEt}_4)_2\text{MgCl}_4$ have been studied by Davies¹³. Four Raman peaks were observed in the solid state, one observed at 257 cm^{-1} was observed as a polarized peak in acetonitrile solution at 253 cm^{-1} . Two peaks were recorded in the IR spectrum of Nujol mull at 143 and 360 cm^{-1} and one peak was observed at 358 cm^{-1} in acetonitrile solution. The spectra strongly indicated a tetrahedral structure for MgCl_4^{2-} anion.

Brooker¹⁴ studied Raman spectra of single crystals of K_2MgCl_4 and Cs_2MgCl_4 at 77 and 298 K, his data were in good agreement with factor group analysis on the space group $I4/mmm$ (D_{4h}^{17}) and Pnma (D_{2h}^{16}) for

K_2MgCl_4 and Cs_2MgCl_4 crystals. The data suggested that the coordination number of magnesium changed from six in solid K_2MgCl_4 to four in the melt, and the existence of tetrahedral species $MgCl_4^{2-}$ in solid and molten Cs_2MgCl_4 . The presence of discrete $MgCl_4^{2-}$ species was supported from the high resolution study of ν_1 region at 77 K, where the Cl^{35} , Cl^{37} isotope splitting was clearly resolved and found to be similar to CCl_4 . Bands were observed at 271.9, 270.3, 268.0, and 266.4 cm^{-1} with relative intensities 37%, 42%, 17%, 4.6%, and 0% due to $Mg^{35}Cl_4^{2-}$, $Mg^{35}Cl_3^{37}Cl^{2-}$, $Mg^{35}Cl_2^{37}Cl_2^{2-}$, $Mg^{35}Cl^{37}Cl_3^{2-}$ and $Mg^{37}Cl_4^{2-}$ respectively. The Raman spectra of the molten salts strongly indicated that $MgCl_4^{2-}$ is the predominant species in the melts. A peak was observed around 225 cm^{-1} in the melts of K_2MgCl_4 and Cs_2MgCl_4 , and the intensity of this peak decreased by increasing the temperature. This peak was attributed to the presence of another species in the form of polynuclear complex $Mg_2Cl_6^{2-}$. It was suggested that the reduction in the intensity of that peak is consistent with the breaking up of the polynuclear complex and the formation of more $MgCl_4^{2-}$ ions.

The Raman spectra of $MgCl_2$ in the melt at 1010 K and in the solid at 77 K and 298 K have been studied¹⁵. The two peaks observed in the solid state spectrum were identical to the ones observed by Capwell¹⁰. It was suggested that $MgCl_2$ does not undergo any phase transition between 77 K and the melting point. Four peaks were detected in the $I_{||}$ spectrum of the melt around 130, 194, 244, and 335 cm^{-1} respectively, and three peaks were detected in the I_{\perp} spectrum of the melt, one broad peak at 335 cm^{-1} and another two weak peaks around 100 and 140 cm^{-1} . On the basis of the relative intensity and polarization characteristics, the peaks at 335, 244, 140, and 100 cm^{-1} were assigned to the ν_3 , ν_1 , ν_4 and ν_2 vibrations of the discrete $MgCl_4^{2-}$ tetrahedral

structure. The peaks at 194 and 130 cm^{-1} were attributed to symmetric stretching vibrations of a polynuclear complex $\text{Mg}_2\text{Cl}_n^{4-n}$. The Raman spectra suggested that MgCl_2 does not melt with retention of the basic lattice structure as was suggested before¹⁰ but melts to give a dynamic equilibrium mixture containing MgCl_4^{2-} , polynuclear complexes, and Mg^{2+} and Cl^- ions. On comparing the intensities of the peaks observed in K_2MgCl_4 melt¹⁴ and MgCl_2 melt in the region 170-270 cm^{-1} , it was concluded that the decrease in the intensity ratio of the peaks at 244 and 194 cm^{-1} , i.e. I_{244}/I_{194} , in MgCl_2 melt is consistent with a decrease in the concentration of MgCl_4^{2-} as the Cl^- concentration decreased and a corresponding increase in polynuclear complex.

The Raman spectra of CsMgCl_3 and Cs_3MgCl_5 in the solid state and as single crystals have been studied.¹⁶ CsMgCl_3 has space group $\text{P6}_3/\text{mmc}(\text{D}_{6h}^4)$, five Raman active modes were predicted, A_{1g} , E_{1g} and $3E_g$. The Raman results were in excellent agreement with these predictions from factor group analysis. The Raman spectra were also obtained at 77 K, and the results indicated that no phase transition occurs between room temperature and 77 K. The Raman results of Cs_3MgCl_5 indicated that discrete MgCl_4^{2-} tetrahedral species are present, and the peak positions in the solid state are quite similar to the molten salt values: $\nu_1(A_1) \sim 250 \text{ cm}^{-1}$; $\nu_2(E) \sim 120 \text{ cm}^{-1}$; $\nu_3(T_2) \sim 350 \text{ cm}^{-1}$ and $\nu_4(T_2) \sim 140 \text{ cm}^{-1}$. The results of the oriented single crystal studies were in excellent agreement with the predictions of the factor group analysis based on the space group $\text{I4}/\text{mcm}(\text{D}_{4h}^{18})$. Both Cs_3MgCl_5 and Cs_2MgCl_4 contain the discrete MgCl_4^{2-} tetrahedral units, the results conclusively showed that Cs_3MgCl_5 has a distinct structure different from Cs_2MgCl_4 ¹⁴ and this structural difference

could be deduced from the difference in the Raman spectra.

Raman spectra in the solid and molten states of composition $\text{MgCl}_2 + n\text{ACl}$ ($n = 0-4$ and $A = \text{Cs}, \text{Rb}, \text{K}, \text{Na}, \text{Li}$) have been studied.¹⁷ Characteristic spectra were observed for each of the predicted double salts, and the results were in excellent agreement with phase diagram studies. The Raman results on the alkali metal-rich region of $\text{RbCl}-\text{MgCl}_2$ and $\text{KCl}-\text{MgCl}_2$ suggested the presence of a new incongruent melting compounds Rb_3MgCl_5 and K_3MgCl_5 . The results suggested that the compounds Cs_2MgCl_4 , Cs_3MgCl_5 and Rb_3MgCl_5 contain the discrete MgCl_4^{2-} tetrahedral ion, and the other solids contain distorted network octahedra with face-, edge-, or corner-shared chlorides. Raman spectra of the melts were characterized by three depolarized peaks at about 110, 145, and 350 cm^{-1} and one polarized peak in the $200-250 \text{ cm}^{-1}$ region. By comparing the melts of low MgCl_2 concentration, a marked cation dependence on the polarized band was observed, the peak maximum was shifted to slightly lower frequencies and the halfwidth of the band increased over the cation series Cs^+ to Li^+ . This was attributed to the fact that the small Li^+ ion can compete quite favourably for the chloride ion which decreases the Mg-Cl force constant and reduces the frequency. An additional Raman peak at $\sim 225 \text{ cm}^{-1}$ was clearly observed for Cs, Rb, and K salts by increasing the MgCl_2 concentration. This peak was attributed to the formation of new equilibrium species in the melts of high MgCl_2 concentration. By analogy with the low melting $\text{CsCl}-\text{AlCl}_3$ system where two peaks at 350 and 312 cm^{-1} were clearly resolved and have been assigned to AlCl_4^- and Al_2Cl_7^- ions on the basis of concentration studies and normal coordinate analysis, it was proposed that the polarized peak at 225 cm^{-1} is due to the $\text{Mg}_2\text{Cl}_7^{3-}$ ion on the

fact that the magnesium can retain its tetrahedral coordination through corner-sharing with other magnesium centered tetrahedrons. Also an edge-shared $\text{Mg}_2\text{Cl}_6^{2-}$ was proposed, but the formation of $\text{Mg}_2\text{Cl}_7^{3-}$ was considered more favourable.

The Raman spectra of MnCl_2 as a single crystal have been investigated¹⁸. Two Raman active modes A_{1g} and E_g were predicted from factor group analysis based on the space group $R\bar{3}m(D_{3d}^5)$. Two bands were observed at 234.5 and 144 cm^{-1} and assigned to A_{1g} and E_g modes. The assignment is consistent with polarization characteristic and Raman results on isomorphous MgCl_2 ^{10,15}. Two peaks were observed in the IR spectrum at 180 and 230 cm^{-1} and assigned to A_{2u} and E_u modes.

The Raman spectra of molten MnCl_2 -KCl system have been studied¹⁹ at various compositions. One totally symmetric stretching mode was observed in the range from 100 cm^{-1} to 400 cm^{-1} for every melt, and the other vibrational frequencies were not observed because of their low intensities and a limited sensitivity of the spectrophotometer. It was observed that the polarized peak in molten MnCl_2 (mol fraction $x = 1.0$) appeared at 208 cm^{-1} , and the frequency of this peak increase with increased KCl content until it reach 251 cm^{-1} for specimen of $x = 0.4$, then it slightly decrease to 245 cm^{-1} for the specimen of $x = 0.1$. The increase of the Raman frequency of the polarized peak was attributed to the dissociation of the $(\text{MnCl}_2)_n$ species upon the addition of KCl to MnCl_2 , and the formation of MnCl_6^{4-} octahedral units was suggested from comparison with $(\text{MnCl}_2)_n$ species in pure MnCl_2 . The existence of a small amount of MnCl_4^{2-} ions was suggested upon the observation of a slight shoulder at $\sim 250 \text{ cm}^{-1}$ in the spectra of the melts, $x = 1.0, 0.9,$ and 0.8 . The existence of the tetrahedral MnCl_4^{2-} ions was proposed as

the predominant species in the region of $x = 0.2$ to $x = 0.4$. Also in this composition range the formation of other types of complex ions such as the pyramidal MnCl_3^- ion or $\text{Mn}_2\text{Cl}_7^{3-}$ was suggested. The presence of an equilibrium between discrete species with characteristic peaks was not confirmed by the present study.

The structure of some chloride complexes of 3d metals have been investigated in the molten salts²⁰. The Raman spectra of melts of MnCl_2 , CoCl_2 , NiCl_2 , ZnCl_2 , and CuCl_2 in CsCl , CsCl-NaCl eutectic, and LiCl-KCl euectic were recorded. For MnCl_2 system and CoCl_2 system, two peaks were observed, one polarized peak in the region $240-280 \text{ cm}^{-1}$ assigned to $\nu_1(A_1)$ mode of T_d symmetry, and another peak in the region $120-130 \text{ cm}^{-1}$ attributed to the deformation vibration $\nu_4(T_2)$. For the NiCl_2 and ZnCl_2 systems, one band was observed in the range $260-275 \text{ cm}^{-1}$ and attributed to the totally symmetric vibration $\nu_1(A_1)$. Three weak peaks at 270 , 150 and 125 cm^{-1} were observed for a melt of 1 mole % CuCl_2 in CsCl-NaCl eutectic, the first peak was attributed to $\nu_1(A_1)$ symmetrical vibration and the other two peaks attributed to B_2 and E modes on the assumption of D_{2d} symmetry.

Molten mixtures of $\text{MnCl}_2\text{-AlCl}_3$ and $\text{MnCl}_2\text{-CsCl}$ were investigated by electronic absorption spectroscopy and Raman spectroscopy²³. For the melt of $\text{MnCl}_2\text{-AlCl}_3$, it was suggested that the Mn^{2+} was octahedrally coordinated to AlCl_4^- or Al_2Cl_7^- groups. The Raman results supported strongly the formation of separate tetrahedral MnCl_4^{2-} units in mixtures of MnCl_2 with excess CsCl .

The Raman spectra of $\text{MnCl}_2\text{-2ACl}$ melts have been studied²⁴. A single polarized peak was observed in the frequency region $100-400 \text{ cm}^{-1}$ for every melt, and the other peaks were not observed because of their

low intensities and the limited sensitivity of the spectrophotometer. It was found that the peak position ν_1 was nearly the same for every melt, and the halfwidths of the peak $\Delta\nu$ varied moderately over the cation series Cs^+ to Li^+ . It was concluded that the type of complex ion in each $\text{MnCl}_2 \cdot 2\text{ACl}$ melt was MnCl_4^{2-} with $\nu_1 \approx 249 \text{ cm}^{-1}$.

Bues²⁵ investigated CdCl_2 -KCl melts, he favored a triangular planar of D_{3h} structure. Tanaka et. al.²⁶ examined the CdCl_2 -KCl system. Four peaks were recorded at 257, 211, 245, and 177 cm^{-1} , and assigned to $\nu_1(A_1)$, $\nu_2(A_1)$, $\nu_3(E)$, and $\nu_4(E)$. The assignment was based on comparison of the data obtained from the corresponding solid system. It was concluded that pyramidal CdCl_3^- was the predominant species in the melt because two Raman peaks were attributed to polarized peaks $\nu_1(A_1)$ and $\nu_2(A_1)$, among the four observed peaks.

The Raman spectra for CdCl_2 -KCl melts containing 65, 50, and 35 mole % CdCl_2 in KCl have been investigated by Maroni and Hathaway²⁷. The spectrum of the sample containing 35 mole % CdCl_2 was not different from that of the sample containing 50 mole % CdCl_2 . A broad polarized envelope centered at 230 cm^{-1} was observed for the sample containing 65 mole % CdCl_2 , and it was suggested that this broad envelope contain two peaks one at 259 cm^{-1} and a second peak associated with polynuclear aggregate. One polarized peak was recorded at 259 cm^{-1} for the sample containing 50 mole % CdCl_2 . The polarized Raman peak observed at 259 cm^{-1} was attributed to a totally symmetric stretching vibration for tetrahedral CdCl_4^{2-} , or planar CdCl_3^- , or pyramidal CdCl_3^- . A shoulder was observed at 80 cm^{-1} and attributed to the bending mode. It was concluded that the Raman spectra of CdCl_2 -KCl melts were incomplete in terms of the assumed structures for CdCl_4^{2-} or CdCl_3^- species but not inconsistent with any of the proposed structures.

Clarke et. al.²⁸ studied the Raman spectra of molten cadmium halides and their molten mixtures with alkali metal halides. They concluded that pure molten cadmium halide has octahedral coordination of Cd^{+2} , and the addition of alkali metal halides results in the replacement of octahedral by tetrahedral Cd^{+2} coordination sites.

The structure of molten MnCl_2 has been examined by x-ray diffraction²⁹. The radial distribution function of MnCl_2 melt was obtained, and a fit to a structural model deduced from possible geometrical orientation among the ions. It was concluded that the coordination number and the nearest distance of the Mn-Cl pair in MnCl_2 melt are about 4.0 and 2.51 Å. A f.c.c. structural model was proposed with loosely distributed Cl atoms with tetrahedral coordination of each Mn atoms. A contribution to the structure from small fraction of octahedrally coordinated Mn could not be ruled out.

Ohno et. al.³⁰ investigated the structure of molten $\text{MnCl}_2 \cdot 2\text{LiCl}$ and $\text{MnCl}_2 \cdot 2\text{KCl}$ by consideration of the radial distribution function. The results indicated that the number of nearest neighbour Mn-Cl pairs of molten $\text{MnCl}_2 \cdot 2\text{KCl}$ and $\text{MnCl}_2 \cdot 2\text{LiCl}$ is 4.0. The data confirmed the existence of $[\text{MnCl}_4^{2-}]$ tetrahedral units in molten $\text{MnCl}_2 \cdot 2\text{KCl}$ and $\text{MnCl}_2 \cdot 2\text{LiCl}$.

Kleppa and McCarty³¹ measured the enthalpies of mixing in MgCl_2 -Alkali chloride systems, except the LiCl-MgCl_2 system, they found a very marked dip in the interaction parameter, $\Delta H/\chi(1-\chi)$, at $X_{\text{MgCl}_2} = 0.33$ which is the concentration corresponding to the formula A_2MgCl_4 . The enthalpy data were interpreted to support the view first suggested by Flood and Urnes³² that the alkali chloride-magnesium chloride systems contain the complex anionic species MgCl_4^{2-} . The stability of this

species depends strongly on the alkali cation, and increases from Lithium to Cesium. Østvoid³³ made e.m.f. measurements in MgCl_2 -Alkali chloride mixtures using glass membrane cells, the entropy curves showed inflection points at $X_{\text{MgCl}_2} = 0.33$. This was accounted for in terms of the presence of an ordered structure in these melts at the composition $X_{\text{MgCl}_2} = 0.33$. Papatheodorou and Kleppa³⁴ have measured calorimetrically the heats of mixing in the binary systems MnCl_2 - AlCl_3 , FeCl_2 - AlCl_3 and CoCl_2 - AlCl_3 . The concentration dependence of the interaction parameters $\Delta H_m / X_1 X_2$ indicated special stabilization of these mixtures at about 33% MCl_2 composition. They attributed this effect to the possible formation of a tetrahedrally coordinated MCl_4^{2-} species. Thermodynamic properties of MnCl_2 - AlCl_3 system were studied³⁵ by emf measurements. The results were interpreted in terms of the presence of MnCl_4^{2-} complex anions.

2. Theory

When⁴⁶ monochromatic light of frequency $\bar{\nu}_0$ is directed at a sample, most of the light passes through the sample. Some of the light is scattered by the sample molecules in all directions. Some of the scattered light has the same frequency $\bar{\nu}_0$ as the incident light, and is called Rayleigh scattering. A small fraction of the scattered light has frequency $\bar{\nu}_i \neq \bar{\nu}_0$. The process of producing light of frequency other than $\bar{\nu}_0$ is called Raman scattering. The amount of scattered light with frequency $\bar{\nu}_i < \bar{\nu}_0$ (Stokes lines) is greater than that with frequency $\bar{\nu}_i > \bar{\nu}_0$ (anti-Stokes lines). As a result of placing a molecule in the electric field of electromagnetic radiation, a dipole moment, $\vec{\mu}_{ind}$, is induced in the molecule and is proportional to the field strength (\vec{E}):

$$\vec{\mu} = \overset{\rightarrow}{\alpha} \vec{E} \quad (2)$$

The polarizability $\overset{\rightarrow}{\alpha}$ is a symmetric tensor containing a combination of symmetric part (α) and asymmetric part (β). The scattered intensity²² may be conveniently divided into two components both theoretically and experimentally, polarized and depolarized and are given by these two equations:

$$I_{\alpha} = I_{iso} = I_{pol} = I_{||} - 4/3 I_{\perp} \quad (3)$$

$$I_{\beta} = I_{aniso} = I_{depol} = I_{\perp} \quad (4)$$

$I_{||}$ is the measured intensity of scattered light polarized in the same

plane as the incident light, and I_{\perp} is the measured intensity of scattered light polarized perpendicular to the incident beam. The anisotropic spectrum I_{β} may be obtained directly from I_{\perp} . The isotropic spectrum may be obtained by the appropriate subtraction of I_{\perp} from I_{\parallel} as may be seen from eqn. 3.

The observed scattered intensity is $I_{(\bar{\nu})}^{obs}$ (either I_{\parallel} or I_{\perp}) and is measured directly from Raman spectrometer. However the intensity of low frequency modes is temperature dependent, and the intensity of these modes is very weak with respect to the intensity of Rayleigh scattering. The contribution from Rayleigh scattering and temperature dependence can be removed by calculation of a corrected intensity $R_2(\bar{\nu})$ as follows²¹:

$$I(i) = K(\bar{\nu}_0 - \bar{\nu}_i)^4 \bar{\nu}_i^{-1} B^{-1} \left(\frac{\partial \alpha}{\partial Q_i} \right)^2 \quad (5)$$

where $R_2(\bar{\nu}) = K \left(\frac{\partial \alpha}{\partial Q_i} \right)^2$ and represents a molar scattering efficiency

$I(i)$ is the intensity of the i^{th} fundamental

K is a constant

$\bar{\nu}_i$ is the frequency of the i^{th} Raman mode in cm^{-1}

$\bar{\nu}_0$ is the excitation frequency in cm^{-1}

$\frac{\partial \alpha}{\partial Q_i}$ is the rate of change in mean molecular polarizability with respect to the normal coordinate, Q_i

B is a factor defined by the following equation

$$B = 1 - \exp(-hc\bar{\nu}_i/k_B T) \quad (6)$$

where k_B is the Boltzmann constant

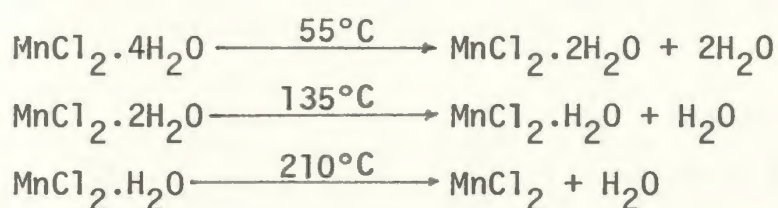
T is the temperature of the sample

The advantage²² of the $R_2(\bar{\nu})$ spectrum is that it suppresses the central Rayleigh peak and emphasizes the Raman peaks so it is quite possible to accurately measure the low frequency region of the Raman spectrum of liquids and melts. The $R_2(\bar{\nu})$ spectrum presents the relative molar scattering efficiencies of Raman bands directly and gives a direct spectrum of the vibrational density of states. In the study which follows both the $I(\bar{\nu})$ and $R_2(\bar{\nu})$ spectra have been constructed from experimental measurements.

3. Experimental Procedures

3.1 Samples Preparation

Analytical reagent $\text{MnCl}_2 \cdot 4\text{H}_2\text{O}$ (BDH) was dehydrated in a vacuum oven, and the temperature was raised slowly over (10 hours) to 180°C . Dehydration was continued in another oven under vacuum at 210°C for 40 hours until all water of hydration has been removed. The dehydrated salt was obtained according to the following equations³⁶:



MgCl_2 (Alpha) was dried under vacuum at 30°C for 24 hours, then the temperature was raised slowly to 180°C where the solid was further dried under vacuum.

Spectrographic grade CsCl and RbCl (Fisher) were dried under vacuum at 180°C for 24 hours.

Reagent grade KCl and NaCl (Anachemia) were recrystallized twice from doubly distilled water and then dried under vacuum at 210°C for 24 hours.

Reagent grade $\text{LiCl} \cdot \text{H}_2\text{O}$ (BDH) was recrystallized twice from doubly distilled water and then dehydrated under vacuum, and the temperature was raised slowly to 120°C . Dehydration was continued at 210°C for 24 hours until the anhydrous LiCl was obtained.

For MnCl_2 -Alkali chloride mixtures, the following samples were prepared according to the appropriate ratios:

- CsMnCl_3 , Cs_2MnCl_4 , Cs_3MnCl_5 , CsMn_4Cl_9
 $\text{CsCl}:\text{MnCl}_2$ (1:2), $\text{CsCl}:\text{MnCl}_2$ (1:3.5)

$\text{CsCl}:\text{MnCl}_2$ (1:4.5)

- RbMnCl_3 , Rb_2MnCl_4 , $\text{Rb}_3\text{Mn}_2\text{Cl}_7$

$\text{RbCl}:\text{MnCl}_2$ (3:1), $\text{RbCl}:\text{MnCl}_2$ (4:1)

- KMnCl_3 , $\text{K}_3\text{Mn}_2\text{Cl}_7$, K_4MnCl_6

$\text{KCl}:\text{MnCl}_2$ (2:1), $\text{KCl}:\text{MnCl}_2$ (3:1)

- NaMnCl_3 , Na_2MnCl_4 , $\text{Na}_2\text{Mn}_3\text{Cl}_8$, NaMn_4Cl_9 , Na_6MnCl_8

$\text{NaCl}:\text{MnCl}_2$ (3:1)

- $\text{LiCl}:\text{MnCl}_2$ (1:1), $\text{LiCl}:\text{MnCl}_2$ (2:1), $\text{LiCl}:\text{MnCl}_2$ (3:1)

For MgCl_2 - Alkali chloride mixtures, the following samples were prepared according to the appropriate ratios:

- CsMgCl_3 , Cs_2MgCl_4

$\text{CsCl}:\text{MgCl}_2$ (1.5:1), $\text{CsCl}:\text{MgCl}_2$ (0.5:1), $\text{CsCl}:\text{MgCl}_2$ (4:1)

- KMgCl_3 , K_2MgCl_4

$\text{KCl}:\text{MgCl}_2$ (1.5:1), $\text{KCl}:\text{MgCl}_2$ (0.5:1)

The appropriate quantities of the salts were placed in 4 mm i.d. quartz tubes, heated under vacuum such that temperature was raised slowly to 210°C , maintained at this value for at least 24 hours, and then the temperature slowly raised until the salt mixtures melted. The salts and the salt mixtures are hygroscopic so all manipulation were performed in a glove box under dry Nitrogen. After melting the salt mixtures, the melts of MnCl_2 samples were clear yellow liquids and showed no evidence of any impurities. The melts of MgCl_2 samples were colorless liquids and showed no evidence of any impurity such as solid MgO . The samples were cooled to room temperature and sealed under vacuum. It appeared that each salt could be characterized by its Raman spectrum since at least one peak occurred for each compound in the region of stability predicted by the phase diagram. Except for one

sample of CsMgCl_3 which was not properly sealed the sample gave reproducible Raman spectra even after an interval of several months.

3.2 Characterization of the Solids

Each solid was characterized by its distinct Raman spectrum. Attempts were made to characterize the solid compounds through X-ray diffraction powder patterns. Powder patterns were obtained for powdered samples sealed in Lindemann tubes by Debye-Scherrer camera methods both at the Earth Science Department, Memorial and at AECL, Pinawa. The results were not very encouraging because the samples deteriorated rapidly in the transfer process from the quartz Raman tube into the Lindemann tube. It was obvious that even in a dry box the grinding operation gave sufficient time and surface area for absorption of considerable water. Powder patterns of RbMnCl_3 and Rb_2MnCl_4 which agreed with the literature were obtained but the powder patterns for CsMnCl_3 and Cs_2MnCl_4 had deteriorated to those of the hydrated salts. Raman and infrared spectra of CsMnCl_3 and Cs_2MnCl_4 from the opened samples also revealed the presence of water of hydration. No attempts were made to obtain powder patterns for the other samples since it would have necessitated destroying the samples prepared for Raman studies.

3.3 Raman Spectroscopic Measurements

3.3.1 Molten Phase

Raman spectra were collected digitally with a Coderg PHO spectrometer. The melts of MnCl_2 and MnCl_2 -Alkali Chloride were recorded

after sample excitation with the 6471 Å (150 mw) and 5682 Å (100 mw) lines of Coherent Laser model 52 Krypton-Argon ion laser or a Control Laser model 552 Krypton ion laser with slit width 2 cm⁻¹. The scan rate was 50 cm⁻¹/min., and the photon counts were accumulated for 0.01 min. Ten scans were collected in both parallel X(ZZ)Y and perpendicular X(ZX)Y orientations, and the digital output recorded on a disk at the M.U.N. Computer Services VAX-11/780. The spectra were averaged, baseline corrected and converted into the R₂ format. The spectra were then plotted on a TEKTRONIX 4662 digital interactive plotter with the aid of a TEKTRONIX 4051 graphics terminal. Subtraction files were created by subtracting I_⊥ (perpendicular) data from I_{||} (parallel) data to obtain the isotropic Raman spectra $I_{iso} = I_{||} - 4/3I_{\perp}$.

The melts of MgCl₂ and MgCl₂-CsCl mixtures were recorded digitally after sample excitation with the 4880 Å (500 mw) line of Control Laser model 553 Argon ion laser with slit width 2 cm⁻¹. The melts of MgCl₂-KCl system were measured after sample excitation with the 4880 Å (500 mw) line of Control Laser model 552 Argon ion laser with slit width 4 cm⁻¹. Ten scans were collected for each orientation. The scan rate was 50 cm⁻¹/min. and the photon counts were accumulated for 0.01 min. for the melts except for MgCl₂ and CsCl:MgCl₂ (4:1) melts the counts were accumulated for 0.02 min. The output spectra were recorded on a computer disk, averaged, baseline corrected, and converted into the R₂ format. The spectra were plotted using the TEKTRONIX devices. Subtraction files were created to obtain isotropic Raman spectra.

All Raman spectra of the melts were viewed and analyzed in the I($\bar{\nu}$) and R₂($\bar{\nu}$) formats. The isotropic spectra in both formats (i.e., I_α($\bar{\nu}$) and R_{2α}($\bar{\nu}$)) were subject to detailed band deconvolution analysis

with a program called FITTER. Both Lorentzian and a Gaussian*Lorentzian product function were employed for each data set but detailed analysis were not very sensitive to the type of function. The best fit data are reported along with the function type.

The $\text{MgCl}_2 \cdot n\text{ACl}$ data for $n \geq 1$ gave clear indication of at least three polarized components in the symmetric stretching region and the curve analysis was restricted to three band fits. Two band fits gave inconsistent results. For $n < 1$ additional low frequency intensity was obvious and a fourth band was employed. For the magnesium system the $I_\alpha(\bar{\nu})$ spectra gave the most consistent results and these results are reported. The $R_2(\bar{\nu})$ spectra seemed to overemphasize the weak broad high frequency component centered at about 300 cm^{-1} . Because of the complexity of the spectra the best fit data reported may not be unique. The peak frequencies of the components are probably accurate to $\pm 2 \text{ cm}^{-1}$ but the error in halfwidths and intensities is difficult to estimate and for this reason only the trends of the three major components at about 210, 250 and 300 cm^{-1} would appear significant for samples with $n \leq 2$. For $n > 2$ the peak frequency and halfwidth of the single component is probably accurate to $\pm 1 \text{ cm}^{-1}$.

The $\text{MnCl}_2 \cdot n\text{ACl}$ data for $n \geq 1$ gave no indication of more than one polarized component. Two band fits were not significantly better than one band fits. Reasonable fits were obtained for both the $I_\alpha(\bar{\nu})$ and $R_{2\alpha}(\bar{\nu})$ formats and the one band fits for the $R_{2\alpha}(\bar{\nu})$ spectra are reported. For $\text{MnCl}_2 \cdot n\text{NaCl}$ melts ($n \geq 1$) a broad low frequency component ~ 150 - 230 cm^{-1} was apparent and a second peak was necessary to fit the data. Because of the breadth and uncertainty of this peak it was not considered significant and could be an artifact of the subtraction routine. The peak frequencies and halfwidths for the intense single component about 250 cm^{-1} are probably accurate to $\pm 2 \text{ cm}^{-1}$.

The spectra of the melts were obtained from samples in a furnace with the inner core wound with nichrome heating coil. The temperatures were monitored with a Chromel-Alumel thermocouple on the sample container as shown (Fig. 1). The thermocouple was calibrated with ice, boiling water and known phase transitions. Temperatures are probably accurate to about 1%.

Plasma lines were removed with the appropriate interference filter for each exciting line. Depolarization measurements for the melts were made by analyzing the scattered light parallel $X(ZZ)Y [I_{||}]$ and perpendicular $X(ZX)Y [I_{\perp}]$ to the incident laser beam.

3.3.2 Solid Phase

Raman spectra were recorded with a Coderg PHO spectrometer. Spectra of yellow compounds Cs_2MnCl_4 and Cs_3MnCl_5 at room and liquid nitrogen temperatures and below their melting points were recorded using the yellow exciting line 5682 \AA (100 mw) of Coherent Laser model 52 Krypton-Argon ion laser with slit width 2 cm^{-1} . For Cs_2MnCl_4 a possible phase change from low-temperature phase to high-temperature phase was investigated. The effect of temperature on the totally symmetric stretching vibration (ν_1) of Cs_2MnCl_4 and Cs_3MnCl_5 was recorded.

Spectra of the red compounds $CsMnCl_3$, $CsMn_4Cl_9$, $Na_2Mn_3Cl_8$, and $NaMn_4Cl_9$ at room temperature were recorded digitally after sample excitation with the 6764 \AA (30 mw) line of Control Laser model 552 Krypton ion laser with 4 cm^{-1} slit width, while the spectra of the other samples were collected digitally at room temperature after sample excitation with the 6471 \AA (150 mw) line of Control Laser model 552 Krypton ion laser with 4 cm^{-1} slit width. Eight scans were collected for each sample, the scan rate

was $50 \text{ cm}^{-1}/\text{min.}$, and the photon counts were accumulated for 0.01 min. The spectra were stored on a computer disk, averaged, base line corrected and converted to $R_2(\bar{\nu})$ format and then plotted using the TEKTRONIX devices. The $I(\bar{\nu})$ spectra are only plotted here.

Plasma lines were removed using an interference filter for each exciting line. The colour of the sample should match the colour of the laser light to minimize absorption. The Raman spectra of the yellow compounds were measured using the exciting line 5682 \AA , while the spectra of the red compounds were recorded using the exciting lines 6471 and 6764 \AA . The visible spectra indicate that these samples have an absorption in the blue and green regions, so the exciting lines 4880 and 5145 \AA could not be used. The exciting line 5682 \AA could not be used for measuring the Raman spectra of the red compounds because these samples have an absorption in the yellow region also. The spectra of red compounds were very difficult to obtain because octahedral manganese has a very broad visible absorption which extends into the red. It is also a highly fluorescent material. Ghost peaks were observed in most of the recorded spectra because these samples are weak scatters and high gain setting were required. Improved relatively ghost free spectra could be obtained by subtraction of a ghost spectrum measured from a white blank scatterer.

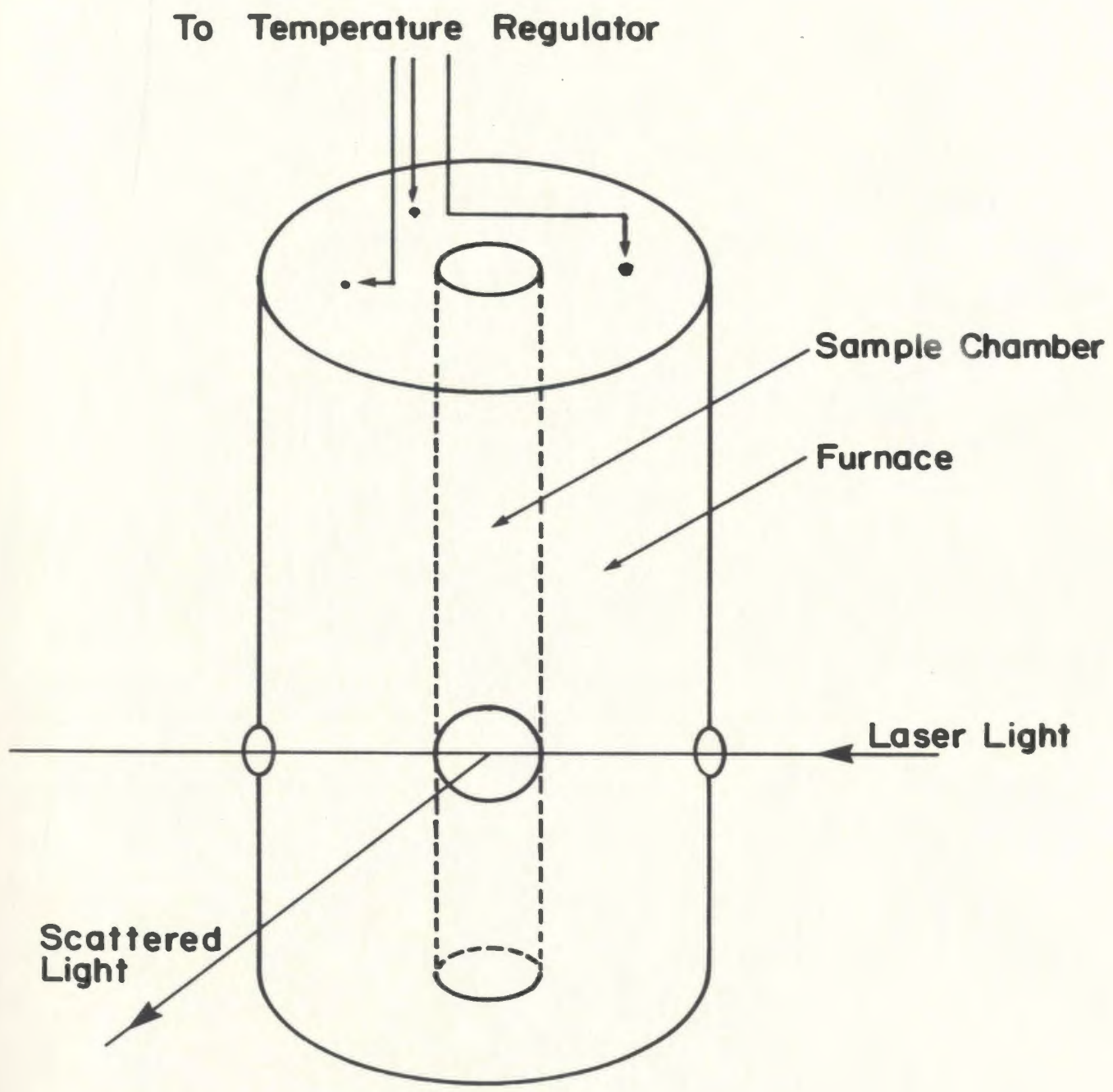
3.4 Visible Spectroscopic Measurements

The visible spectra of the solids and the melts were obtained in the optical range 23042 to 15042 cm^{-1} . The spectra were recorded digitally using the Coderg PH0 spectrometer as an absorption spectrometer with a projection lamp of 300 watts (Canadian General Electric 32).

Slit widths 4 and 2 cm^{-1} were employed for the solids and the melts. The spectra of the melts were obtained from samples in a furnace as shown in figure 1. The scan rate was 50 $\text{cm}^{-1}/\text{min.}$, and the counts were accumulated for 0.04 min. One scan was collected for the projection lamp and another scan for the sample. After subtracting the two files, the subtracted file represented the visible spectrum of the sample. The relative absorbances of the visible spectra can not be directly related to the usual visible absorbance values since the spectra were obtained by different method whereas in conventional visible spectrometers the absorbance values are ratioed against the reference beam. All visible spectra were plotted on a TEKTRONIX 4662 digital interactive plotter with the aid of a TEKTRONIX 4051 graphics terminal.

Attempts were made to obtain the visible spectra using a Cary 17 spectrometer but the difficulty of maintaining the sample under dry conditions in the sample compartment prevented measurement of a satisfactory spectrum. Several attempts to melt samples into very thin glass tubes still resulted in samples that were too thick and resulted in total absorption of the incident light. The use of the Coderg PHO spectrometer with its very sensitive photomultiplier tube permitted the measurement of visible spectra of melts and solids in the same sample tubes as employed for the Raman studies.

Figure 1. Sample furnace.



4. Results and Discussion

4.1 Raman Studies of MnCl₂.nAcl: Solid state

4.1.1 MnCl₂

MnCl₂⁷¹ has the CdCl₂ structure with space group R $\bar{3}m(D_{3d}^5)$ and one molecule per unit cell. Mn atoms occupy D_{3d} site symmetry while Cl atoms occupy C_{3v} sites. Nine modes are predicted from factor group analysis and distributed as follows:

$$\begin{aligned}
 \Gamma_{\text{Mn}} &= A_{2u} + E_u \\
 \Gamma_{\text{Cl}} &= A_{1g} + E_g + A_{2u} + E_u \\
 \Gamma_{\text{total}} &= A_{1g} + E_g + 2A_{2u} + 2E_u \\
 \Gamma_{\text{acoustic}} &= A_{2u} + E_u
 \end{aligned} \tag{7}$$

A_{1g} and E_g modes are Raman active, while A_{2u} and E_u modes are IR active. The Raman spectrum of solid MnCl₂ is shown in figure 2 and peak frequencies and assignments are shown in Table 1.

4.1.2 MnCl₂-CsCl System

The phase diagram of the MnCl₂-CsCl system^{37,38} indicates the presence of four double salts, three congruent compounds; CsMnCl₃, melting point 593°C; Cs₂MnCl₄, melting point 538°C; Cs₃MnCl₅, melting point 511°C, and one incongruent melting CsMn₄Cl₉, melting point 537°C.

(i) Cs₂MnCl₄

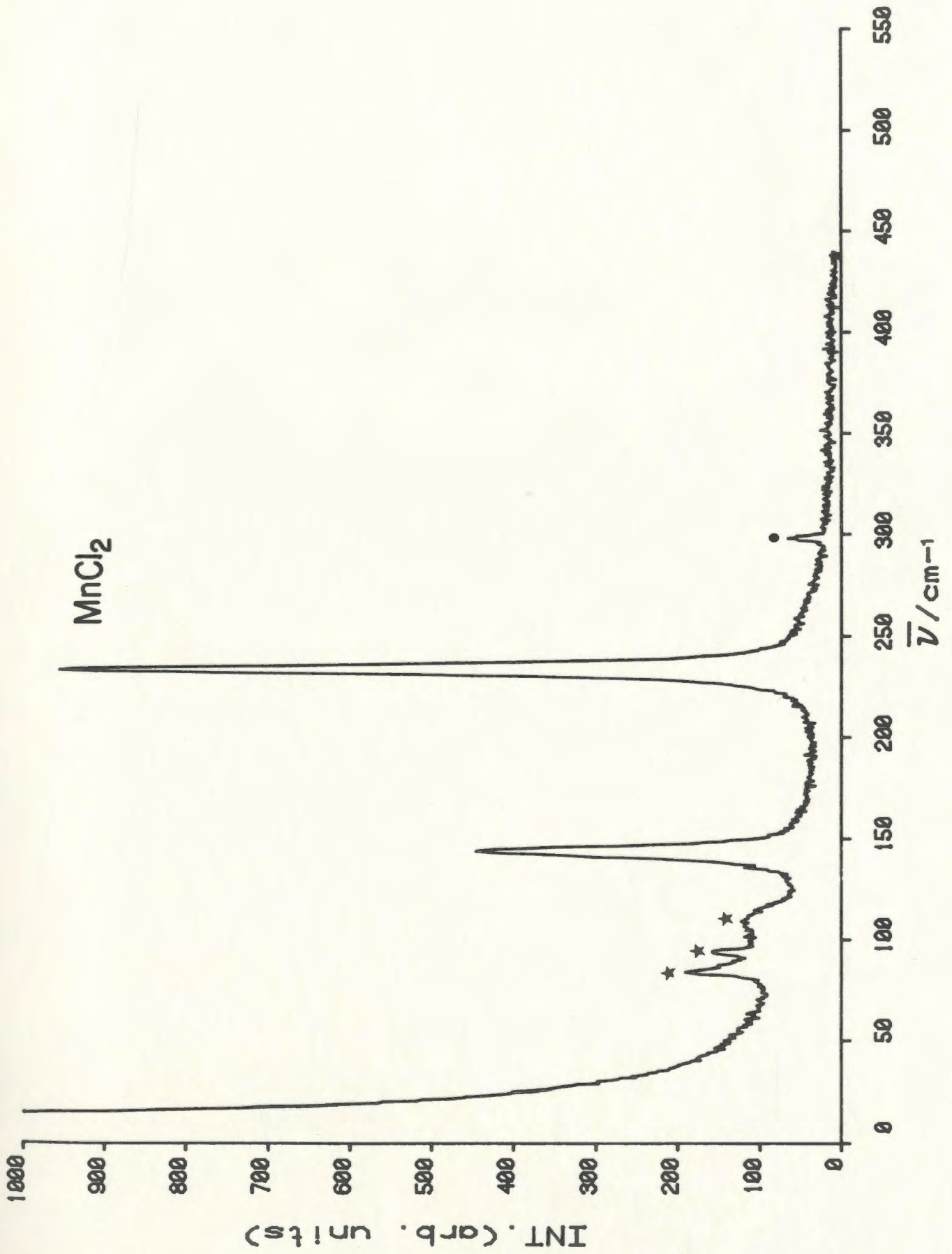
The reports on the structure of Cs₂MnCl₄ are not consistent.^{39,41,43,44,45} It has been reported that at room temperature Cs₂MnCl₄ has the Cs₂MnBr₄ structure⁴⁰: space group Pnma(D_{2h}¹⁶), four formulas per unit cell. This structure is isomorphous with Cs₂MgCl₄⁴² which contains discrete MgCl₄²⁻ ions. On the other hand it has been reported^{43,44} that

Table 1. Peak frequencies in cm^{-1} and assignments for solid MnCl_2 .

Frequency	Assignments
143 m-s	E_g
233 v.s	A_{1g}

m-s: medium-strong, v.s: very strong

Figure 2. Raman spectrum of solid MnCl_2 at room temperature. The stars indicate ghost peaks. The dot indicate plasma line.



Cs_2MnCl_4 exists in two phases; a tetragonal room temperature form called $\alpha\text{-Cs}_2\text{MnCl}_4$ or (T-form) and an orthorhombic high temperature form stable above 298°C called $\beta\text{-Cs}_2\text{MnCl}_4$ or (H-form). It has been proposed that the α -form has space groups $I4/mmm(D_{4h}^{17})$ and is isomorphous with K_2NiF_4 and K_2MgCl_4 ⁴² but the β -form has space group $\text{Pnma}(D_{2h}^{16})$ and is isomorphous with Cs_2ZnCl_4 and Cs_2MgCl_4 . Seifert^{43,44} also reported that the red α -phase transformed to the yellow β -phase at 298°C . In the present study it was found that Cs_2MnCl_4 had a greenish yellow color at all temperatures, and the Raman spectra of the compound obtained over a wide range of temperatures from 77 K to the melting point remained the same as long as the sample remained sealed under vacuum. Attempts were made to follow the reported⁷⁵ $\alpha\rightarrow\beta$ phase transformation by thermally annealing the sample above and below the reported phase transition but no evidence of a phase transformation could be found. However if the sample was opened to the atmosphere, absorption of a small amount of water ($\sim 0.2\%$) was sufficient to cause the yellow compound to turn pale red. This red compound which could be written as $\text{Cs}_2\text{MnCl}_4 \cdot 0.16\text{H}_2\text{O}$ was very stable and the Raman spectrum indicated that this compound probably does have the K_2NiF_4 structure type. Furthermore the red compound could be converted to the yellow by heating to about 300°C , at which point water condensed in the cold part of the tube. The Raman spectra of Cs_2MnCl_4 at 77, 298 and 800 K strongly confirm the presence of discrete MnCl_4^{2-} ions and this indicate that Cs_2MnCl_4 is isostructural with Cs_2MgCl_4 . Most previous studies of Cs_2MnCl_4 at room temperature have really been made for the hydrate $\text{Cs}_2\text{MnCl}_4 \cdot 0.16\text{H}_2\text{O}$.

Manganese is tetrahedrally coordinated with distinct MnCl_4^{2-} ions present in the Cs_2MnCl_4 lattice. As shown from equation (1), four Raman active vibrations are expected for MnCl_4^{2-} ions, two stretching $\nu_1(A_1)$; $\nu_3(T_2)$ and two bending $\nu_2(E)$; $\nu_4(T_2)$. These four vibrations are calculated from group theoretical prediction^{46,47} by counting the number of unmoved atoms under each operation of the point group T_d , and multiply these numbers by the character $\Gamma_{x,y,z}$ under each operation to obtain $\Gamma_{\text{red.}}$ as shown in Table 2. From $\Gamma_{\text{red.}}$, Γ_{total} and then $\Gamma_{\text{vib.}}$ are obtained.

$$\begin{aligned}
 \Gamma_{\text{total}} &= A_1 + E + T_1 + 3T_2 \\
 \Gamma_{\text{trans}} &= T_2 \\
 \Gamma_{\text{rot}} &= T_1 \\
 \Gamma_{\text{vib}} &= A_1 + E + 2T_2 \qquad (8)
 \end{aligned}$$

A description of these vibrations⁴⁸ is shown in figure 3.

Cs_2MnCl_4 has space group $\text{Pnma}(D_{2h}^{16})$ with four formula units per primitive unit cell, and the site symmetries of the ions are as follows: MnCl_4^{2-} , C_s ; 2Cs^{+1} , C_s . One expect $3.N.Z = 3.7.4 = 84$ modes distributed as follows:

Modes due to MnCl_4^{2-} ions

Internal modes = 36

Lattice modes (external modes) = 24

Modes due to Cs^{+1} ions

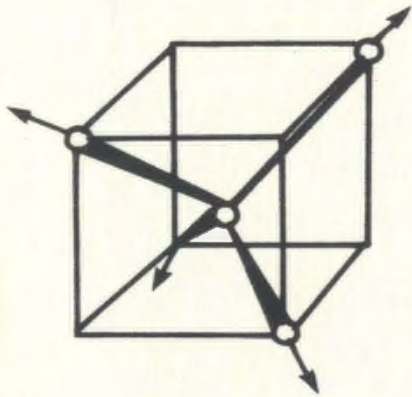
Lattice modes (external modes) = 24

These modes are calculated using the correlation method as shown in Tables 3, 4, 5 and 6.

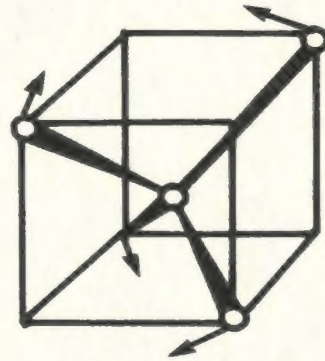
Table 2. Determination of $\Gamma_{\text{red.}}$ for MnCl_4^{2-} ion.

T_d	E	$8C_3$	$3C_2$	$6S_4$	$6\sigma_d$
unmoved atoms	5	2	1	1	3
$\Gamma_{x,y,z}$	3	0	-1	-1	1
$\Gamma_{\text{red.}}$	15	0	-1	-1	3

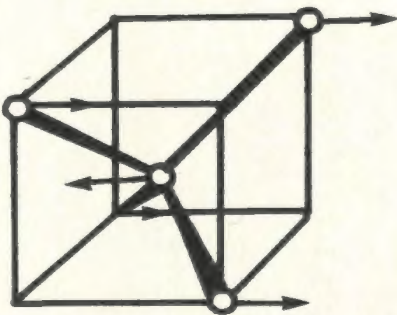
Figure 3. Normal vibrations of a tetrahedral molecule.



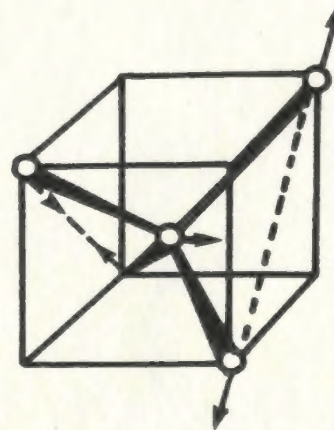
$\nu_1(A_1)$



$\nu_2(E)$



$\nu_3(T_2)$



$\nu_4(T_2)$

Table 3. Internal modes of MnCl_4^{2-} ion.

$f=Z \cdot \nu_{\text{vib}}$	ν_{vib}	Molecular Symmetry (T_d)	<u>correlation</u>	Site Symmetry (C_s)	<u>correlation</u>	Space Group (D_{2h})
4	$1(\nu_1)$	$1A_1$		$(1+1+2+2)A'$	A_g 6 B_{1g} 6 B_{2u} 6 B_{3u} 6	
8	$2(\nu_2)$	$1E$		$(1+2)A''$	B_{2g} 3 B_{3g} 3 A_u 3 B_{1u} 3	
<u>24</u>	$6(\nu_3, \nu_4)$	$2T_2$				
36 modes						36 modes

Table 4. Lattice modes of MnCl_4^{2-} ion (Translation).

$f^\gamma = z \cdot t^\gamma$	t^γ	C_s Site Symmetry species containing translation (γ)	<u>correlation</u>	D_{2h} Space group
8	$2(T_x, T_y)$	A'	A_g	2
			B_{1g}	2
			B_{2u}	2
			B_{3u}	2
4	$1T_z$	A''	B_{2g}	1
			B_{3g}	1
			A_u	1
			B_{1u}	1
12 modes				12 modes

Table 5. Lattice modes of MnCl_4^{2-} ion (Rotation).

$f^{\gamma} = z.t^{\gamma}$	t^{γ}	C_s Site Symmetry species containing rotation (γ)	<u>correlation</u>	D_{2h} Space group	
4	$1R_z$	A'		A_g	1
				B_{1g}	1
				B_{2u}	1
				B_{3u}	1
8	$2(R_x, R_y)$	A''		B_{2g}	2
				B_{3g}	2
				A_u	2
				B_{1u}	2
12 modes				12 modes	

Table 6. Lattice modes of Cs⁺¹ ions.

$f^{\gamma} = Z \cdot t^{\gamma}$	t^{γ}	C_s Site Symmetry species containing translation (γ)	<u>correlation</u>	D_{2h} Space group
16	$2(T_x, T_y)$	A'	A_g	4
			B_{1g}	4
			B_{2u}	4
			B_{3u}	4
8	$1T_z$	A''	B_{2g}	2
			B_{3g}	2
			A_u	2
			B_{1u}	2
24 modes				24 modes

$$\Gamma_{\text{total}} = \Gamma_{\text{MnCl}_4^{2-}} \text{ (internal modes)} + \Gamma_{\text{MnCl}_4^{2-}} \text{ (lattice modes) (trans.)} \\ + \Gamma_{\text{MnCl}_4^{2-}} \text{ (lattice modes) (rot.)} + \Gamma_{2\text{Cs}^+1} \text{ (lattice modes)}$$

$$\Gamma_{\text{MnCl}_4^{2-}} \text{ internal modes} = 6A_g + 6B_{1g} + 6B_{2u} + 6B_{3u} + 3B_{2g} + 3B_{3g} + 3A_u + 3B_{1u}$$

$$\Gamma_{\text{MnCl}_4^{2-}} \text{ lattice modes (trans.)} = 2A_g + 2B_{1g} + 2B_{2u} + 2B_{3u} + B_{2g} + B_{3g} + A_u + B_{1u}$$

$$\Gamma_{\text{MnCl}_4^{2-}} \text{ lattice modes (rot.)} = A_g + B_{1g} + B_{2u} + B_{3u} + 2B_{2g} + 2B_{3g} + 2A_u + 2B_{1u}$$

$$\Gamma_{2\text{Cs}^+1} \text{ lattice modes} = 4A_g + 4B_{1g} + 4B_{2u} + 4B_{3u} + 2B_{2g} + 2B_{3g} + 2A_u + 2B_{1u}$$

$$\Gamma_{\text{total}} = 13A_g + 13B_{1g} + 13B_{2u} + 13B_{3u} + 8B_{2g} + 8B_{3g} + 8A_u + 8B_{1u} \quad (9)$$

$$\Gamma_{\text{acoustic}} = B_{2u} + B_{3u} + B_{1u}$$

As shown from equation (9) eighty-four modes are predicted, three of which are acoustic. All g modes are Raman active, all u modes are IR active, and A_u is inactive. The Raman spectra of Cs_2MnCl_4 in the solid at 77, 298, and 800 K are shown in figure 4. The spectra strongly indicate the existence of the tetrahedral MnCl_4^{2-} ion. The totally symmetric vibration⁴⁹ (ν_1) of MnCl_4^{2-} has been reported in the solid at 258 cm^{-1} and in solution as a polarized line at 251 cm^{-1} . A peak due to ν_4 was reported as shoulder at 116 cm^{-1} . The present assignments have been made by analogy with spectrum of Cs_2MgCl_4 ¹⁴. Peak positions and assignments are shown in Table 7.

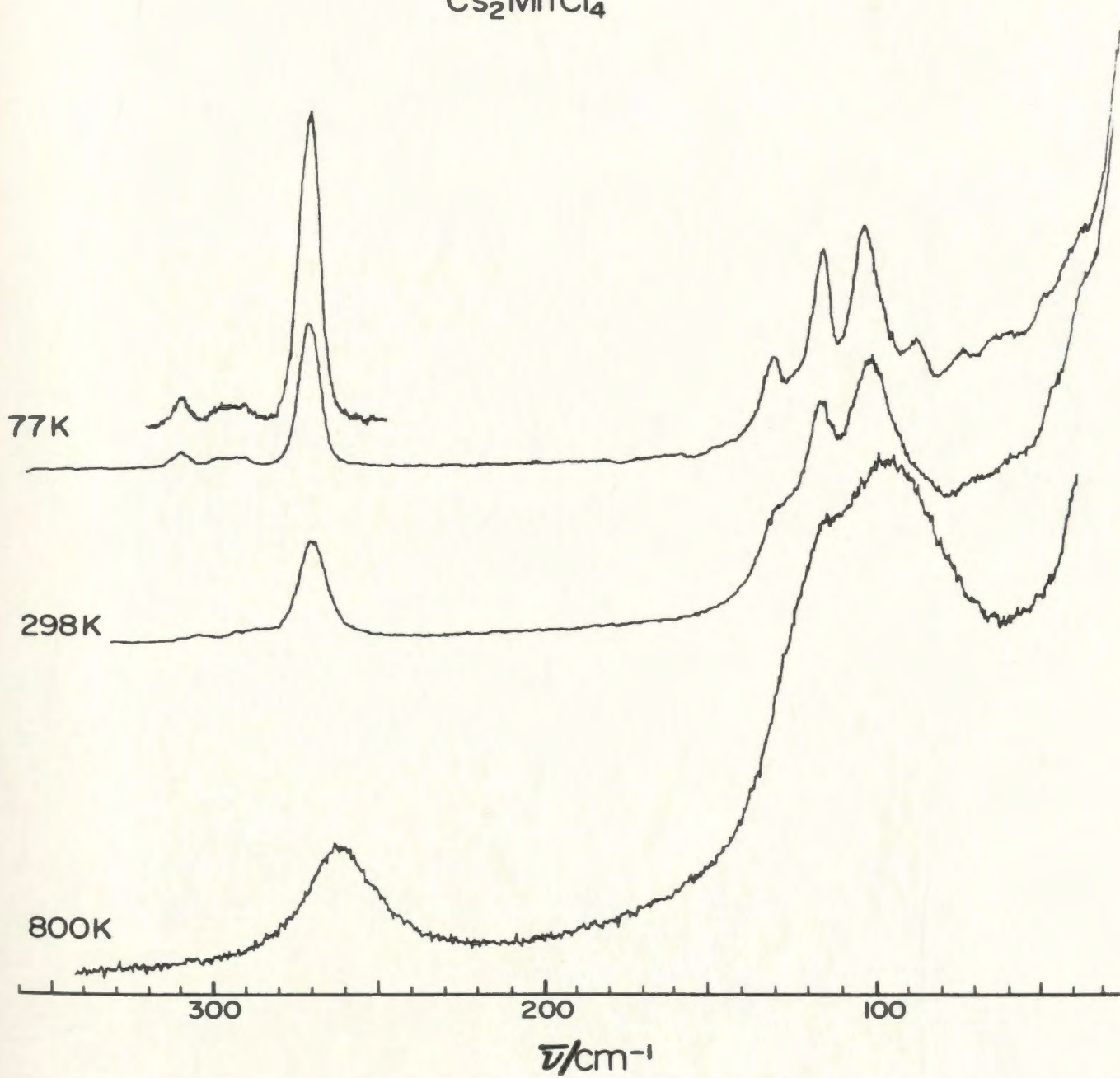
Table 7. Assignments and peak positions in cm^{-1} for solid Cs_2MnCl_4 .

77 K	Frequency		Assignments	
	298 K	800 K		
40 sh,m	39 sh,m		$B_{1g} + B_{2g} + B_{3g}$	} Lattice modes
51 sh,w	47 sh,m-w		B_{2g}	
63 w	61 v.w		A_g	
75 w	72 v.w		$A_g + B_{1g}$	
89 w	85 sh,v.w		$B_{2g} + B_{3g}$	} ν_2
106 m	102 m	98 m	A_g	
118 m	117 m	116 s	$B_{2g} + B_{3g}$	} ν_4
133 m-w	131 sh, m		A_g	
272 m (7.5) ^a	271 m (10.3)	262 m (25)	A_g	ν_1
292 v.w	293 v.w		$A_g + B_{1g}$	} ν_3
298 v.w			$B_{2g} + B_{3g}$	
310 v.w	306 v.w		$A_g + B_{1g}$	

a: half band width is given in parenthesis

v.w: very weak, w: weak, m: medium, s: strong, sh: shoulder

Figure 4. Raman spectra of solid Cs_2MnCl_4 at 77, 298,
and 800 K.



(ii) Cs_3MnCl_5

The X-ray study⁵¹ on single crystal of Cs_3MnCl_5 indicated that Cs_3MnCl_5 is isomorphous with Cs_3CoCl_5 and has space group $I4/mcm$ (D_{4h}^{18}) with two formula units per primitive unit cell. In the structure the Mn ion is coordinated by Cl(2) ions to form individual MnCl_4^{2-} tetrahedra, and the structure can be considered as composed of Cs^+ , $[\text{MnCl}_4]^{2-}$ and $\text{Cl}(1)^-$ ions. The site symmetries of the ions are as follows: MnCl_4^{2-} , D_{2d} ; $\text{Cs}(1)$, D_4 ; $\text{Cs}(2)$, C_{2v} ; $\text{Cl}(1)$, C_{4h} .

Since the number of formulas per primitive unit cell are two, fifty-four modes are predicted from factor group analysis and distributed as follows:

- 18 modes due to internal modes of MnCl_4^{2-} ion
- 12 modes due to lattice modes of MnCl_4^{2-} ion
- 12 modes due to lattice modes of $\text{Cs}(2)$ ion
- 6 modes due to lattice modes of $\text{Cs}(1)$ ion
- 6 modes due to lattice modes of $\text{Cl}(1)$ ion

$$\Gamma_{\text{total}} = \Gamma_{\text{Mn}} + \Gamma_{\text{Cl}(2)} + \Gamma_{\text{Cl}(1)} + \Gamma_{\text{Cs}(1)} + \Gamma_{\text{Cs}(2)}$$

but

$$\Gamma_{\text{Mn}} + \Gamma_{\text{Cl}(2)} = \Gamma_{\text{MnCl}_4^{2-}} (\text{internal modes}) + \Gamma_{\text{MnCl}_4^{2-}} (\text{lattice modes})$$

$$\begin{aligned} \Gamma_{\text{total}} &= \Gamma_{\text{MnCl}_4^{2-}} (\text{internal modes}) + \Gamma_{\text{MnCl}_4^{2-}} (\text{lattice modes}) \\ &+ \Gamma_{\text{Cs}(1)} + \Gamma_{\text{Cs}(2)} + \Gamma_{\text{Cl}(1)} \end{aligned}$$

$\Gamma_{\text{Cs}(1)}$, $\Gamma_{\text{Cs}(2)}$, and $\Gamma_{\text{Cl}(1)}$ are shown in equations (10), (11), and (12).

$$\Gamma_{\text{Cs}(1)} = A_{2g} + E_g + A_{2u} + E_u \quad (10)$$

$$\Gamma_{\text{Cs}(2)} = A_{1g} + A_{2g} + B_{1g} + B_{2g} + E_g + A_{2u} + B_{1u} + 2E_u \quad (11)$$

$$\Gamma_{\text{Cl}(1)} = A_{1u} + A_{2u} + 2E_u \quad (12)$$

The internal and lattice modes for MnCl_4^{2-} ion are shown by correlation method in Tables 8, 9, and 10.

$$\Gamma_{\text{total}} = 3A_{1g} + 3A_{2g} + 2B_{1g} + 4B_{2g} + 6E_g + 2A_{1u} + 6A_{2u} + 3B_{1u} + B_{2u} + 9E_u \quad (13)$$

$$\Gamma_{\text{acoustic}} = A_{2u} + E_u$$

B_{1u} and B_{2u} are inactive, all the u modes are IR active and all the g modes are Raman active according to the rule of mutual exclusion.

The Raman spectra of Cs_3MnCl_5 at 77 K, 298 K, and 760 K are shown in figure 5. The spectra strongly indicate the presence of tetrahedral MnCl_4^{2-} species as suggested before²³. For the totally symmetric vibration (ν_1), splittings are observed due to ^{35}Cl and ^{37}Cl isotopes. The three peaks observed at 272.5, 273.8, and 275.9 cm^{-1} are assigned to $\text{Mn}^{35}\text{Cl}_2^{37}\text{Cl}_2^{2-}$, $\text{Mn}^{35}\text{Cl}_3^{37}\text{Cl}^{2-}$, and $\text{Mn}^{35}\text{Cl}_4^{2-}$ ions. Assignments are made by analogy with the spectrum of Cs_3MgCl_5 ¹⁶. Peak positions and assignments are shown in Table 11.

(iii) CsMnCl_3

It has been reported⁷⁶ that CsMnCl_3 has space group R3m, however

Table 8. Internal modes of MnCl_4^{2-} ion.

$f=Z \cdot \nu_{\text{vib}}$	ν_{vib}	Molecular Symmetry (T_d)	correlation	Site Symmetry (D_{2d})	correlation	Space Group (D_{4h})	
2	$1(\nu_1)$	A_1	—	A_1	—	A_{1g}	1
						B_{1u}	1
4	$2(\nu_2)$	E	—	A_1	—	A_{1g}	1
						B_{1u}	1
				B_1	—	B_{1g}	1
						A_{1u}	1
						E_g	1 d
				E	—	E_u	1 d
6	$3(\nu_3)$	T_2	—	B_2	—	B_{2g}	1
						A_{2u}	1
				E	—	E_g	1 d
						E_u	1 d
				B_2	—	B_{2g}	1
						A_{2u}	1
18 modes							18 modes

d: doubly degenerate mode

Table 9. Lattice modes of MnCl_4^{2-} ion (Translation).

$f^{\gamma} = z \cdot t^{\gamma}$	t^{γ}	D_{2d} Site Symmetry species containing translation (γ)	<u>correlation</u>	D_{4h} Space group
2	$1T_z$	B_2	B_{2g}	1
			A_{2u}	1
4	$2(T_x, T_y)$	E	E_g	1 d
			E_u	1 d
6 modes			6 modes	

d: doubly degenerate mode

Table 10. Lattice modes of $MnCl_4^{2-}$ ion (Rotation).

$f^{\gamma} = z \cdot t^{\gamma}$	t^{γ}	D_{2d} Site Symmetry species containing rotation (γ)	<u>correlation</u>	D_{4h} Space group	
2	$1R_z$	A_2		A_{2g}	1
				B_{2u}	1
4	$2(R_x, R_y)$	E		E_g	1 d
				E_u	1 d
6 modes				6 modes	

d: doubly degenerate mode

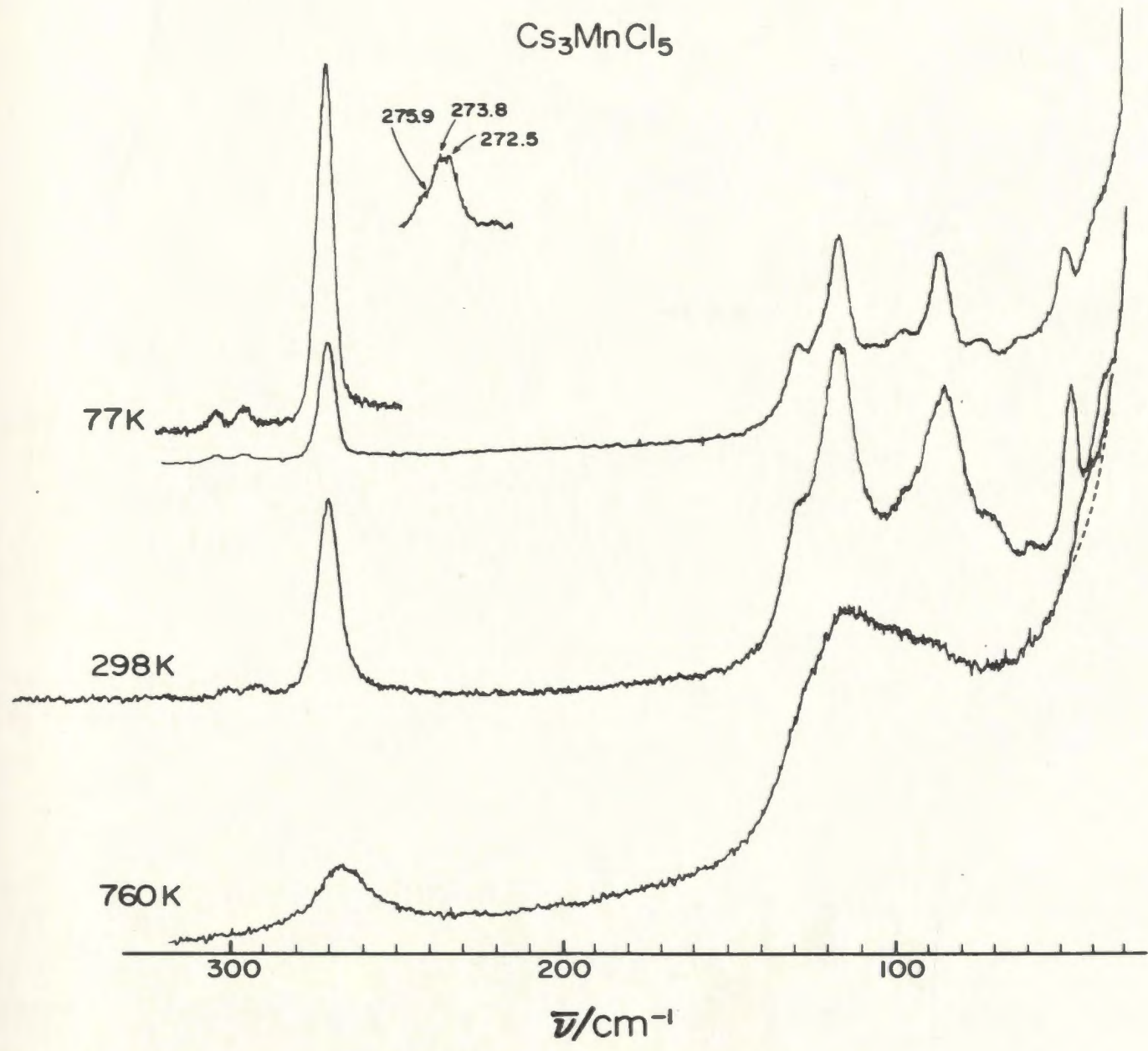
Table 11. Assignments and frequencies in cm^{-1} for solid Cs_3MnCl_5 .

77 K	Frequency		Assignments
	298 K	760 K	
41 sh,m-w	38 sh,m-w	~41 sh,m	$\left. \begin{array}{l} E_g \\ B_{2g} \\ A_{1g} \\ E_g \end{array} \right\} \text{Lattice modes}$
51 m-w	49 m		
64 v.w	61 v.w		
77 v.w	72 w		
88 m-w	87 m	~90 w	$\left. \begin{array}{l} A_{1g} \\ B_{1g} \end{array} \right\} \nu_2$
100 v.w	99 sh, v.w		
119 m	118 m	114 m-s	$\left. \begin{array}{l} E_g \\ B_{2g} \end{array} \right\} \nu_4$
131 sh,m	130 sh,m		
273 m (5.8) ^a	272 m (8.0)	265 m-w (20)	$A_{1g} \quad \nu_1$
298 v.w	294 v.w		$\left. \begin{array}{l} E_g \\ B_{2g} \end{array} \right\} \nu_3$
307 v.w	303 v.w		

a: half band width is given in parenthesis

v.w: very weak, w: weak, m: medium, s: strong, sh: shoulder

Figure 5. Raman spectra of solid Cs_3MnCl_5 at 77, 298, and 760 K.



neutron diffraction data⁵³ indicated that CsMnCl_3 has space group $R\bar{3}m$. A recent⁵² crystal structure determination on a single crystal of CsMnCl_3 confirmed that CsMnCl_3 crystallizes in the centric space group $R\bar{3}m (D_{3d}^5)$ with three formulas per primitive unit cell. The compound consists of $[\text{Mn}_3\text{Cl}_{12}]$ trimers with each trimer linked to the other trimers by corner sharing, the central manganese atom of a trimer has D_{3d} site symmetry, and the two terminal manganese atoms of a trimer have C_{3v} site symmetry. The site symmetries of Cs(1), Cs(2), Cl(1), and Cl(2) atoms are: D_{3d} , C_{3v} , C_{2h} , C_s respectively. Forty-five modes are predicted from factor group analysis and distributed as follows:

$$\begin{aligned}
 \Gamma_{\text{Cs}(1)} &= A_{2u} + E_u \\
 \Gamma_{\text{Mn}(1)} &= A_{2u} + E_u \\
 \Gamma_{\text{Cs}(2)} &= A_{1g} + E_g + A_{2u} + E_u \\
 \Gamma_{\text{Mn}(2)} &= A_{1g} + E_g + A_{2u} + E_u \\
 \Gamma_{\text{Cl}(1)} &= 4A_{2u} + A_{1u} + 2E_u \\
 \Gamma_{\text{Cl}(2)} &= 4A_{1g} + A_{2g} + 2E_g + 4A_{2u} + A_{1u} + 2E_u \\
 \Gamma_{\text{total}} &= 6A_{1g} + A_{2g} + 4E_g + 12A_{2u} + 2A_{1u} + 8E_u \quad (14) \\
 \Gamma_{\text{acoustic}} &= A_{2u} + E_u
 \end{aligned}$$

A_{2g} and A_{1u} are inactive, while the u modes are IR active and g modes are Raman active. Ten Raman active modes are predicted as shown from equation (14), but we observed only five Raman peaks. The spectrum of CsMnCl_3 is shown in figure 6.

Since $(\text{CH}_3)_4\text{NMnCl}_3$ ⁵⁴ consists of infinite linear chains composed of manganese atoms bridged by three chlorine atoms $-\text{MnCl}_3^-$, and the single crystal Raman of this compound has been reported⁵⁵, the observed

peaks are assigned by analogy with the peaks observed in the spectrum of $(\text{CH}_3)_4\text{NMnCl}_3$. Peak positions and assignments are shown in Table 12.

(iv) CsMn_4Cl_9

An X-ray study³⁹ on single crystal of CsMn_4Cl_9 indicated that this compound crystallizes in space group $I4_1/a$ (C_{4h}^6) with two formulas per unit cell. The Mn is octahedrally coordinated by Cl atoms, and each MnCl_6 octahedron is linked to six neighbouring octahedra by sharing five edges and one vertex. The site symmetries are as follows: Cs; S_4 , Mn; C_1 , Cl(1); C_1 , Cl(2); C_1 , Cl(3); S_4 . Eighty-four modes are predicted from factor group analysis and distributed as follows:

$$\begin{aligned}
 \Gamma_{\text{Cs}} &= B_g + E_g + A_u + E_u \\
 \Gamma_{\text{Cl(3)}} &= B_g + E_g + A_u + E_u \\
 \Gamma_{\text{Mn}} &= 2A_g + 2B_g + 4E_g + 2A_u + 2B_u + 4E_u \\
 \Gamma_{\text{Cl(1)}} &= 2A_g + 2B_g + 4E_g + 2A_u + 2B_u + 4E_u \\
 \Gamma_{\text{Cl(2)}} &= 2A_g + 2B_g + 4E_g + 2A_u + 2B_u + 4E_u \\
 \Gamma_{\text{total}} &= 6A_g + 8B_g + 14E_g + 8A_u + 6B_u + 14E_u \\
 \Gamma_{\text{acoustic}} &= A_u + E_u
 \end{aligned} \tag{15}$$

The g modes are Raman active, and u modes are IR active except A_u is inactive. The Raman spectra of CsMn_4Cl_9 and other mixtures in this composition region are shown in figure 6. Tentative assignments and peak frequencies are shown in Table 13.

Table 12. Assignments and peak frequencies in cm^{-1} for CsMnCl_3 and $(\text{CH}_3)_4\text{NMnCl}_3$.

CsMnCl_3	Assignments	$(\text{CH}_3)_4\text{NMnCl}_3$	Assignments
48 m-w	E_g	88	E_{2g}
100 m	E_g	118	E_{1g}
154 m-w	E_g	129	E_{2g}
191 w	E_g	182	E_{2g}
250 w	A_{1g}	256	A_g

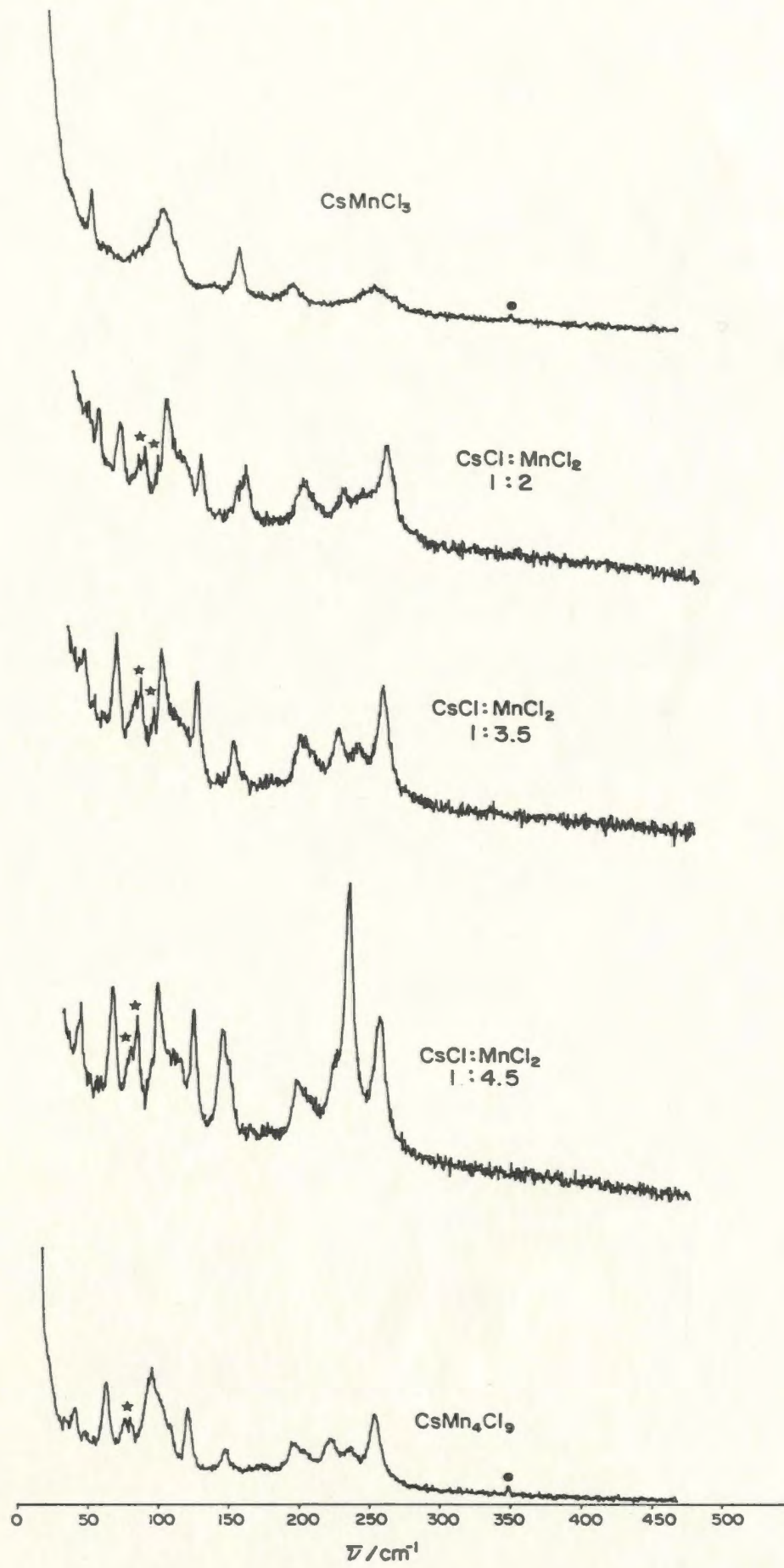
w: weak, m: medium

Table 13. Peak frequencies in cm^{-1} and assignments for the solid compounds formed in CsCl-MnCl_2 mixtures.

CsMn_4Cl_9 I	CsCl:MnCl_2 (1:4.5) I	CsCl:MnCl_2 (1:3.5) I	CsCl:MnCl_2 (1:2) I	Assignments
41 w	42 m-w	42 m-w	41 w	I (E_g)
50 v.w	50 v.w	50 w	50 m-w	I
63 m	66 m	66 m	65 m	I
96 m	98 m	98 m	99 m	I
102 w,br.				I
108 sh,w	110 w	110 m,br.	108 sh,m-w	I
121 m	124 m	123 m	123 w	I
	144 m		146 sh,w	E_g (MnCl_2)
148 w	148 sh,m	149 m-w	154.5 m-w	I
196 w	197 w	200 m-w	196 m-w	I
222 w	226 sh,m-w	224 w	224 w	I
238 v.w	234 s	239 w	238 v.v.w	A_{1g} (MnCl_2)
254 m	257 m	256 m	256 m	I (A_g)

v.w: very weak, w: weak, m: medium, s: strong, sh: shoulder,
br: broad

Figure 6. Raman spectra of solids formed from the CsCl-MnCl₂ system. The stars indicate ghost peaks. The dots indicate plasma lines.



4.1.3 MnCl₂ - RbCl System

The phase diagram of MnCl₂-RbCl system^{37,38} indicates the presence of three compounds, one congruent compound, RbMnCl₃; melting point 552°C, and two incongruent compounds, Rb₂MnCl₄; melting point 462°C and Rb₃Mn₂Cl₇; melting point 475°C.

(i) RbMnCl₃

An X-ray study⁵⁶ on single crystal of RbMnCl₃ indicated that this compound has space group P6₃/mmc (D_{6h}⁴) with six formulas per unit cell. The unit cell has six layers of RbCl₃ with the Mn ion situated between the layers and octahedrally coordinated by Cl ions. The site symmetries are as follows: Rb(1); C_{2h}, Rb(2); D_{3h}, Mn(1); C_{2h}, Mn(2); D_{3d}, Cl(1); C₁, Cl(2); C₂. Ninety modes are predicted from factor group analysis, and distributed as follows:

$$\begin{aligned}
 \Gamma_{\text{Rb}(1)} &= && A_{1u} + 2A_{2u} + B_{1u} + 4B_{2u} + E_{1u} \\
 &&& && && && +E_{2u} \\
 \Gamma_{\text{Rb}(2)} &= && B_{1g} && + E_{2g} && + A_{2u} && + E_{1u} \\
 \Gamma_{\text{Mn}(1)} &= && && && A_{1u} + 2A_{2u} + B_{1u} + 4B_{2u} + E_{1u} \\
 &&& && && && + E_{2u} \\
 \Gamma_{\text{Mn}(2)} &= && && && A_{2u} && + B_{2u} + E_{1u} \\
 &&& && && && + E_{2u} \\
 \Gamma_{\text{Cl}(1)} &= 4A_{1g} + A_{2g} + B_{1g} + 4E_{1g} + 5E_{2g} && + A_{2u} + B_{1u} && + 4E_{1u} \\
 &&& && && && + E_{2u} \\
 \Gamma_{\text{Cl}(2)} &= A_{1g} + 4A_{2g} + 2B_{1g} + 2E_{1g} + 2E_{2g} && + B_{1u} && + E_{1u} \\
 \Gamma_{\text{total}} &= 5A_{1g} + 5A_{2g} + 4B_{1g} + 6E_{1g} + 8E_{2g} + 2A_{1u} + 7A_{2u} + 4B_{1u} + 9B_{2u} + 9E_{1u} \\
 &&& && && && + 4E_{2u} \quad (16) \\
 \Gamma_{\text{acoustic}} &= && && && A_{2u} && + E_{1u}
 \end{aligned}$$

A_{2g} and B_{1g} are inactive while A_{1g} , E_{1g} , and E_{2g} are Raman active, and the u modes are IR active except B_{1u} and B_{2u} which are inactive.

The Raman spectrum of $RbMnCl_3$ is shown in figure 7. The assignments have been made by analogy with the Raman spectrum of $RbMnCl_3$ crystal⁷⁰ at 50 K. Assignments and peak positions are shown in Table 14.

(ii) Rb_2MnCl_4

An X-ray diffraction pattern⁵⁷ and neutron diffraction data⁴⁵ of Rb_2MnCl_4 showed that this compound crystallizes in space group $I4/mmm$ (D_{4h}^{17}) with one formula per unit cell. The compound is isostructural with K_2MgCl_4 ⁴². The Mn atom is octahedrally coordinated by Cl atoms, and the site symmetries are as follows: Rb; C_{4v} , Mn; D_{4h} , Cl(1); D_{2h} , Cl(2); C_{4v} . Twenty-one modes are predicted from factor group analysis, and distributed as follows:

$$\begin{aligned}
 \Gamma_{Rb} &= A_{1g} + E_g + A_{2u} + E_u \\
 \Gamma_{Mn} &= A_{2u} + E_u \\
 \Gamma_{Cl(1)} &= A_{2u} + B_{2u} + 2E_u \\
 \Gamma_{Cl(2)} &= A_{1g} + E_g + A_{2u} + E_u \\
 \Gamma_{total} &= 2A_{1g} + 2E_g + 4A_{2u} + B_{2u} + 5E_u \\
 \Gamma_{acoustic} &= A_{2u} + E_u
 \end{aligned}
 \tag{17}$$

All g modes are Raman active, and the u modes are IR active except B_{2u} is inactive. Four modes are predicted in the Raman spectrum, two peaks are observed, and the other two peaks are not detected in the spectrum because of the presence of a ghost in the range $80-120\text{ cm}^{-1}$.

The assignments are made by analogy with the spectrum of single crystal

Table 14. Assignments and frequencies in cm^{-1} for solid RbMnCl_3 .

RbMnCl_3 Solid at room temperature	RbMnCl_3^{70} Crystal at 50 K	Assignments
	19	A_{1g}
	28	E_{1g}
	44	E_{2g}
52 sh,m	53	E_{2g}
	74	E_{2g}
	130	E_{1g}
	135	A_{1g}
152 w	150	E_{2g}
171.5 v.w	170	A_{1g}
	180	E_{2g}
	218	E_{2g}
258 v.w	257	A_{1g}

v.w: very weak, w: weak, m: medium, sh: shoulder

Rb_2MnCl_4 ^{59,60}. The spectra of Rb_2MnCl_4 , $\text{RbCl}:\text{MnCl}_2$ (3:1), and $\text{RbCl}:\text{MnCl}_2$ (4:1) are shown in figure 7, and peak frequencies and assignments are shown in Table 15.

(iii) $\text{Rb}_3\text{Mn}_2\text{Cl}_7$

The X-ray diffraction pattern^{43,57} of $\text{Rb}_3\text{Mn}_2\text{Cl}_7$ indicated that this incongruent melting compound is isostructural with $\text{Sr}_3\text{Ti}_2\text{O}_7$ ⁶¹, and has space group $I4/mmm$ (D_{4h}^{17}) with two formulas per unit cell. The site symmetries are as follows: Mn; C_{4v} , Rb(1); D_{4h} , Rb(2); C_{4v} , Cl(1); D_{4h} , Cl(2); C_{2v} , Cl(3); C_{4v} . Factor group analysis predicted seventy-two modes distributed as follows:

$$\begin{aligned}
 \Gamma_{\text{Cl}(1)} &= && 2A_{2u} &+ 2E_u \\
 \Gamma_{\text{Rb}(1)} &= && 2A_{2u} &+ 2E_u \\
 \Gamma_{\text{Rb}(2)} &= 2A_{1g} &+ 2E_g &+ 2A_{2u} &+ 2E_u \\
 \Gamma_{\text{Mn}} &= 2A_{1g} &+ 2E_g &+ 2A_{2u} &+ 2E_u \\
 \Gamma_{\text{Cl}(3)} &= 2A_{1g} &+ 2E_g &+ 2A_{2u} &+ 2E_u \\
 \Gamma_{\text{Cl}(2)} &= 2A_{1g} + 2B_{1g} + 4E_g &+ 2A_{2u} &+ 2B_{2u} &+ 4E_u \\
 \Gamma_{\text{total}} &= 8A_{1g} + 2B_{1g} + 10E_g &+ 12A_{2u} &+ 2B_{2u} &+ 14E_u \\
 \Gamma_{\text{acoustic}} &= && A_{2u} &+ E_u
 \end{aligned} \tag{18}$$

All g modes are Raman active, while A_{2u} and E_u modes are IR active and B_{2u} is inactive. The Raman spectrum of $\text{Rb}_3\text{Mn}_2\text{Cl}_7$ is shown in figure 7. The spectrum seems to be similar to the spectra of RbMnCl_3 and Rb_2MnCl_4 . Assignments have been made by analogy with RbMnCl_3 and Rb_2MnCl_4 . Recently⁶⁰ six Raman peaks were observed without assignments for $\text{Rb}_3\text{Mn}_2\text{Cl}_7$. Tentative assignments and frequencies in cm^{-1} are shown in Table 16.

Table 15. Peak frequencies in cm^{-1} and assignments for the solid compounds formed in RbCl-MnCl_2 mixtures.

Rb_2MnCl_4 I	RbCl:MnCl_2 (3:1) I	RbCl:MnCl_2 (4:1) I	$\text{Rb}_2\text{MnCl}_4^{59}$ at 300 K	Assignments
52 s-m	52 m	52 m	52	$E_g(I)$
			89.5	A_{1g}
			97.5	E_g
200 m-w	200 m-w	200 m-w	201	$A_{1g}(I)$

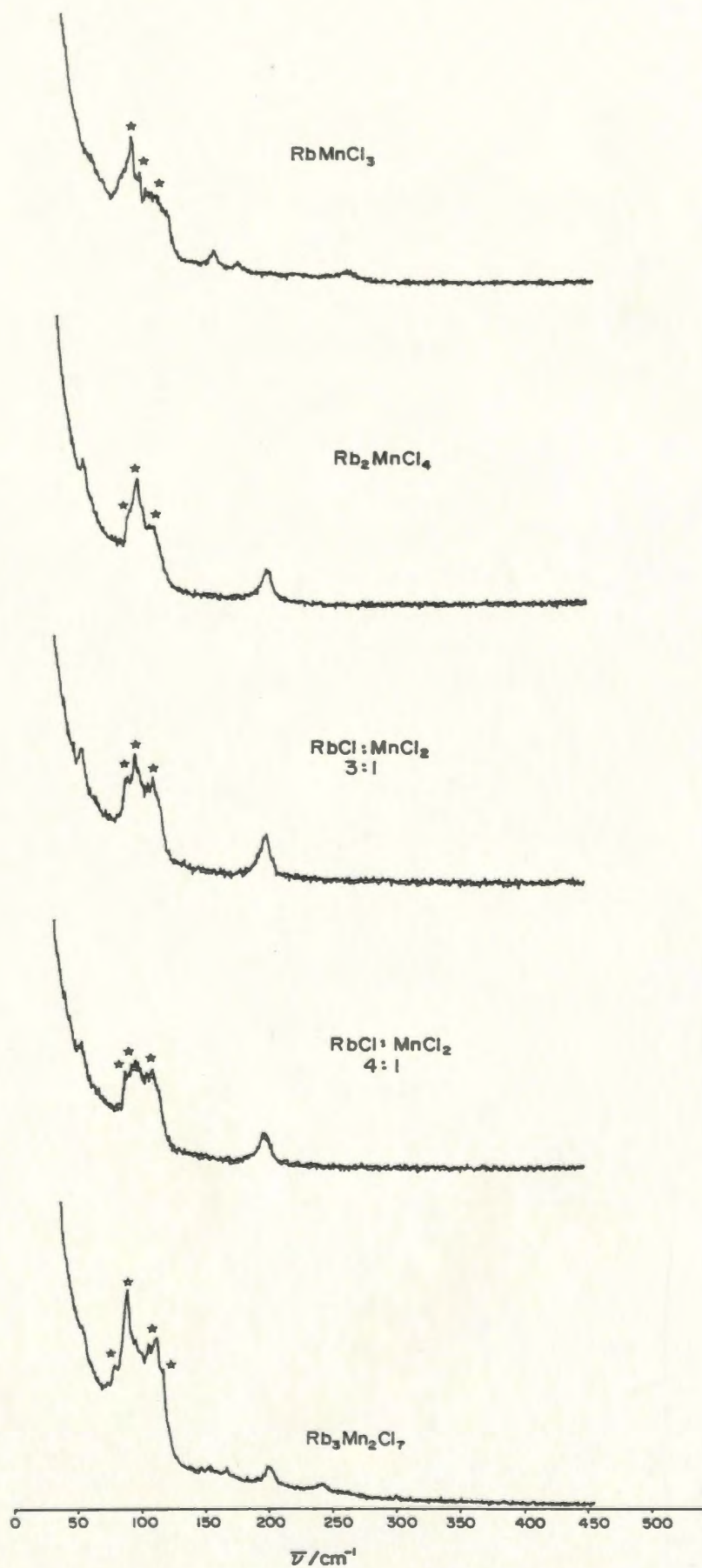
w: weak, m: medium, s: strong

Table 16. Assignments and peak frequencies in cm^{-1} for solid $\text{Rb}_3\text{Mn}_2\text{Cl}_7$.

$\text{Rb}_3\text{Mn}_2\text{Cl}_7$	$\text{Rb}_3\text{Mn}_2\text{Cl}_7^{60}$	Assignments
	36	
51 sh,w		$\left\{ \begin{array}{l} E_{2g} (\text{RbMnCl}_3) \\ E_g (\text{Rb}_2\text{MnCl}_4) \end{array} \right.$
	78	
	98	
	115	
148 v.w		$E_g (\text{MnCl}_2)$
156 v.w		$E_{2g} (\text{RbMnCl}_3)$
166 v.w.	166	$A_{1g} (\text{RbMnCl}_3)$
200 w		$A_{1g} (\text{Rb}_2\text{MnCl}_4)$
240 v.w	242	$A_{1g} (\text{MnCl}_2)$

v.w: very weak, w: weak, sh: shoulder

Figure 7. Raman spectra of solids formed from the RbCl-MnCl_2 system. The stars indicate ghost peaks.



4.1.4 MnCl₂-KCl System

The phase diagram of MnCl₂-KCl system^{37,57} indicated the presence of three double salts, one congruent compound, KMnCl₃; melting point 490°C, and two incongruent compounds, K₃Mn₂Cl₇; melting point 437°C and K₄MnCl₆; melting point 448°C. Kuzmenko et. al⁵⁸ reported that there are three coordination compounds for KCl-MnCl₂ system, one congruent compound KMnCl₃, and two incongruent compounds K₃Mn₂Cl₇ and K₂MnCl₄.

K₃Mn₂Cl₇^{43,57} is isostructural with Rb₃Mn₂Cl₇^{43,57}, and the number of modes predicted from factor group analysis are given by equation 18. KMnCl₃⁴³ is isostructural with KMgCl₃⁷⁷ with space group Pnma (D_{2h}¹⁶) and four formulas per unit cell. Seifert⁴³ reported a high temperature phase which we have not studied. The site symmetries are as follows: K; C_s, Mn; C_i, Cl(1); C_s, Cl(2); C₁. The number of modes predicted from factor group analysis are distributed as follows:

$$\begin{aligned}
 \Gamma_{\text{Mn}} &= && 3A_u + 3B_{1u} + 3B_{2u} + 3B_{3u} \\
 \Gamma_{\text{K}} &= 2A_g + 2B_{1g} + B_{2g} + B_{3g} + A_u + B_{1u} + 2B_{2u} + 2B_{3u} \\
 \Gamma_{\text{Cl(1)}} &= 2A_g + 2B_{1g} + B_{2g} + B_{3g} + A_u + B_{1u} + 2B_{2u} + 2B_{3u} \\
 \Gamma_{\text{Cl(2)}} &= 3A_g + 3B_{1g} + 3B_{2g} + 3B_{3g} + 3A_u + 3B_{1u} + 3B_{2u} + 3B_{3u} \\
 \Gamma_{\text{total}} &= 7A_g + 7B_{1g} + 5B_{2g} + 5B_{3g} + 8A_u + 8B_{1u} + 10B_{2u} + 10B_{3u} \quad (19) \\
 \Gamma_{\text{acoustic}} &= && B_{1u} + B_{2u} + B_{3u}
 \end{aligned}$$

A_u is inactive, and u modes are IR active while the g modes are Raman active.

K₄MnCl₆^{62,63} has space group R $\bar{3}c$ (D_{3d}⁶) with two formulas per unit cell. The site symmetries are as follows: K(1), C_{3i}, K(2); C_i, Mn; D₃, Cl; C₁. The number of modes predicted from factor group analysis are distributed as follows:

$$\begin{aligned}
 \Gamma_{\text{Mn}} &= A_{2g} + E_g + A_{2u} + E_u \\
 \Gamma_{\text{K(1)}} &= A_{1u} + A_{2u} + 2E_u \\
 \Gamma_{\text{K(2)}} &= 4A_{1u} + 4A_{2u} + 5E_u \\
 \Gamma_{\text{Cl}} &= 3A_{1g} + 3A_{2g} + 10E_g + 3A_{1u} + 3A_{2u} + 2E_u \\
 \Gamma_{\text{total}} &= 3A_{1g} + 4A_{2g} + 11E_g + 8A_{1u} + 9A_{2u} + 10E_u \\
 \Gamma_{\text{acoustic}} &= A_{2u} + E_u
 \end{aligned} \tag{20}$$

A_{2g} and A_{1u} are inactive, while A_{1g} and E_g are Raman active and A_{2u} and E_u are IR active.

The Raman spectra for KMnCl_3 , $\text{K}_3\text{Mn}_2\text{Cl}_7$, K_4MnCl_6 , $\text{KCl}:\text{MnCl}_2$ (2:1) and $\text{KCl}:\text{MnCl}_2$ (3:1) are shown in figure 8. Assignments and peak frequencies are shown in Table 17. The Raman spectrum can not distinguish whether the compound is K_2MnCl_4 or K_4MnCl_6 .

4.1.5 MnCl_2 -NaCl System

The phase diagram study^{43,64} indicated the presence of five incongruent compounds, NaMnCl_3 ; melting point 424°C , Na_2MnCl_4 ; melting point 442°C , $\text{Na}_2\text{Mn}_3\text{Cl}_8$; melting point 413°C , NaMn_4Cl_9 ; melting point 451°C , Na_6MnCl_8 ; melting point 459°C .

An X-ray study⁶⁵ on single crystal of NaMnCl_3 indicated that NaMnCl_3 crystallizes in space group $R\bar{3}$ (C_{3i}^2) with two formulas per unit cell. It is isomorphous with FeTiO_3 ⁶⁶. The site symmetries are as follows: Na; C_3 , Mn; C_3 , Cl; C_1 . Thirty modes are predicted from factor group analysis, and distributed as follows:

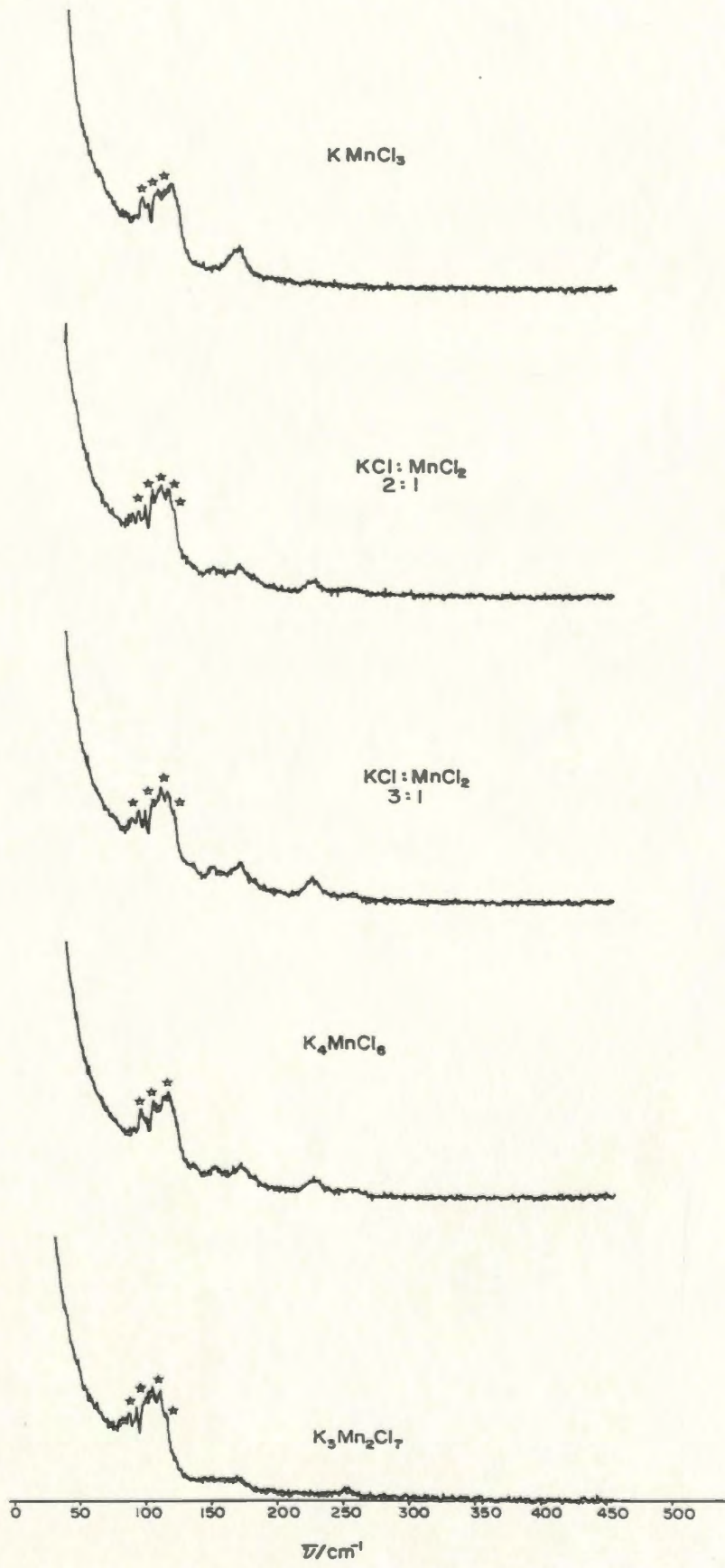
$$\begin{aligned}
 \Gamma_{\text{Na}} &= A_g + E_g + A_u + E_u \\
 \Gamma_{\text{Mn}} &= A_g + E_g + A_u + E_u \\
 \Gamma_{\text{Cl}} &= 3A_g + 3E_g + 3A_u + 3E_u \\
 \Gamma_{\text{total}} &= 5A_g + 5E_g + 5A_u + 5E_u \\
 \Gamma_{\text{acoustic}} &= A_u + E_u
 \end{aligned} \tag{21}$$

Table 17. Assignments and peak frequencies in cm^{-1} for the solid compounds formed in KCl-MnCl_2 system.

KMnCl_3	$\text{K}_3\text{Mn}_2\text{Cl}_7$	K_4MnCl_6	KCl:MnCl_2 (2:1) III	KCl:MnCl_2 (3:1) III	Assignments
I	II	III			
		130 v.w	128 v.w	130 v.w	III
		146 v.w	146 v.w	144 v.w	E_g (MnCl_2)
162 w					I
		165 w	164 w	166 w	III
	174 v.w				II
		222 w	222 w	222 w	III
	251 v.w				II
		250 v.w	250 v.w	252 v.w	III

v.w: very weak, w: weak

Figure 8. Raman spectra of solids formed from the KCl-MnCl_2 system. The stars indicate ghost peaks.



All the g modes are Raman active, and all the u modes are IR active.

An X-ray study⁶⁷ on single crystal of Na_2MnCl_4 indicated that Na_2MnCl_4 has space group Pbam (D_{2h}^9) with two formulas per unit cell. The site symmetries are as follows: Mn; C_{2h} , Na; C_s , Cl(1); C_s , Cl(2); C_s .

Forty-two modes are predicted as follows:

$$\begin{aligned}
 \Gamma_{\text{Mn}} &= && 2B_{2u} + 2B_{3u} + A_u + B_{1u} \\
 \Gamma_{\text{Na}} &= 2A_g + 2B_{1g} + B_{2g} + B_{3g} + 2B_{2u} + 2B_{3u} + A_u + B_{1u} \\
 \Gamma_{\text{Cl}(1)} &= 2A_g + 2B_{1g} + B_{2g} + B_{3g} + 2B_{2u} + 2B_{3u} + A_u + B_{1u} \\
 \Gamma_{\text{Cl}(2)} &= 2A_g + 2B_{1g} + B_{2g} + B_{3g} + 2B_{2u} + 2B_{3u} + A_u + B_{1u} \\
 \Gamma_{\text{total}} &= 6A_g + 6B_{1g} + 3B_{2g} + 3B_{3g} + 8B_{2u} + 8B_{3u} + 4A_u + 4B_{1u} \quad (22) \\
 \Gamma_{\text{acoustic}} &= && B_{2u} + B_{3u} + B_{1u}
 \end{aligned}$$

A_u is inactive, all the u modes are IR active, while the g modes are Raman active.

An X-ray study⁶⁸ on powder samples of Na_6MnCl_8 and $\text{Na}_2\text{Mn}_3\text{Cl}_8$ have been made. The results indicated that $\text{Na}_2\text{Mn}_3\text{Cl}_8$ has space group $R\bar{3}m$ (D_{3d}^5) with one formula per unit cell, and the site symmetries are as follows: Na; C_{3v} , Mn; C_{2h} , Cl(1); C_{3v} , Cl(2); C_s . Na_6MnCl_8 has space group $\text{Fm}\bar{3}m$ (O_h^5), with one formula per unit cell, the site symmetries are as follows:

Na; D_{2h} , Mn; O_h , Cl(1); T_d , Cl(2); C_{4v} . The number of modes predicted from factor group analysis for $\text{Na}_2\text{Mn}_3\text{Cl}_8$ are as follows:

$$\begin{aligned}
 \Gamma_{\text{Na}} &= A_{1g} + E_g + A_{2u} + E_u \\
 \Gamma_{\text{Cl}(1)} &= A_{1g} + E_g + A_{2u} + E_u \\
 \Gamma_{\text{Mn}} &= 4A_{2u} + A_{1u} + 2E_u
 \end{aligned}$$

$$\begin{aligned}
 \Gamma_{Cl(2)} &= 4A_{1g} + A_{2g} + 2E_g + 4A_{2u} + A_{1u} + 2E_u \\
 \Gamma_{total} &= 6A_{1g} + A_{2g} + 4E_g + 10A_{2u} + 2A_{1u} + 6E_u \\
 \Gamma_{acoustic} &= \qquad \qquad \qquad A_{2u} \qquad \qquad + E_u
 \end{aligned}
 \tag{23}$$

A_{2g} and A_{1u} are inactive, while A_{1g} and E_g are Raman active and A_{2u} and E_u are IR active.

Forty-five modes are predicted from factor group analysis for Na_6MnCl_8 , and distributed as follows:

$$\begin{aligned}
 \Gamma_{Mn} &= \qquad \qquad \qquad T_{1u} \\
 \Gamma_{Cl(1)} &= \qquad \qquad \qquad 2T_{1u} \\
 \Gamma_{Na} &= \qquad \qquad \qquad 6T_{1u} \\
 \Gamma_{Cl(2)} &= A_{1g} + E_g + 2T_{2g} + 3T_{1u} \\
 \Gamma_{total} &= A_{1g} + E_g + 2T_{2g} + 12T_{1u} \\
 \Gamma_{acoustic} &= \qquad \qquad \qquad T_{1u}
 \end{aligned}
 \tag{24}$$

All g modes are Raman active and T_{1u} is IR active.

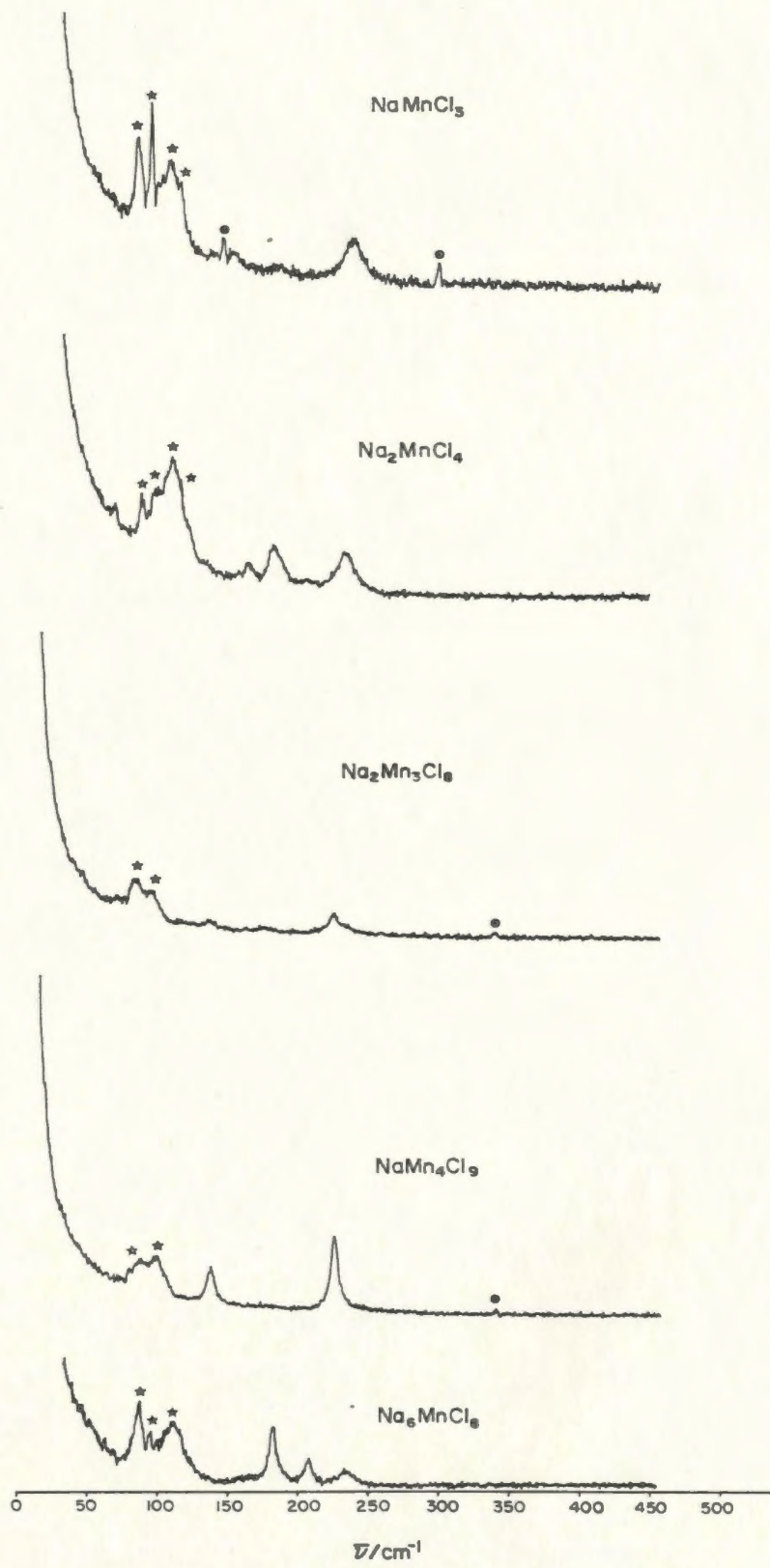
The crystal structure of $NaMn_4Cl_9$ has not yet been determined. Two peaks were observed at 232 and 142 cm^{-1} for $NaMn_4Cl_9$, and these two peaks are most probably due to $MnCl_2$. The failure to detect peaks that can be assigned to a $NaMn_4Cl_9$ compound suggest that the compound does not exist or that the Raman features are too weak to detect. The spectrum of Na_6MnCl_8 is assigned by analogy with the Raman spectrum⁶⁹ of the Suzuki phase ($6NaCl:MnCl_2$). The Raman spectra of $NaMnCl_3$, Na_2MnCl_4 , $Na_2Mn_3Cl_8$, $NaMn_4Cl_9$, and Na_6MnCl_8 are shown in figure 9. Assignments and peak frequencies are shown in Table 18.

Table 18. Assignments and frequencies in cm^{-1} for the solid compounds formed in $\text{MnCl}_2\text{-NaCl}$ system.

NaMnCl_3 I	Na_2MnCl_4 II	$\text{Na}_2\text{Mn}_3\text{Cl}_8$ III	NaMn_4Cl_9 IV	Na_6MnCl_8 V	Suzuki phase ⁶⁹	Assignments
	68 w					II
					123	T_{2g}
		123 v.w				III
	132 v.w					II
139 v.w						I
		142 v.w	142 m-w			E_g (MnCl_2)
151 v.w						I
	166 v.w					II
		182 v.w				III
				182 m	180	T_{2g}
	183 w					II
185 v.w						I
				208 w	206	A_{1g}
236 w	234 w	232 w	232 m	235 w		A_{1g} (MnCl_2)

v.w: very weak, w: weak, m: medium

Figure 9. Raman spectra of solids formed from the NaCl-MnCl₂ system. The stars indicate ghost peaks. The dots indicate plasma lines.



4.1.6 MnCl₂-LiCl System

It has been reported⁷² that, the MnCl₂-LiCl system forms a solid solution over the whole composition range. However, the Raman spectrum of the LiCl:MnCl₂ (1:1) mixture indicates that this mixture has separated into crystalline MnCl₂ and LiCl, and it may contain a small concentration of Li₂MnCl₄. A neutron diffraction study⁷³ concluded that Li₂MnCl₄ has space group Fd3m (O_h^7) with two formulas per unit cell, and the site symmetries of the atoms are as follows: Li(1); D_{3d}, Li(2); Td, Mn; D_{3d}, Cl; C_{3v}.

Forty-two modes are predicted from factor group analysis and distributed as follows:

$$\begin{aligned}
 \Gamma_{\text{Li}(2)} &= T_{2g} + T_{1u} \\
 \Gamma_{\text{Li}(1)} &= A_{2u} + E_u + T_{1u} \\
 \Gamma_{\text{Mn}} &= A_{2u} + E_u + T_{1u} \\
 \Gamma_{\text{Cl}} &= 2A_{1g} + 2E_g + 2T_{2g} + 2A_{2u} + 2E_u + 2T_{1u} \\
 \Gamma_{\text{total}} &= 2A_{1g} + 2E_g + 3T_{2g} + 4A_{2u} + 4E_u + 5T_{1u} \\
 \Gamma_{\text{acoustic}} &= T_{1u}
 \end{aligned} \tag{25}$$

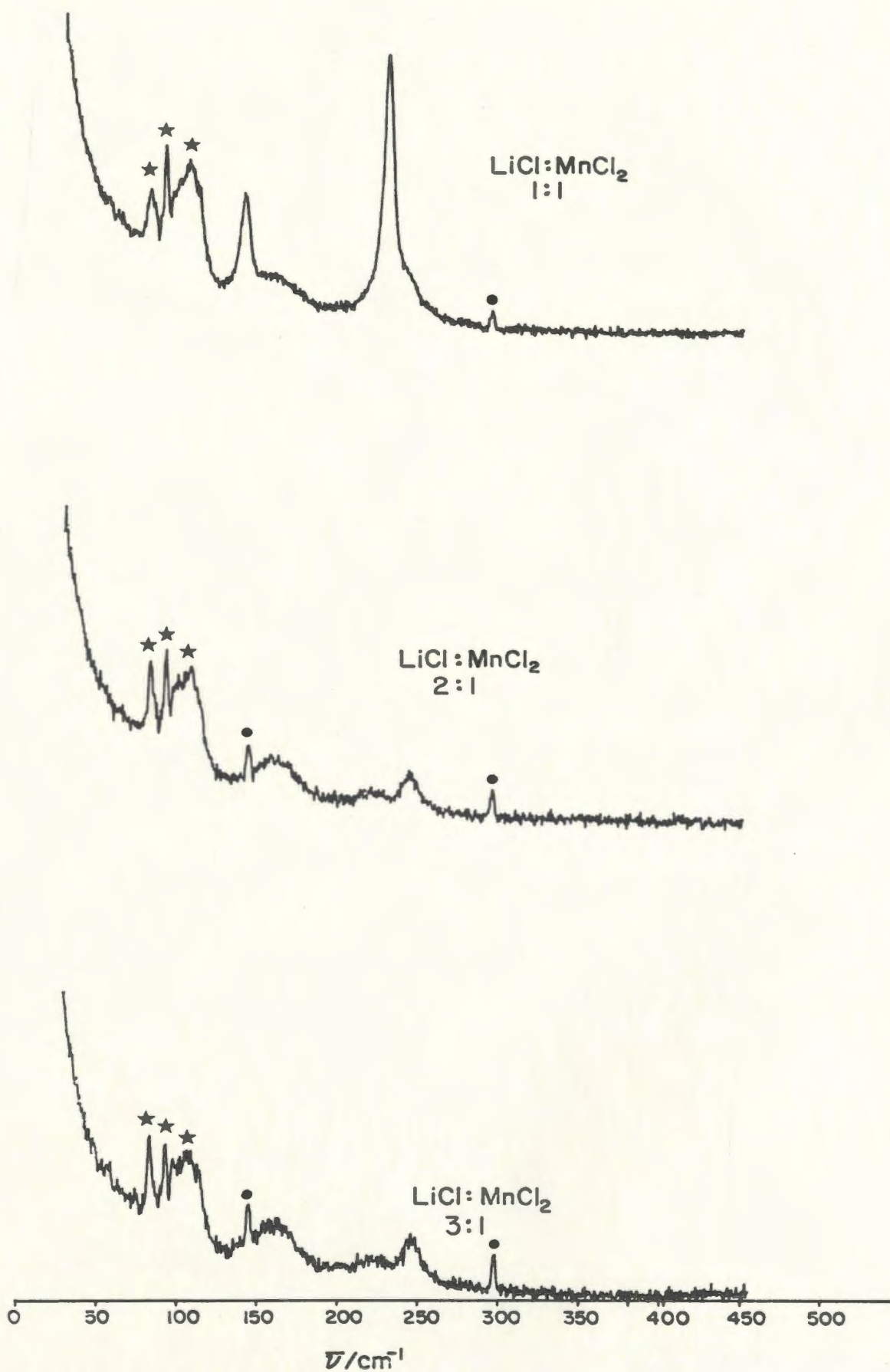
All the g modes are Raman active and T_{1u} is IR active. A_{2u} and E_u are inactive. The Raman spectra in the solid state of LiCl:MnCl₂ (1:1), Li₂MnCl₄, and LiCl:MnCl₂ (3:1) are shown in figure 10, and the peak frequencies in cm⁻¹ and assignments are shown in Table 19.

Table 19. Peak frequencies in cm^{-1} and assignments for the solid compounds formed in LiCl-MnCl_2 system.

LiCl:MnCl_2 (1:1) I	Li_2MnCl_4 II	$\text{Li}_2\text{MnCl}_4^{74}$ II	LiCl:MnCl_2 (3:1) II	Assignments
		70		II
		120		II
143 m				E_g (MnCl_2)
166 sh,w	164 w	163	162 w	II
	222 v.w	227	225 v.w	II
233 s				A_{1g} (MnCl_2)
247 sh,w	246 w	248	246 w	II

v.w: very weak, w: weak, m: medium, s: strong, sh: shoulder

Figure 10. Raman spectra of solids formed from the LiCl-MnCl_2 system. The stars indicate ghost peaks. The dots indicate plasma lines.



4.2 Raman Studies of $\text{MnCl}_2 \cdot n\text{ACl}$: Molten State

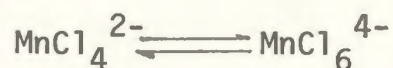
4.2.1 MnCl_2 , and MnCl_2 -CsCl Melts

The Raman spectra of MnCl_2 , Cs_2MnCl_4 , Cs_3MnCl_5 , CsMnCl_3 , and CsMn_4Cl_9 are shown in figures 11, 12, 13, 14, and 15 respectively. Two sets of spectra are shown for each melt, one in which the observed intensity, $I_{(\bar{\nu})}^{\text{obs}}$ is plotted as a function of frequency ($\bar{\nu}$ in cm^{-1}) and which is what the Raman spectrometer measures directly, and the other which is the corrected intensity $R_2(\bar{\nu})$ and is directly related to the density of vibrational states as discussed previously.

The spectra can be assigned to modes expected from a tetrahedral MnCl_4^{2-} species. A totally symmetric stretching mode (ν_1) is observed in each spectrum in the range 160 - 350 cm^{-1} . The ν_2 and ν_4 modes are observed as an overlapped peaks in the region 75 - 135 cm^{-1} . The anti-symmetric stretching mode ν_3 should appear around $\sim 300 \text{ cm}^{-1}$ but is too weak to be observed or is probably obscured under the polarized peak centered at $\sim 250 \text{ cm}^{-1}$. A peak due to ν_3 was observed⁵⁰ as strong band at 284 cm^{-1} in the IR spectrum of solid $(\text{Et}_4\text{N})_2\text{MnCl}_4$.

The spectra of melts of composition $\text{MnCl}_2 \cdot n\text{CsCl}$ ($n \geq 2$) strongly indicate the presence of an isolated tetrahedral MnCl_4^{2-} ion, but for melts of composition $\text{MnCl}_2 \cdot n\text{CsCl}$ ($n < 2$) tetrahedral MnCl_4^{2-} ions with corner shared Cl are suggested. A previous Raman study¹⁹ of $\text{MnCl}_2 \cdot \text{KCl}$ melts suggested that MnCl_2 melt has $(\text{MnCl}_2)_n$ species in which Mn^{2+} ion is octahedrally coordinated by six Cl^- ions and each Cl^- ion is shared by Mn^{2+} ions, also the existence of a small amount of MnCl_4^{2-} was proposed. However, tetrahedral coordination of Cl ions around a Mn ion through corner sharing was proposed²⁹ from molten MnCl_2 by x-ray diffraction. In the present study one broad polarized peak was observed

for MnCl_2 melt and melts of higher MnCl_2 concentration and this peak was attributed to Mn-Cl stretching vibration of tetrahedral MnCl_4^{2-} ion. MnCl_2 melt and melts of higher MnCl_2 content appear to have a rapid equilibrium of ions with most Mn retaining a tetrahedral coordination but octahedral coordination may be present to a small extent.



The existence of short lived $\text{Mn}_2\text{Cl}_7^{3-}$ ions seem probable and the visible spectra of the MnCl_2 melt and melt mixtures of high MnCl_2 content suggest the presence of small amount of octahedrally coordinated Mn^{2+} , see figures 117, 118, 119 and 120.

It has been reported that the half band width of the totally symmetric mode of MnCl_2 -KCl melts¹⁹ increased with increased MnCl_2 content. The present results confirmed this increment in the half band width upon increasing MnCl_2 concentration for the CsCl- MnCl_2 system, see Table 20.

The Raman spectra for solid Cs_2MnCl_4 and Cs_3MnCl_5 are recorded at several temperatures up to their melting points. The results for the totally symmetric mode (ν_1) for Cs_2MnCl_4 and Cs_3MnCl_5 are shown in figures 16 and 17. The band position moved to lower values as the temperature was increased, while the half band width increased with increased temperature.

Table 20. Summary of results of curve resolution analysis for MnCl_2 and MnCl_2 -CsCl Melts.

Compound	Frequency (cm^{-1})	Intensity	Half band width (cm^{-1})	Function
Cs_3MnCl_5	255.7	904	35.3	L
Cs_2MnCl_4	256.7	914	39.9	L
CsMnCl_3	262.7 ^a	817 ^a	81.8 ^a	G * L
	262.3 ^a	859 ^a	78.9 ^a	L
CsMn_4Cl_9	245.5	683	114.5	G * L
MnCl_2	235.3	794	135.4	G * L

G: Gaussian, L: Lorentzian

^a Comparison of the fits for G * L and L models indicates the insensitivity to chosen function.

Figure 11. Raman spectra of molten MnCl_2 at 942 K, $I_{||}$
and I_{\perp} .

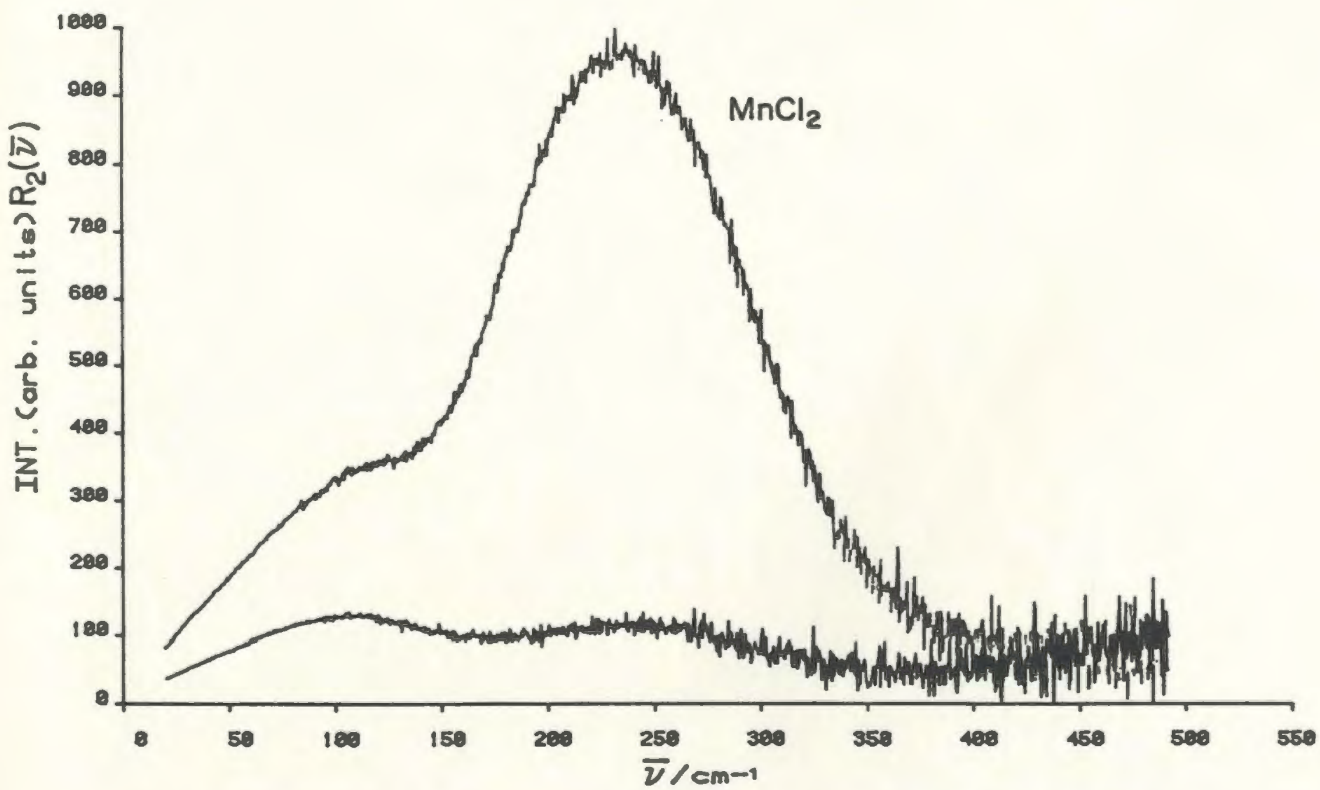
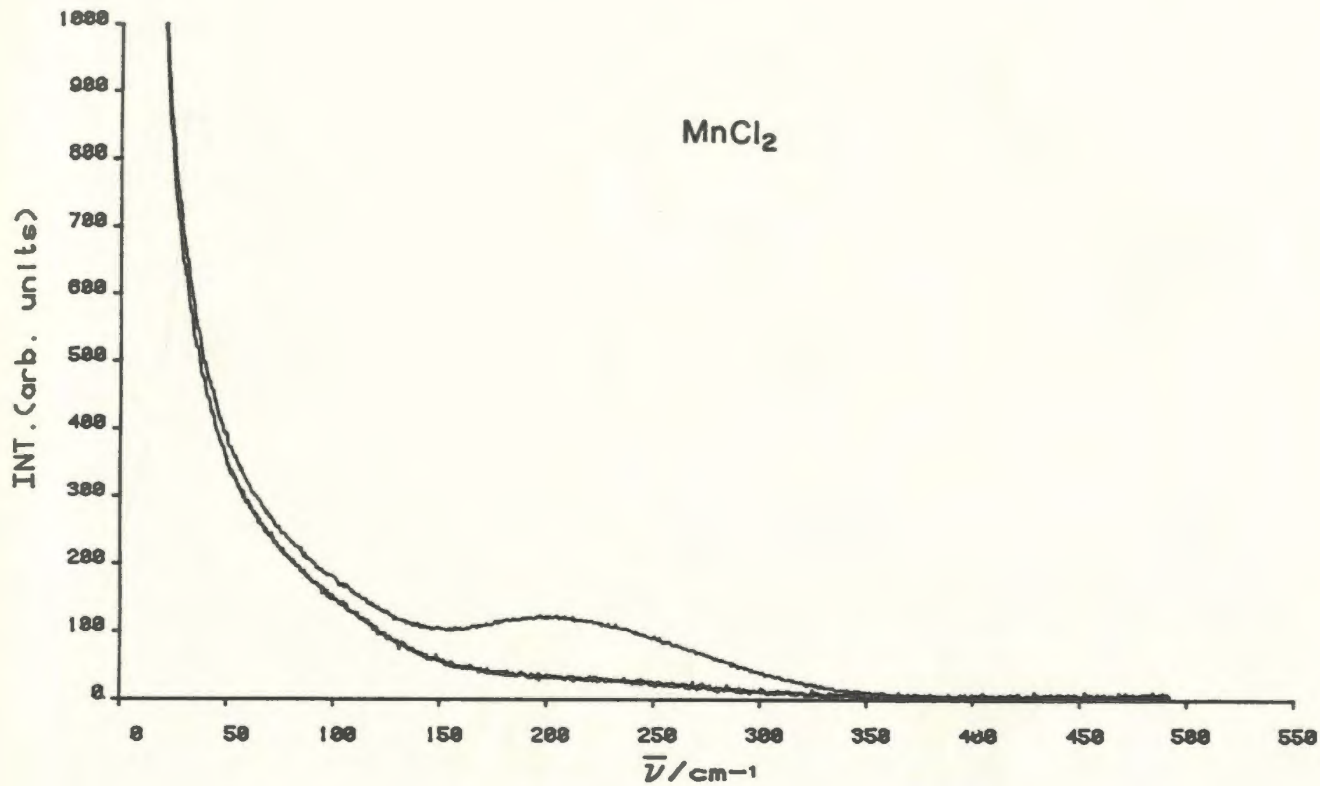


Figure 12. Raman spectra of molten Cs_2MnCl_4 at 844 K, $I_{||}$
and I_{\perp} .

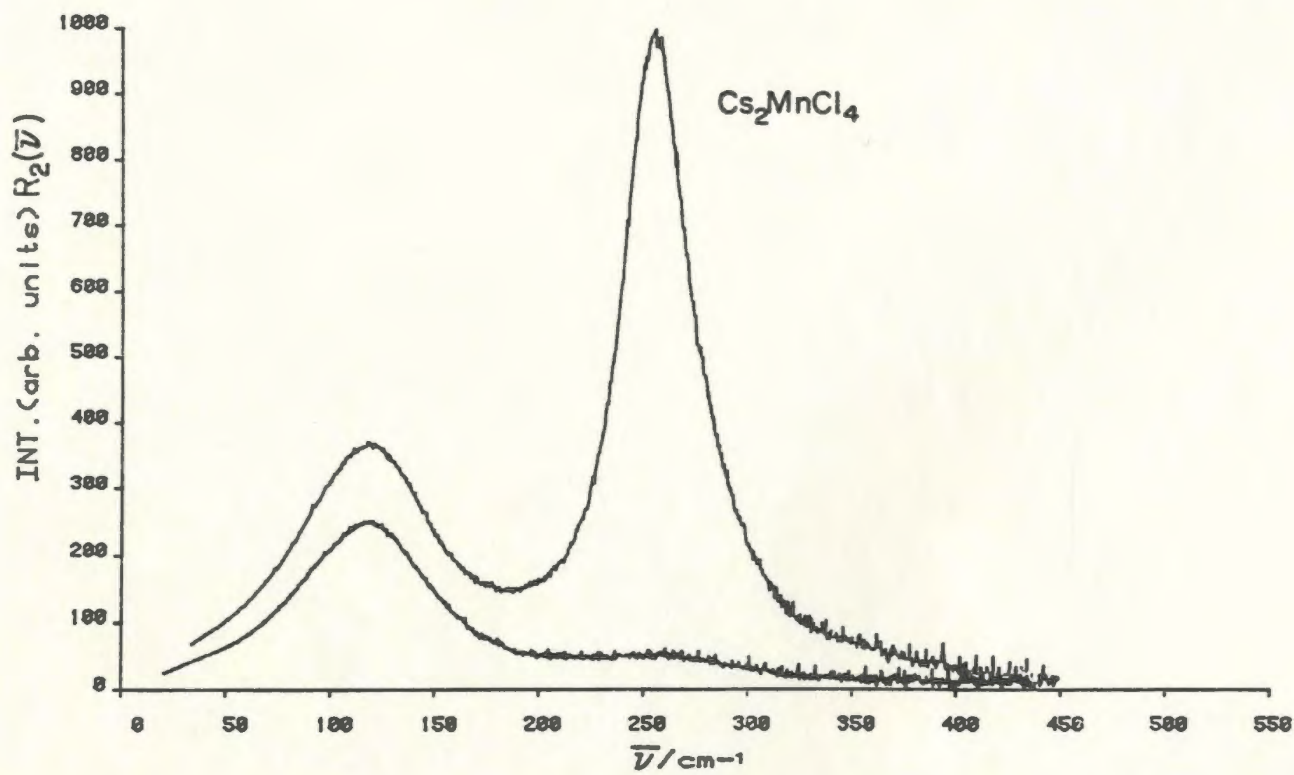
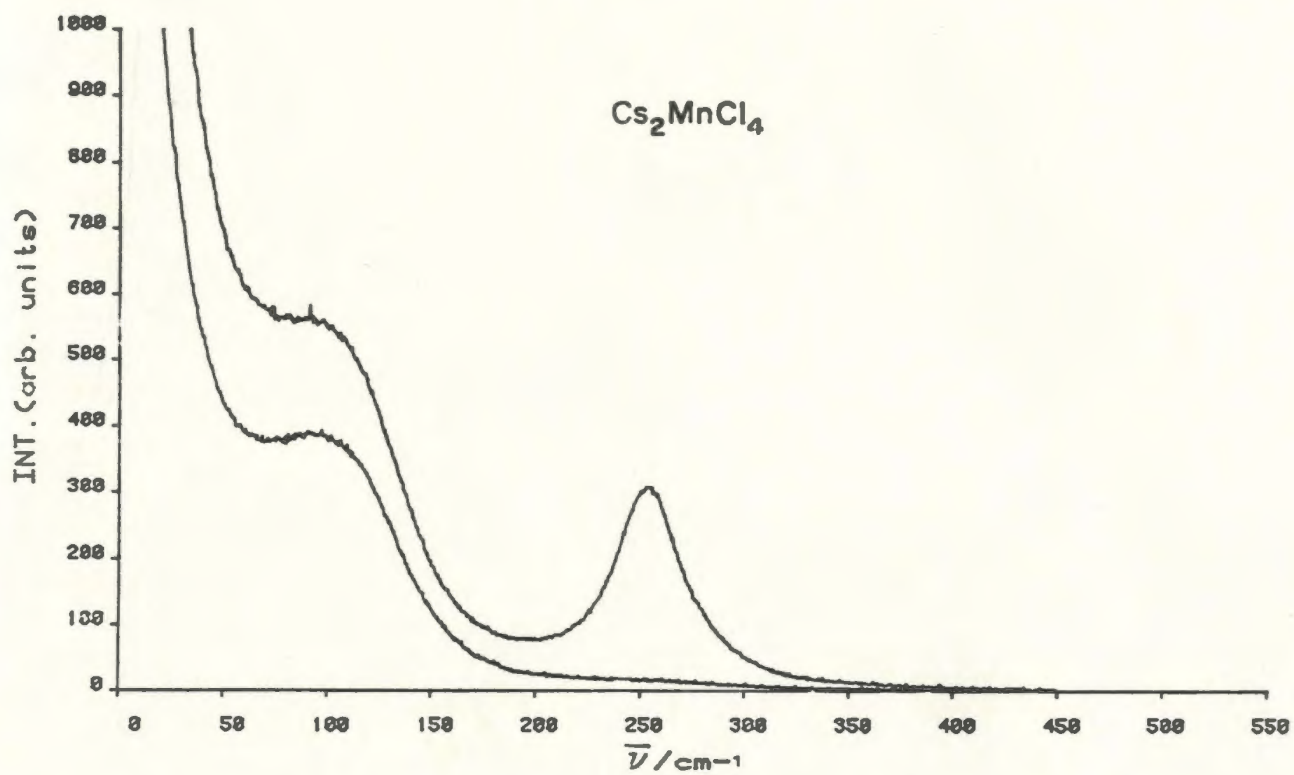


Figure 13. Raman spectra of molten Cs_3MnCl_5 at 844 K, $I_{||}$
and I_{\perp} .

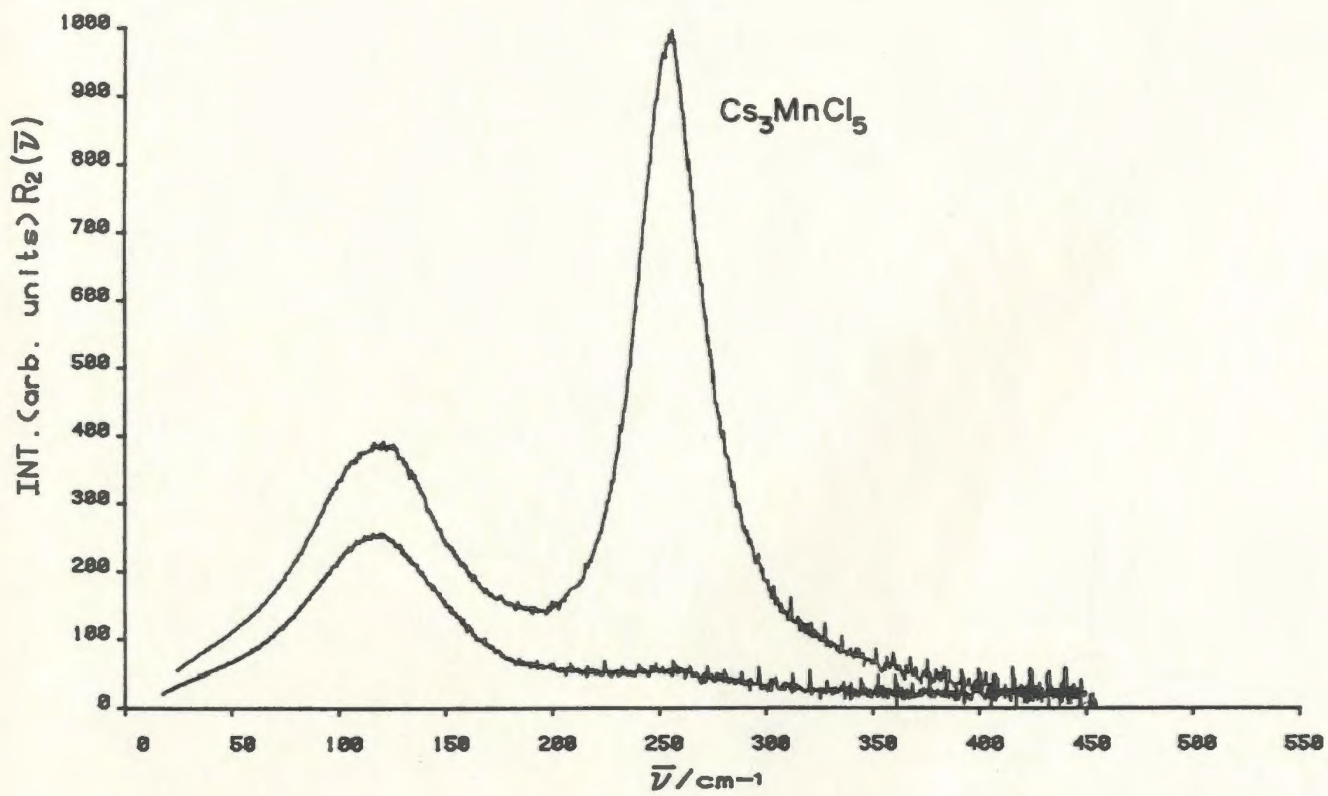
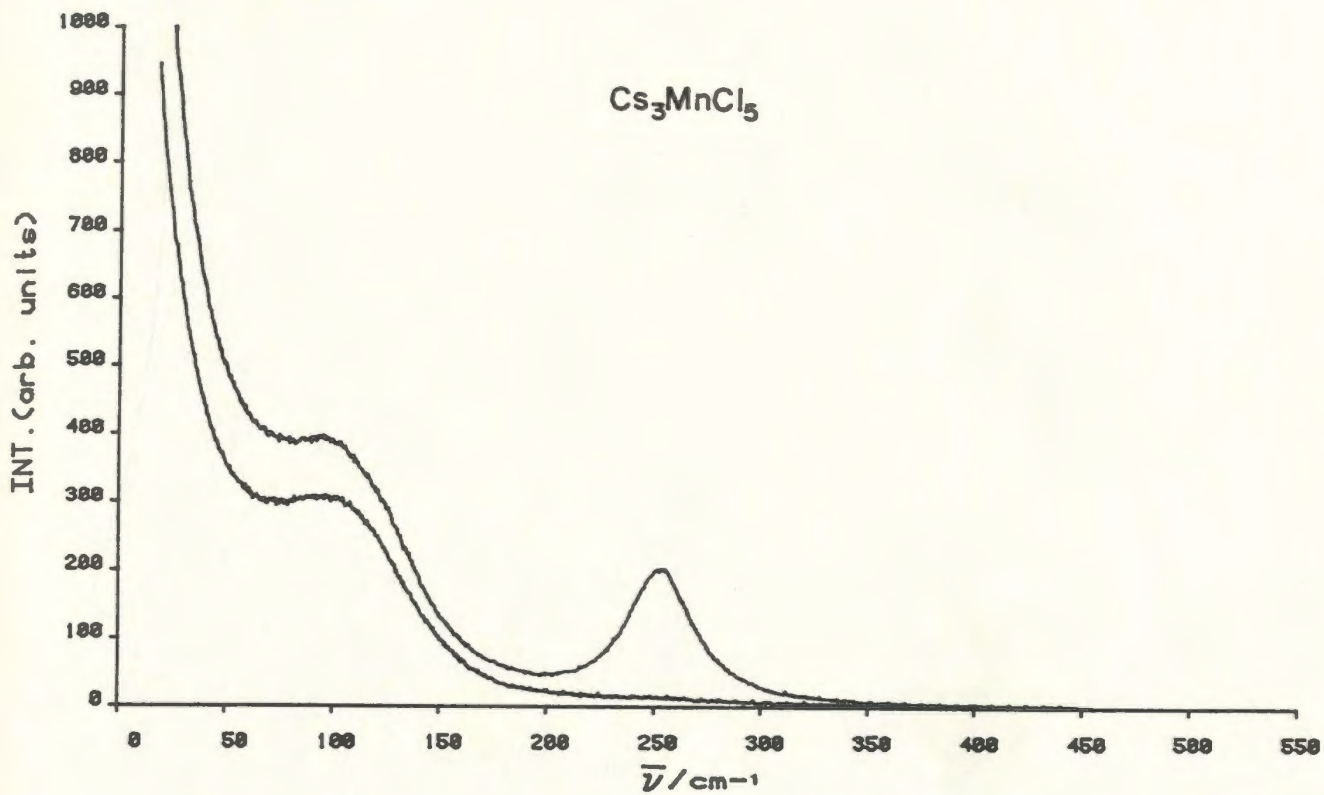


Figure 14. Raman spectra of molten CsMnCl_3 at 916 K, $I_{||}$
and I_{\perp} .

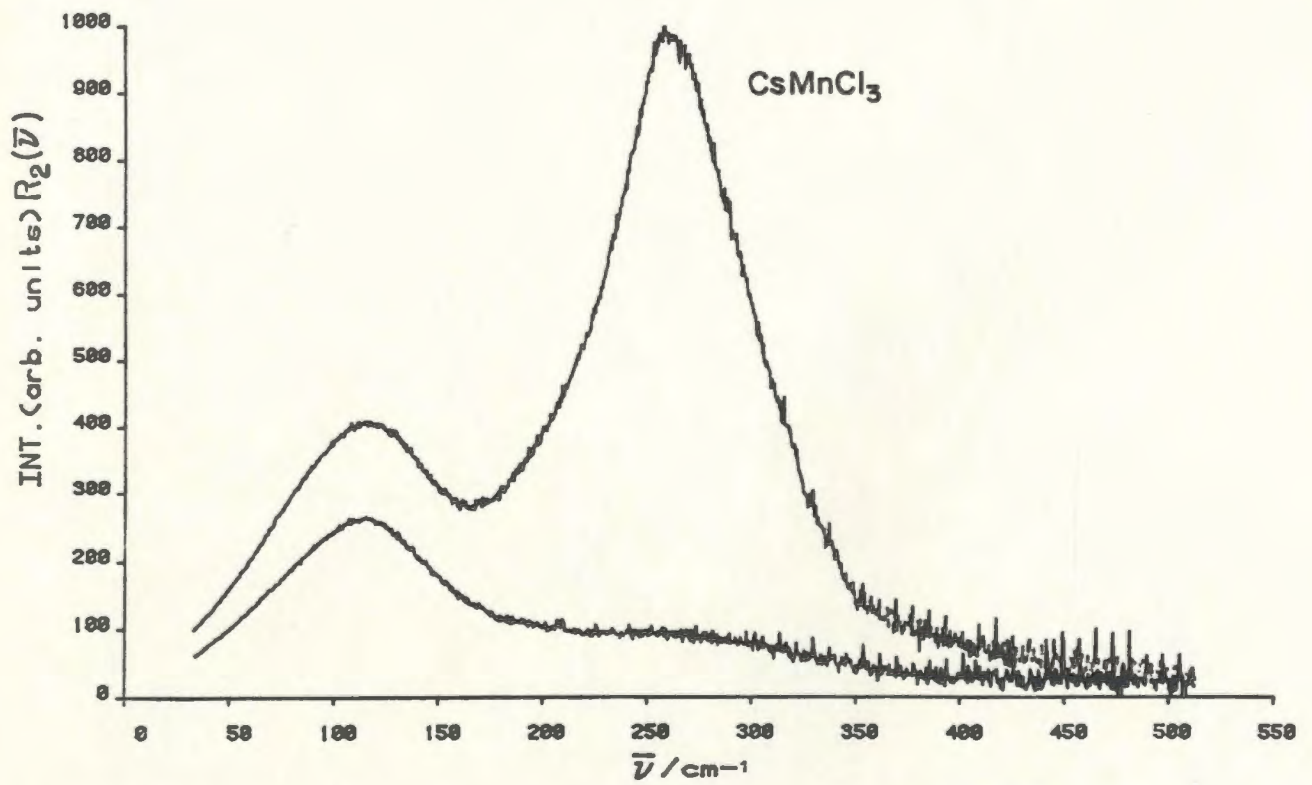
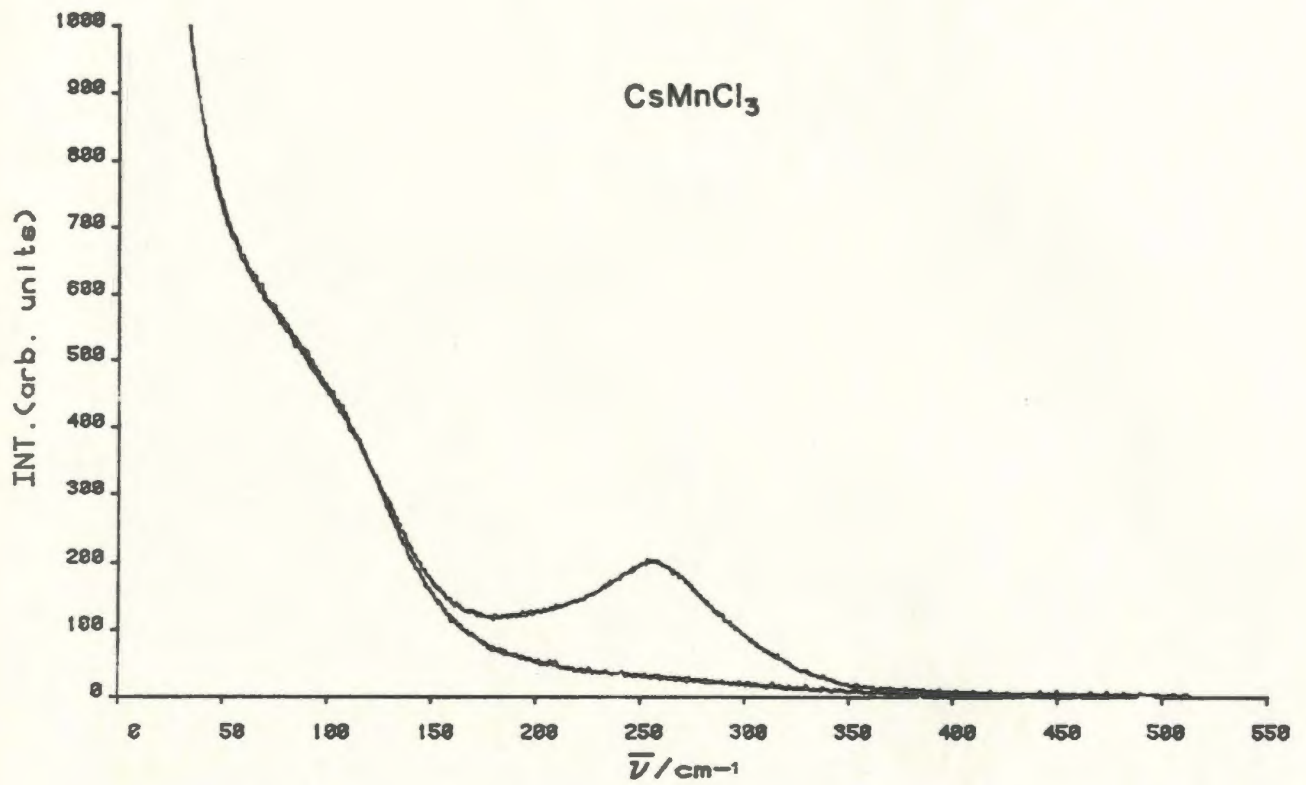


Figure 15. Raman spectra of molten CsMn_4Cl_9 at 865 K, $I_{||}$
and I_{\perp} .

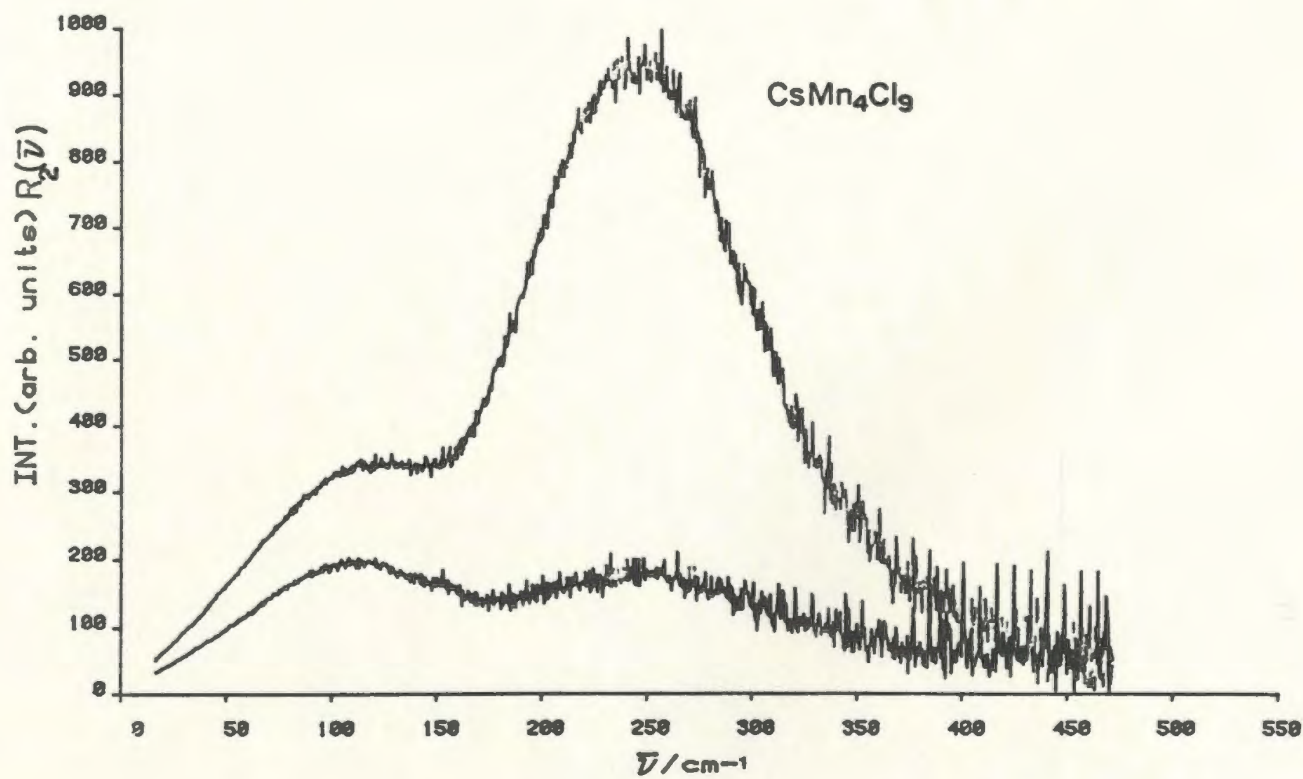
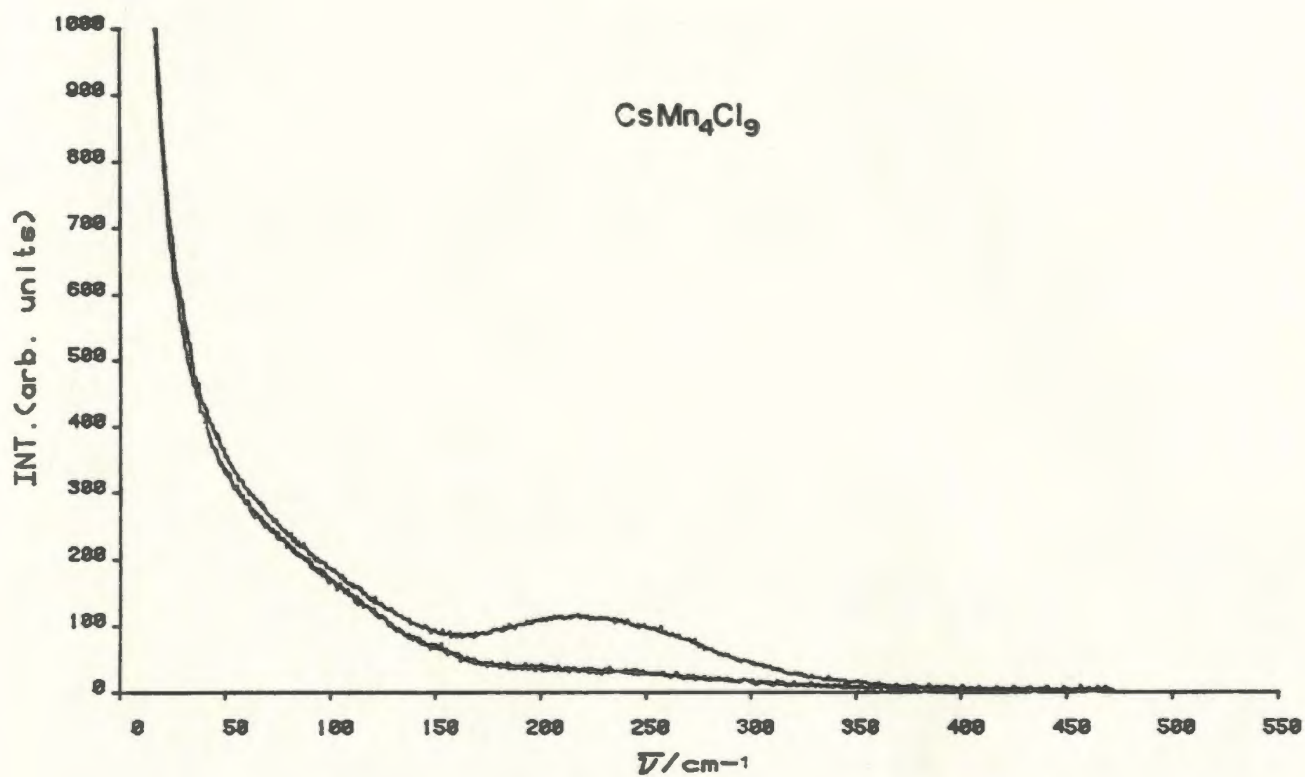


Figure 16. Effect of temperature on ν_1 mode of Cs_2MnCl_4 .

A. Plot of band position (cm^{-1}) vs temperature.

B. Plot of half band width (cm^{-1}) vs temperature.

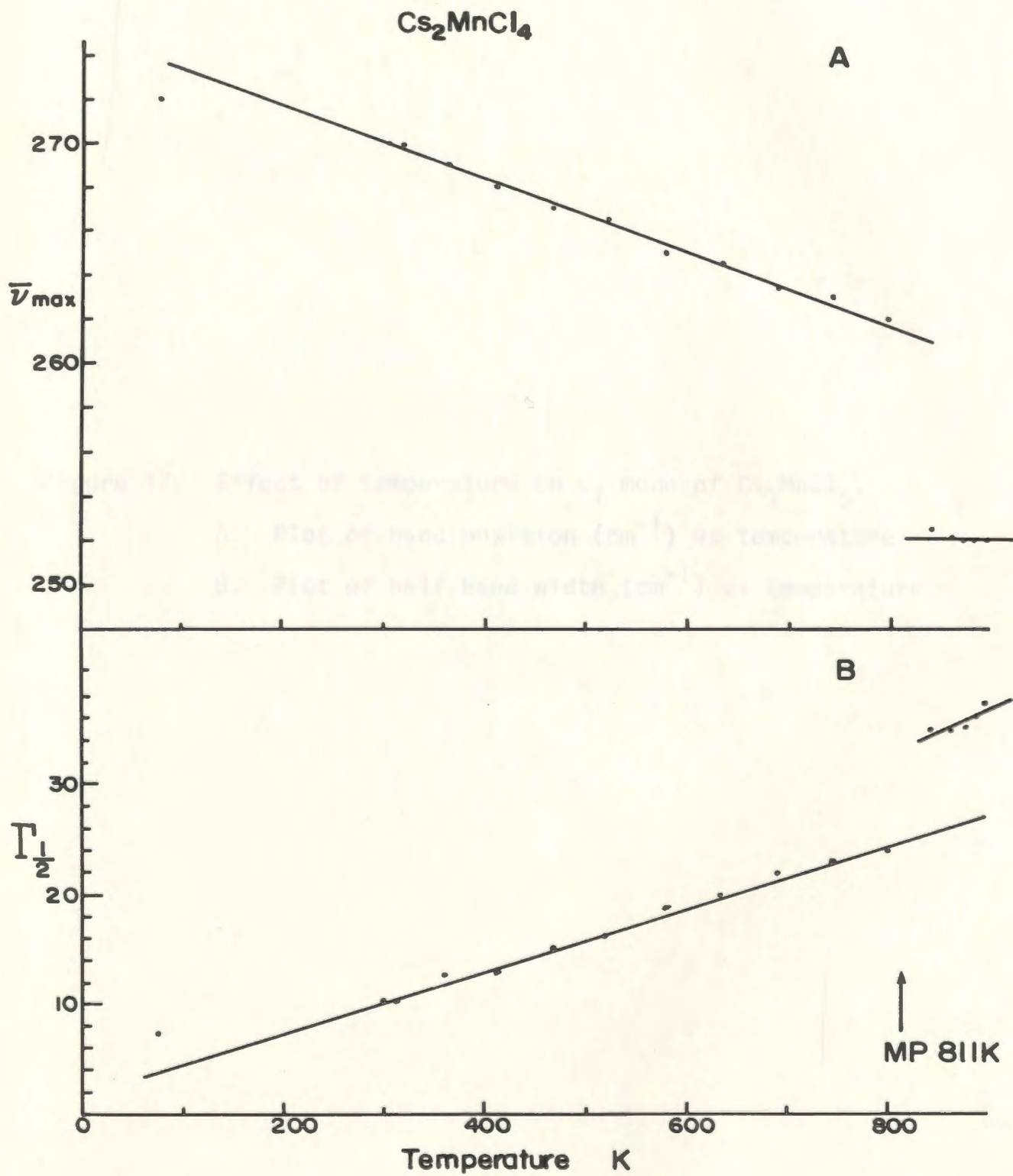


Figure 17. Effect of temperature on ν_{\max} and $\Gamma_{\frac{1}{2}}$ of Cs_2MnCl_4 .
A. Plot of band position (cm^{-1}) vs. temperature.
B. Plot of half band width (cm^{-1}) vs. temperature.

Figure 17. Effect of temperature on ν_1 mode of Cs_3MnCl_5 .

A. Plot of band position (cm^{-1}) vs temperature.

B. Plot of half band width (cm^{-1}) vs temperature.

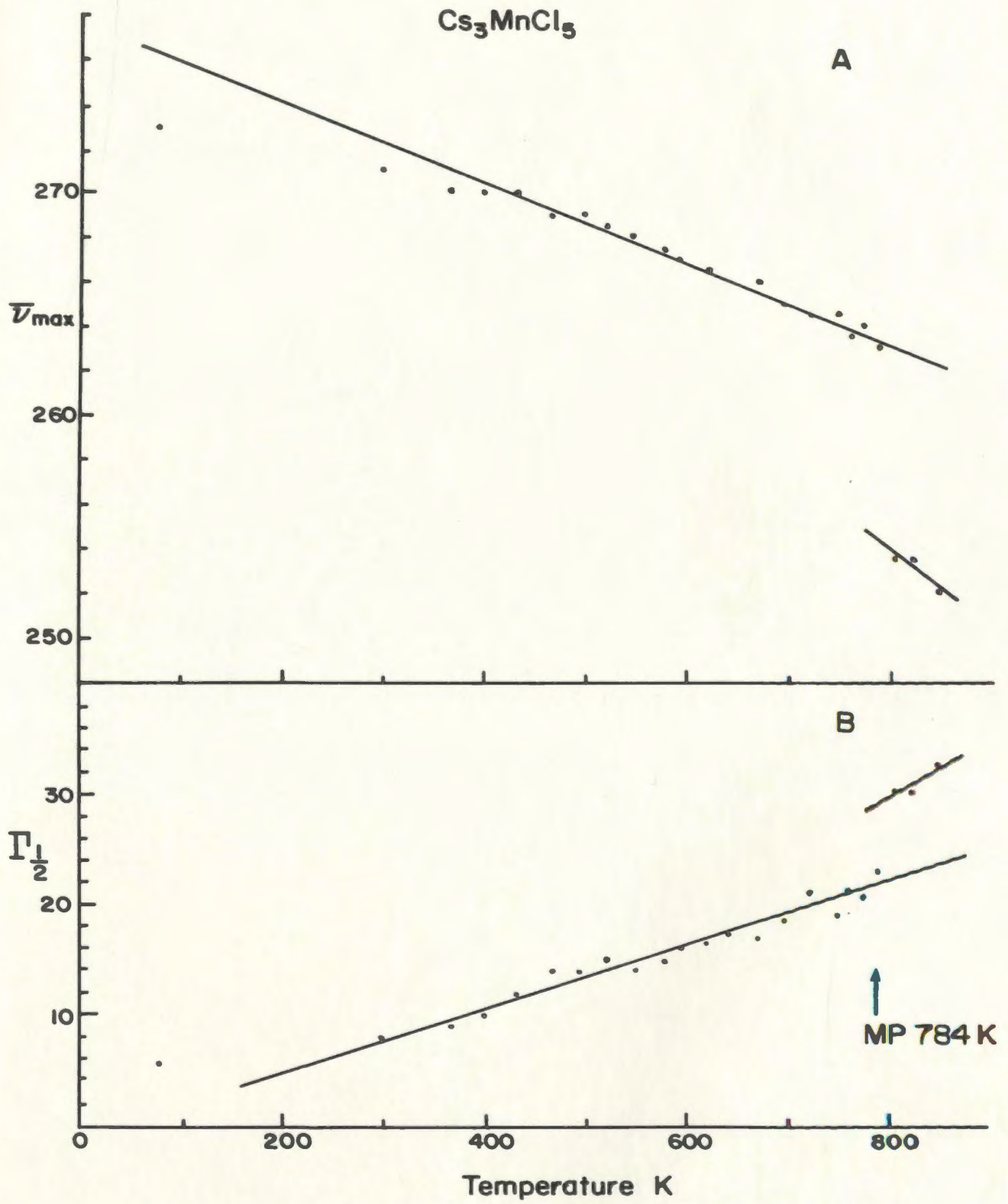
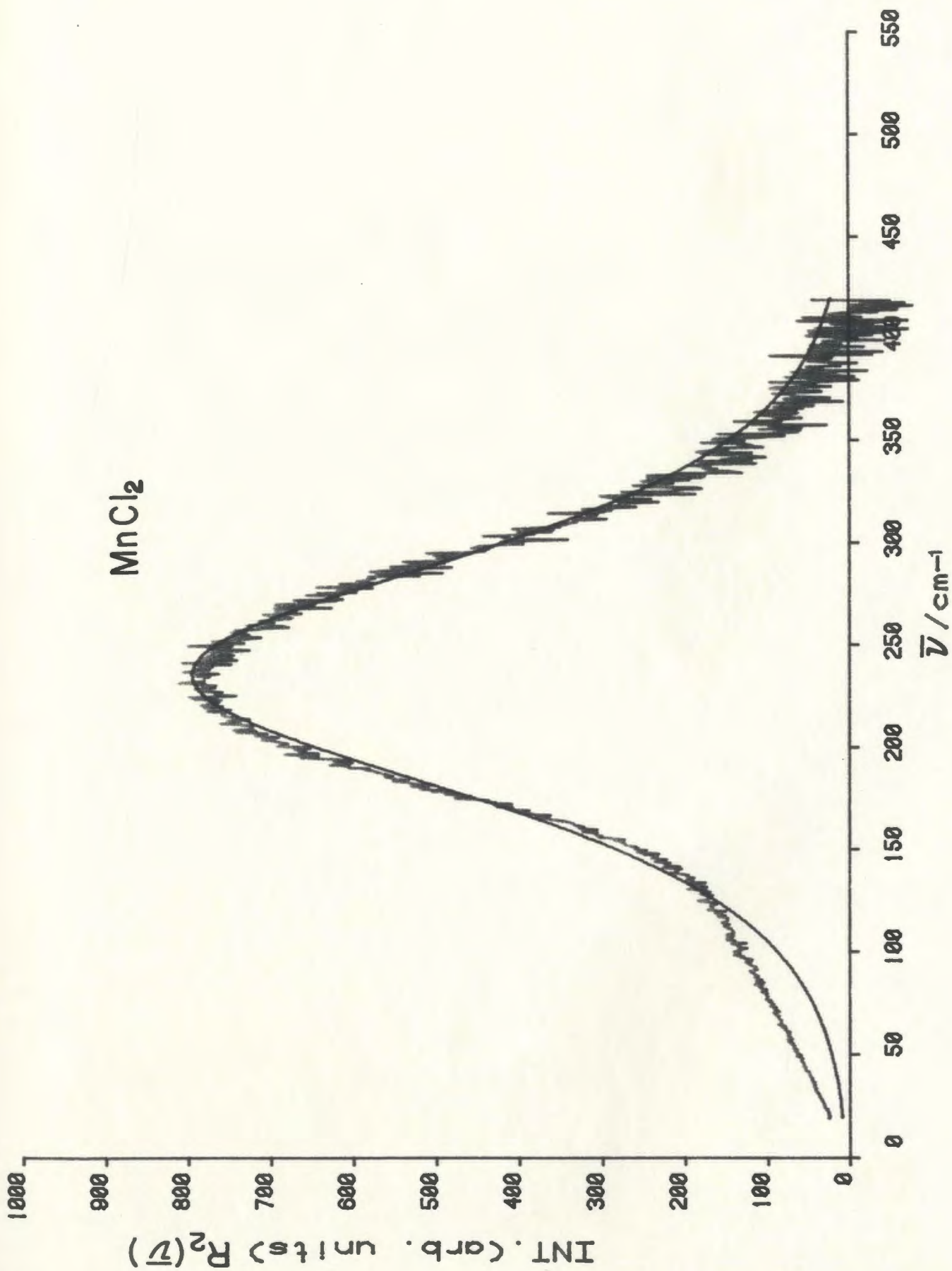


Figure 18. Isotropic Raman spectra of molten MnCl_2 . The smooth line is the best-fit curve calculated with a single Gaussian*Lorentzian function.



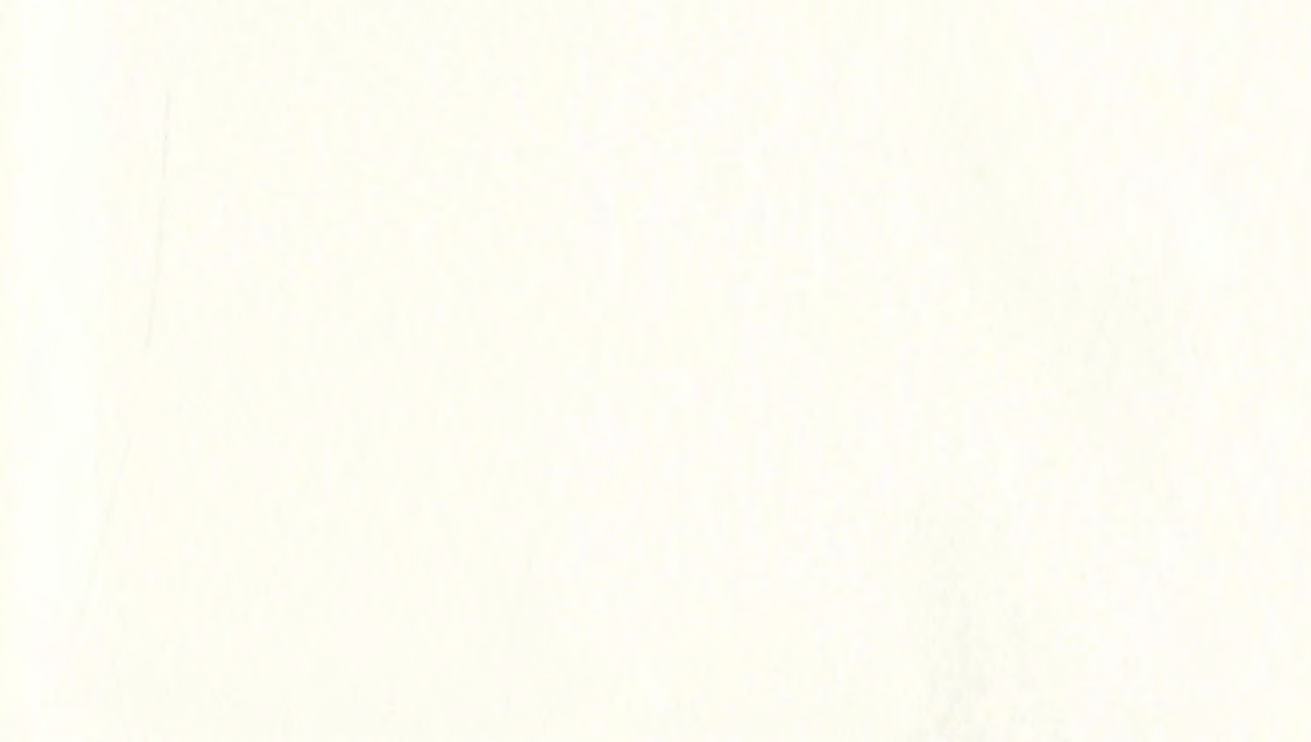


Figure 19. Isotropic Raman spectra of molten Cs_2MnCl_4 . The smooth line is the best-fit curve calculated with a single Lorentzian function.

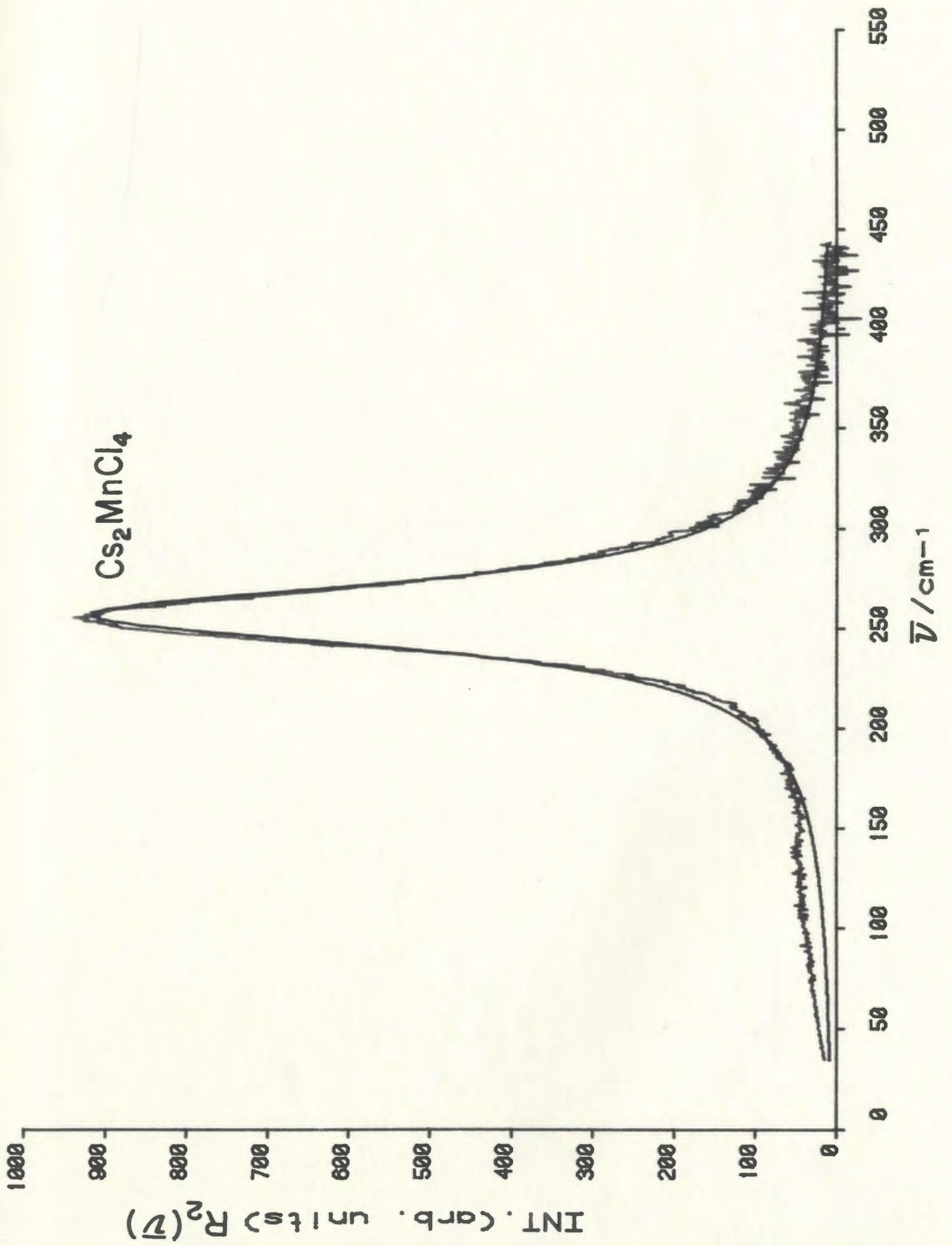


Figure 20. Isotropic Raman spectra of molten Cs_3MnCl_5 . The smooth line is the best-fit curve calculated with a single Lorentzian function.

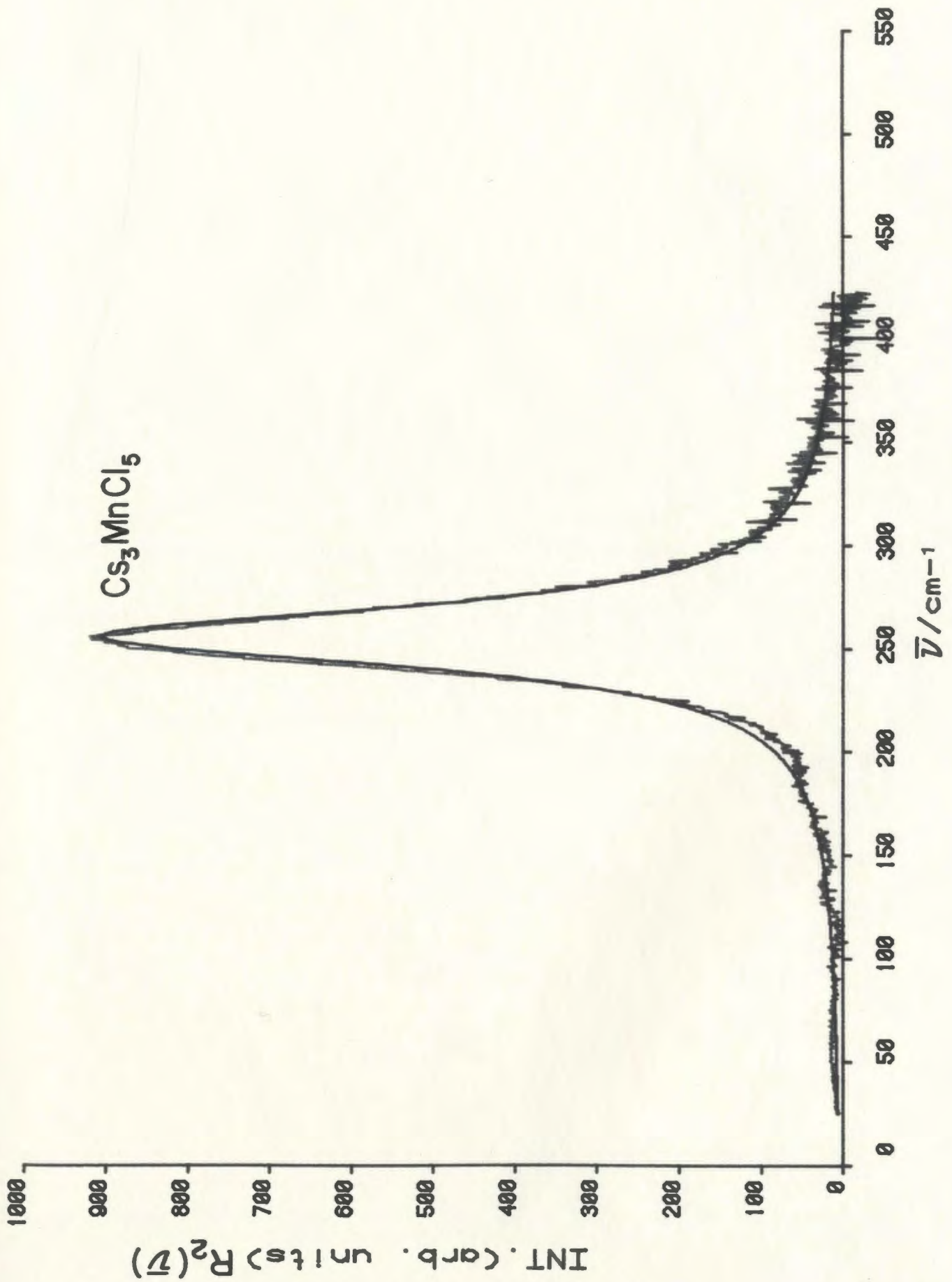


Figure 21. Isotropic Raman spectra of molten CsMnCl_3 . The smooth line is the best-fit curve calculated with a single Gaussian*Lorentzian function.

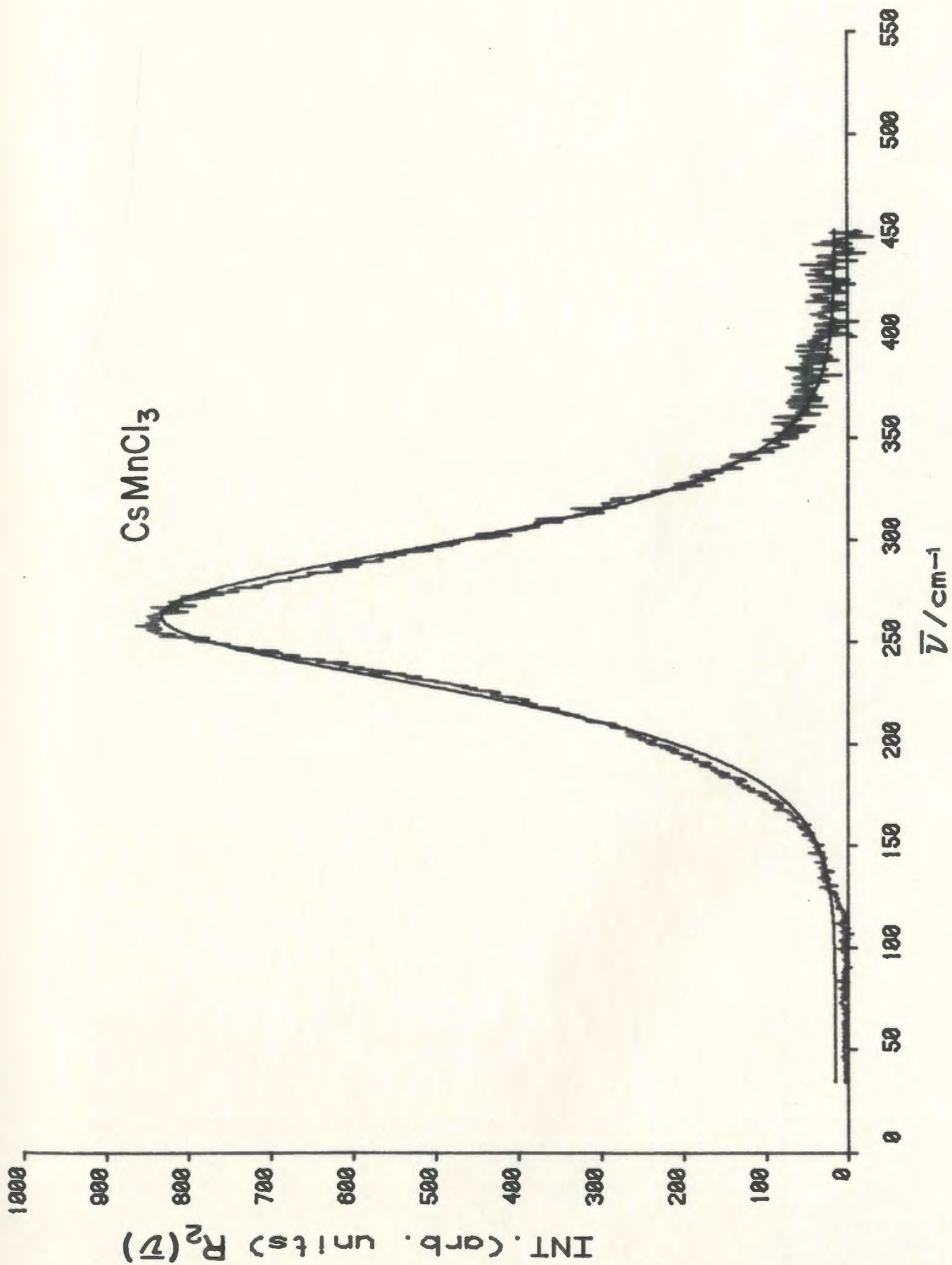


Figure 22. Isotropic Raman spectra of molten CsMnCl_3 . The smooth line is the best-fit curve calculated with a single Lorentzian function.

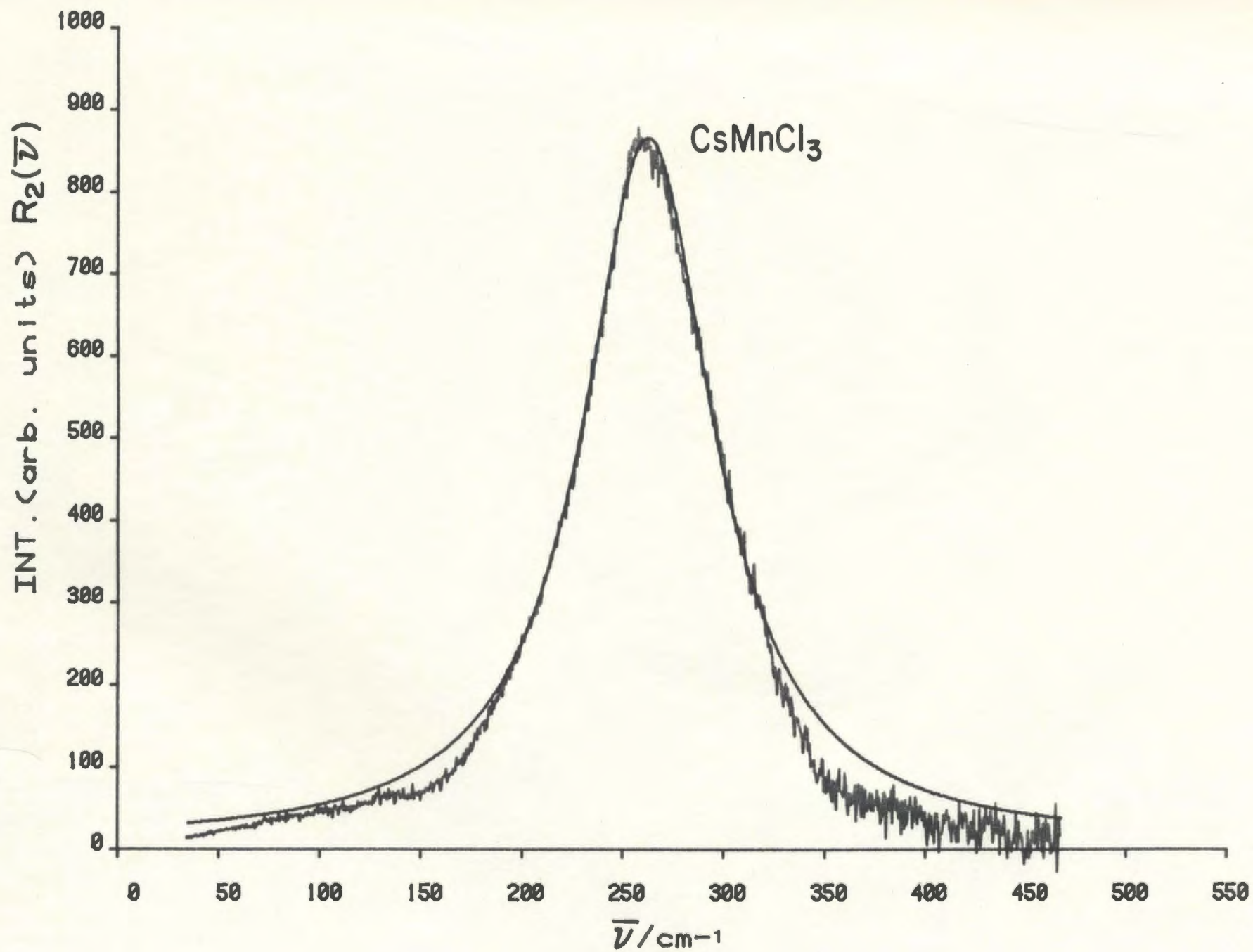
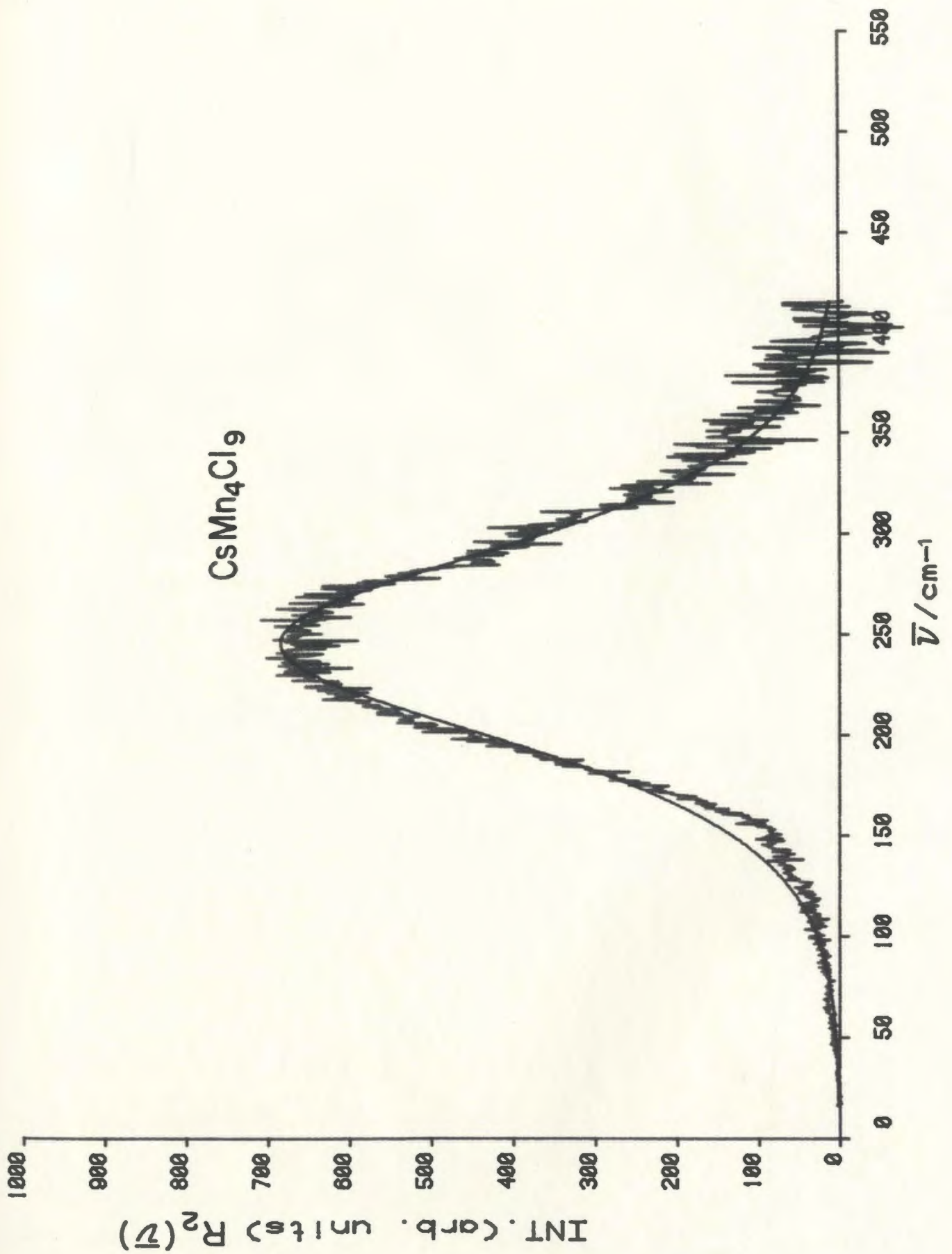


Figure 23. Isotropic Raman spectra of molten CsMn_4Cl_9 . The smooth line is the best-fit curve calculated with a single Gaussian*Lorentzian function.

CsMn4Cl9



The polarized peak from the $R_2(\bar{\nu})$ spectrum was fitted to Lorentzian and Gaussian*Lorentzian functions. The results are shown in figures 18, 19, 20, 21, 22, and 23. The frequency (cm^{-1}), intensity, half band width (cm^{-1}) and type of fit are shown in Table 20. For CsMnCl_3 both the Lorentzian and Gaussian*Lorentzian fits are given to show that the results are not very dependent on the choice of function.

4.2.2 MnCl₂-RbCl Melts

The Raman spectra of RbMnCl_3 , Rb_2MnCl_4 , $\text{RbCl}:\text{MnCl}_2$ (3:1), and $\text{Rb}_3\text{Mn}_2\text{Cl}_7$ melts are shown in figures 24, 25, 26, and 27. The results indicate the presence of MnCl_4^{2-} species. An isolated MnCl_4^{2-} tetrahedral ion is proposed for melts of composition $\text{MnCl}_2 \cdot n\text{RbCl}$ ($n \geq 2$) but for RbMnCl_3 and $\text{Rb}_3\text{Mn}_2\text{Cl}_7$ melts ($n < 2$) a tetrahedral species with corner sharing are expected. The half band width of the stretching mode (ν_1) increased by increasing MnCl_2 content. The ν_3 peak is too weak to be observed, while ν_2 and ν_4 are observed as overlapped peaks in the region 70-135 cm^{-1} .

The polarized peak from the $R_2(\bar{\nu})$ spectrum was fitted to Gaussian*Lorentzian and Lorentzian functions. The results are shown in figures 28, 29, 30, and 31 and tabulated in Table 21.

4.2.3 MnCl₂-KCl Melts

The Raman spectra of KMnCl_3 , $\text{KCl}:\text{MnCl}_2$ (2:1), $\text{KCl}:\text{MnCl}_2$ (3:1), $\text{K}_3\text{Mn}_2\text{Cl}_7$, and K_4MnCl_6 melts are shown in figures 32, 33, 34, 35, and 36. One polarized peak (ν_1) appears in each spectrum in the range 200-325 cm^{-1} , ν_2 and ν_4 are observed in the region 70-140 cm^{-1} , ν_3 appear around $\sim 300 \text{ cm}^{-1}$ but is weak to be observed. The data indicate

Table 21. Summary of results of curve resolution analysis for
 MnCl_2 - RbCl Melts.

Compound	Frequency (cm^{-1})	Intensity	Half band width (cm^{-1})	Function
$\text{RbCl}:\text{MnCl}_2$ (3:1)	254.4	890	41.0	L
Rb_2MnCl_4	258.0	918	42.5	L
$\text{Rb}_3\text{Mn}_2\text{Cl}_7$	259.6	869	62.0	L
RbMnCl_3	252.1	828	85.1	G * L

G: Gaussian, L: Lorentzian

Figure 24. Raman spectra of molten RbMnCl_3 at 878 K, $I_{||}$
and I_{\perp} .

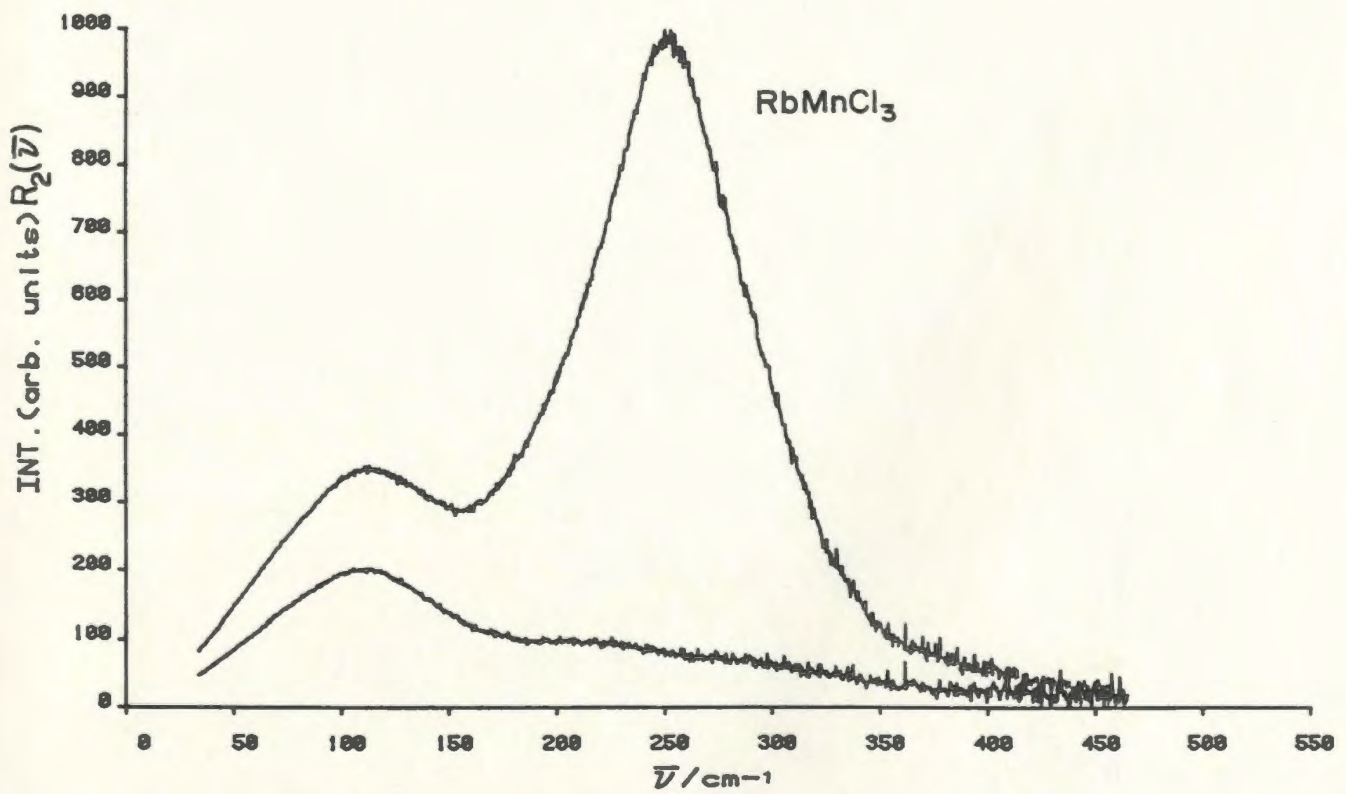
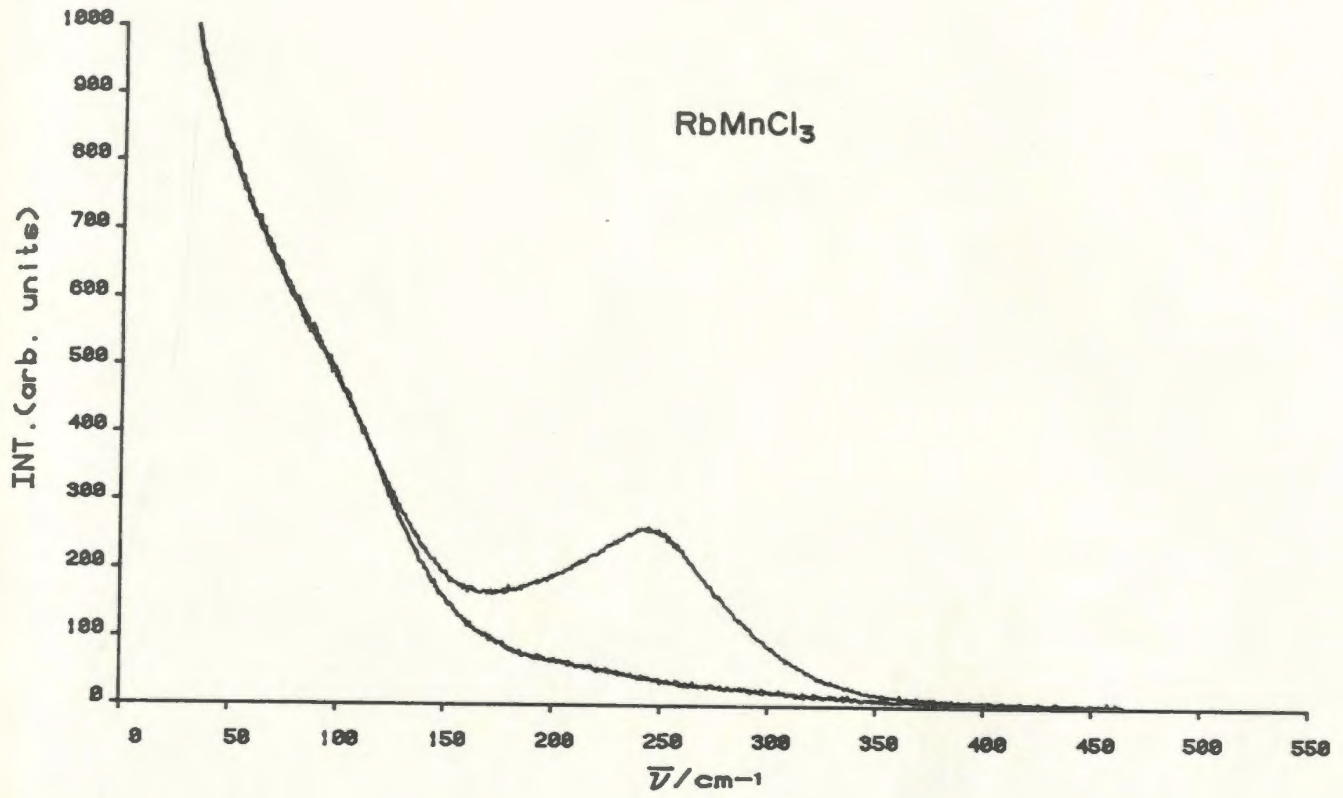


Figure 25. Raman spectra of molten Rb_2MnCl_4 at 753 K, $I_{||}$
and I_{\perp} .

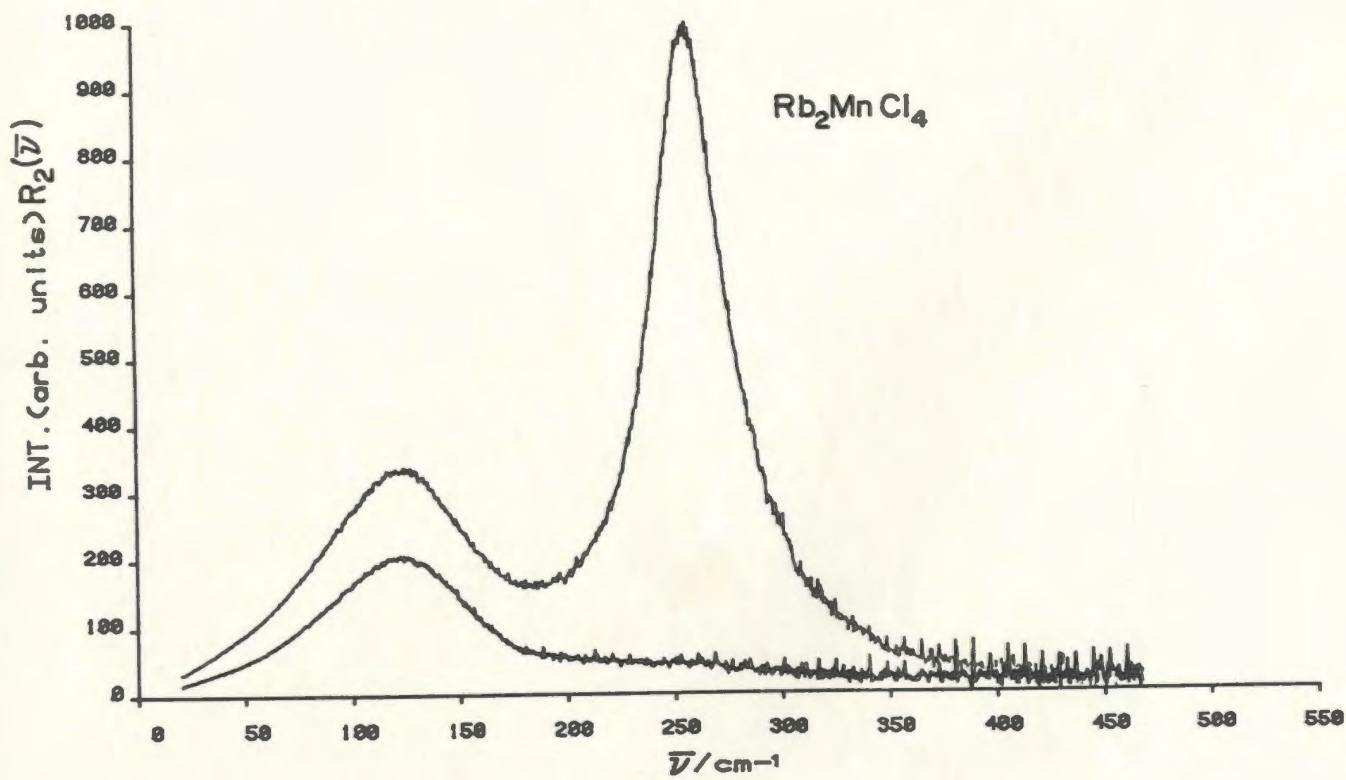
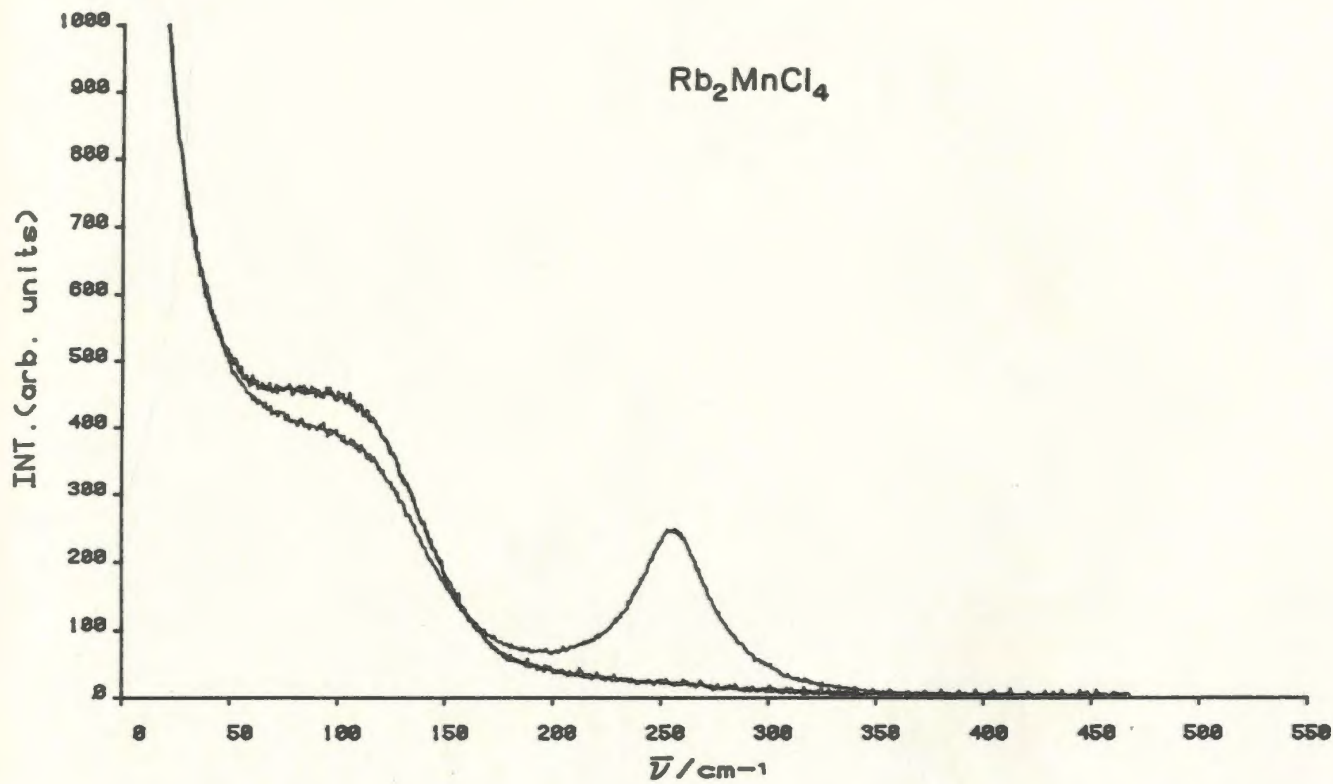


Figure 26. Raman spectra of molten $\text{RbCl}:\text{MnCl}_2$ (3:1) at
882 K, $I_{||}$ and I_{\perp} .

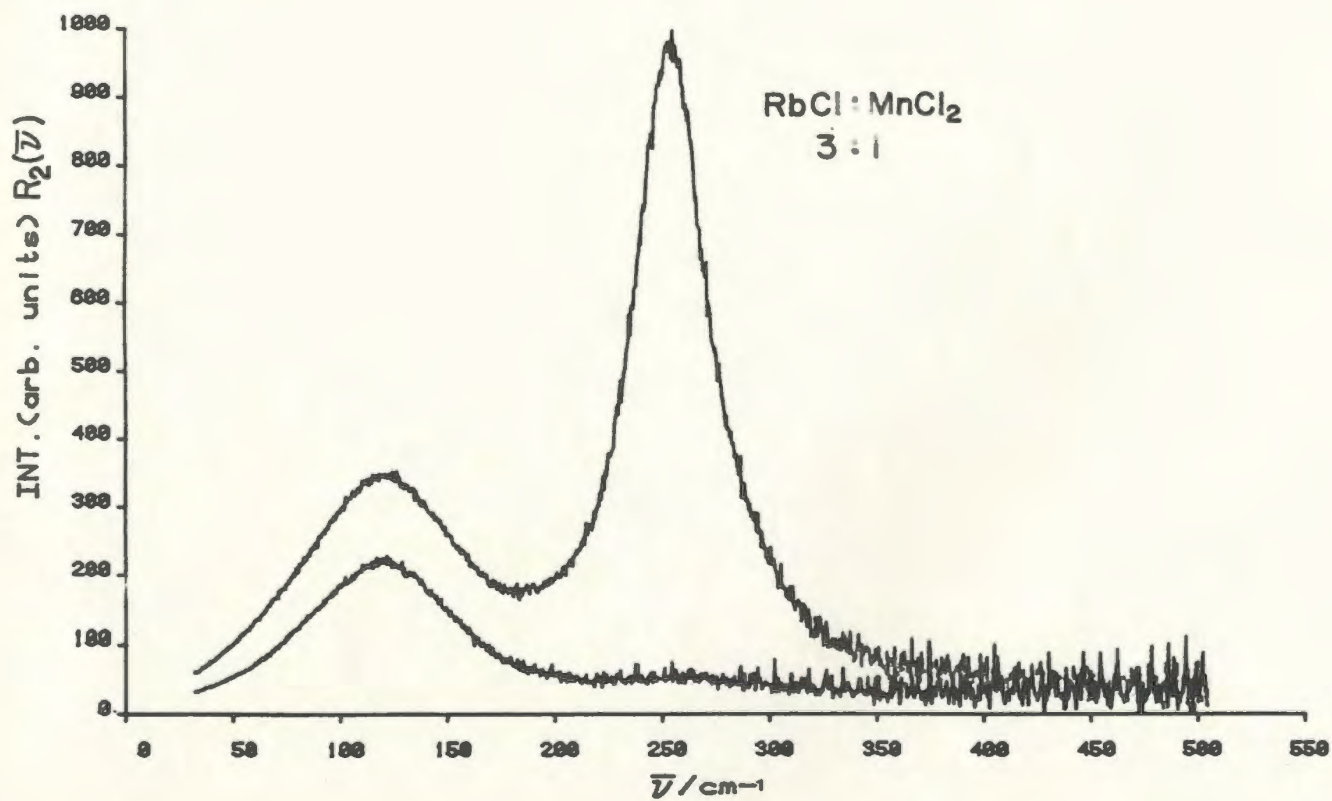
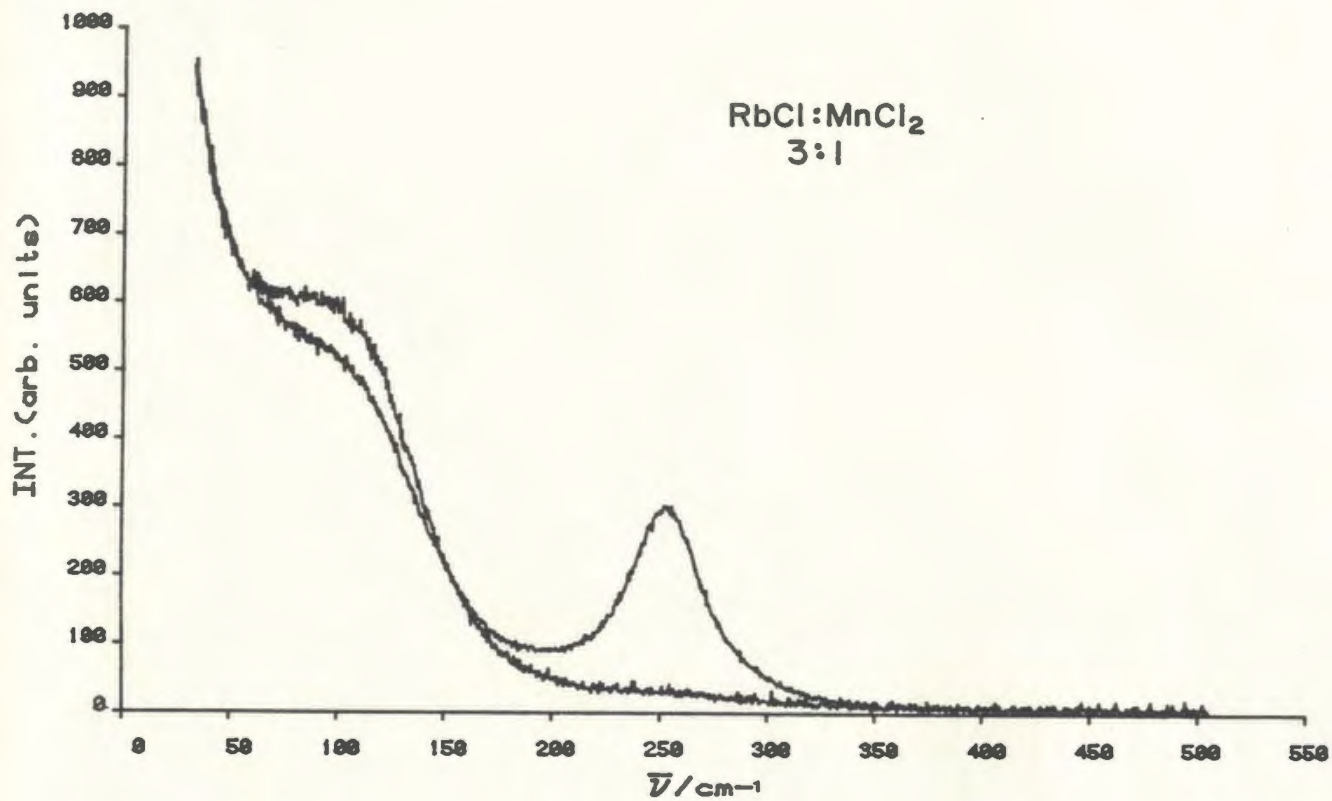


Figure 27. Raman spectra of molten $\text{Rb}_3\text{Mn}_2\text{Cl}_7$ at 889 K,

$I_{||}$ and I_{\perp} .

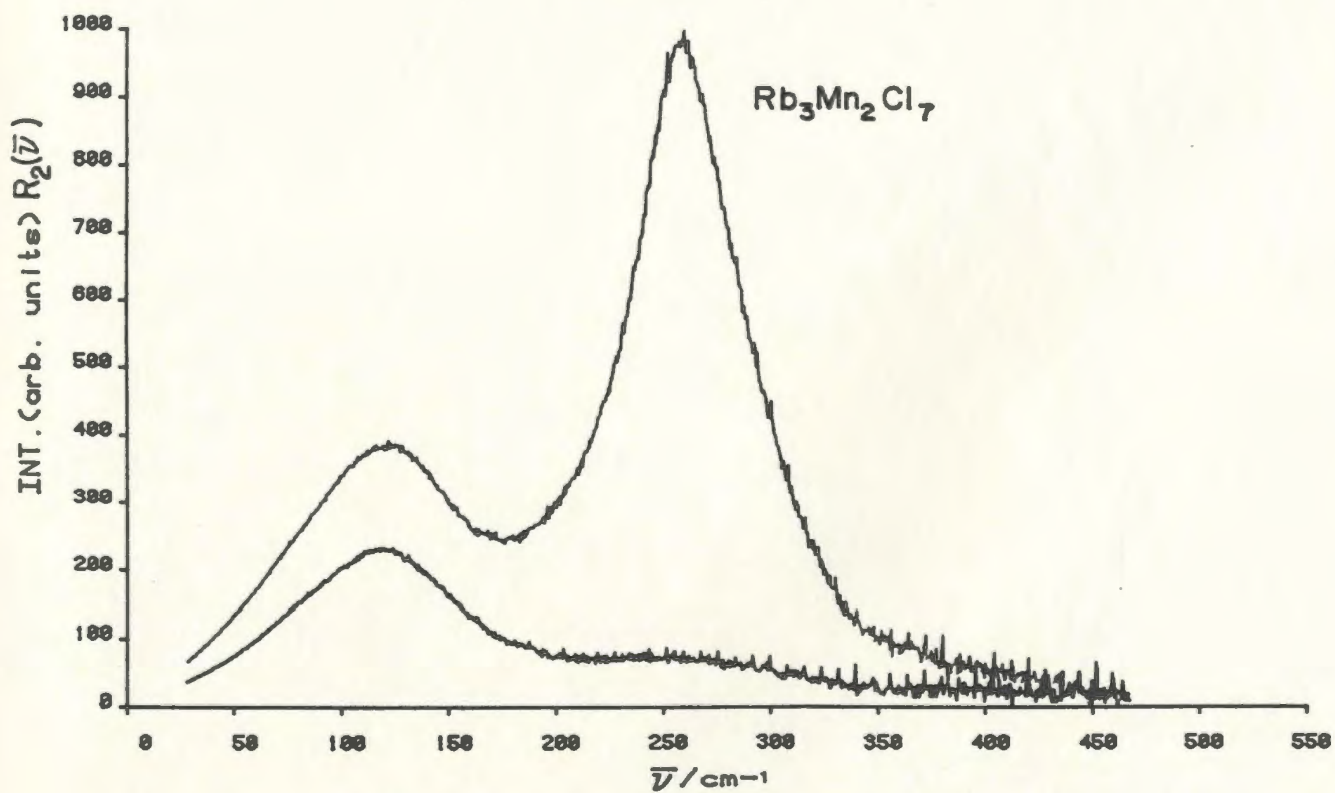
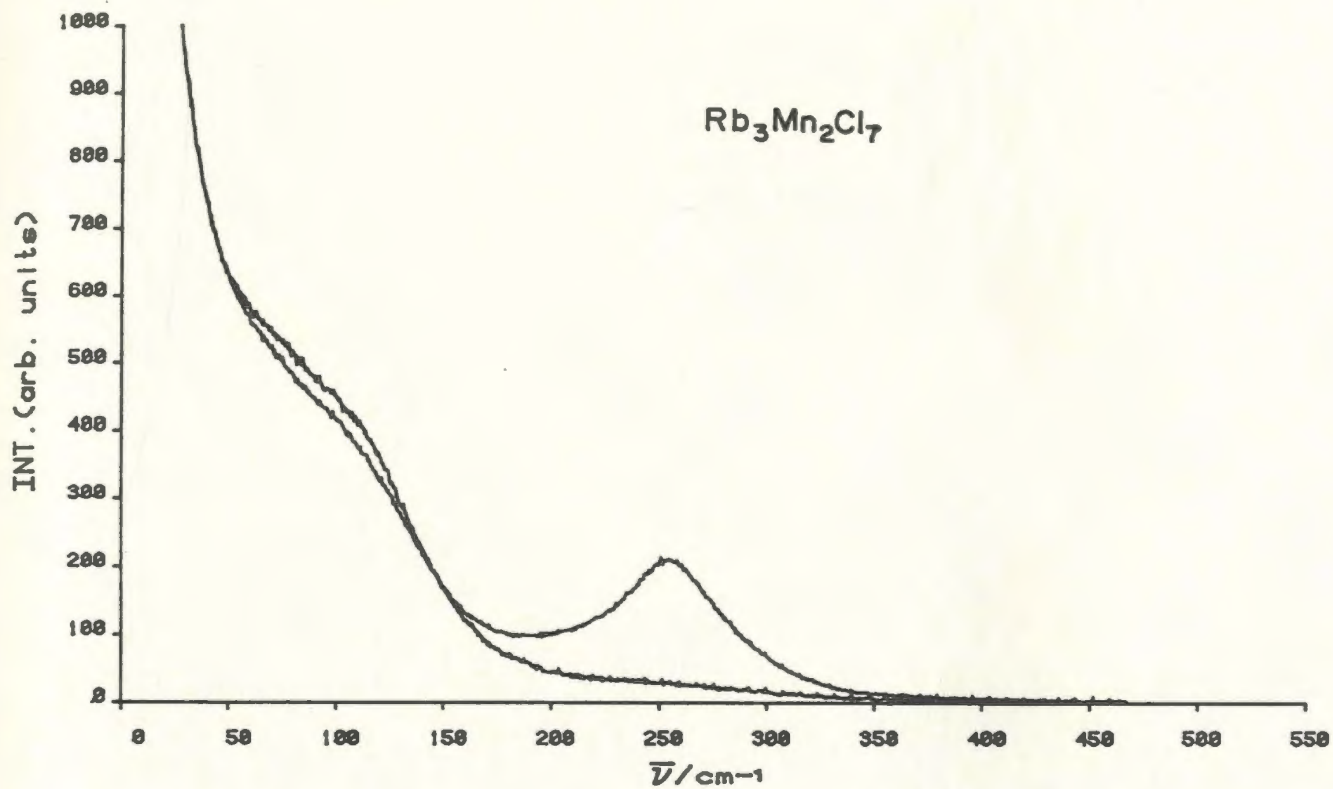


Figure 28. Isotropic Raman spectra of molten RbMnCl_3 . The smooth line is the best-fit curve calculated with a single Gaussian*Lorentzian function.

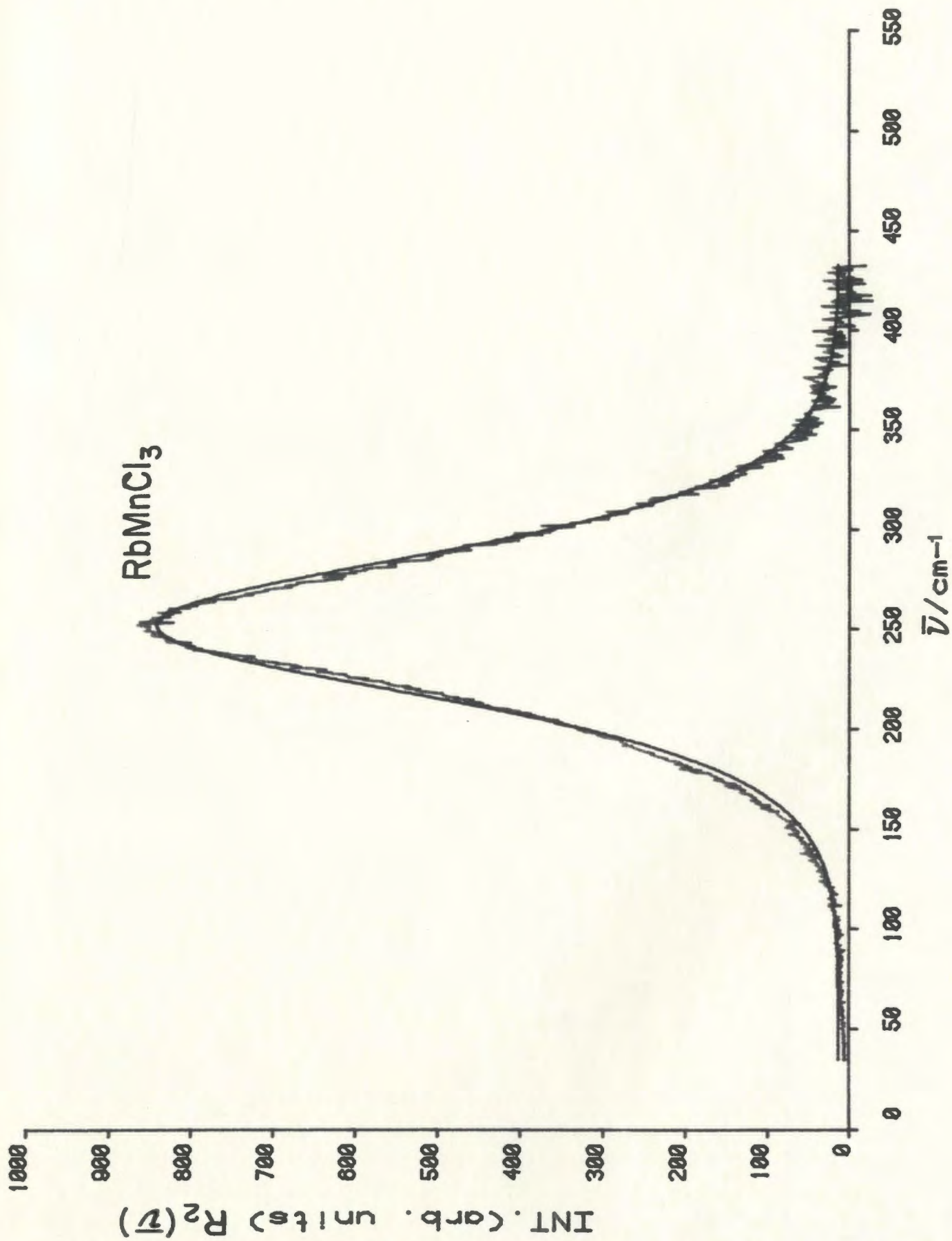


Figure 29. Isotropic Raman spectra of molten Rb_2MnCl_4 . The smooth line is the best-fit curve calculated with a single Lorentzian function.

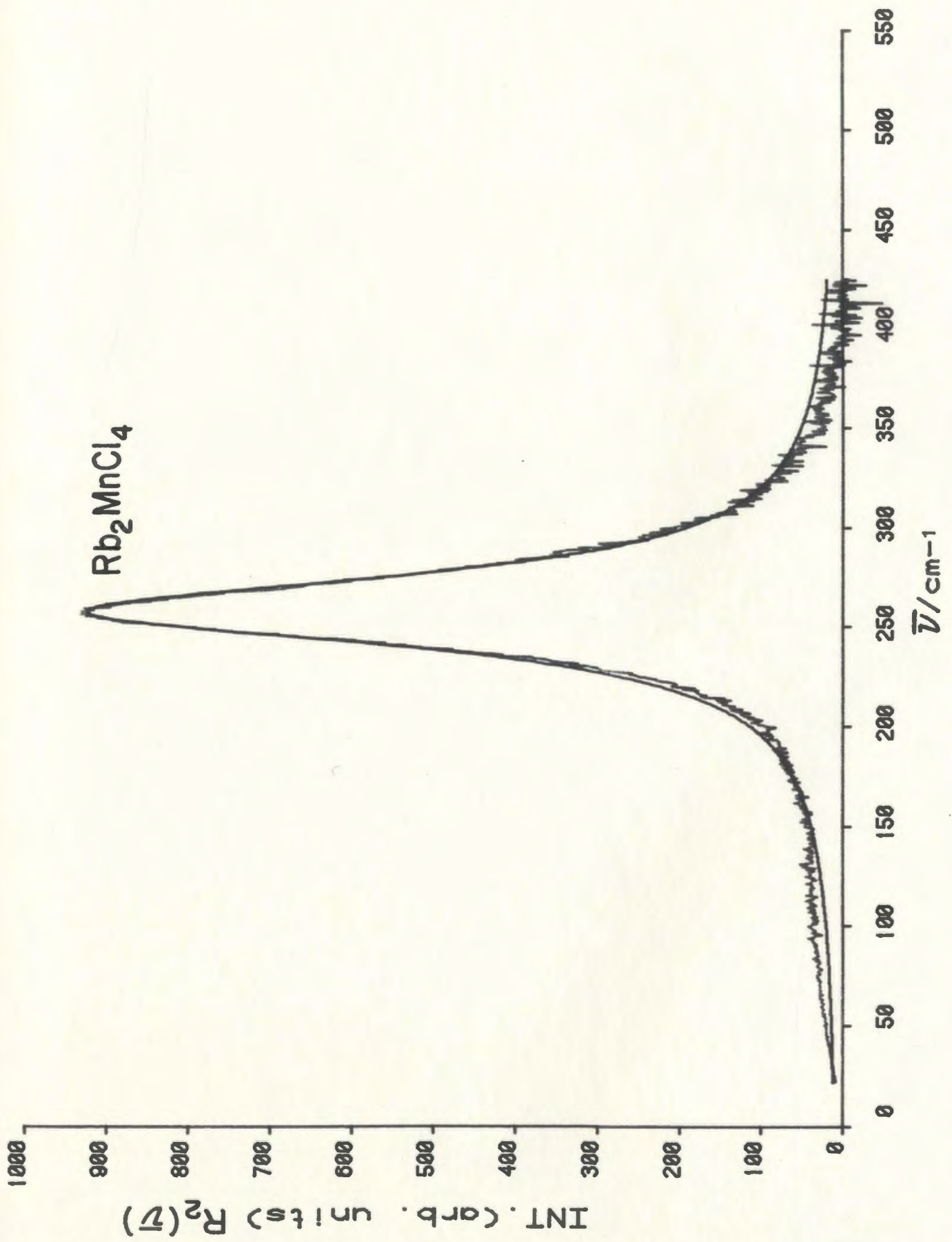




Figure 30. Isotropic Raman spectra of molten RbCl:MnCl₂ (3:1).
The smooth line is the best-fit curve calculated with
a single Lorentzian function.

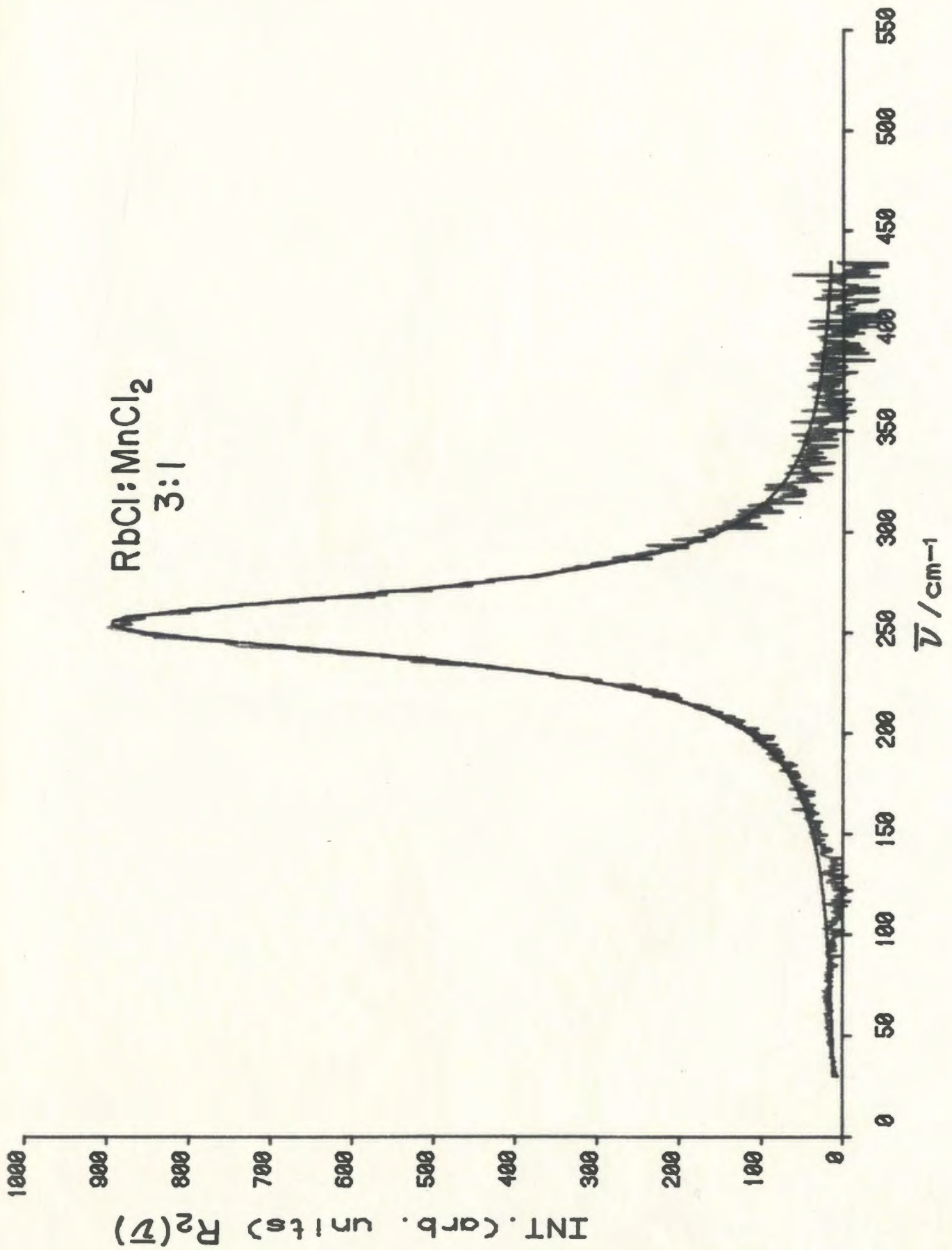
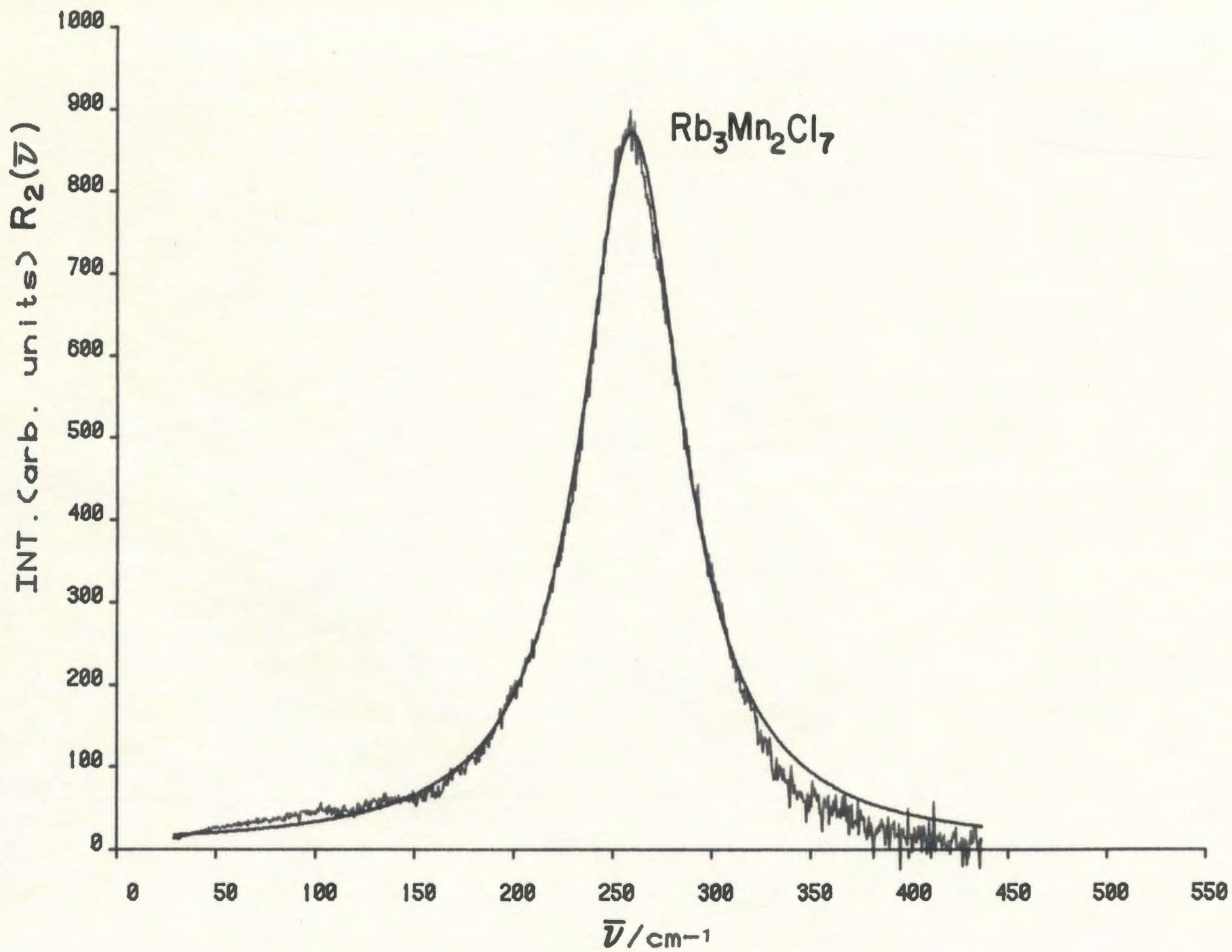


Figure 31. Isotropic Raman spectra of molten $\text{Rb}_3\text{Mn}_2\text{Cl}_7$. The smooth line is the best-fit curve calculated with a single Lorentzian function.



the existence of MnCl_4^{2-} as an isolated entities for melts with high KCl content or with corner sharing for melts with low KCl content. For $\text{KCl} \cdot X\text{MnCl}_2$ melts ($X = 0.2, 0.3, 0.4$). A previous Raman study¹⁹ proposed the tetrahedral MnCl_4^{2-} ion as the predominant species in this concentration range, but pyramidal MnCl_3^- ion or $\text{Mn}_2\text{Cl}_7^{3-}$ were also proposed in this composition range, whereas MnCl_6^{4-} ion was proposed in the concentration range ($x = 0.9, 0.8, 0.67$) and small amount of MnCl_4^{2-} ion was also suggested.

It was reported¹⁹ that the half band width of the totally symmetric mode increased with increased MnCl_2 concentration and the effect attributed to sharing of Cl ion. The present results confirmed the increment in the half band width upon increasing MnCl_2 mole fraction, see Table 22.

The polarized peak from the $R_2(\bar{\nu})$ spectrum was fitted to Gaussian*Lorentzian and Lorentzian functions. The results are shown in figures 37, 38, 39, 40 and 41 and tabulated in Table 22.

4.2.4 MnCl_2 -NaCl Melts

The Raman spectra of NaMnCl_3 , Na_2MnCl_4 , $\text{NaCl}:\text{MnCl}_2$ (3:1), $\text{Na}_2\text{Mn}_3\text{Cl}_8$, NaMn_4Cl_9 , and Na_6MnCl_8 are shown in figures 42, 43, 44, 45, 46 and 47. One polarised peak was observed in each spectrum and assigned to the symmetric mode (ν_1). The ν_2 and ν_4 modes were observed in the region 70-140 cm^{-1} . The antisymmetric mode ν_3 of the tetrahedral ion is usually weak in the Raman spectrum and appear around $\sim 300 \text{ cm}^{-1}$. The spectra indicate the presence of tetrahedral species in the melts. The half band width of the symmetric mode ν_1 increased with increased MnCl_2 concentration, see Table 23.

Table 22. Summary of results of curve resolution analysis for $\text{MnCl}_2\text{-KCl}$ Melts.

Compound	Frequency (cm^{-1})	Intensity	Half band width (cm^{-1})	Function
K_4MnCl_6	256.0	887	45.9	L
$\text{KCl}:\text{MnCl}_2$ (3:1)	255.7	801	48.2	L
$\text{KCl}:\text{MnCl}_2$ (2:1)	255.0	850	51.4	L
$\text{K}_3\text{Mn}_2\text{Cl}_7$	258.4	879	63.6	L
KMnCl_3	258.9	770	86.7	G * L

G: Gaussian, L: Lorentzian

Figure 32. Raman spectra of molten KMnCl_3 at 816 K, $I_{||}$
and I_{\perp} .

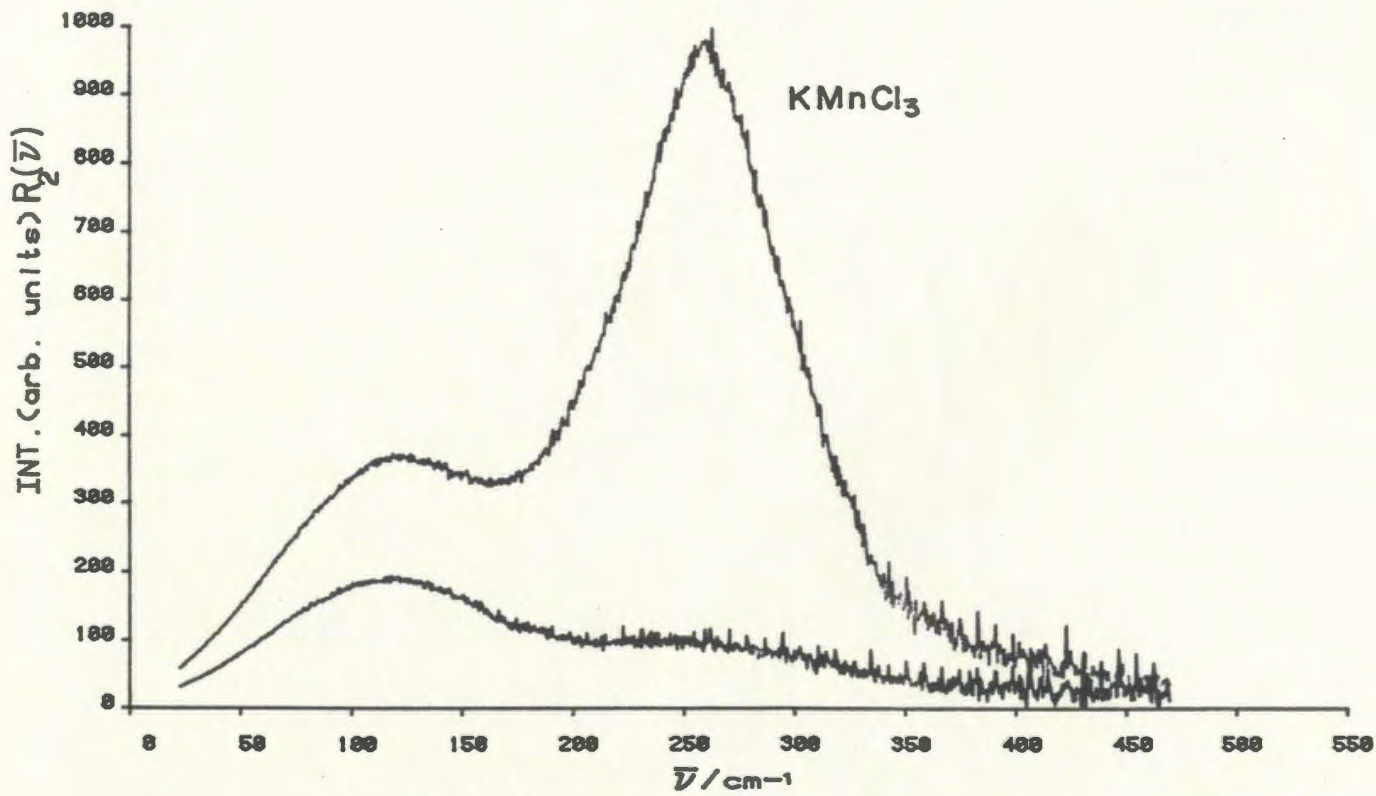
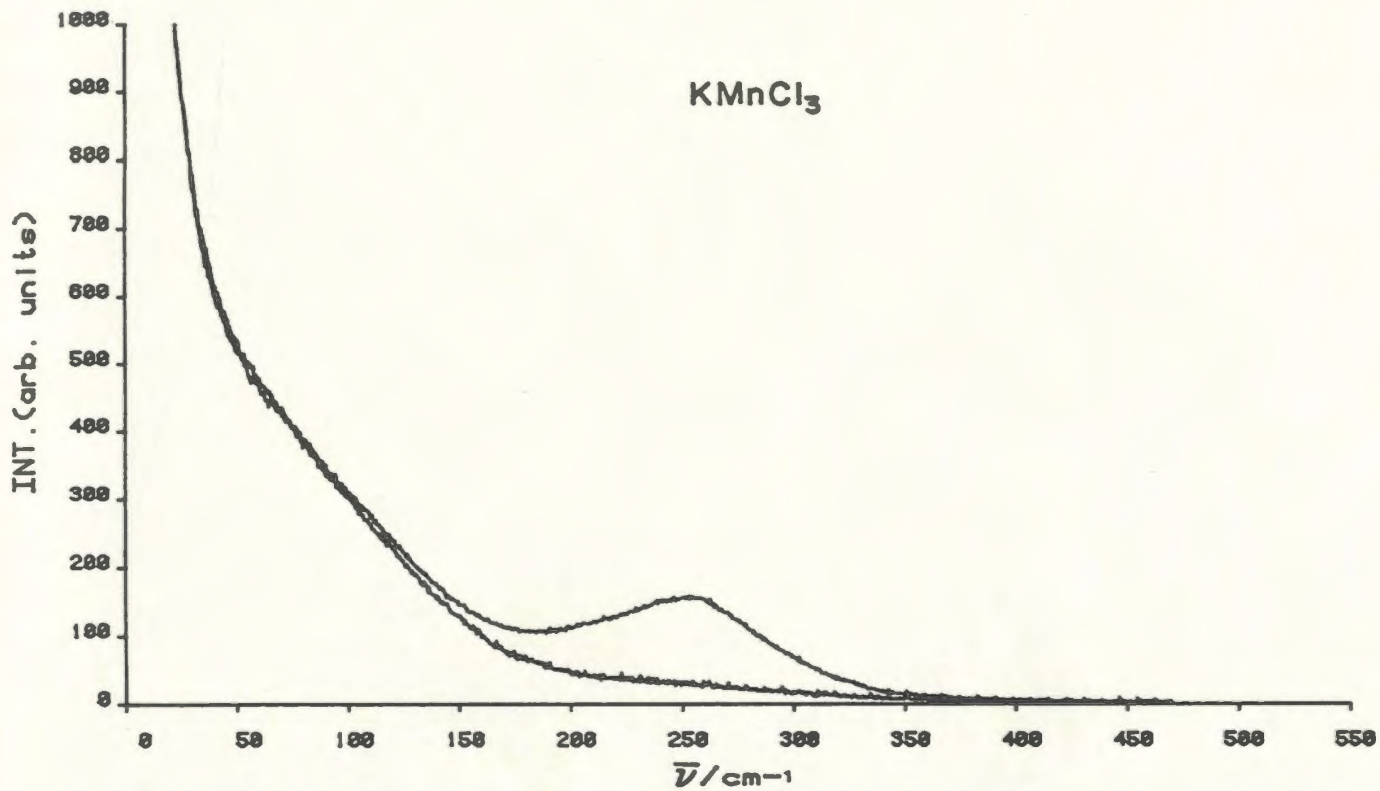


Figure 33. Raman spectra of molten KCl:MnCl_2 (2:1) at 882 K, $I_{||}$ and I_{\perp} .

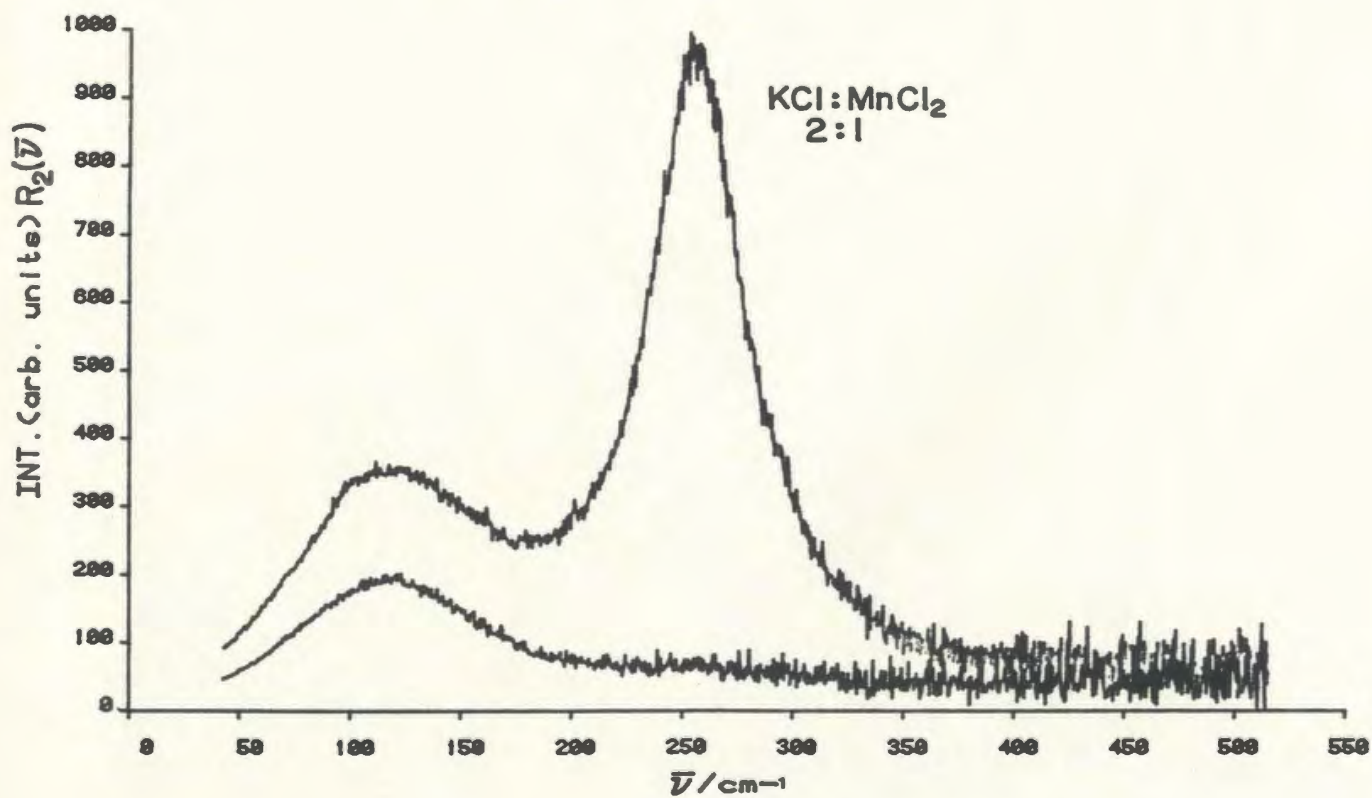
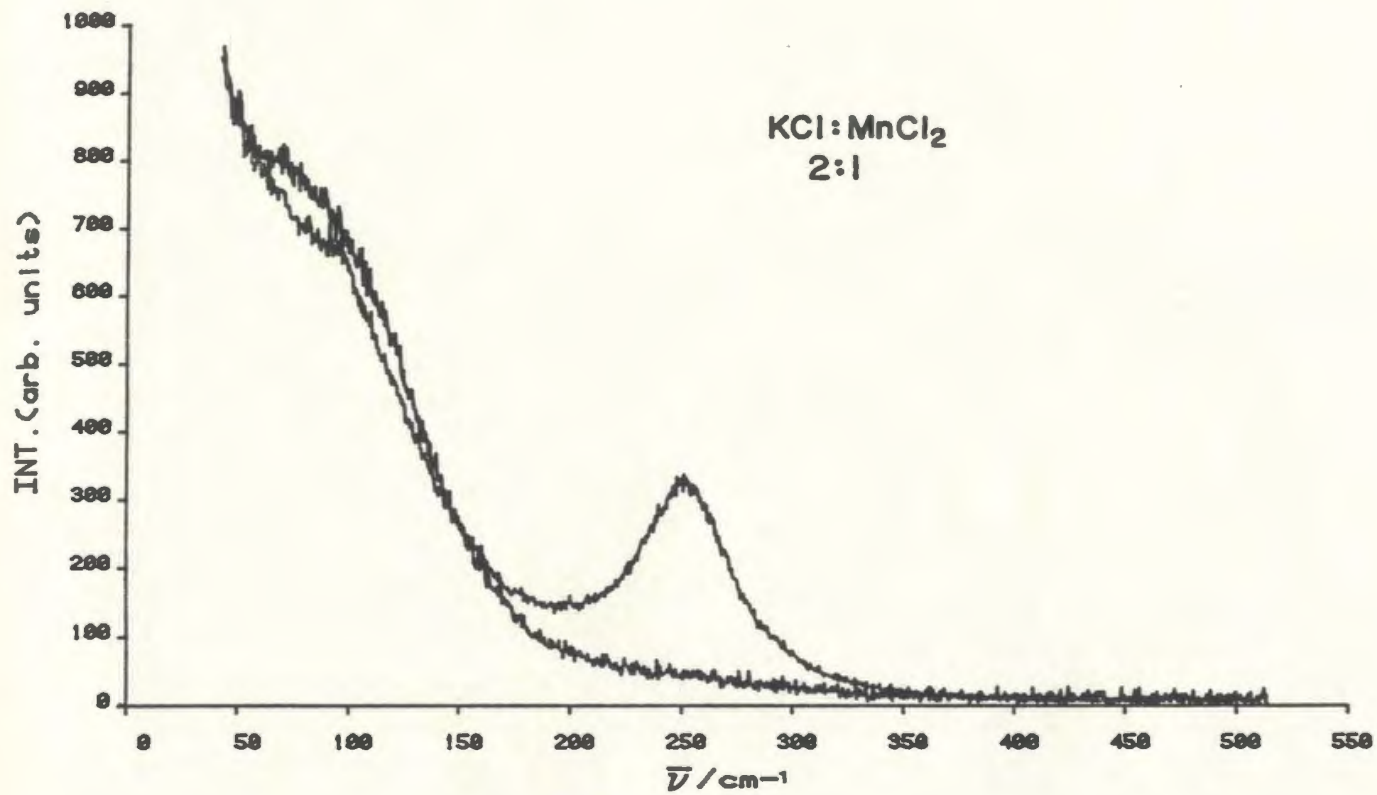


Figure 34. Raman spectra of molten $\text{KCl}:\text{MnCl}_2$ (3:1) at 882 K, $I_{||}$ and I_{\perp} .

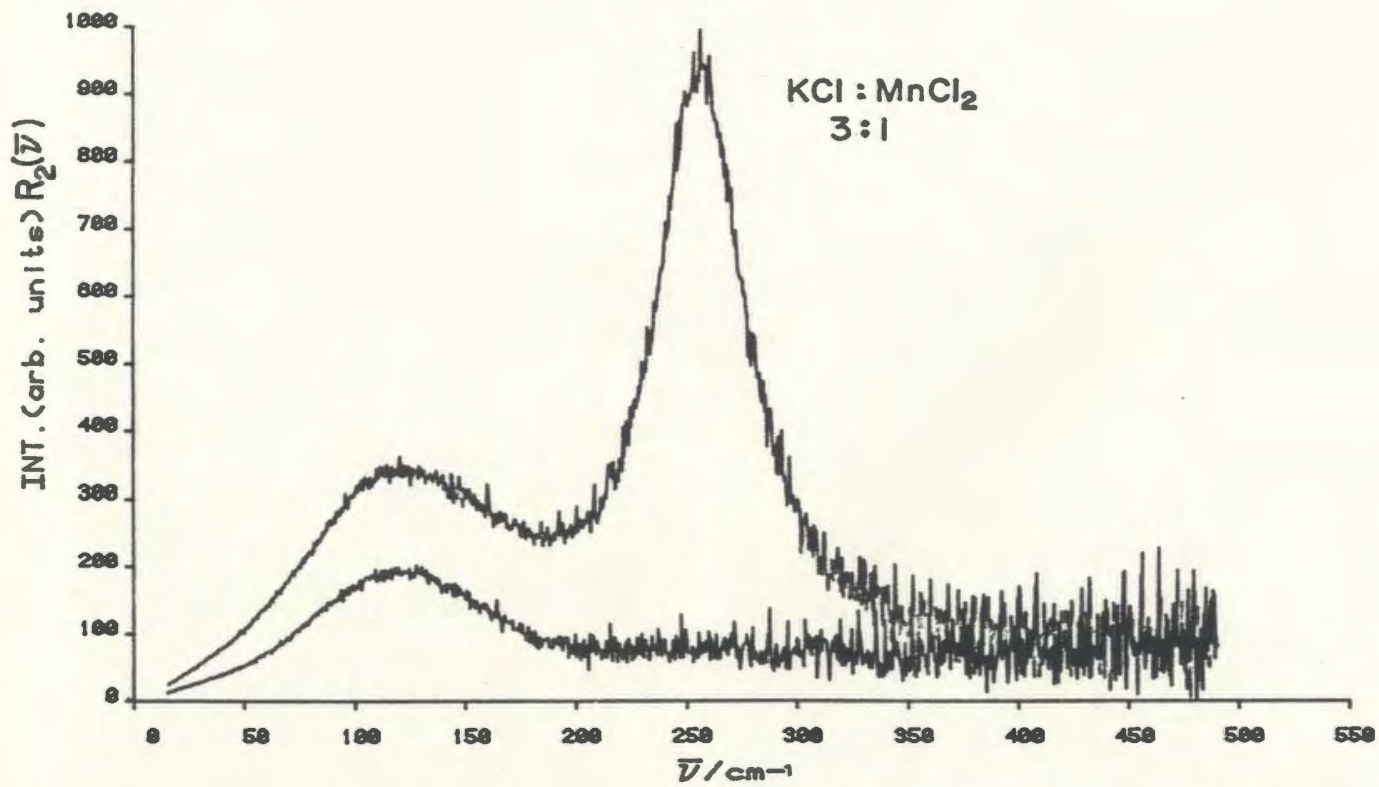
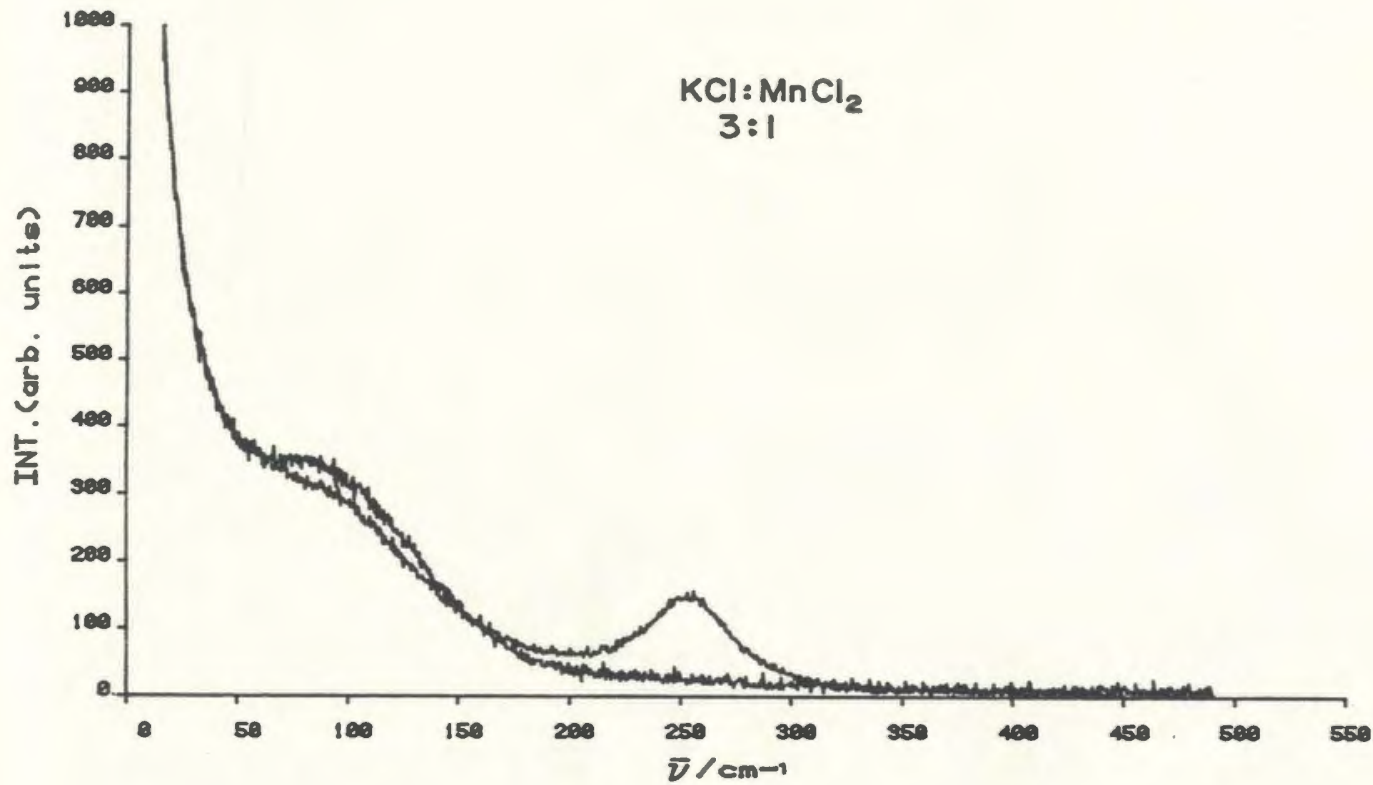


Figure 35. Raman spectra of molten $K_3Mn_2Cl_7$ at 794 K, $I_{||}$
and I_{\perp} .

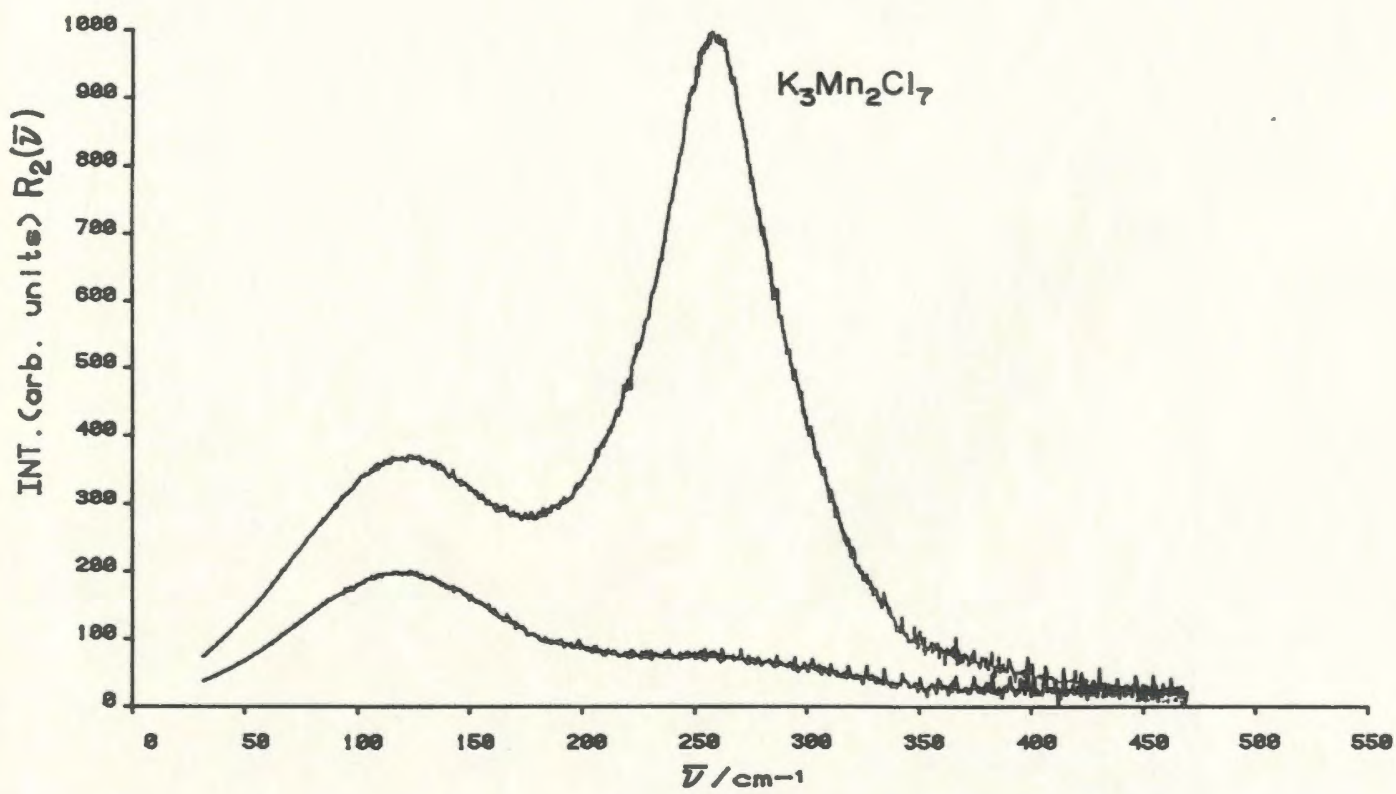
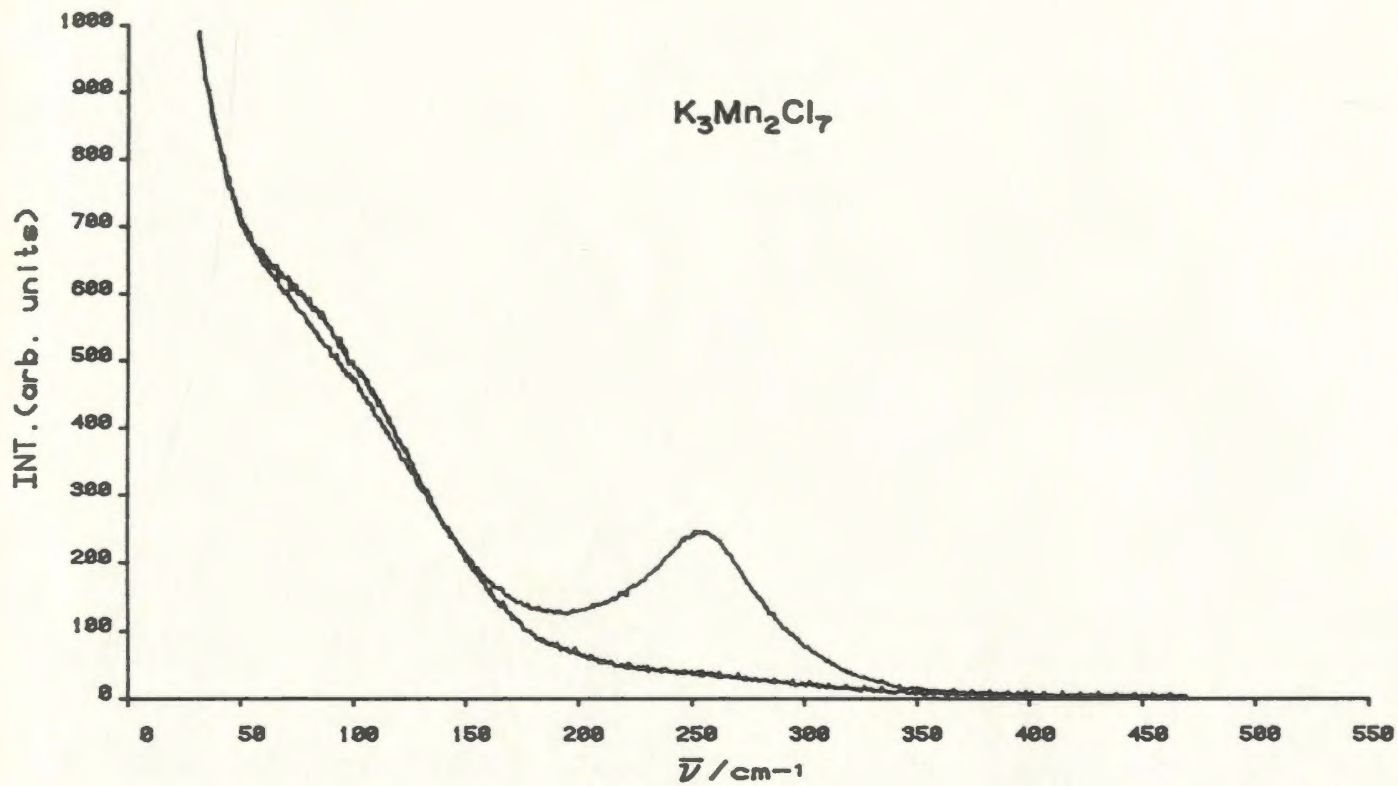


Figure 36. Raman spectra of molten K_4MnCl_6 at 816 K, $I_{||}$
and I_{\perp} .

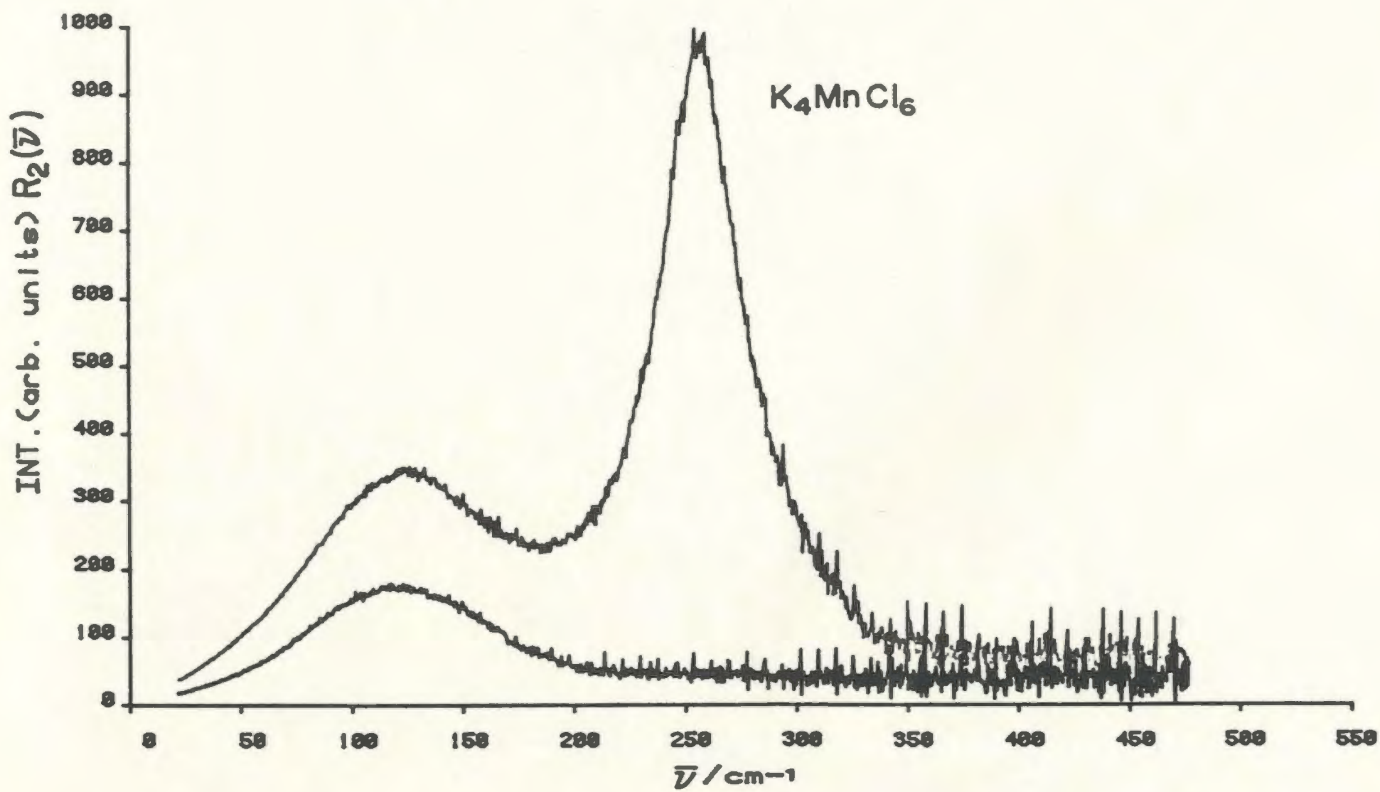
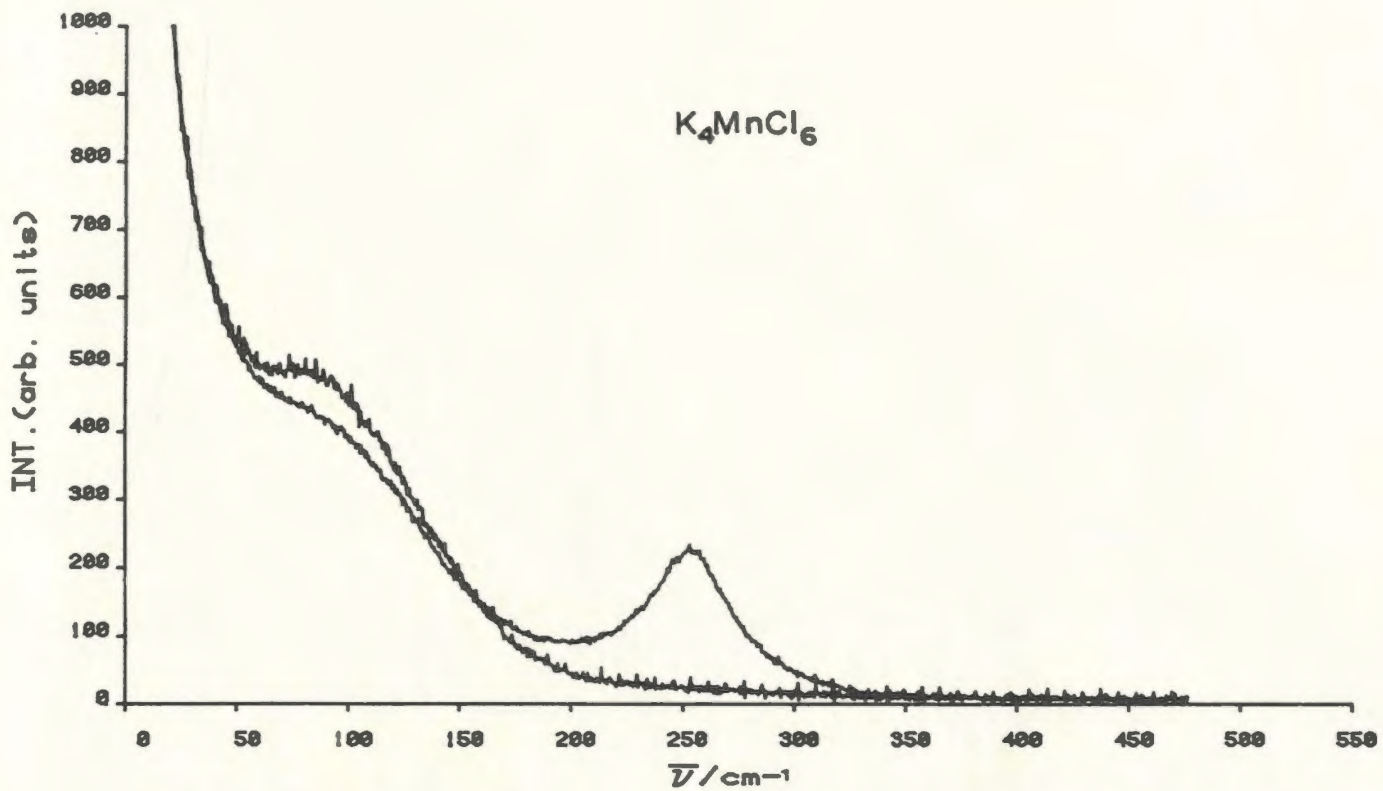




Figure 37. Isotropic Raman spectra of molten KMnCl_3 . The smooth line is the best-fit curve calculated with a single Gaussian*Lorentzian function.

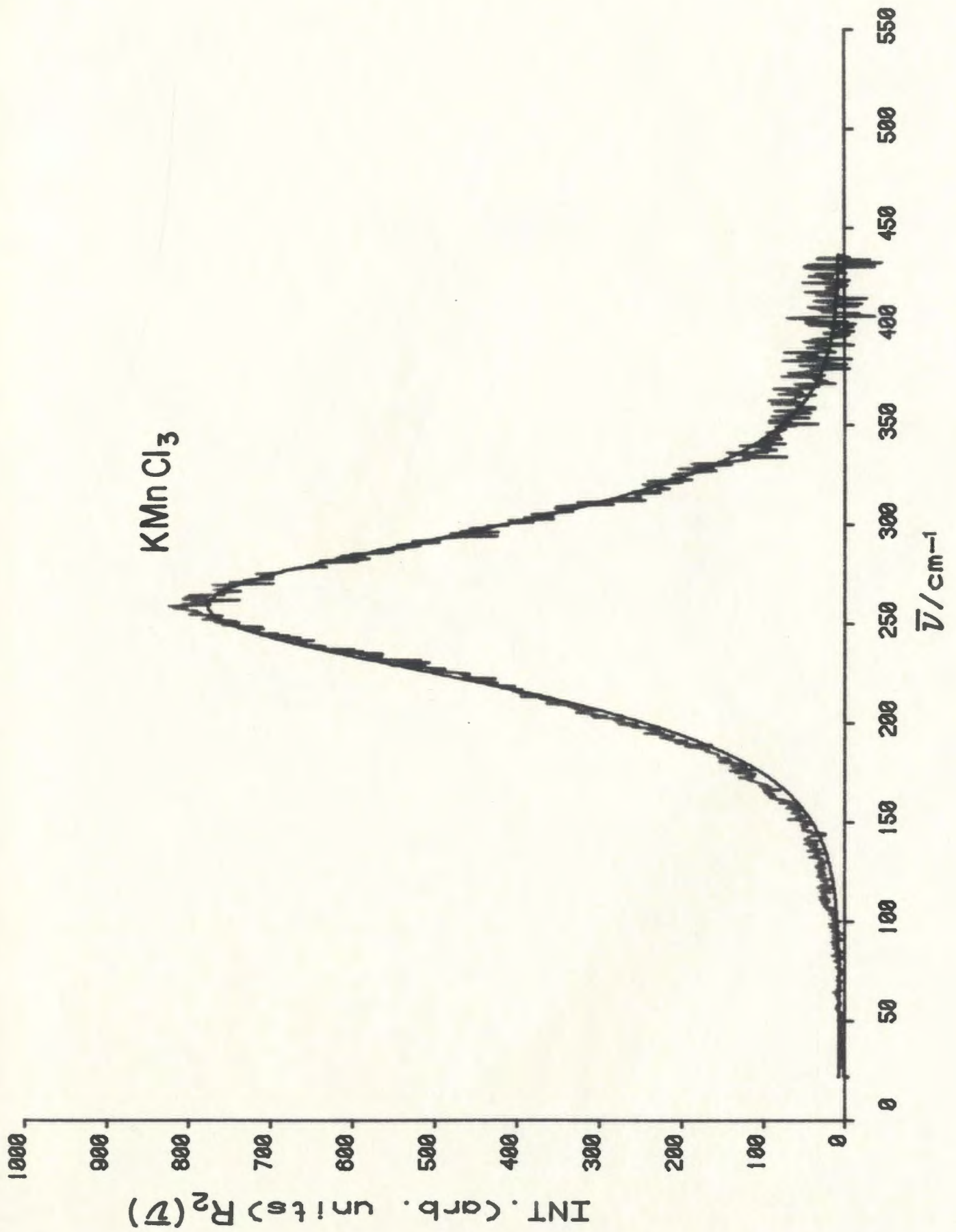


Figure 38. Isotropic Raman spectra of molten $\text{KCl}:\text{MnCl}_2$ (2:1).
The smooth line is the best-fit curve calculated with
a single Lorentzian function.

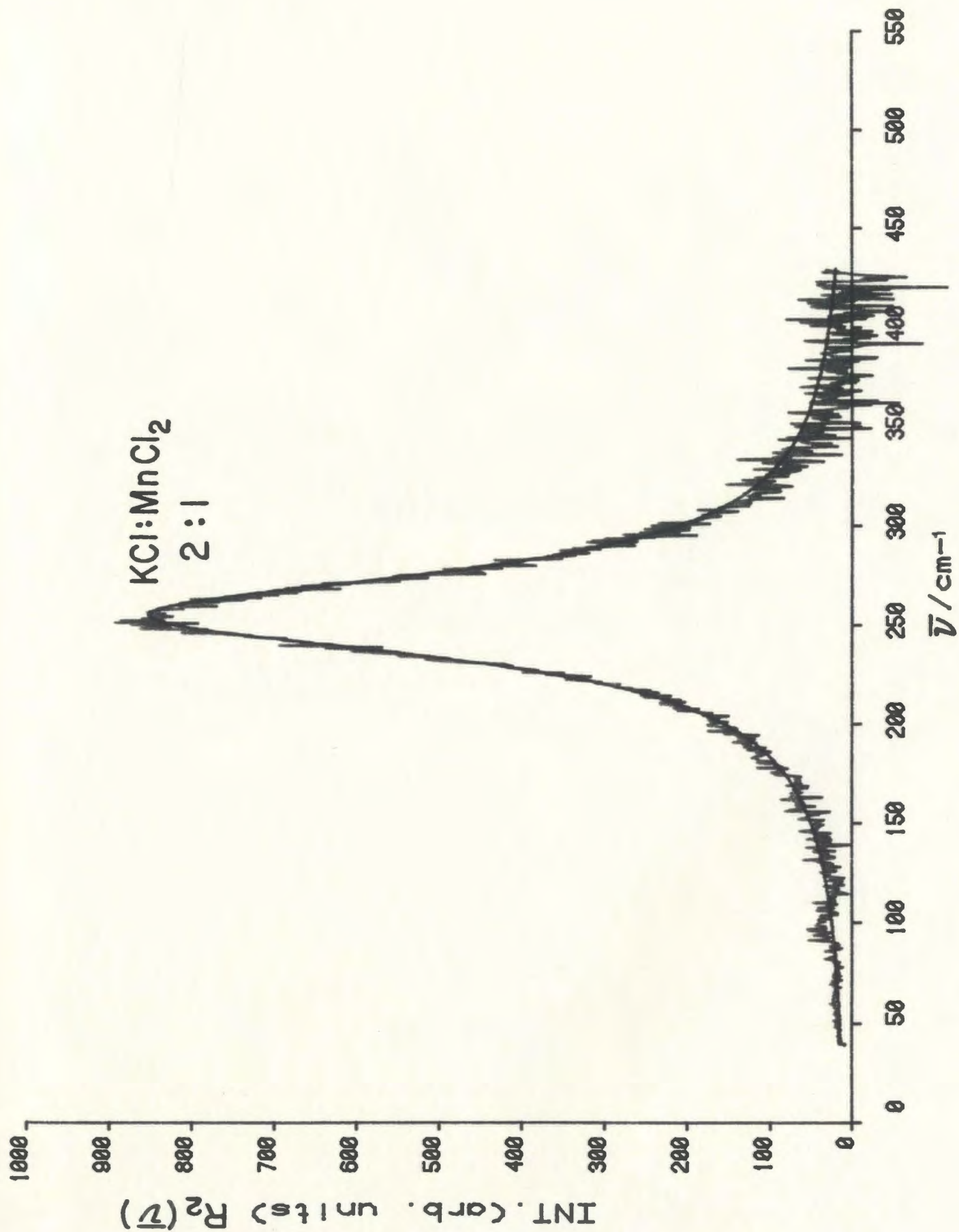


Figure 39. Isotropic Raman spectra of molten $\text{KCl}:\text{MnCl}_2$ (3:1).
The smooth line is the best-fit curve calculated with
a single Lorentzian function.

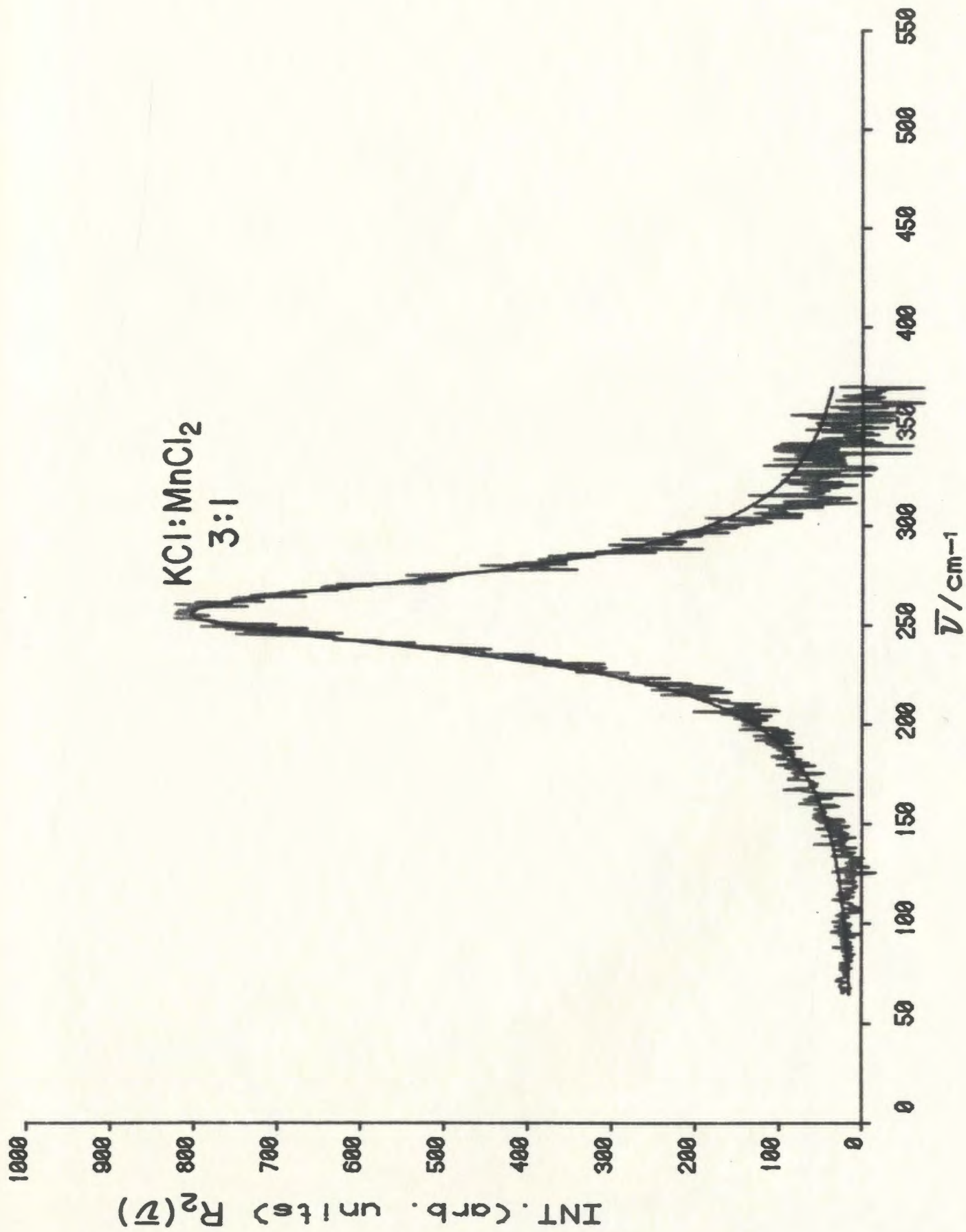


Figure 40. Isotropic Raman spectra of molten $K_3Mn_2Cl_7$. The smooth line is the best-fit curve calculated with a single Lorentzian function.

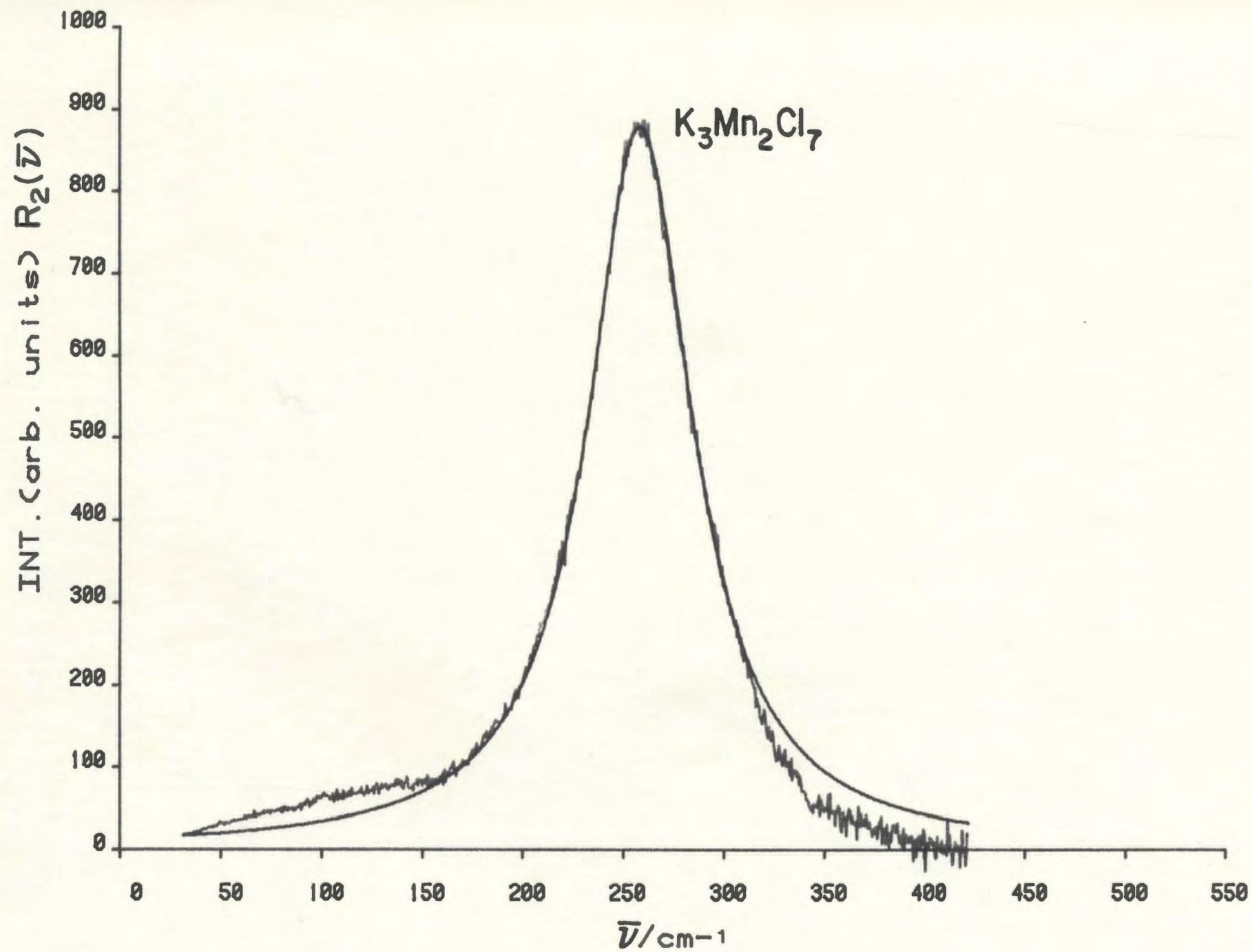


Figure 41. Isotropic Raman spectra of molten K_4MnCl_6 . The smooth line is the best-fit curve calculated with a single Lorentzian function.

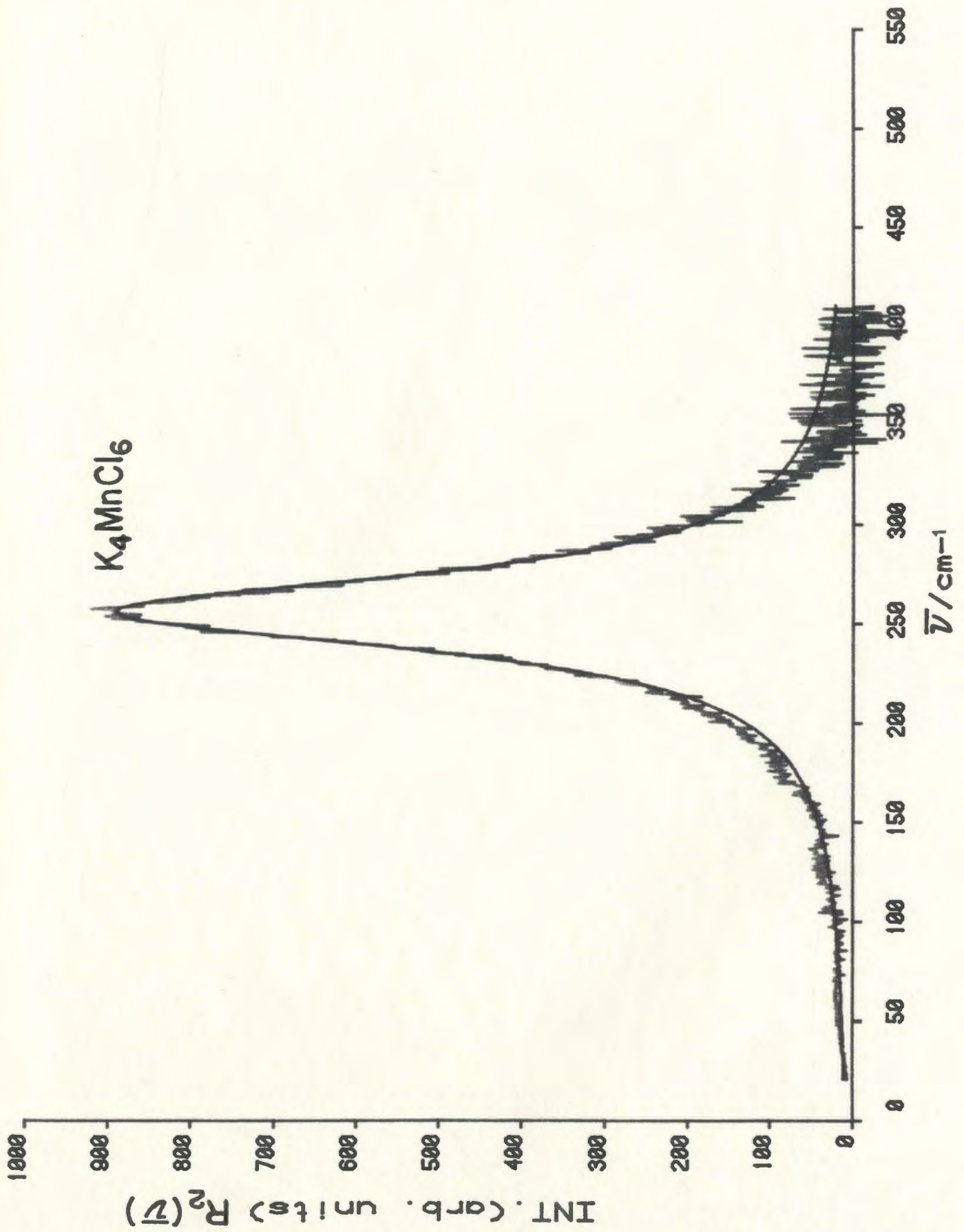


Table 23. Summary of results of curve resolution analysis for MnCl_2 -NaCl Melts.

Compound	Frequency (cm^{-1})	Intensity	Half band width (cm^{-1})	Function
Na_6MnCl_8	255.6	832	77.6	G * L
$\text{NaCl}:\text{MnCl}_2$ (3:1)	254.4	819	79.4	G * L
Na_2MnCl_4	257.9	762	82.0	G * L
NaMnCl_3	253.3	699	92.3	G * L
$\text{Na}_2\text{Mn}_3\text{Cl}_8$	249.3	665	111.2	G * L
NaMn_4Cl_9	244.1	757	129.5	G * L

G: Gaussian, L: Lorentzian

Figure 42. Raman spectra of molten NaMnCl_3 at 773 K, $I_{||}$
and I_{\perp} .

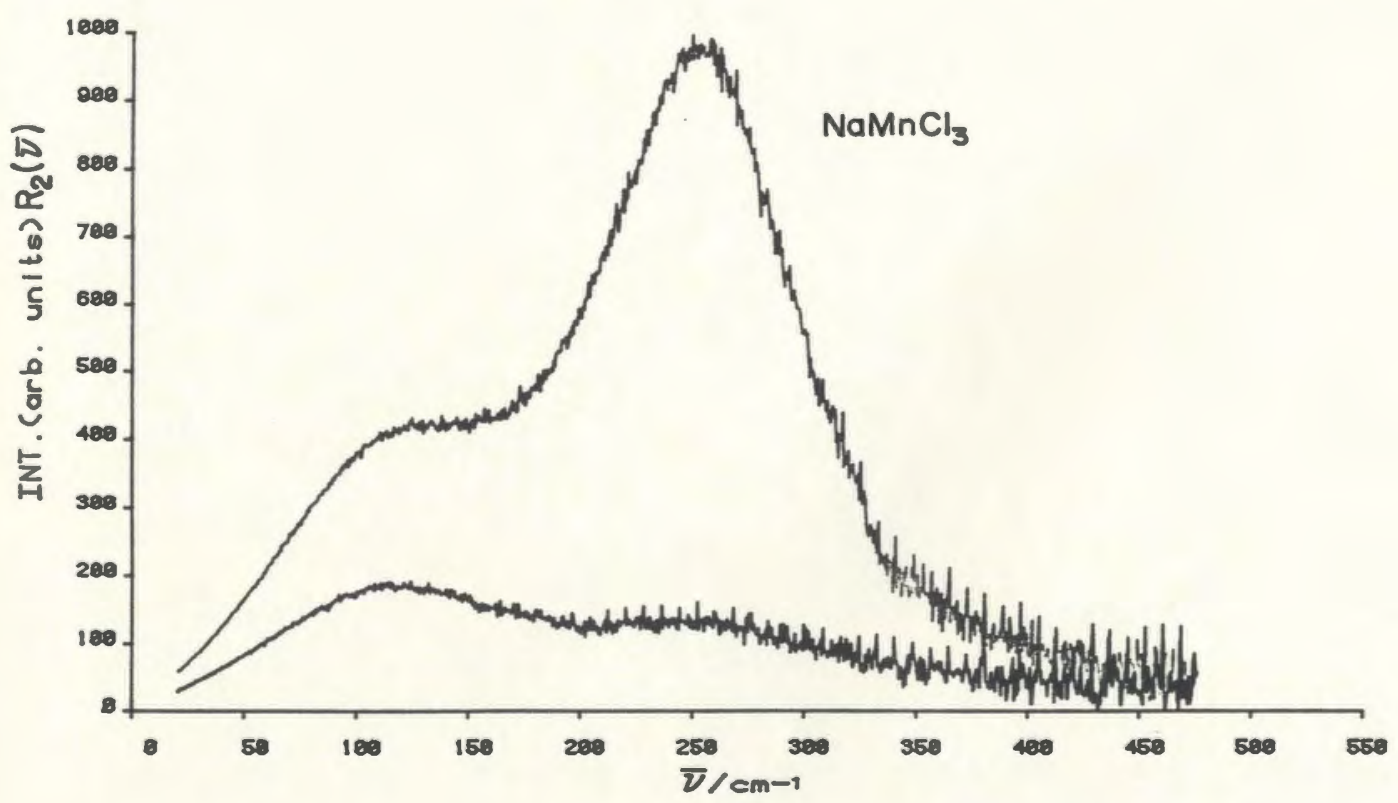
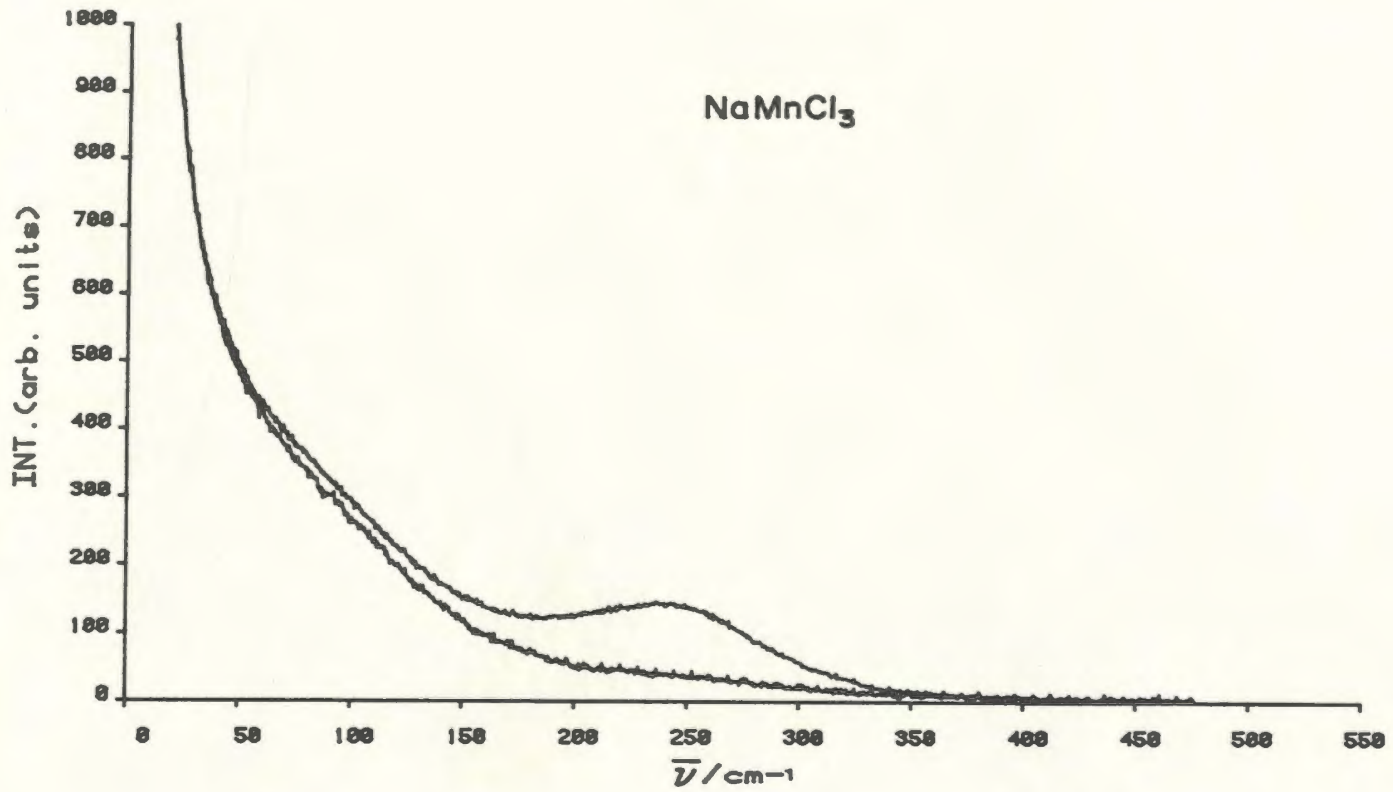


Figure 43. Raman spectra of molten Na_2MnCl_4 at 794 K, $I_{||}$
and I_{\perp} .

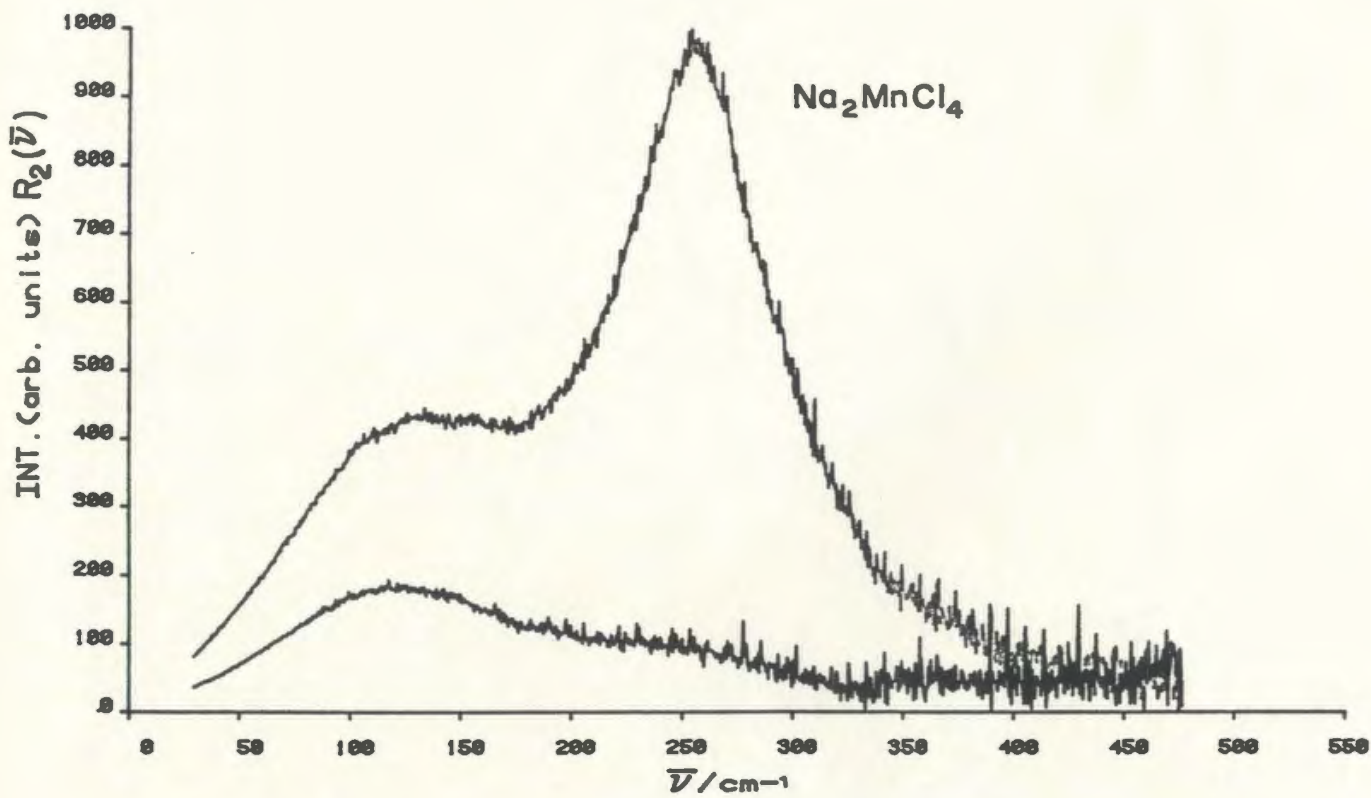
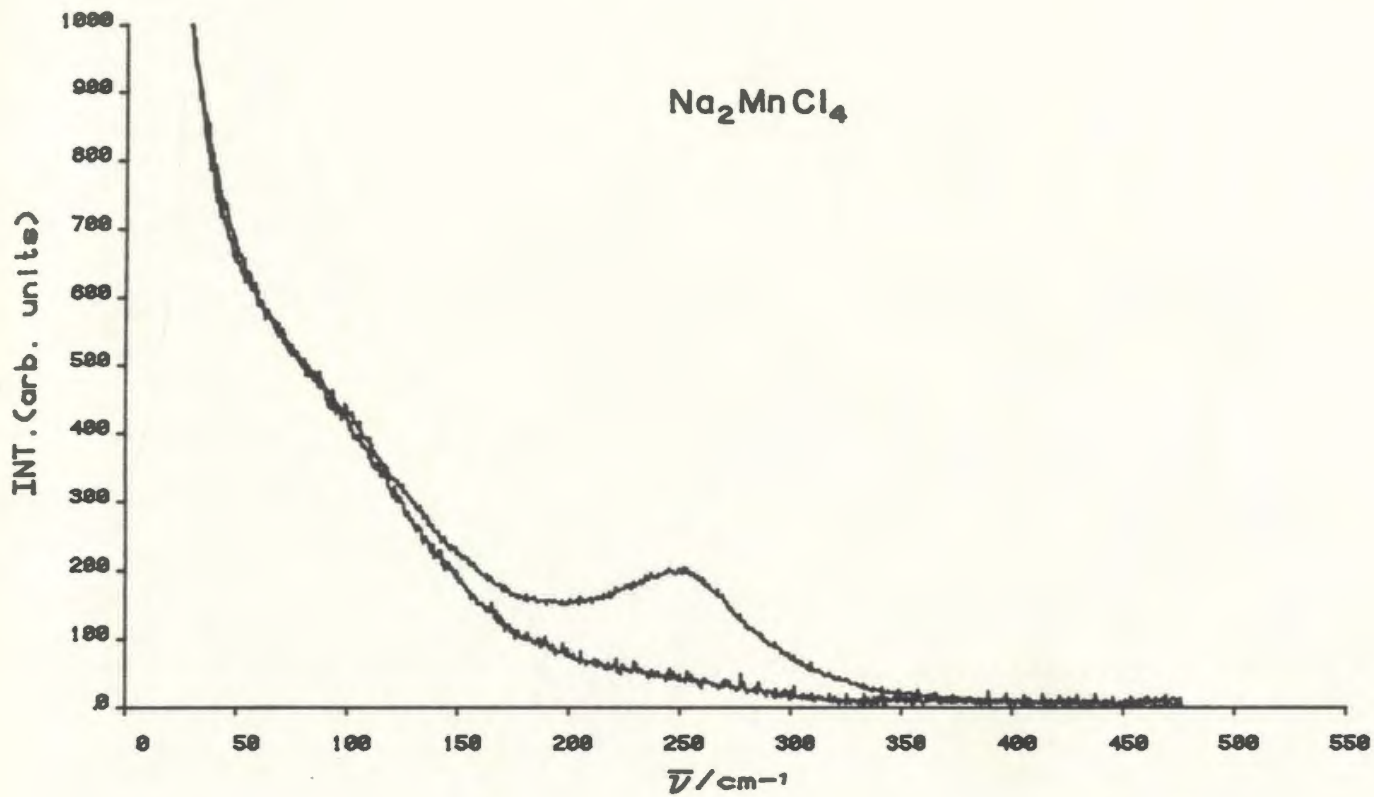


Figure 44. Raman spectra of molten $\text{NaCl}:\text{MnCl}_2$ (3:1) at 973 K, $I_{||}$ and I_{\perp} .

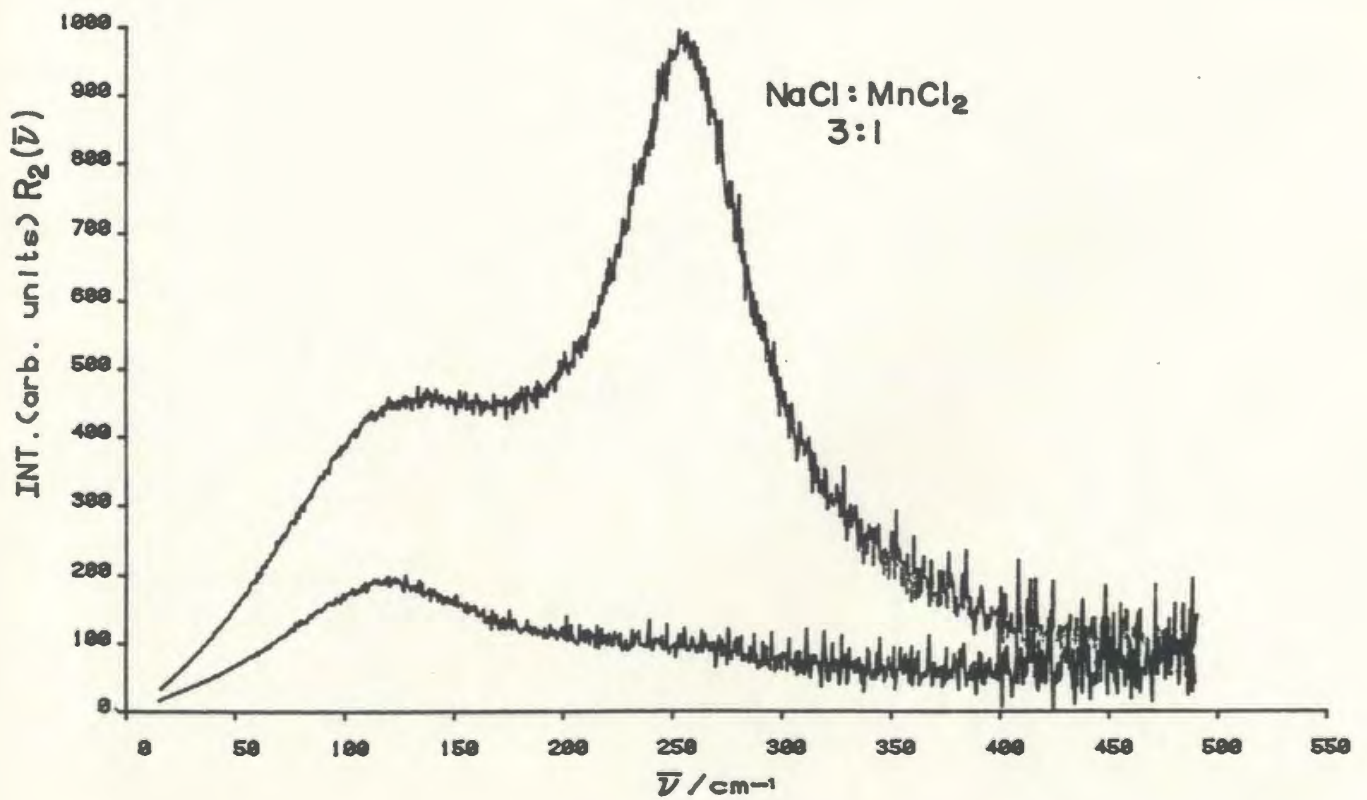
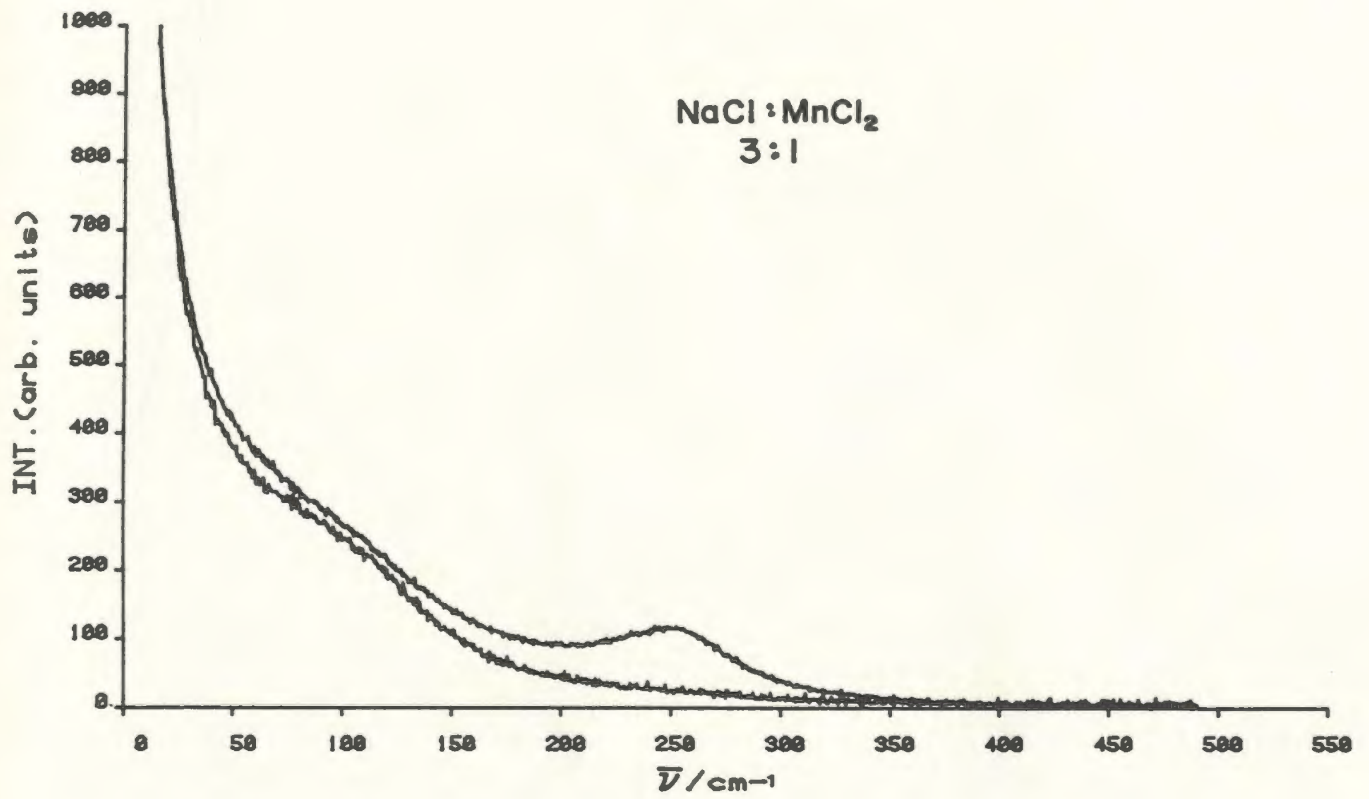


Figure 45. Raman spectra of molten $\text{Na}_2\text{Mn}_3\text{Cl}_8$ at 816 K,

$I_{||}$ and I_{\perp} .

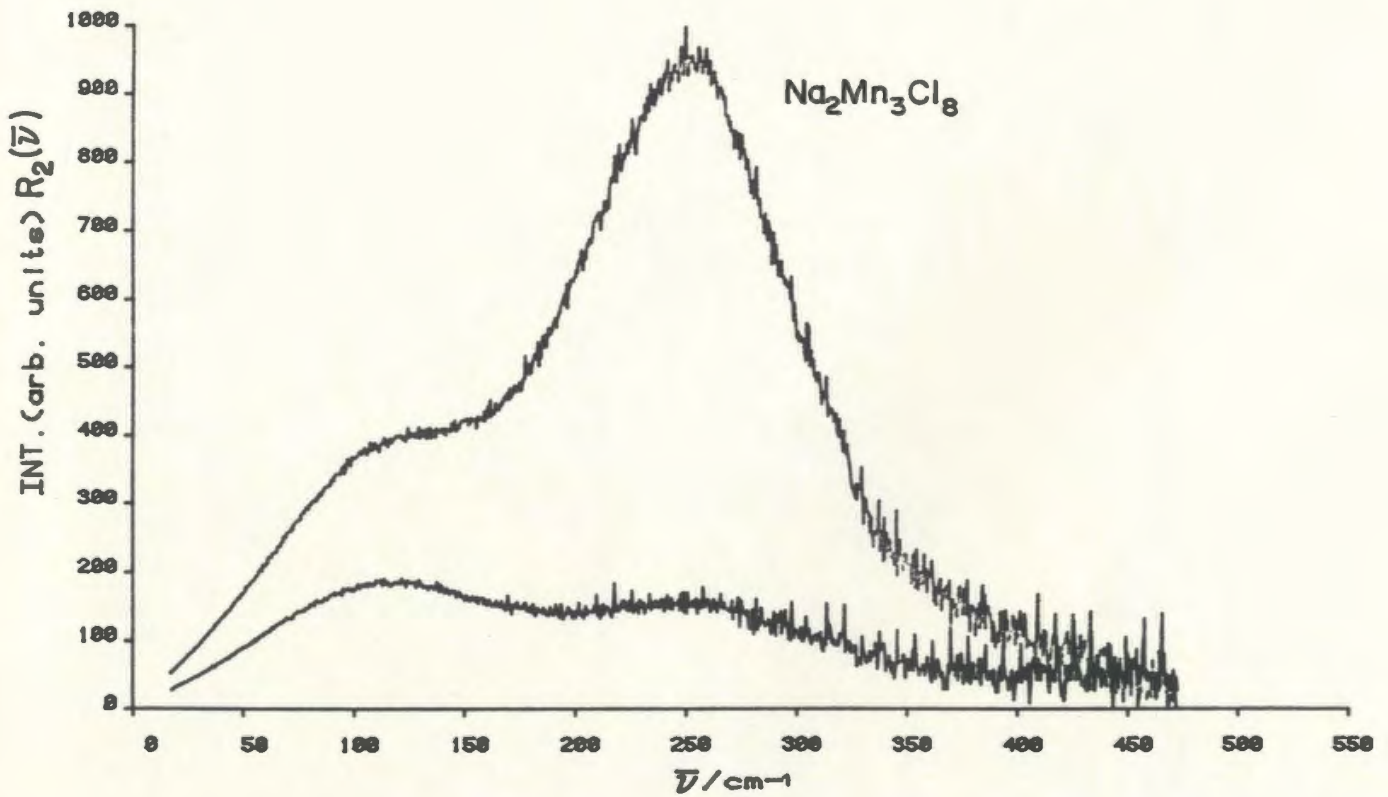
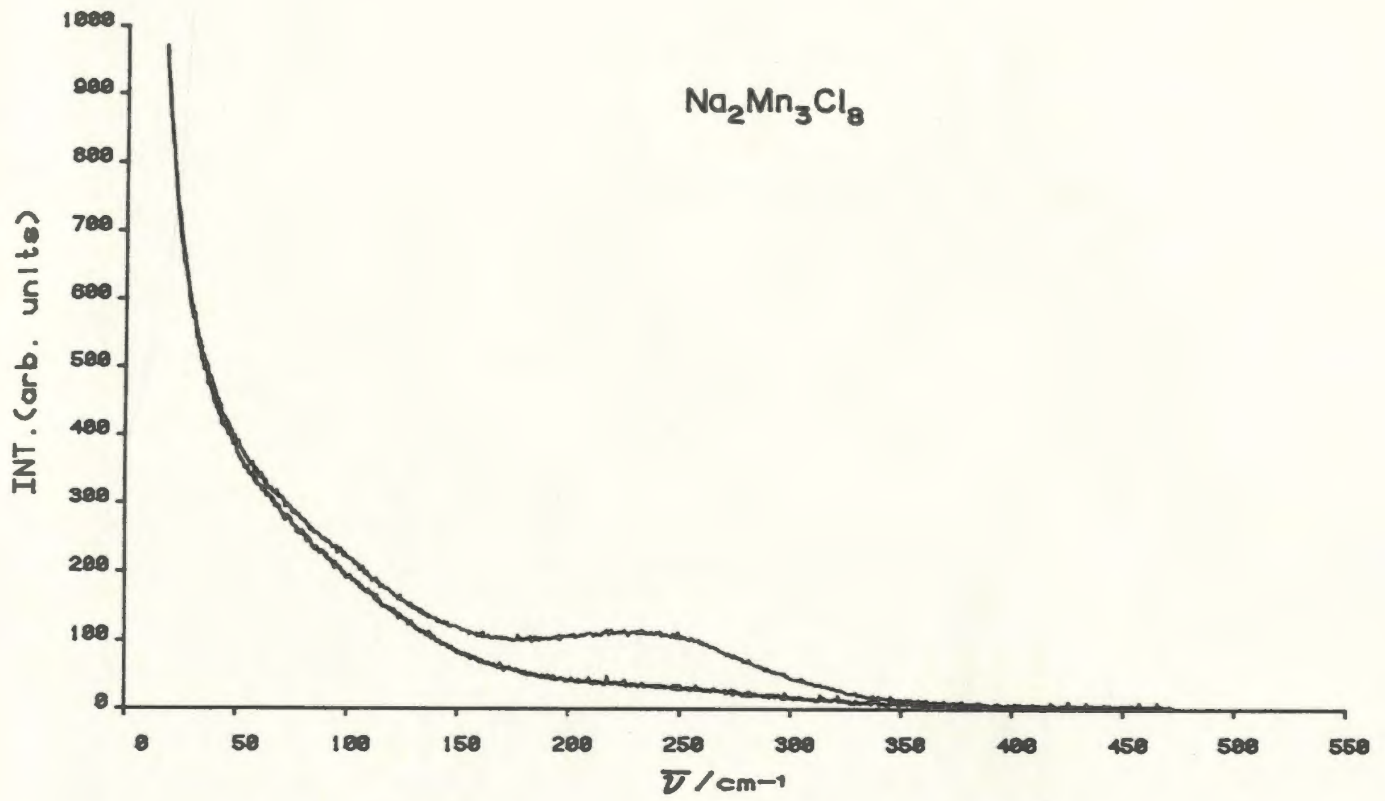


Figure 46. Raman spectra of molten NaMn_4Cl_9 at 937 K, $I_{||}$
and I_{\perp} .

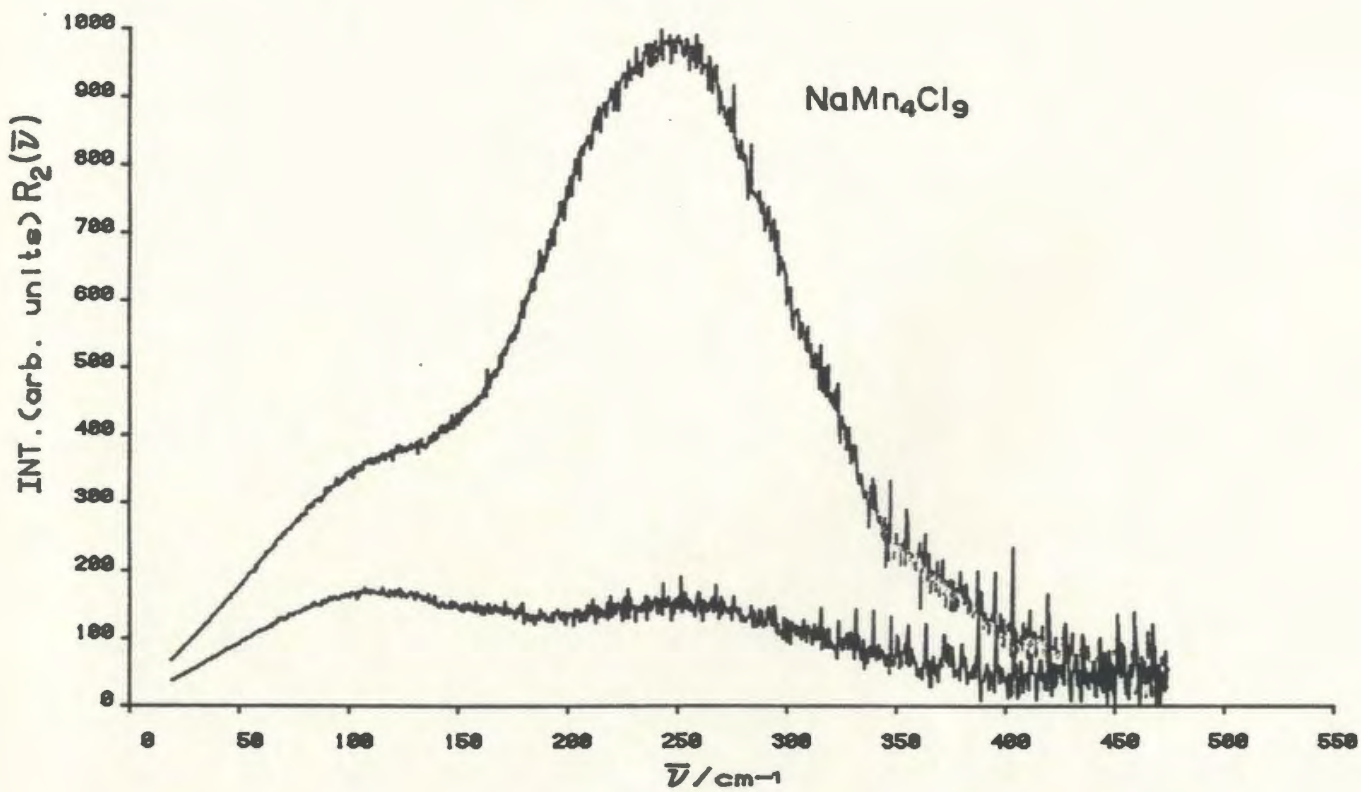
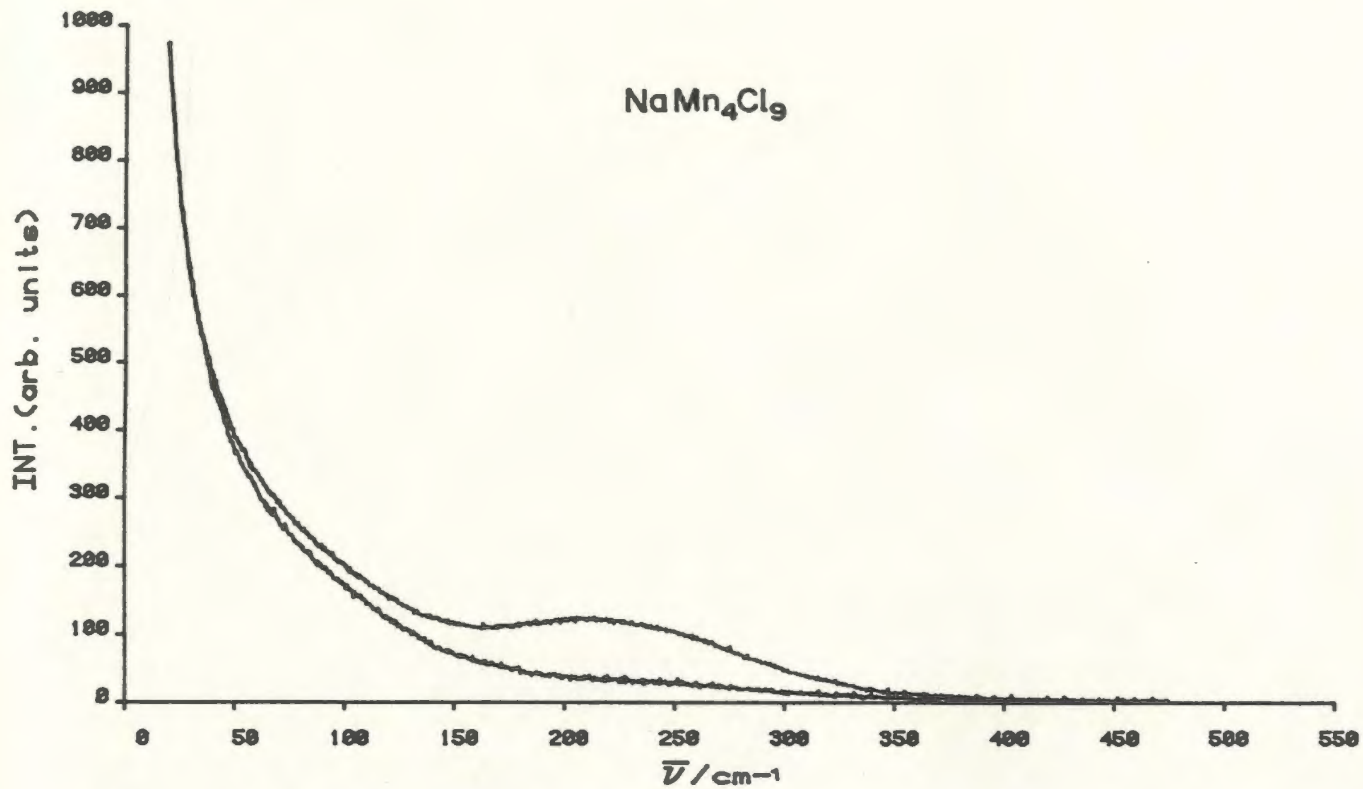


Figure 47. Raman spectra of molten Na_6MnCl_8 at 988 K, $I_{||}$
and I_{\perp} .

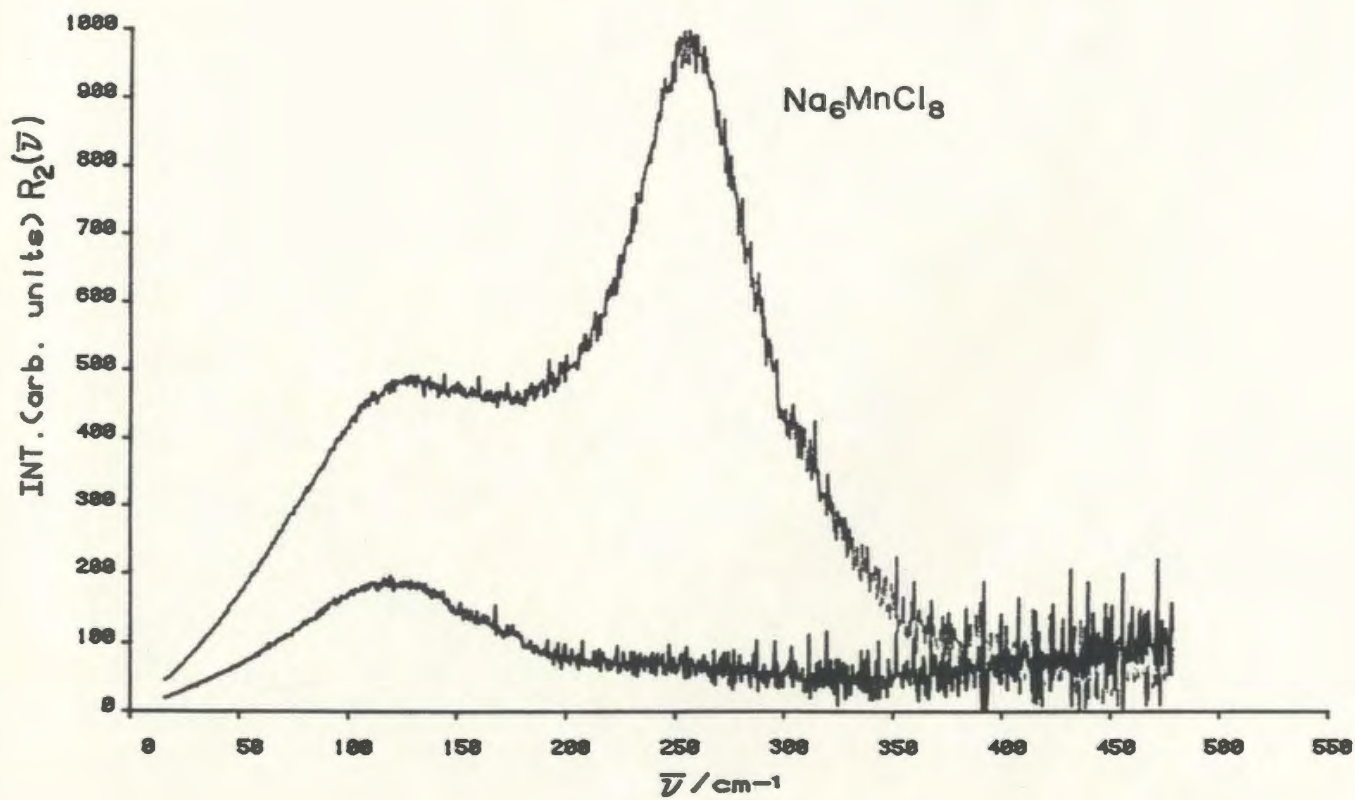
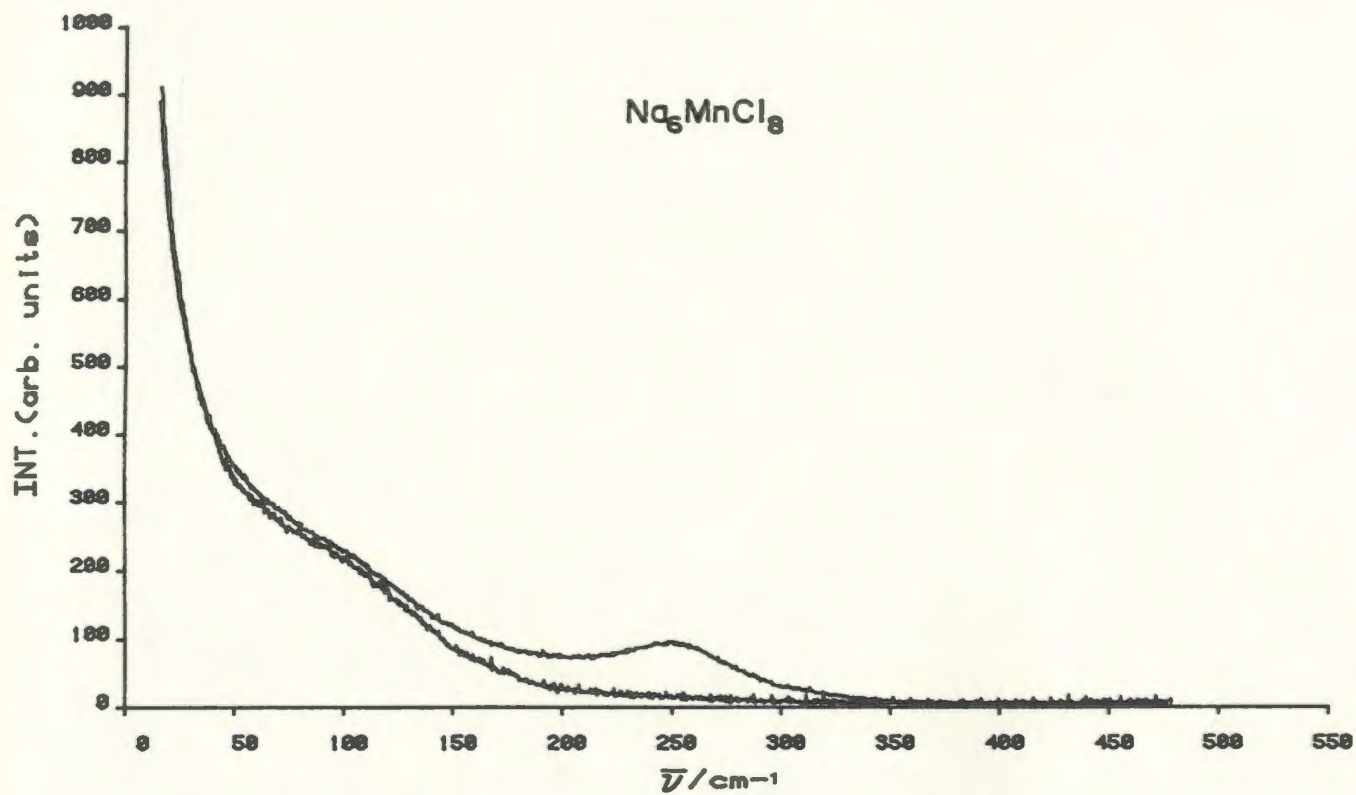


Figure 48. Isotropic Raman spectra of molten NaMnCl_3 . The smooth line is the best-fit curve calculated as a sum of two Gaussian*Lorentzian functions. The second low frequency peak has only been added to improve the base line.

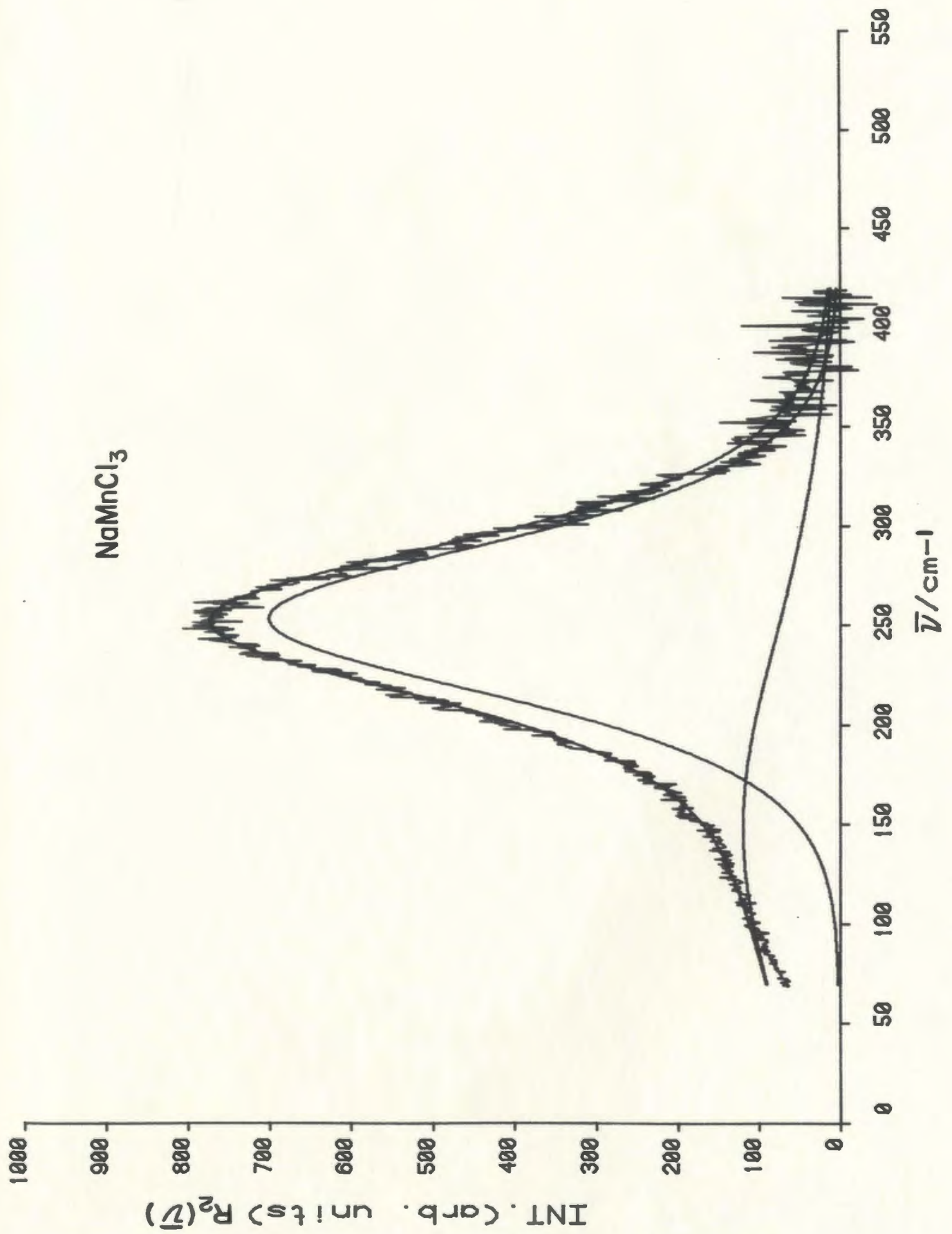


Figure 49. Isotropic Raman spectra of molten Na_2MnCl_4 . The smooth line is the best-fit curve calculated as a sum of two Gaussian*Lorentzian functions. The second low frequency peak has only been added to improve the base line.

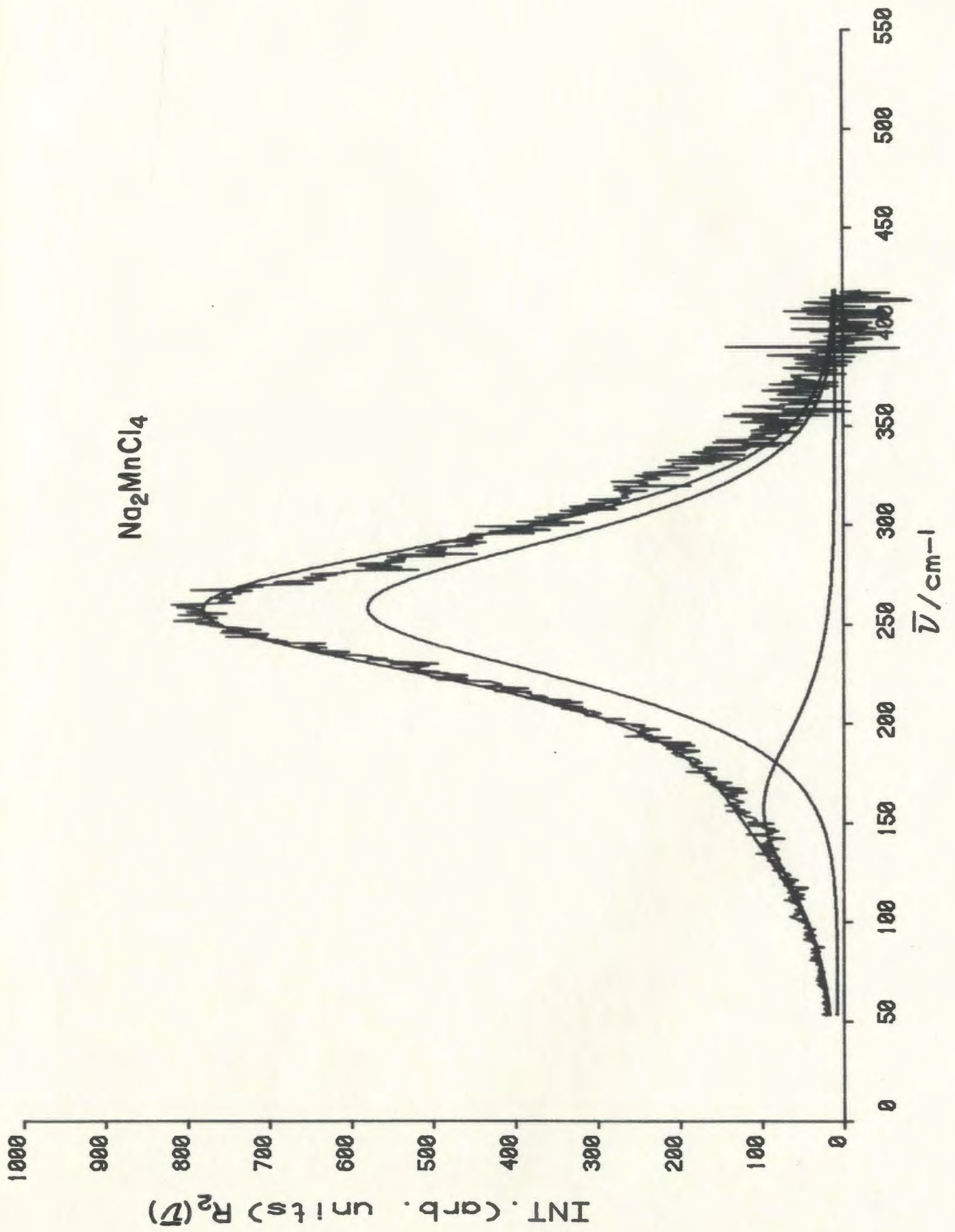


Figure 50. Isotropic Raman spectra of molten $\text{NaCl}:\text{MnCl}_2$ (3:1).
The smooth line is the best-fit curve calculated as a sum of two Gaussian*Lorentzian functions. The second low frequency peak has only been added to improve the base line.

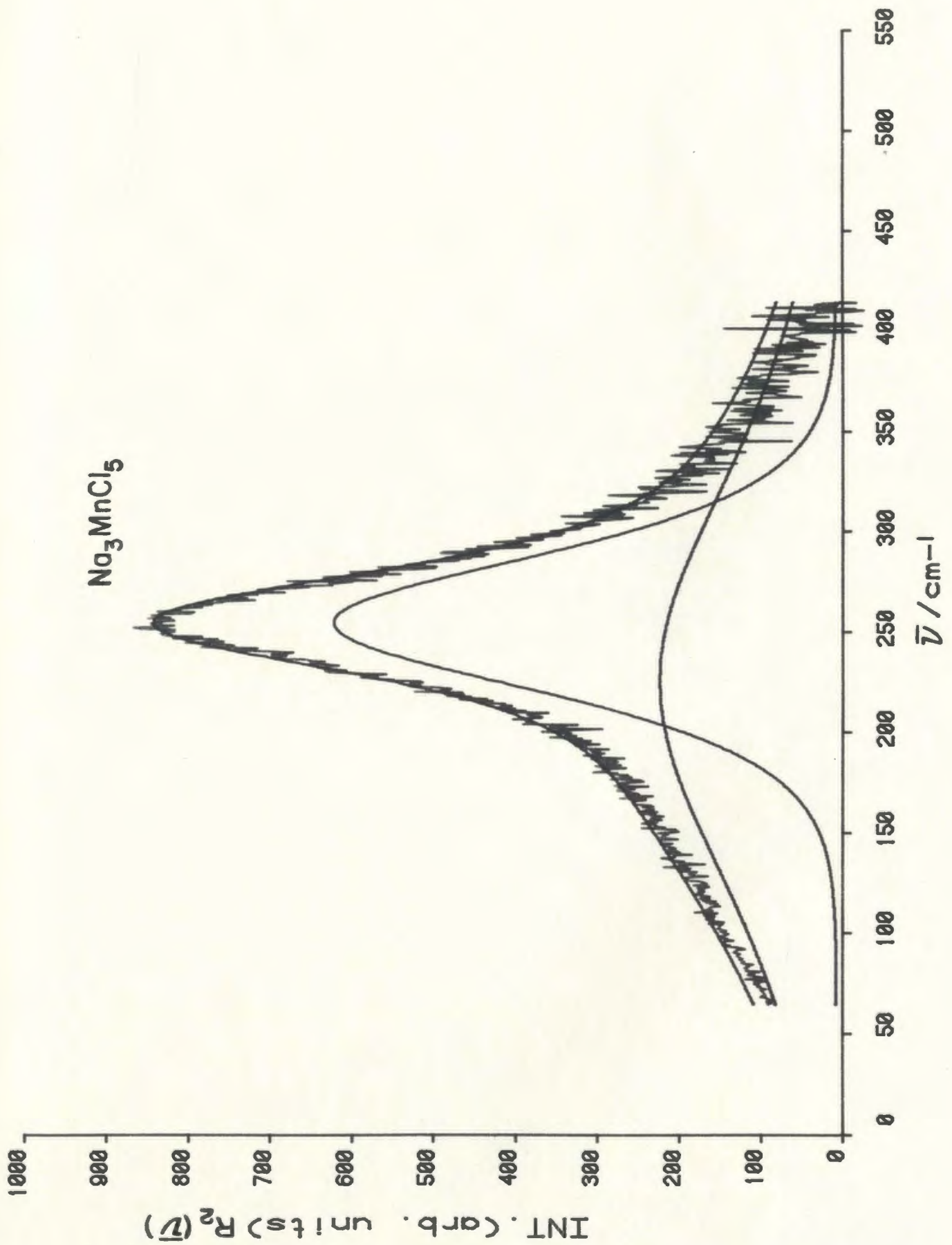


Figure 51. Isotropic Raman spectra of molten $\text{Na}_2\text{Mn}_3\text{Cl}_8$. The smooth line is the best-fit curve calculated with a single Gaussian*Lorentzian function.

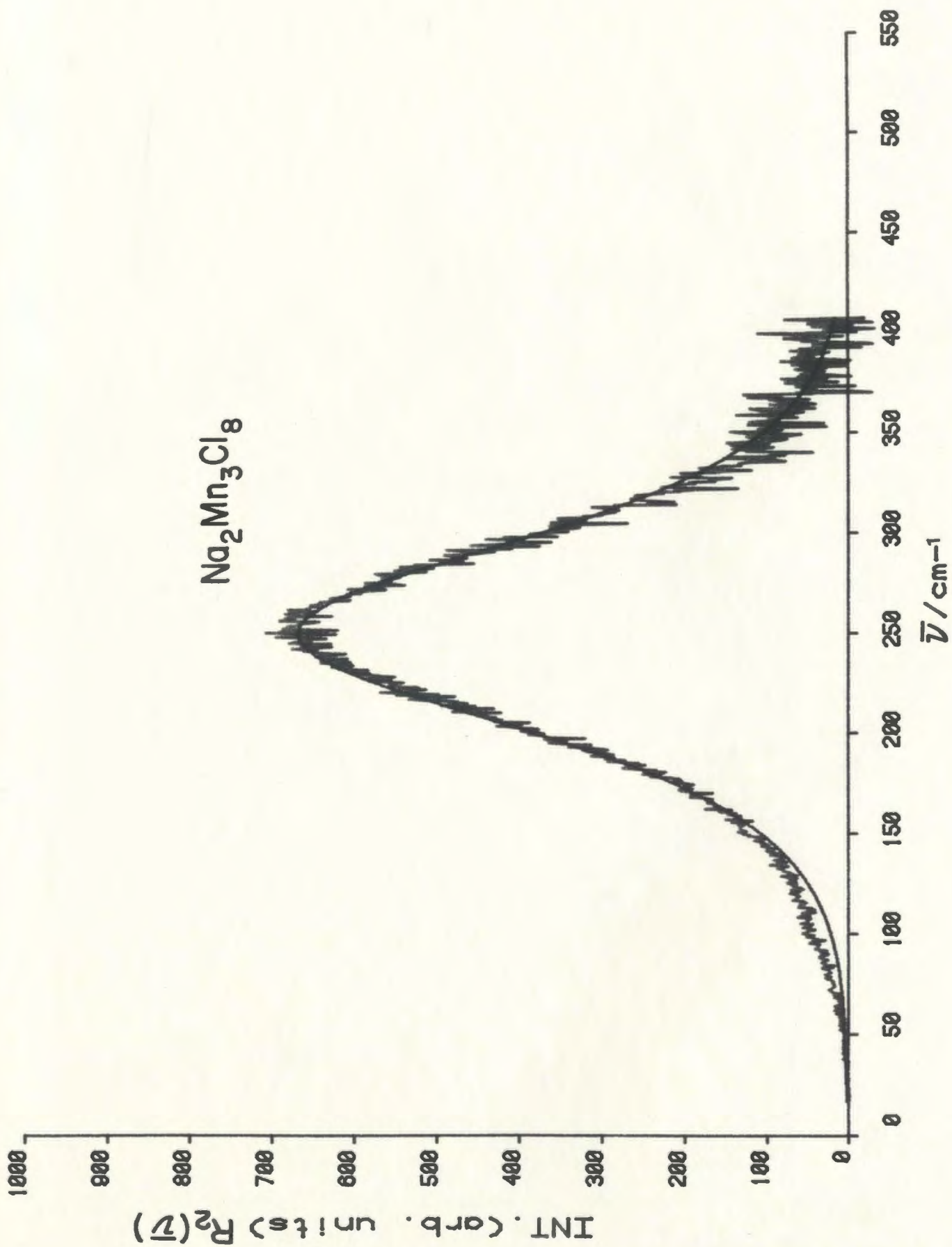


Figure 52. Isotropic Raman spectra of molten NaMn_4Cl_9 . The smooth line is the best-fit curve calculated with a single Gaussian*Lorentzian function.

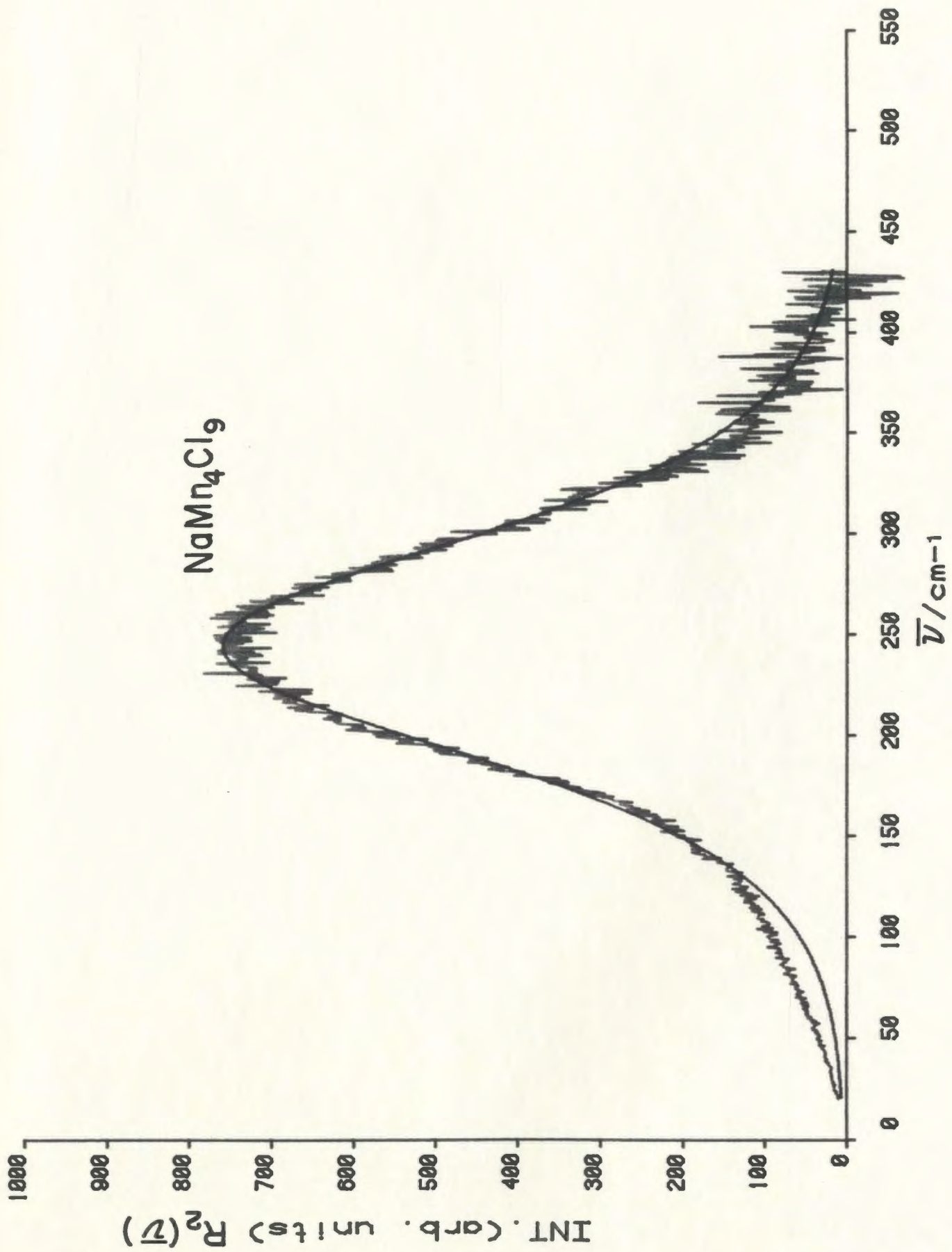
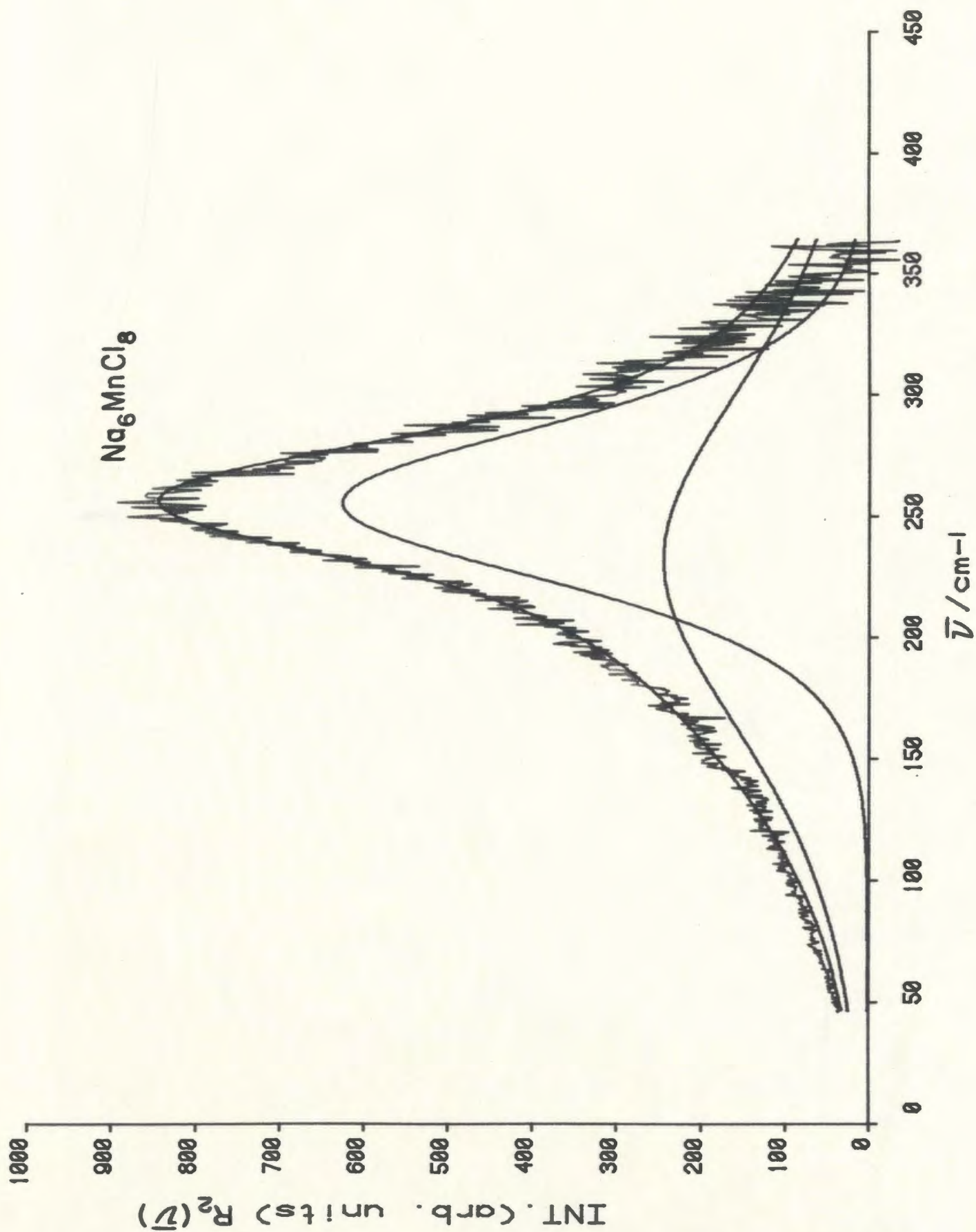


Figure 53. Isotropic Raman spectra of molten Na_6MnCl_8 . The smooth line is the best-fit curve calculated as a sum of two Gaussian*Lorentzian functions. The second low frequency peak has only been added to improve the base line.



The polarized peak from the $R_2(\bar{\nu})$ spectrum was fitted to Gaussian*Lorentzian function. The results are shown in figures 48, 49, 50, 51, 52 and 53. The half band width in cm^{-1} , the intensity, and the frequency in cm^{-1} for the symmetric mode ν_1 are shown in Table 23. For the NaCl-MnCl₂ mixtures only it was necessary to add a second component to account for excess scattering in the $R_{2\alpha}(\bar{\nu})$ spectrum at low $\bar{\nu}$. The excess scattering could be due to the Na⁺Cl⁻ pair which may contribute in this region²² or it could be just poor baseline subtraction.

4.2.5 MnCl₂-LiCl Melts

The Raman spectra of MnCl₂:LiCl (1:1), MnCl₂:LiCl (1:2), MnCl₂:LiCl (1:3) melts are shown in figures 54, 55 and 56. The results indicate the presence of tetrahedral MnCl₄²⁻ species in the melt. The curve resolution results are shown in figures 57, 58 and 59, and tabulated in Table 24.

4.2.6 Half band width of ν_1 mode for ACl.MnCl₂ melts

The half band width of the symmetric mode (ν_1) increased over the cation series Cs⁺ to Li⁺. This increment of the half band width is expected because¹⁷ the symmetric stretching mode of the tetrahedral ion will occur in a greater range of environmental conditions in the neighborhood of the smaller and lighter Li⁺ and Na⁺ cations than for the larger Rb⁺ and Cs⁺ ions. A summary of the half band widths in cm^{-1} for (1:1), (2:1) and (3:1) ACl-MnCl₂ melts are collected in Table 25.

Table 24. Summary of results of curve resolution analysis for $\text{MnCl}_2\text{-LiCl}$ Melts.

Compound	Frequency (cm^{-1})	Intensity	Half band width (cm^{-1})	Function
LiCl:MnCl_2 (3:1)	246.5	675	109.7	G * L
LiCl:MnCl_2 (2:1)	252.5	684	117.4	G * L
LiCl:MnCl_2 (1:1)	249.2	644	123.9	G * L

G: Gaussian, L: Lorentzian

Figure 54. Raman spectra of molten $\text{LiCl}:\text{MnCl}_2$ (1:1) at 945 K, $I_{||}$ and I_{\perp} .

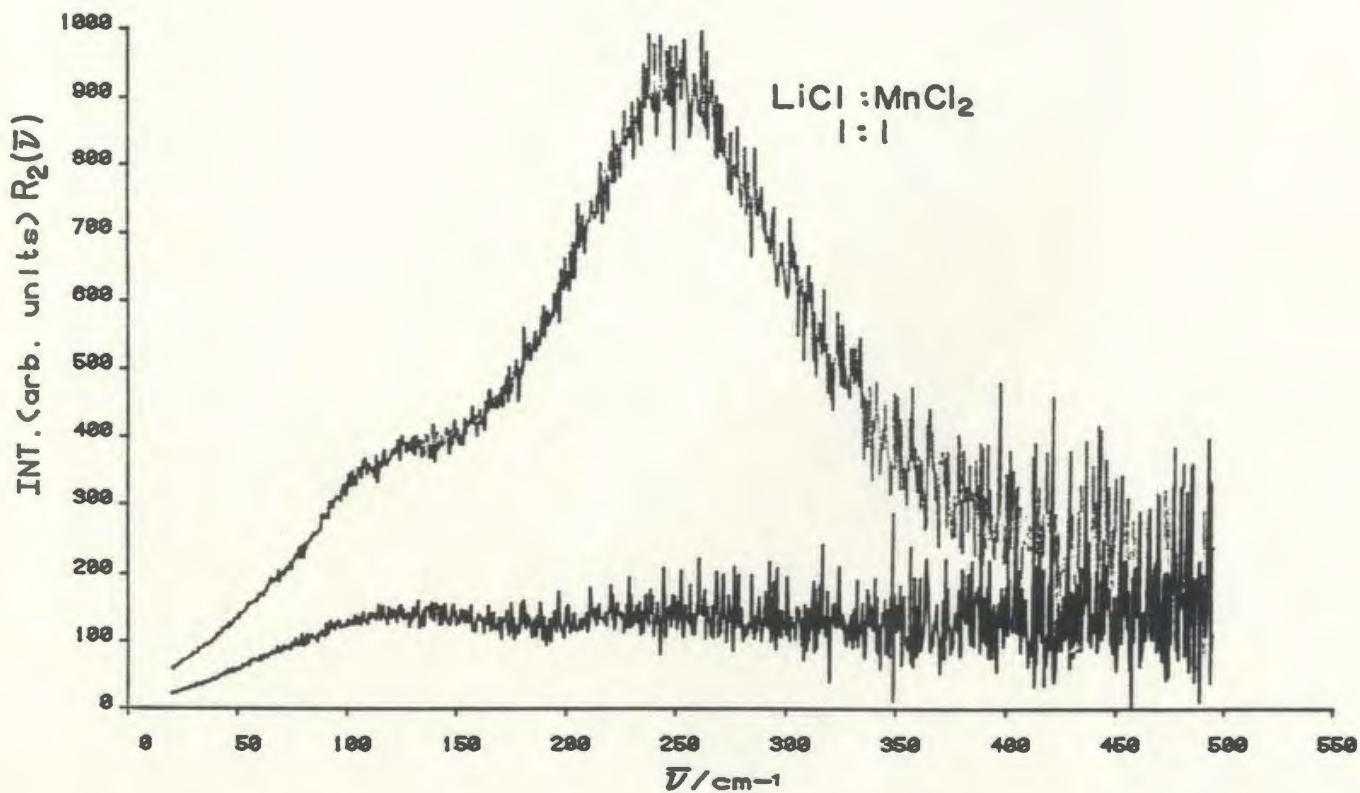
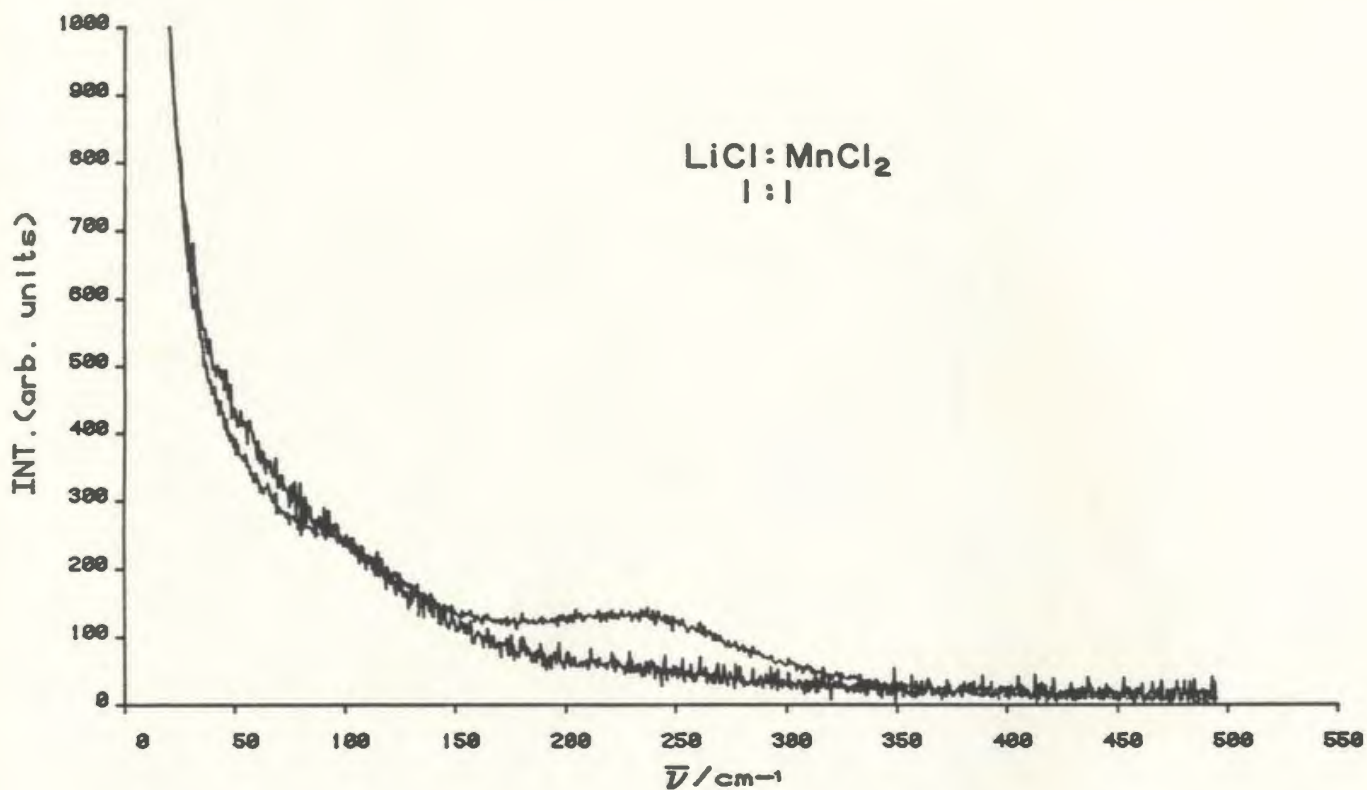


Figure 55. Raman spectra of molten $\text{LiCl}:\text{MnCl}_2$ (2:1) at 953 K, $I_{||}$ and I_{\perp} .

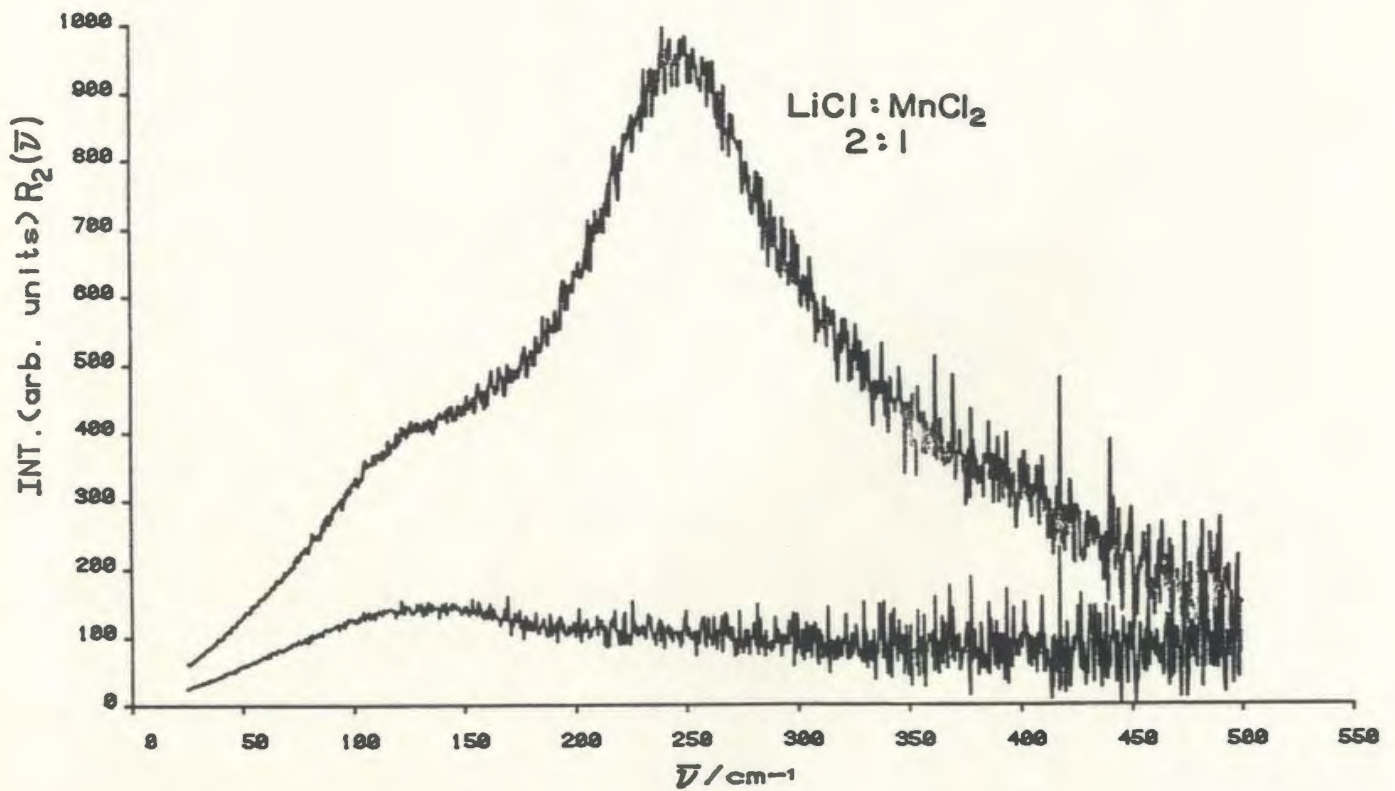
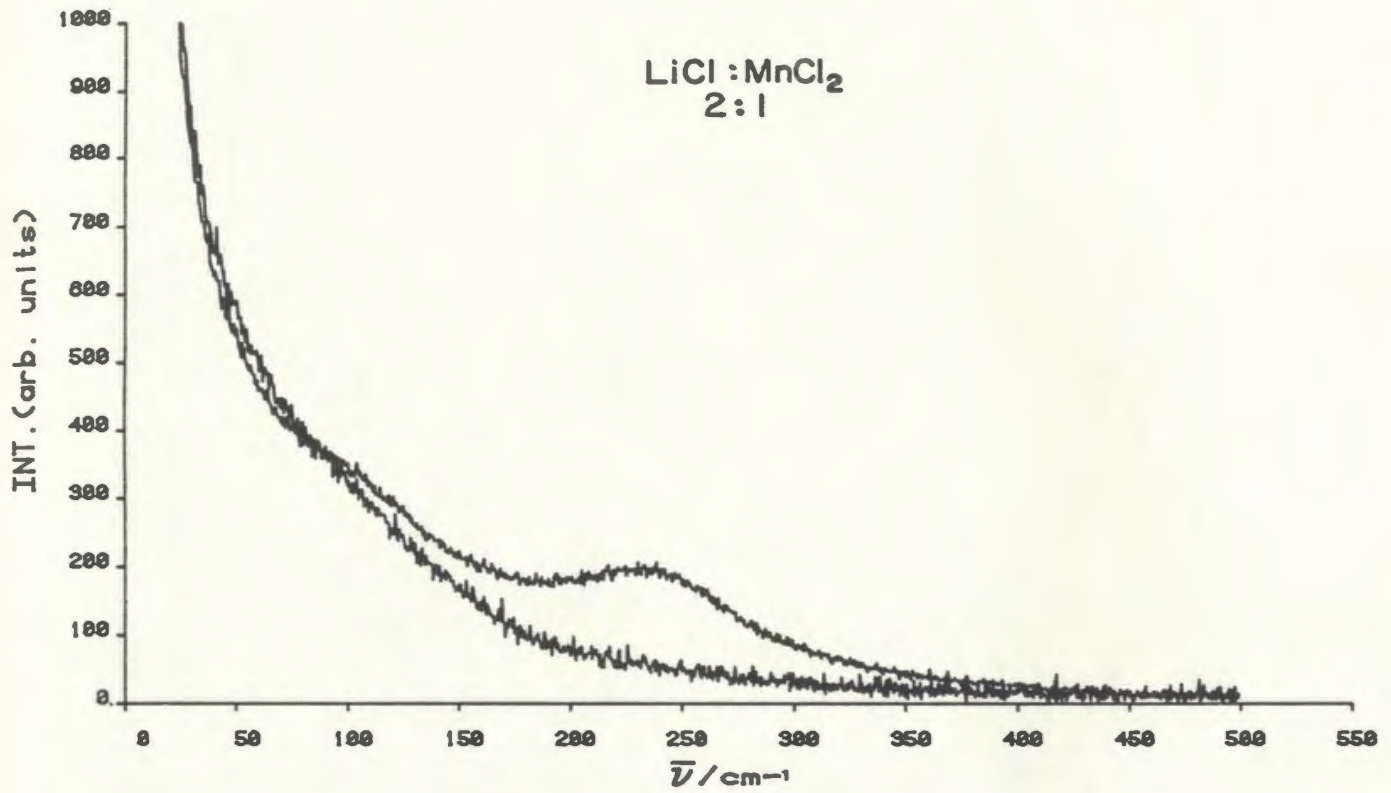


Figure 56. Raman spectra of molten $\text{LiCl}:\text{MnCl}_2$ (3:1) at
973 K, $I_{||}$ and I_{\perp} .

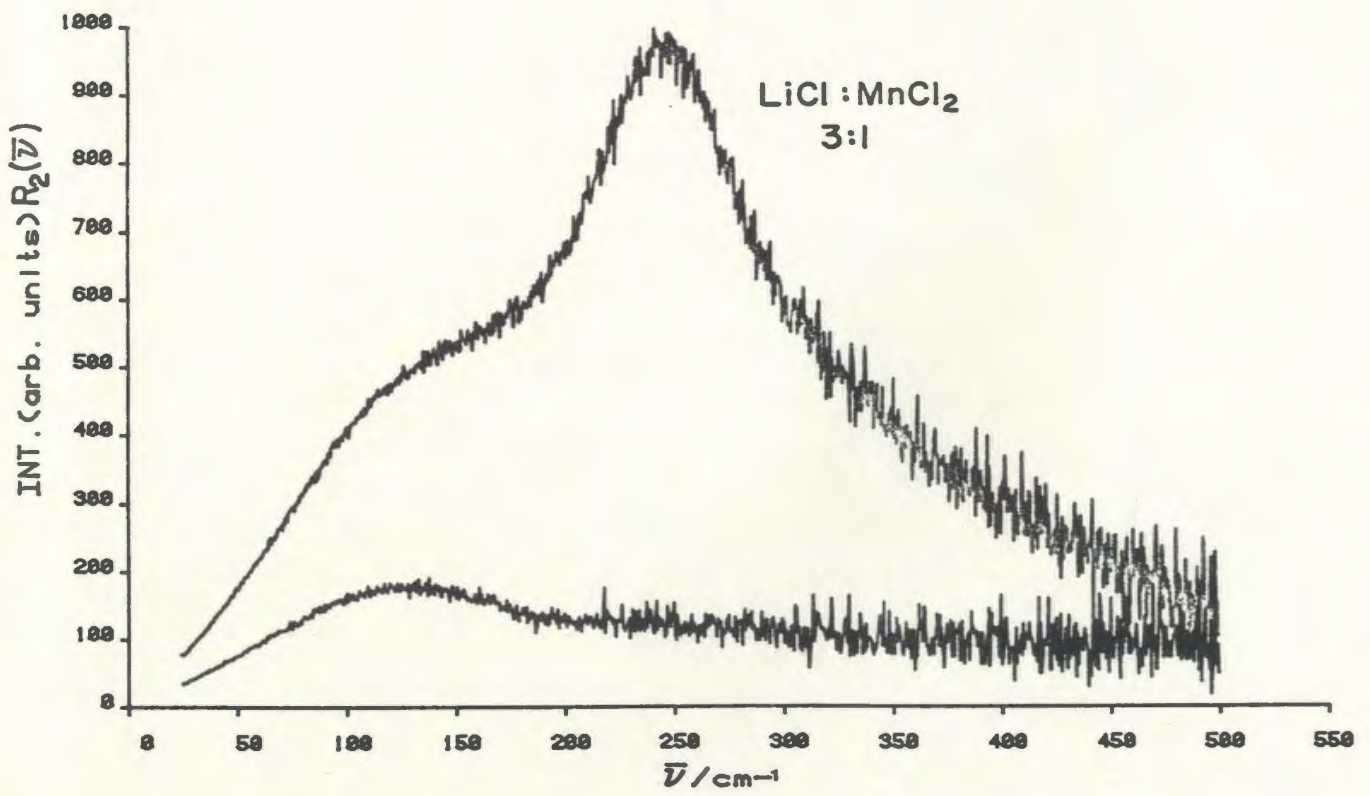
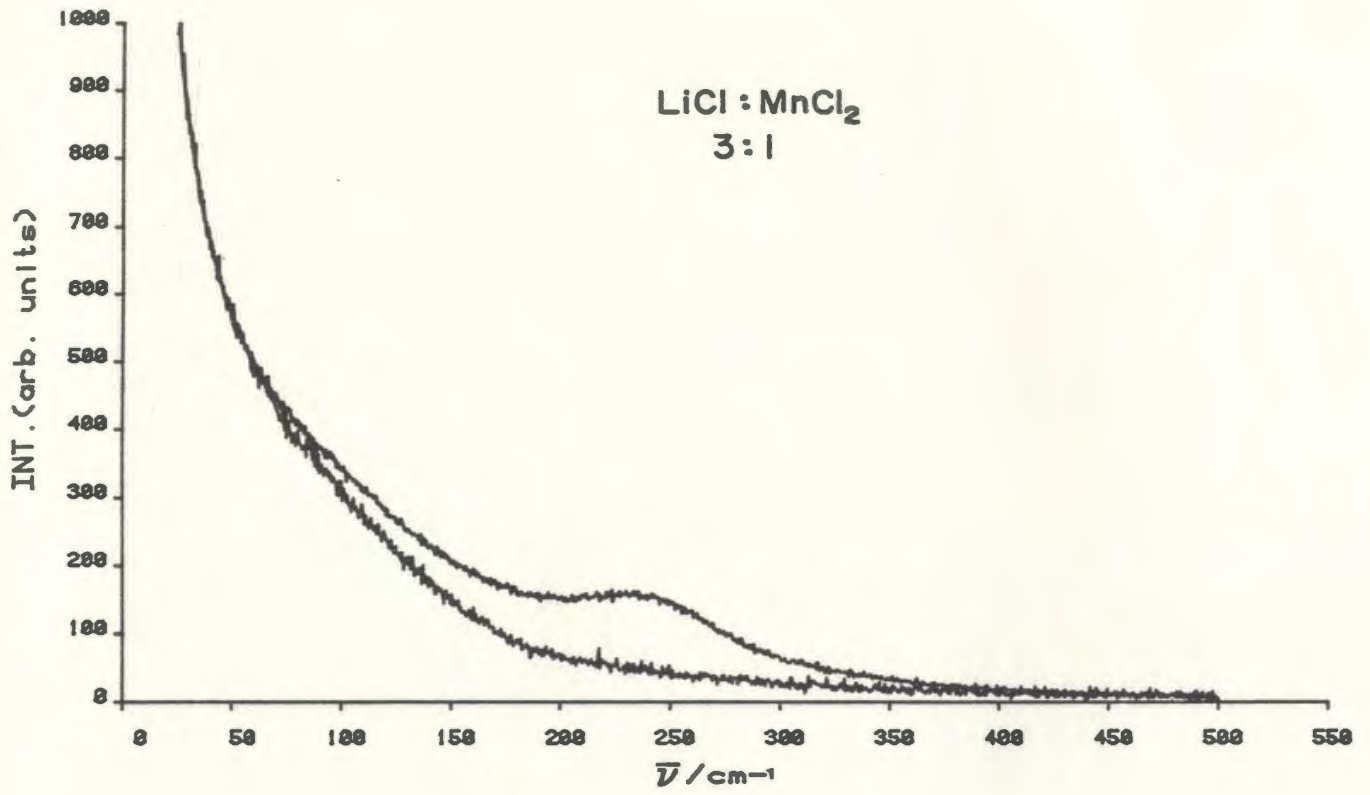


Figure 57. Isotropic Raman spectra of molten $\text{LiCl}:\text{MnCl}_2$ (1:1).
The smooth line is the best-fit curve calculated with
a single Gaussian*Lorentzian function.

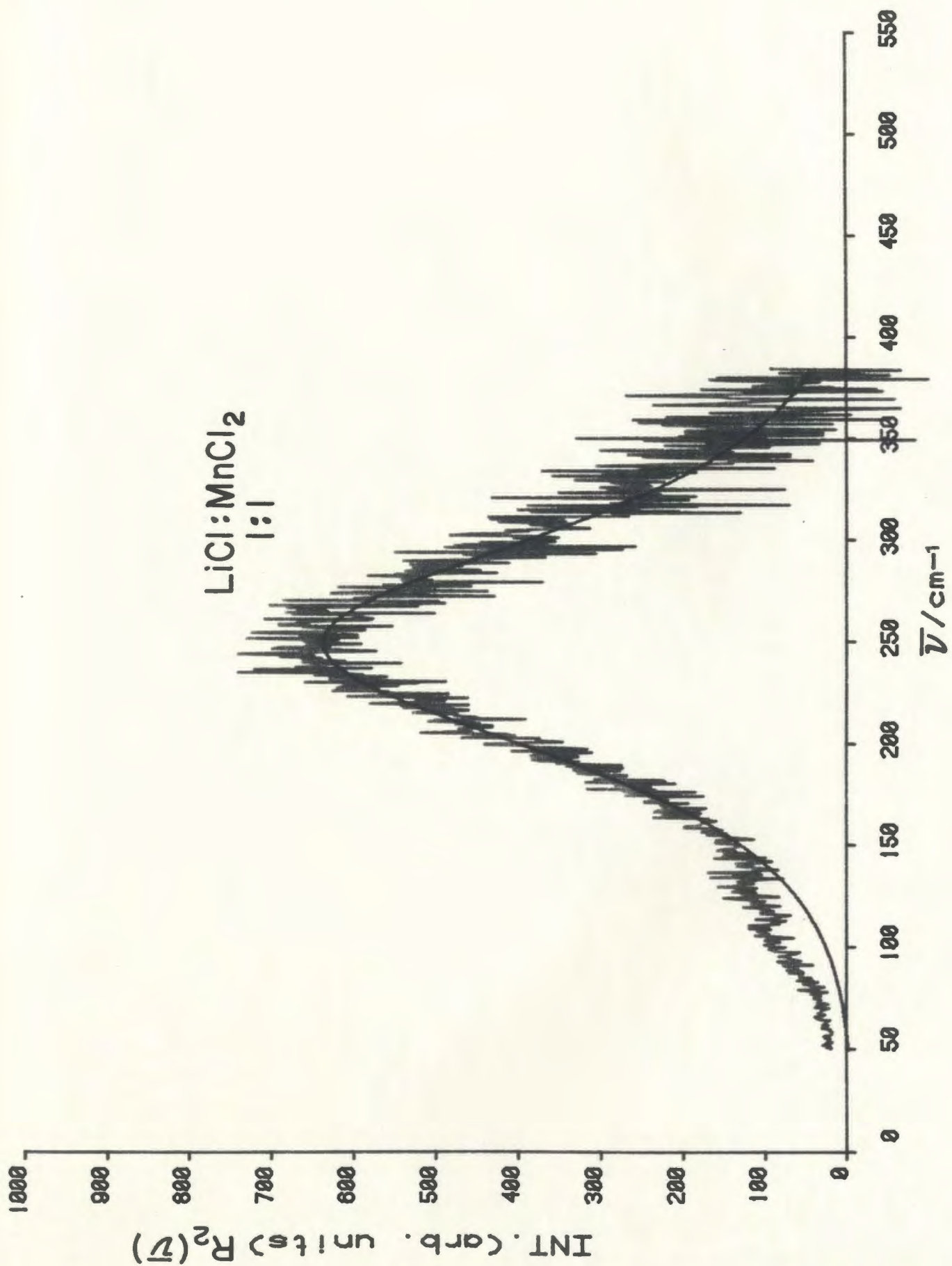


Figure 58. Isotropic Raman spectra of molten $\text{LiCl}:\text{MnCl}_2$ (2:1).
The smooth line is the best-fit curve calculated with
a single Gaussian*Lorentzian function.

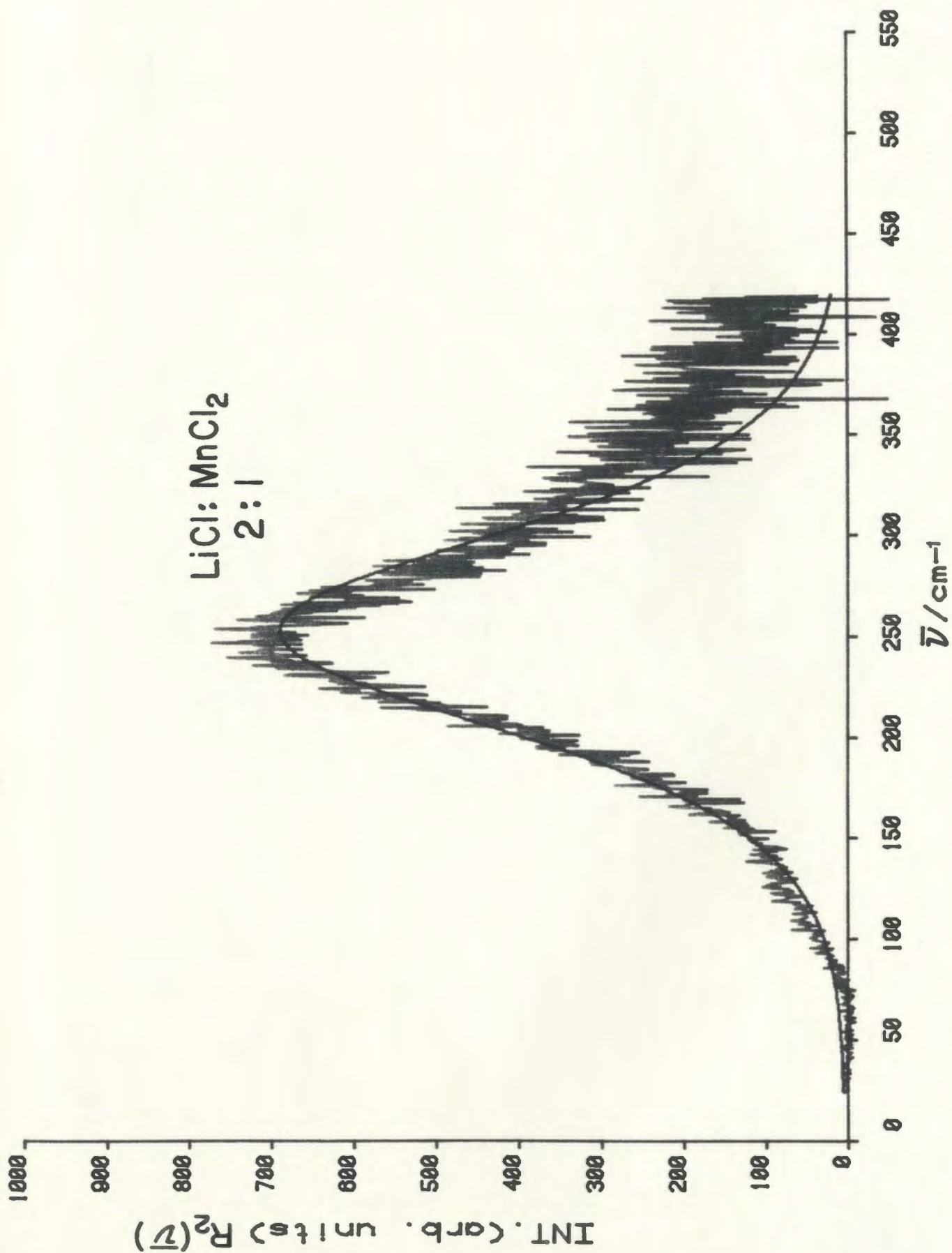


Figure 59. Isotropic Raman spectra of molten $\text{LiCl}:\text{MnCl}_2$ (3:1).
The smooth line is the best-fit curve calculated with
a single Gaussian*Lorentzian function.

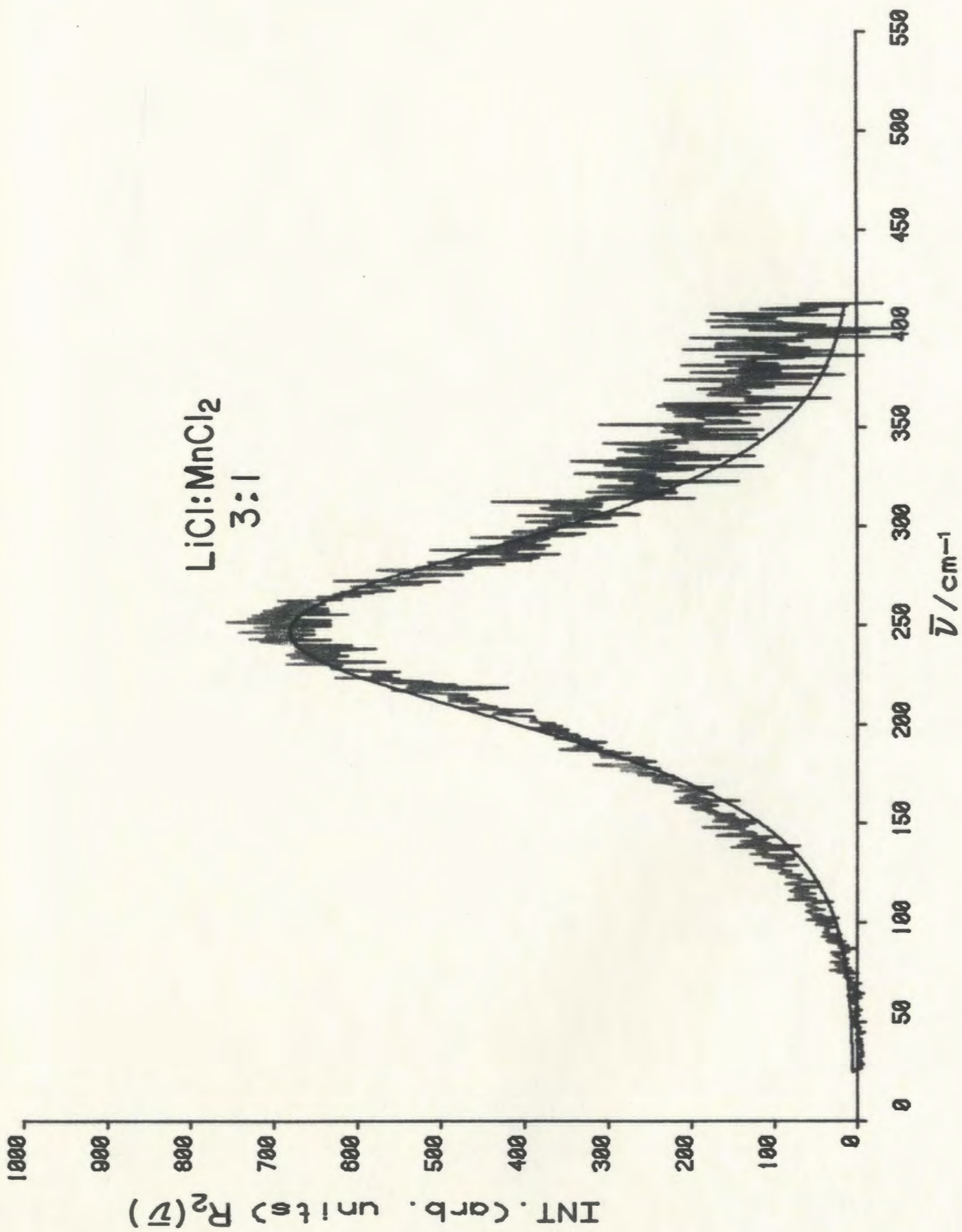


Table 25. Half band width for $ACl-MnCl_2$ melts.

Cations	Cs	Rb	K	Na	Li
$ACl:MnCl_2$ 1:1	81.8	85.1	86.7	92.3	123.9
$ACl:MnCl_2$ 2:1	39.9	42.5	51.4	82.0	117.4
$ACl:MnCl_2$ 3:1	35.3	41.0	48.2	79.4	109.7

4.3 Raman Studies of $\text{MgCl}_2 \cdot n\text{ACl}$: Molten State

4.3.1 MgCl_2 and MgCl_2 - CsCl Melts

The Raman spectra of $\text{CsCl}:\text{MgCl}_2$ (4:1), Cs_2MgCl_4 , $\text{CsCl}:\text{MgCl}_2$ (1.5:1), CsMgCl_3 , $\text{CsCl}:\text{MgCl}_2$ (0.5:1), and MgCl_2 melts are shown in figures 60, 61, 62, 63, 64 and 65 respectively. For melts of composition $\text{MgCl}_2 \cdot n\text{CsCl}$ for $n \geq 2$ there is a strong, sharp polarized peak at 250 cm^{-1} which may be assigned to ν_1 mode of MgCl_4^{2-} ion. A depolarized band due to ν_3 is observed as a very weak peak in the range $335\text{-}355 \text{ cm}^{-1}$, and previously was observed in the infrared mull spectrum¹³ of MgCl_4^{2-} ion as a very strong peak at 360 cm^{-1} . The depolarized peaks due to ν_2 and ν_4 are observed in the region $100\text{-}150 \text{ cm}^{-1}$. Since one polarized peak is clearly resolved at 250 cm^{-1} , and three depolarized peaks are observed, the results strongly indicate the formation of MgCl_4^{2-} ions in $\text{CsCl}:\text{MgCl}_2$ (4:1) melt. In the melts of composition $\text{MgCl}_2 \cdot n\text{CsCl}$ for $n \leq 2$ the polarized feature consists of at least two overlapped peaks estimated at 225 and 250 cm^{-1} and one broad shoulder around $\sim 300 \text{ cm}^{-1}$. The intensity of the low frequency peak $\sim 225 \text{ cm}^{-1}$ and the high frequency peak at 300 cm^{-1} quite clearly increase in relative intensity with increasing MgCl_2 concentration, figures 61, 62 and 63. The formation of a new equilibrium species in the melts of high MgCl_2 concentration was suggested¹⁷ based on the presence of the low frequency peak. The results indicate the existence of tetrahedral MgCl_4^{2-} species in equilibrium with another species. This new species was attributed to the $\text{Mg}_2\text{Cl}_7^{3-}$ ion since for this structure the magnesium may retain its tetrahedral coordination through corner sharing with another tetrahedral ion. A $\text{Mg}_2\text{Cl}_6^{2-}$ ion in which the magnesium is tetrahedrally coordinated through edge sharing with another tetrahedral ion would also be logical.

These results are exactly parallel to the case of $\text{AlCl}_3 \cdot \text{AlCl}$ melts² where two well resolved peaks at ~ 310 and 430 cm^{-1} due to the symmetric stretching motions of the Al_2Cl_7^- ion increase at the expense of a peak at $\sim 350 \text{ cm}^{-1}$ due to AlCl_4^- for melts of appropriate molar ratio. The greater band overlap in the $\text{MgCl}_2 \cdot \text{AlCl}$ system is caused by environmental broadening factors such as the weaker bond energy and thermal motion.

The results of curve resolution analysis of the $I_\alpha(\bar{\nu})$ spectra are shown in figures 66 to 71 and Table 26. Excellent fits for the $\text{MgCl}_2 \cdot n\text{CsCl}$ melts with $n = 2.0, 1.5$ and 1.0 were achieved with the three band model for peaks at $\sim 220, 250$ and 300 cm^{-1} . Two band fits gave poor agreement with the observed spectra and were physically unrealistic. The intensity ratio of the peaks at 220 and 300 increased together at the expense of intensity at 250 cm^{-1} as the MgCl_2 concentration was increased (ie. an increase of $\text{Mg}_2\text{Cl}_7^{3-}$ versus MgCl_4^{2-}). For melts of high MgCl_2 content and pure MgCl_2 the simple two species equilibrium model did not give good fits to the data because of a significant polarized intensity increase about 150 cm^{-1} . In the $\text{AlCl}_3 \cdot \text{AlCl}$ system peaks due to $\text{Al}_3\text{Cl}_{10}^-$ and Al_2Cl_6 have been identified² but the band overlap in the $\text{MgCl}_2 \cdot n\text{AlCl}$ systems precludes detailed analysis of melts with $n \geq 0.5$ and the curve analysis for these systems may not be unique. A broad three band fit adequately reproduced the spectrum of pure MgCl_2 melt.

Three polarized peaks may be resolved for the pure MgCl_2 melt, the one resolved at 237 cm^{-1} is attributed to the symmetric stretching mode (ν_1) of the tetrahedral ion, while the other two polarized peaks are resolved at 194 and 161 cm^{-1} were reported previously¹⁵ at 194 and 130 cm^{-1} and attributed to symmetric stretching vibrations of poly-

nuclear species $\text{Mg}_2\text{Cl}_2^{2+}$, or Mg_2Cl_3^+ , or Mg_2Cl_4 . The polarized peak resolved at 145 cm^{-1} in the spectrum of $\text{CsCl}:\text{MgCl}_2$ (0.5:1) melt appears to correspond to the one resolved at 161 cm^{-1} in the spectrum of MgCl_2 melt and attributed to polynuclear species. The Raman results suggest that $\text{CsCl}:\text{MgCl}_2$ (0.5:1) melt contains an equilibrium mixture of MgCl_4^{2-} ions, $\text{Mg}_2\text{Cl}_7^{3-}$ ions, and polynuclear species as positive or neutral ions. The presence of the depolarized peak at $\sim 350\text{ cm}^{-1}$ in pure MgCl_2 melts suggests that an MgCl_4^{2-} unit may be present. It should be emphasized that the minimum number of bands necessary to obtain a good fit was the guiding factor in the curve analysis. More bands would give better fits and could give more realistic representation species concentrations. The important consequence of the curve analysis is the fact that at least two species and probably a third must be present to generate the observed spectra. This should be contrasted to the results for the manganese chloride system discussed previously where possible species had lifetimes that were too short to give discrete peaks.

4.3.2 MgCl_2 -KCl Melts

The Raman spectra of K_2MgCl_4 , $\text{KCl}:\text{MgCl}_2$ (1.5:1), KMgCl_3 , and $\text{KCl}:\text{MgCl}_2$ (0.5:1) melts are shown in figures 72, 73, 74 and 75. The peaks due to ν_2 and ν_4 of the tetrahedral MgCl_4^{2-} ion are observed in the region 100 - 150 cm^{-1} , while the peak due to ν_3 is observed as a weak peak at $\sim 350\text{ cm}^{-1}$. Only one broad polarized envelop is observed in each melt, and this envelop changes shape and broadens with increasing MgCl_2 concentration. The broadening of the polarized feature indicates that there is another species in equilibrium with the tetrahedral MgCl_4^{2-} ions. The curve analysis gives results similar to the CsCl

Table 26. Summary of results of curve resolution analysis for MgCl_2 and MgCl_2 - CsCl Melts.

Compound	Frequency (cm^{-1})	Intensity	Half band width (cm^{-1})	Assignments
$\text{CsCl}:\text{MgCl}_2$ (4:1)	249.6	334	23.0	$(\nu_1) \text{MgCl}_4^{2-}$
Cs_2MgCl_4	225.4	99	44.7	$(\nu) \text{Mg}_2\text{Cl}_7^{3-}$
	250.1	361	24.6	$(\nu_1) \text{MgCl}_4^{2-}$
	297.0	25	56.7	$(\nu) \text{Mg}_2\text{Cl}_7^{3-}$
$\text{CsCl}:\text{MgCl}_2$ (1.5:1)	224.6	138	55.4	$(\nu) \text{Mg}_2\text{Cl}_7^{3-}$
	250.0	189	27.1	$(\nu_1) \text{MgCl}_4^{2-}$
	294.8	28	72.9	$(\nu) \text{Mg}_2\text{Cl}_7^{3-}$
CsMgCl_3	220.6	200	57.4	$(\nu) \text{Mg}_2\text{Cl}_7^{3-}$
	250.6	160	35.9	$(\nu_1) \text{MgCl}_4^{2-}$
	291.8	42	103.2	$(\nu) \text{Mg}_2\text{Cl}_7^{3-}$
$\text{CsCl}:\text{MgCl}_2$ (0.5:1)	145.4	47	66.1	(ν) polynuclear species
	213.3	155	55.8	$(\nu) \text{Mg}_2\text{Cl}_7^{3-}$
	244.5	146	63.0	$(\nu_1) \text{MgCl}_4^{2-}$
	315.7	12	112.3	$(\nu) \text{Mg}_2\text{Cl}_7^{3-}$
MgCl_2	161.1	248	204.3	(ν) polynuclear species
	194.2	163	52.9	
	237.0	129	71.4	$(\nu_1) \text{MgCl}_4^{2-}$

Figure 60. Raman spectra of molten CsCl:MgCl_2 (4:1) at 840 K, $I_{||}$ and I_{\perp} .

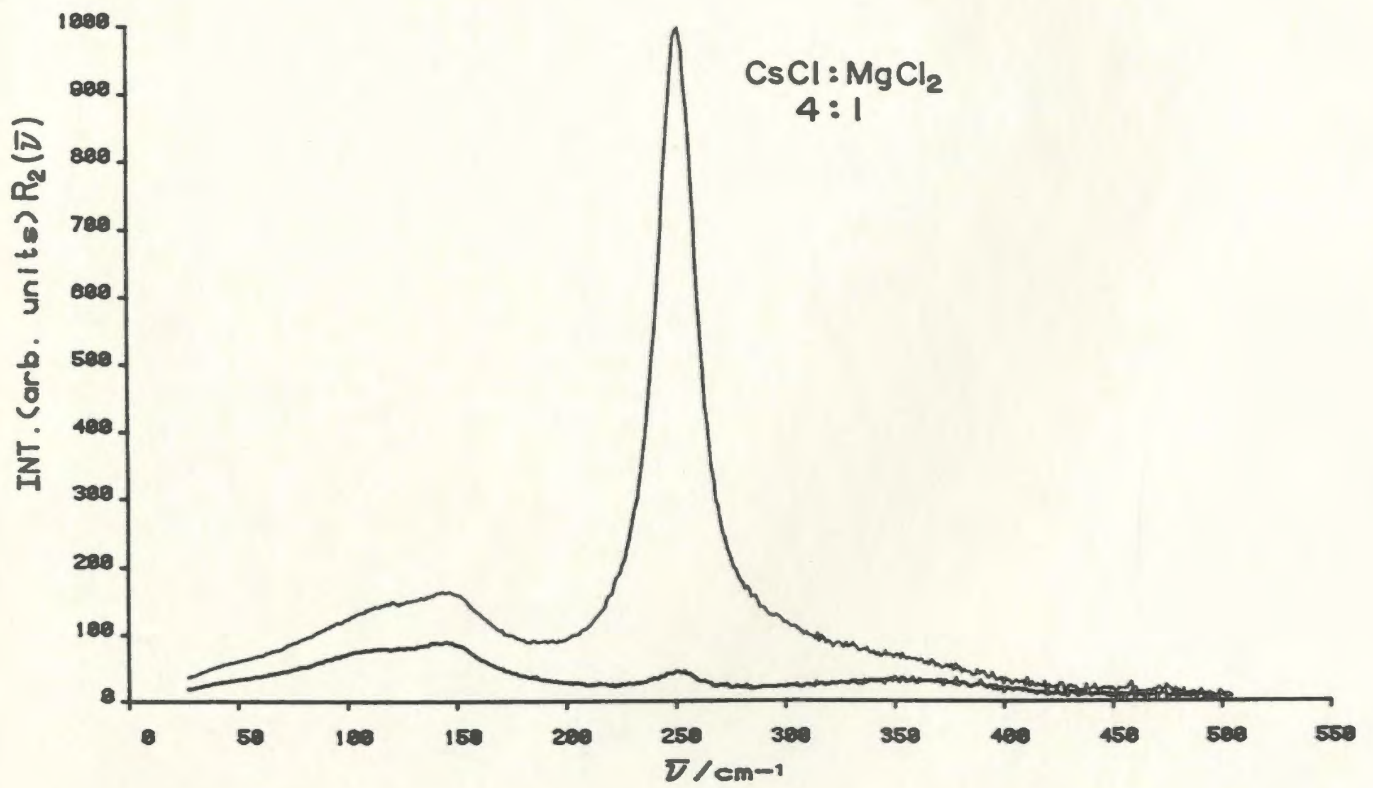
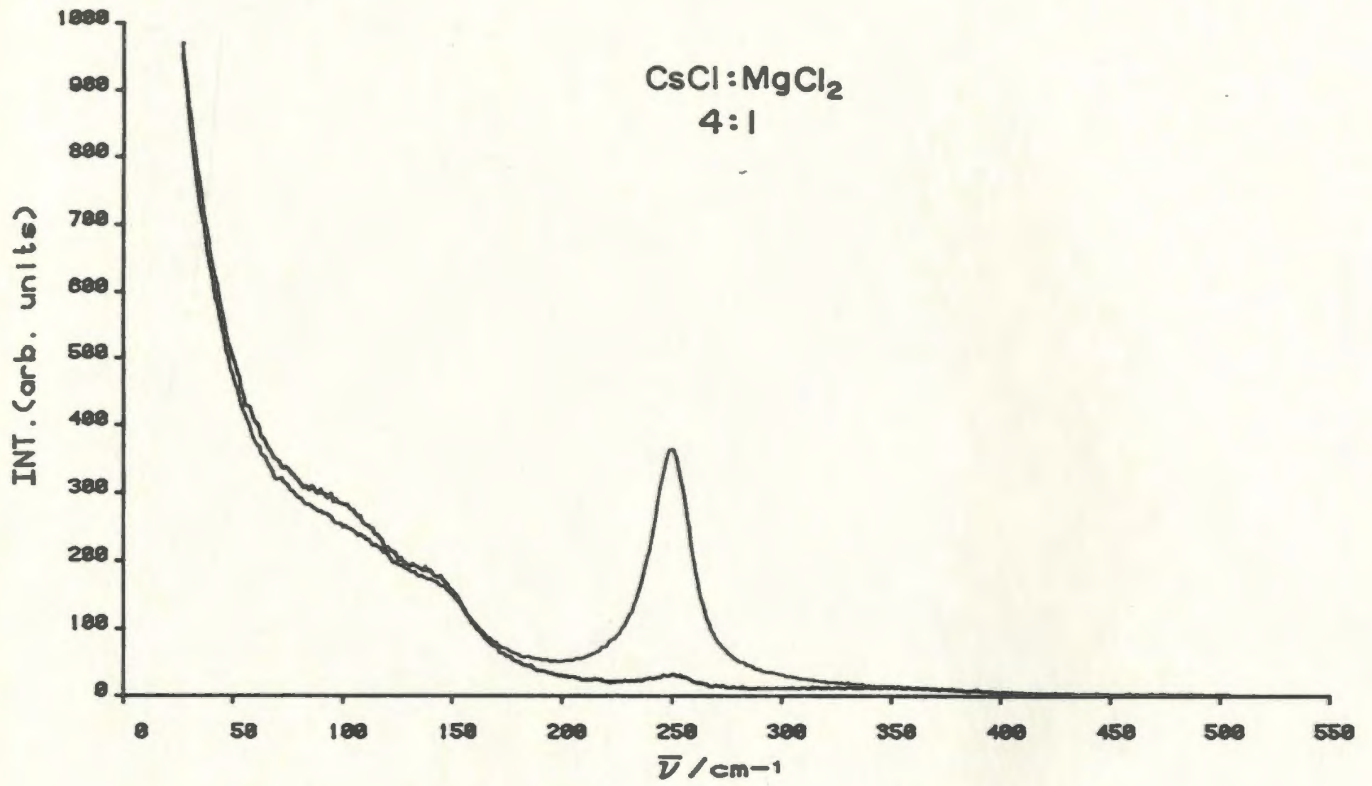


Figure 61. Raman spectra of molten Cs_2MgCl_4 at 896 K,

$I_{||}$ and I_{\perp} .

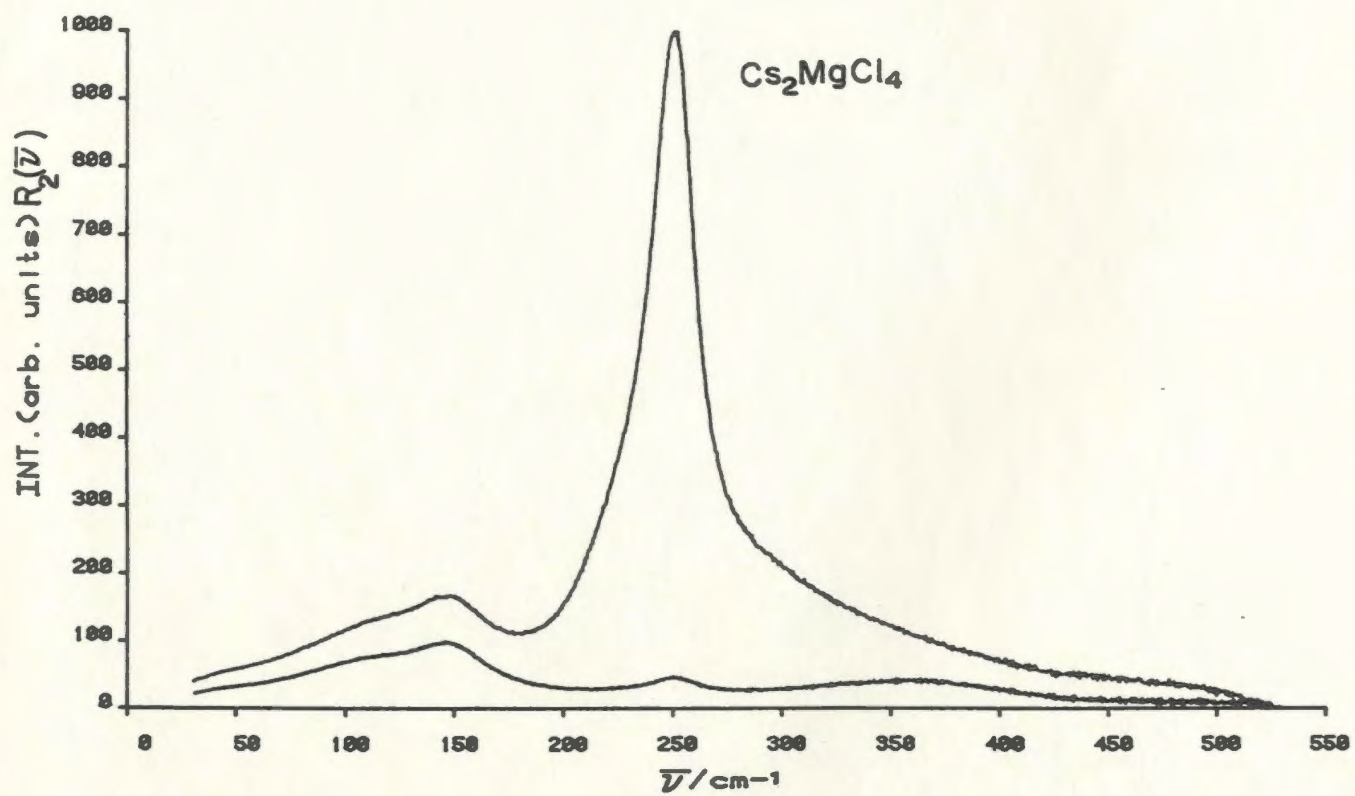
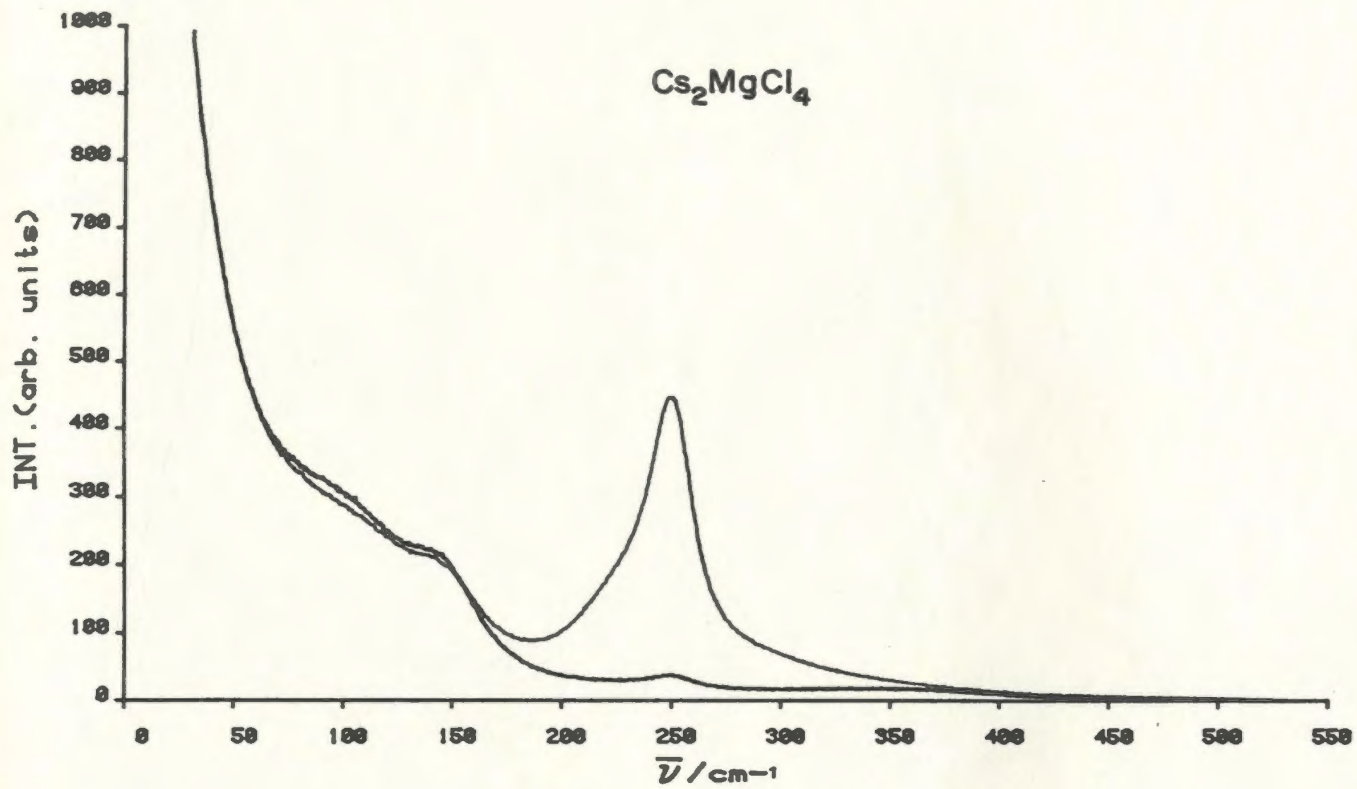


Figure 62. Raman spectra of molten $\text{CsCl}:\text{MgCl}_2$ (1.5:1) at
915 K, $I_{||}$ and I_{\perp} .

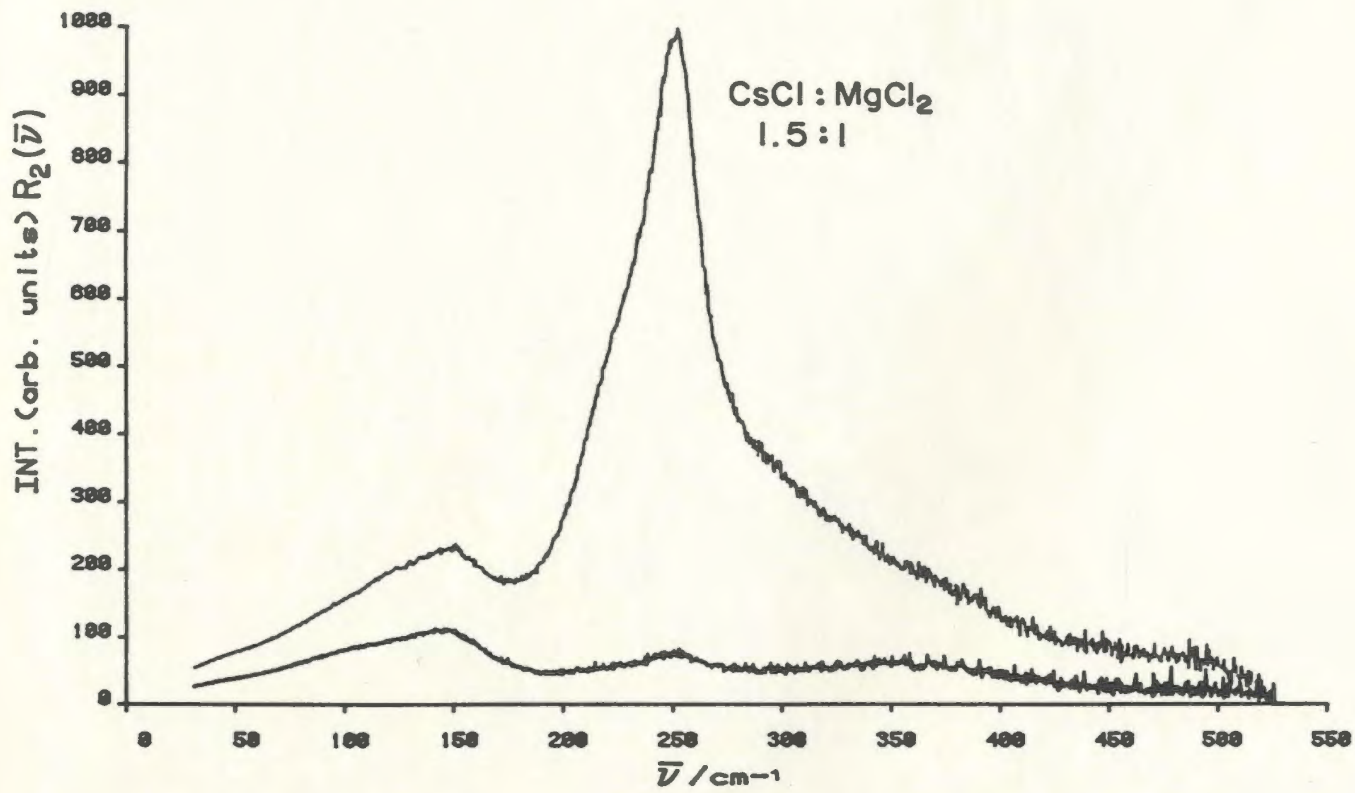
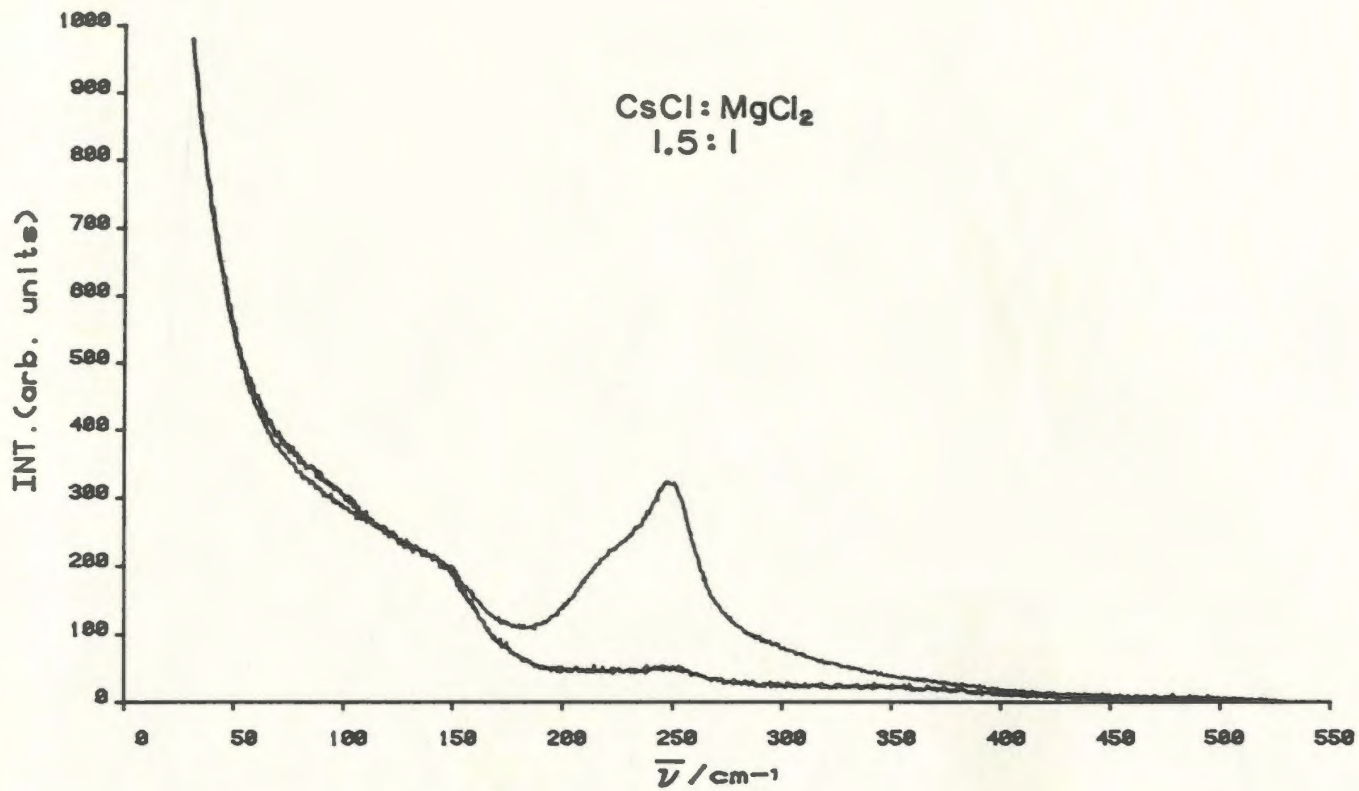


Figure 63. Raman spectra of molten CsMgCl_3 at 896 K,

$I_{||}$ and I_{\perp} .

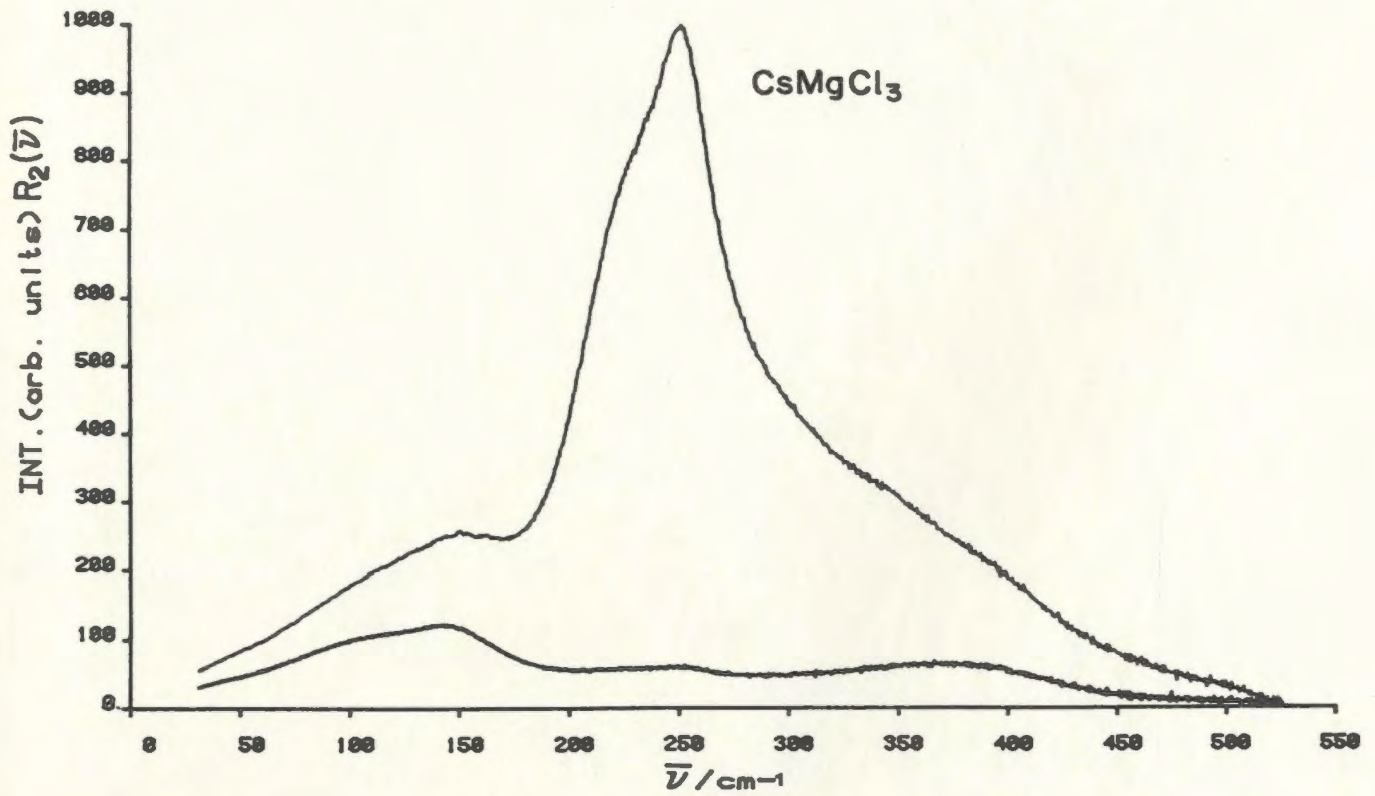
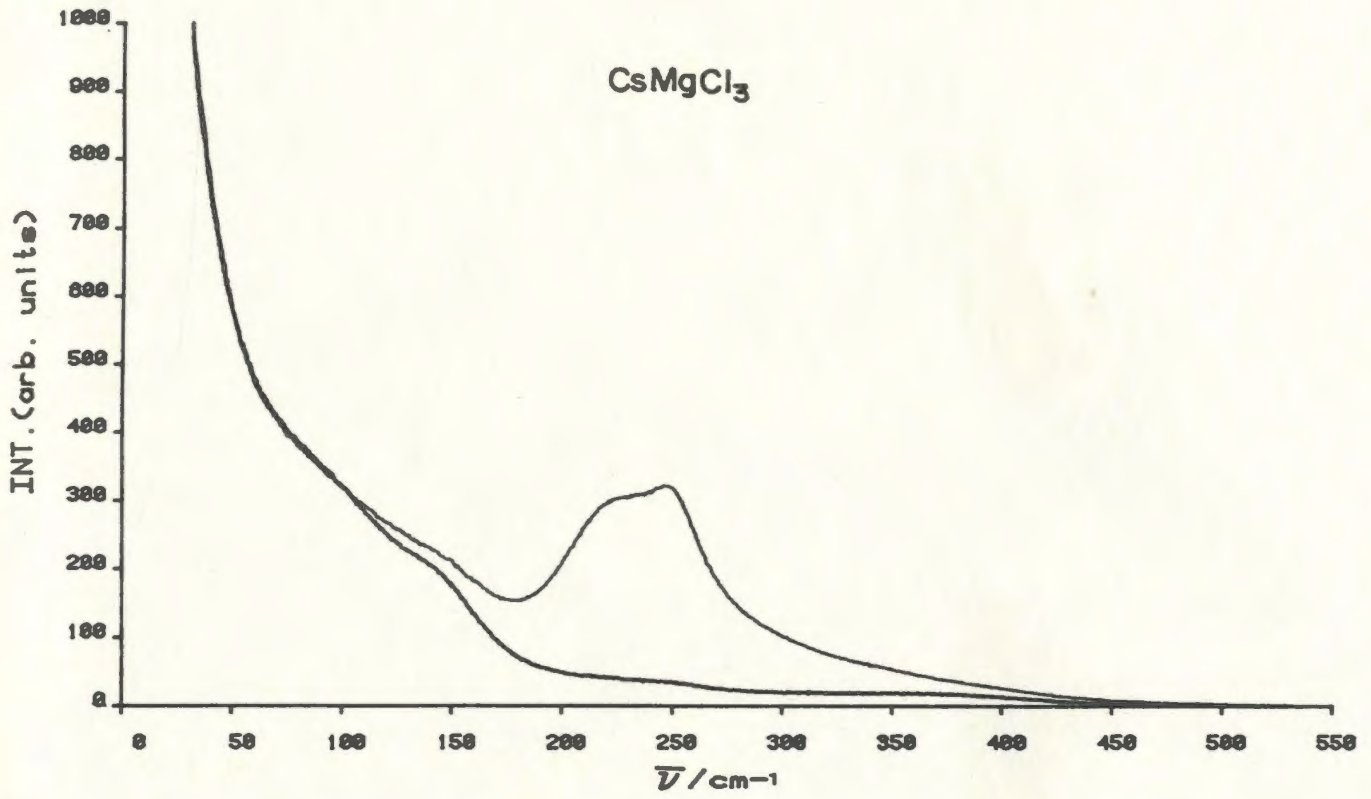


Figure 64. Raman spectra of molten $\text{CsCl}:\text{MgCl}_2$ (0.5:1) at
915 K, $I_{||}$ and I_{\perp} .

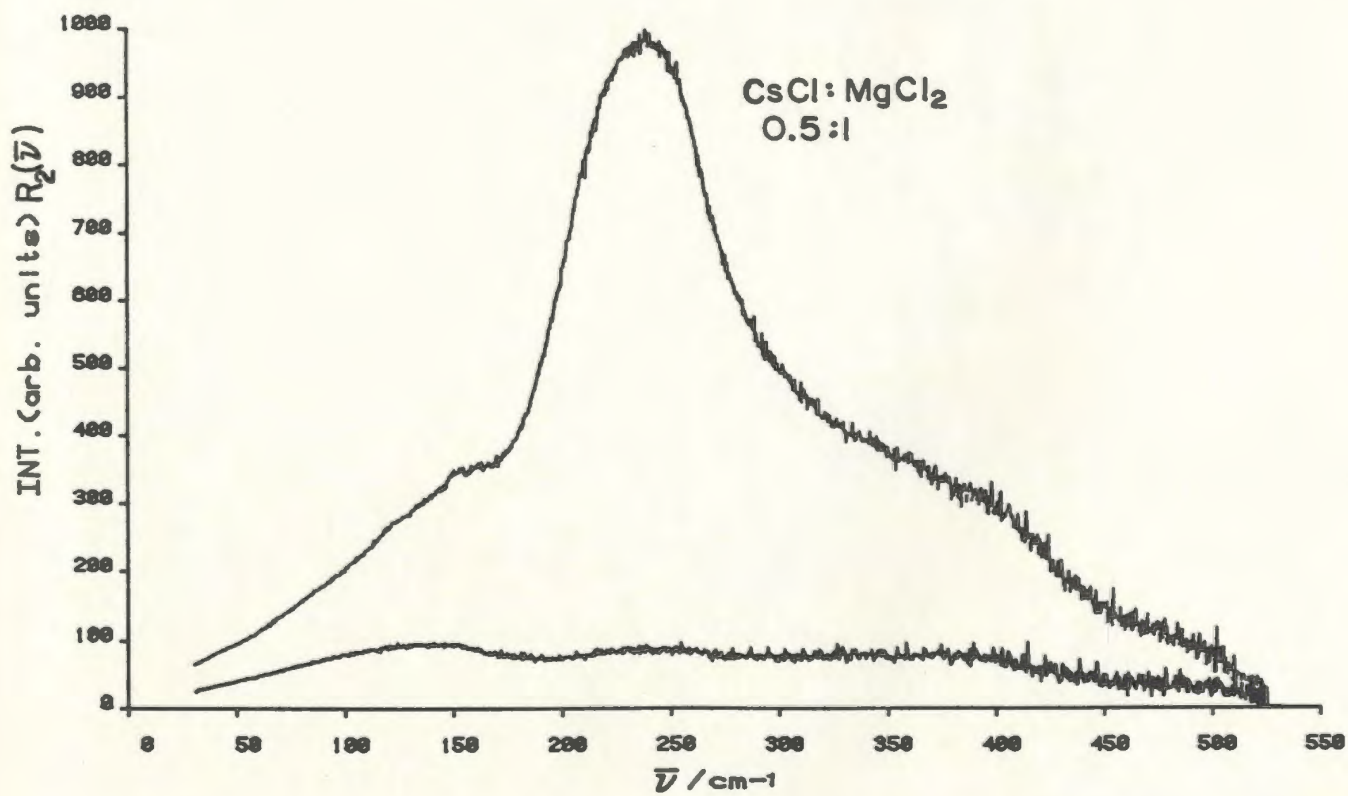
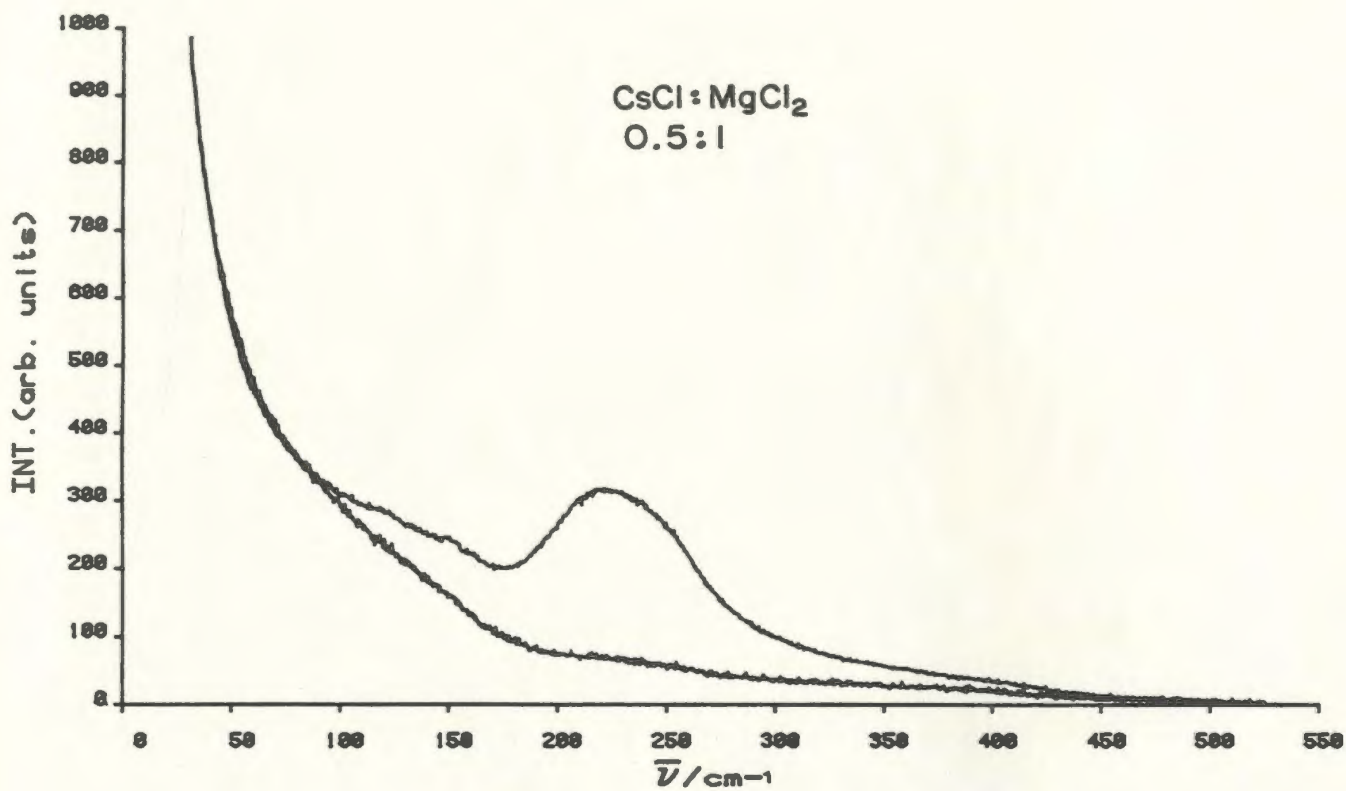


Figure 65. Raman spectra of molten MgCl_2 at 1056 K, $I_{||}$
and I_{\perp} .

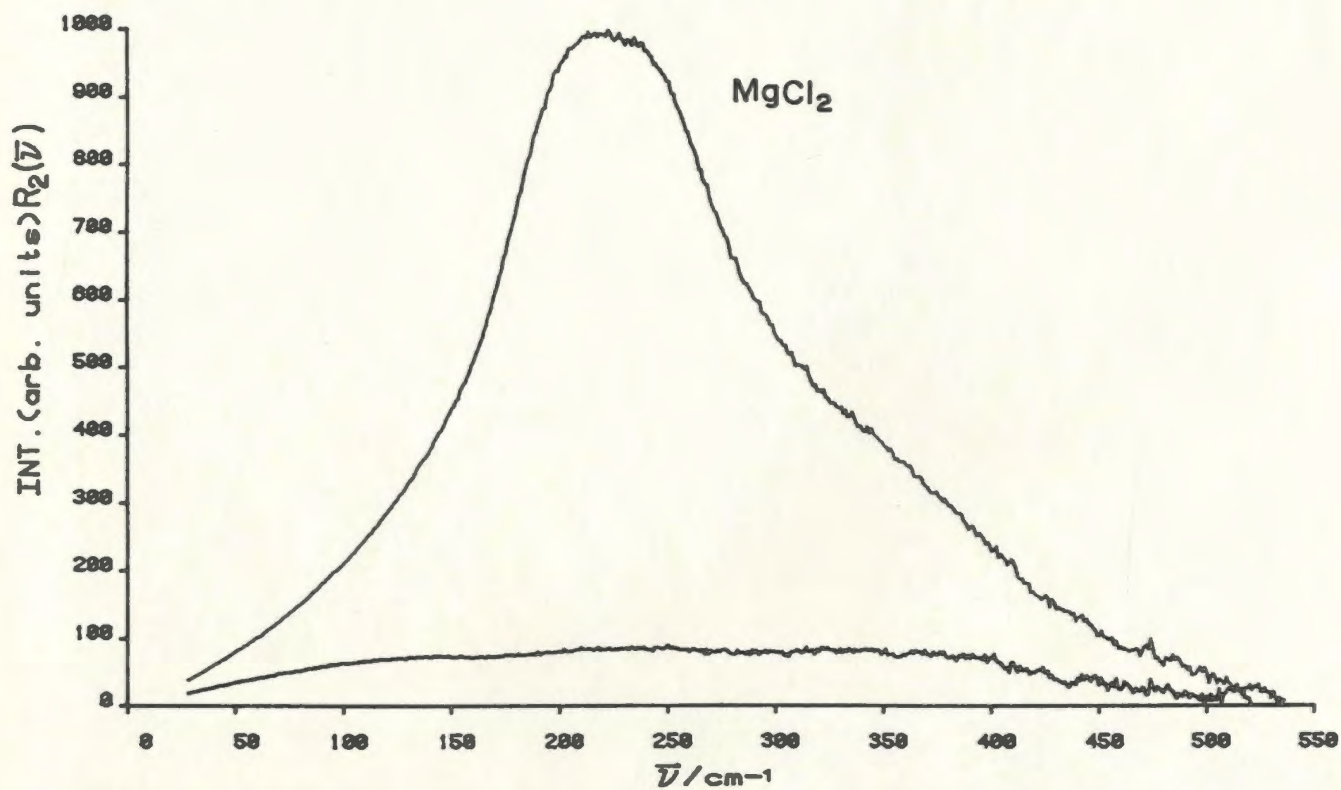
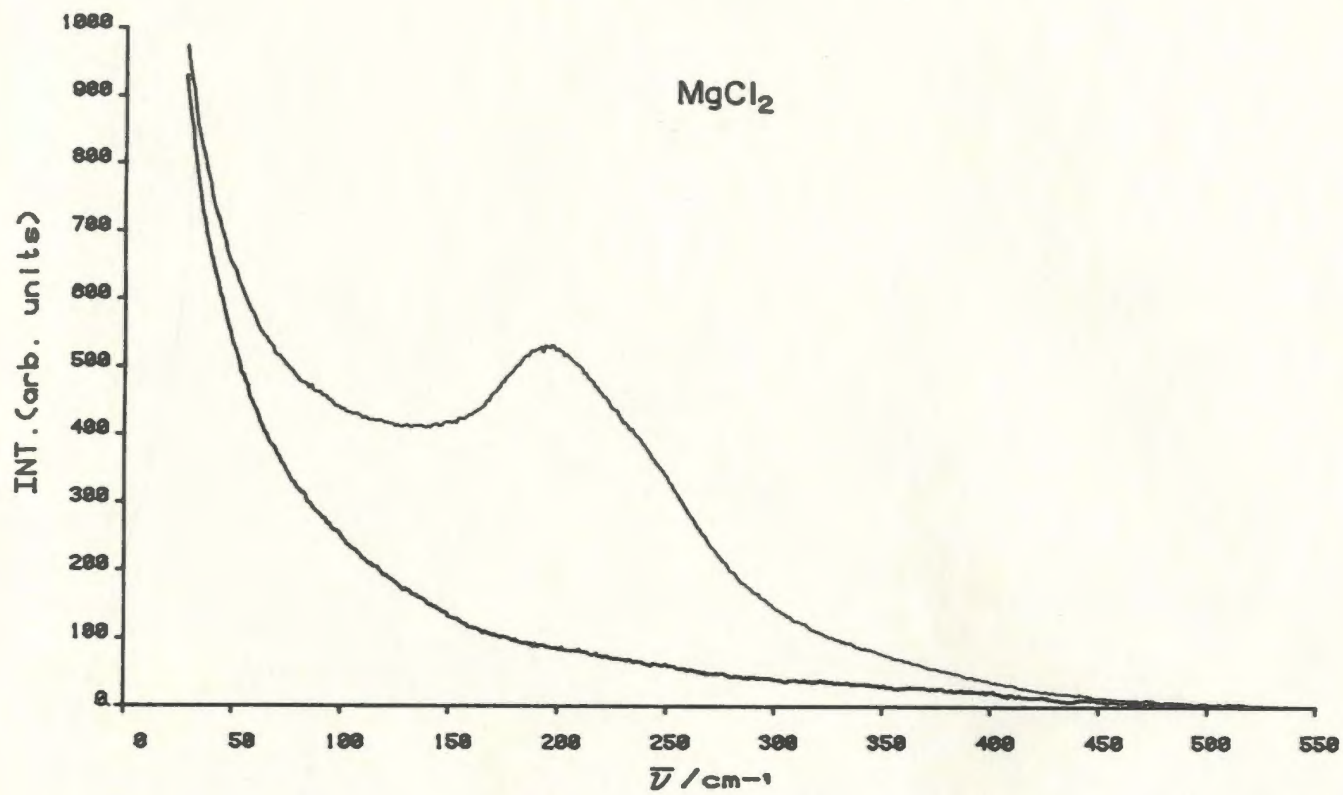


Figure 66. Isotropic Raman spectra of molten CsCl:MgCl_2 (4:1).
The smooth line is the best-fit curve calculated with
a single Lorentzian function.

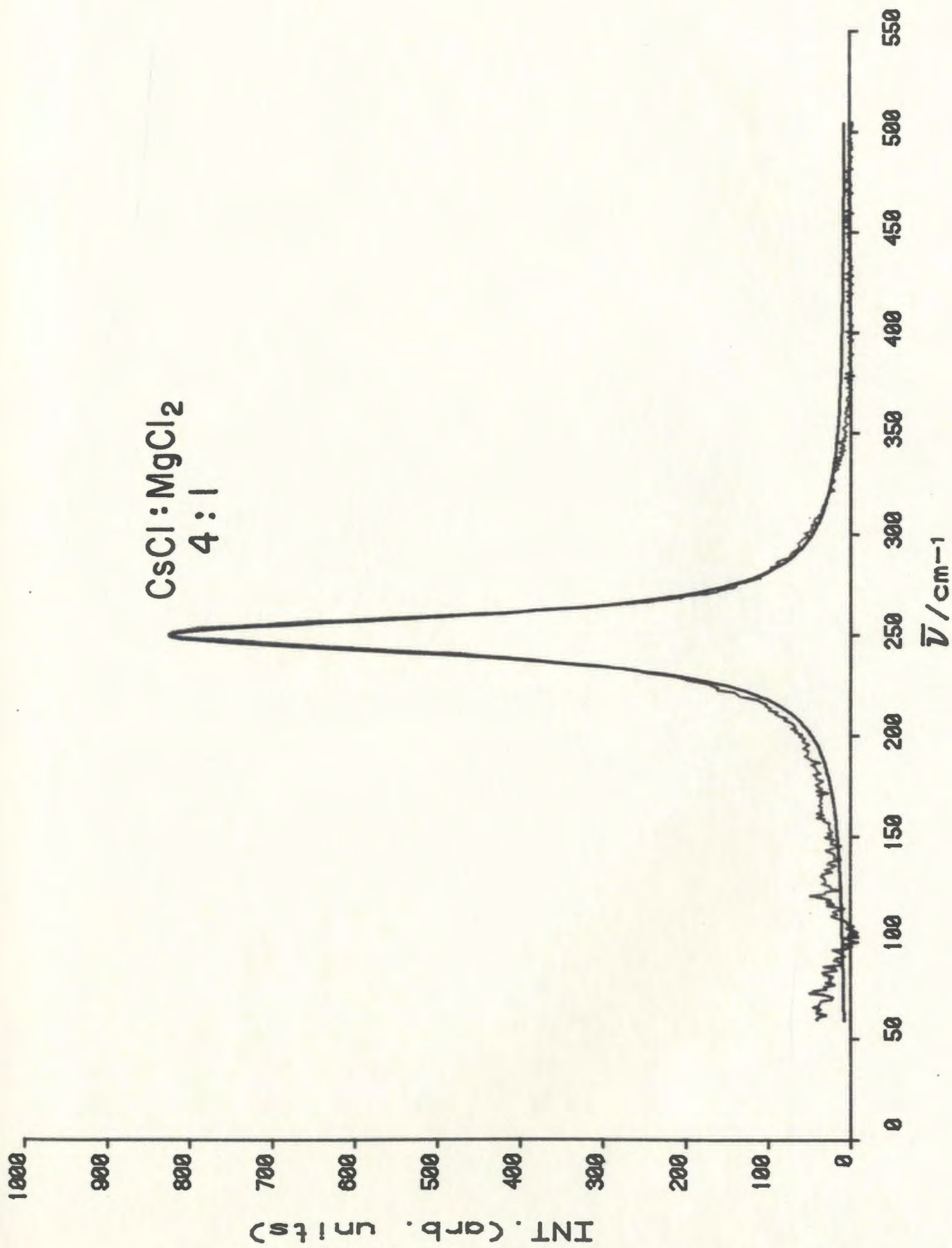


Figure 67. Isotropic Raman spectra of molten Cs_2MgCl_4 .
The smooth line is the best-fit curve calculated
as a sum of three Lorentzian functions.

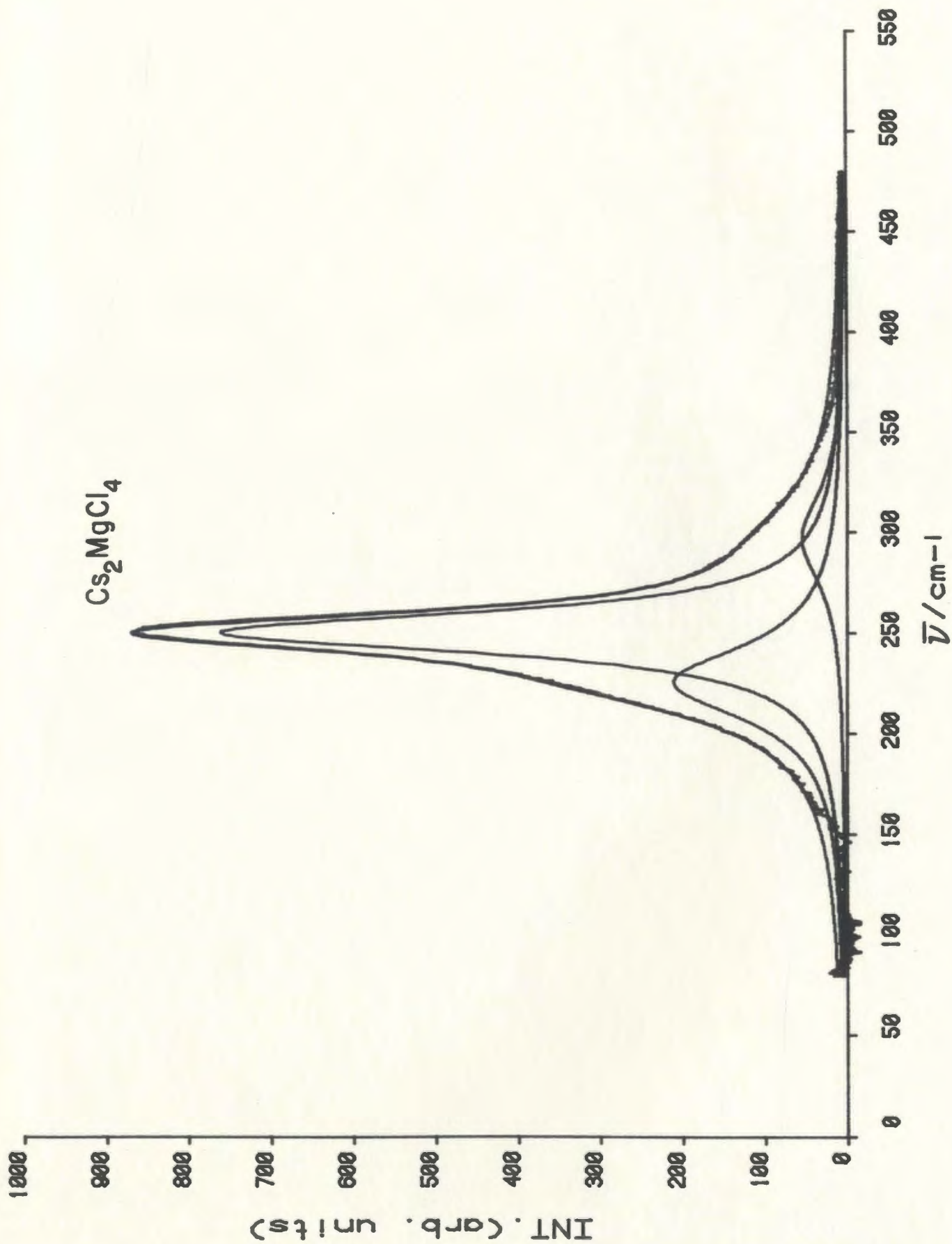


Figure 68. Isotropic Raman spectra of molten $\text{CsCl}:\text{MgCl}_2$ (1.5:1). The smooth line is the best-fit curve calculated as a sum of three Lorentzian functions.

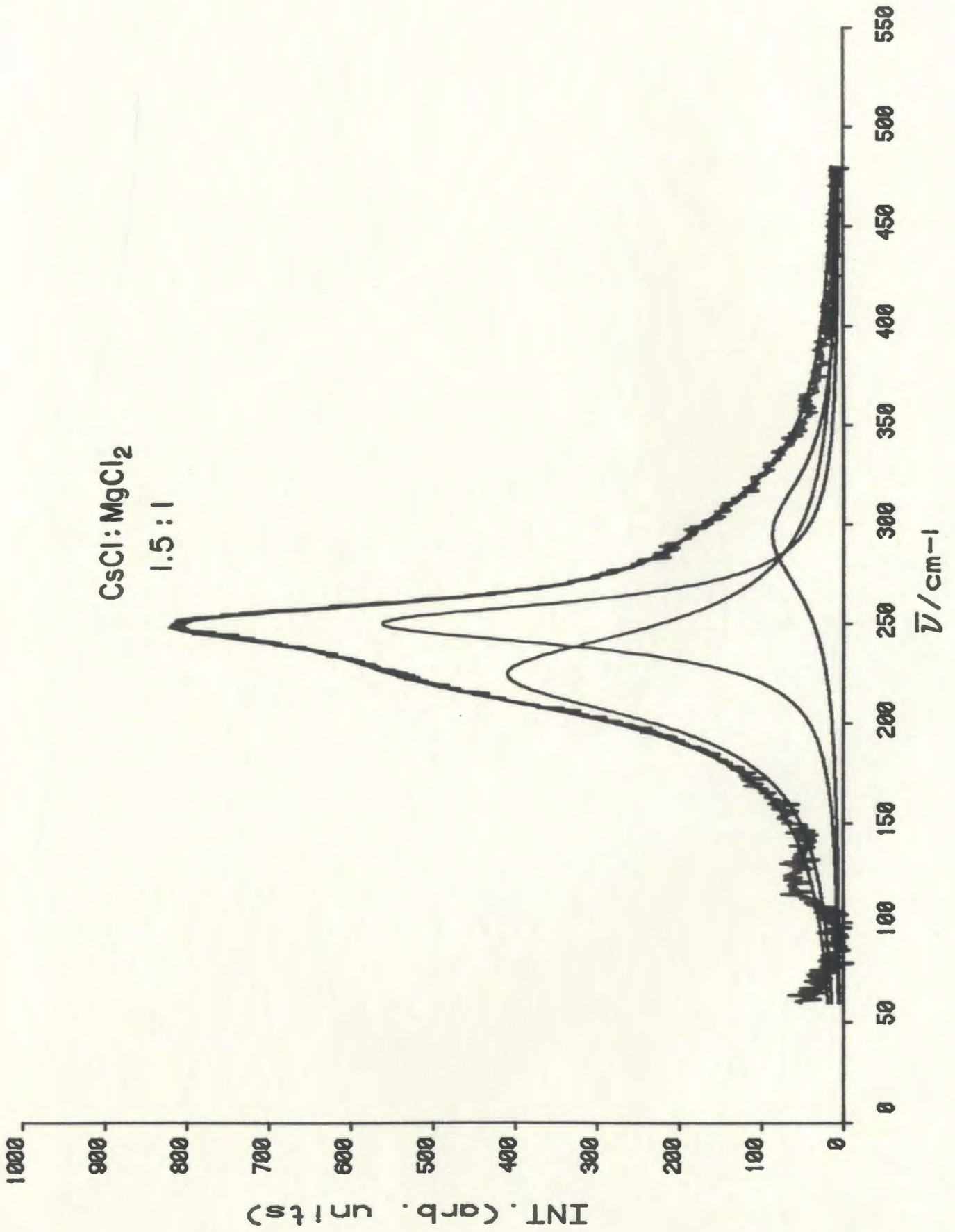


Figure 69. Isotropic Raman spectra of molten CsMgCl_3 . The smooth line is the best-fit curve calculated as a sum of three Lorentzian functions.

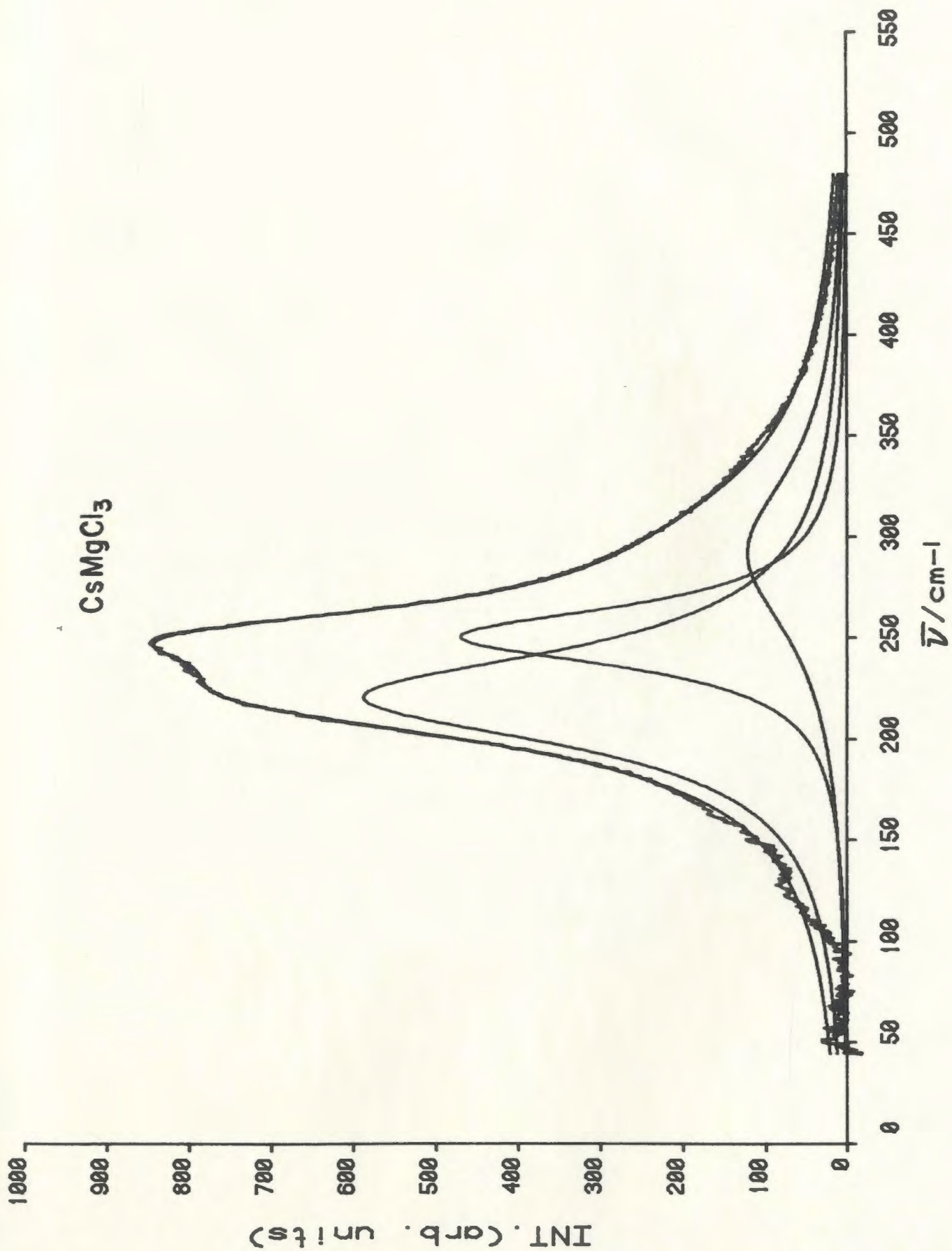


Figure 70. Isotropic Raman spectra of molten $\text{CsCl}:\text{MgCl}_2$ (0.5:1). The smooth line is the best-fit curve calculated as a sum of four Lorentzian functions.

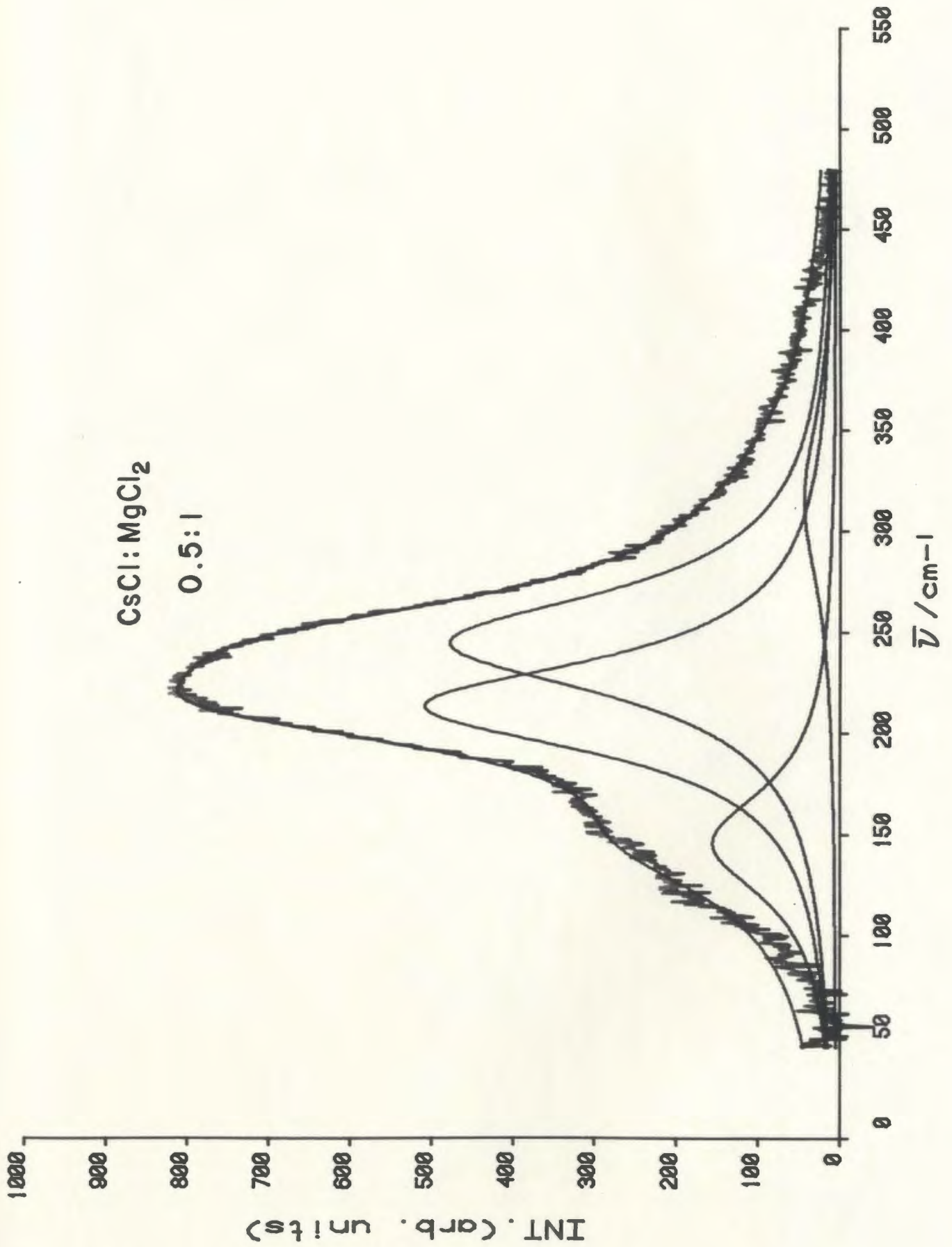
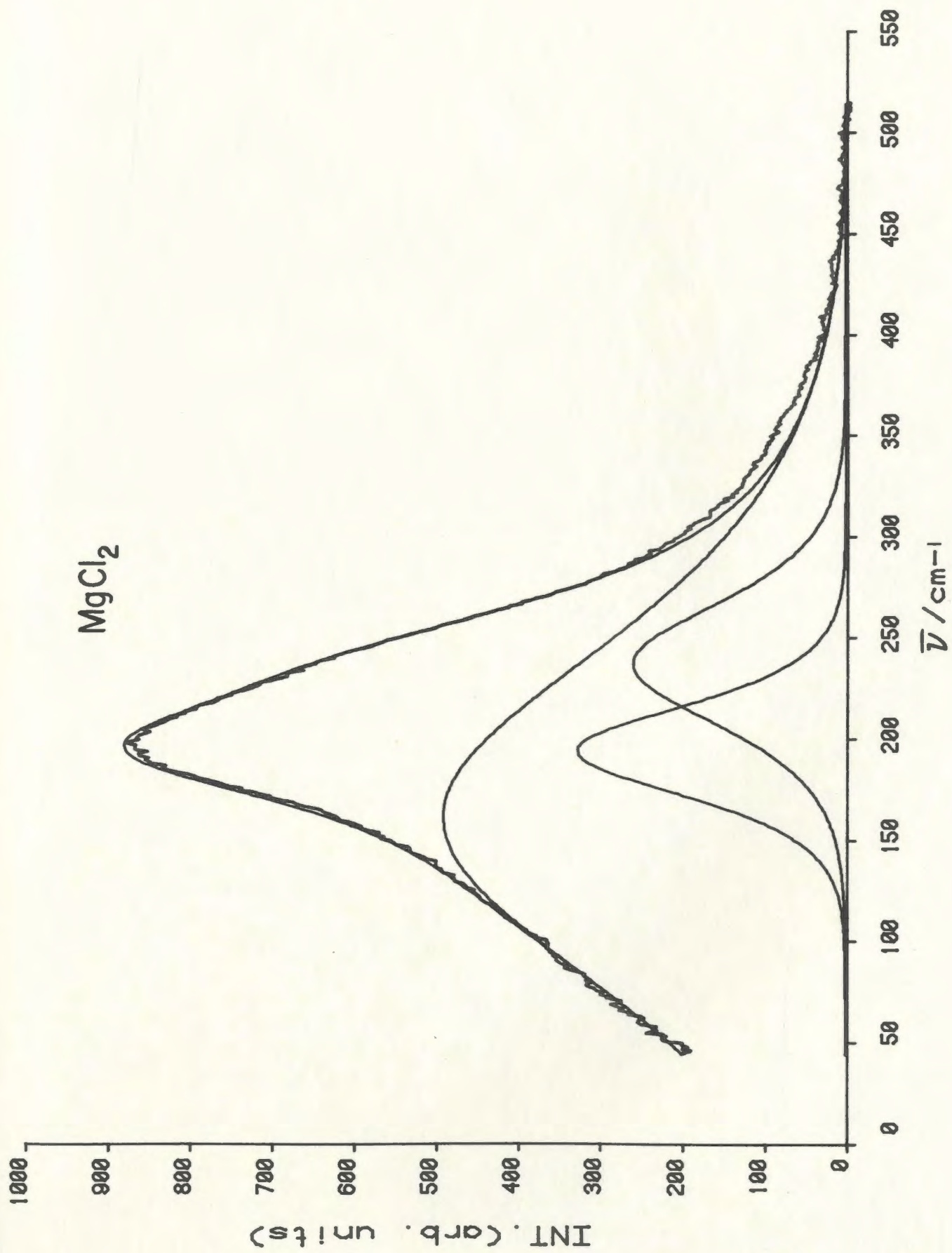


Figure 71. Isotropic Raman spectra of molten MgCl_2 . The smooth line is the best-fit curve calculated as a sum of three Gaussian*Lorentzian functions.



system the smaller K^+ ion results in greater environmental broadening. The peak resolved around $\sim 250 \text{ cm}^{-1}$ is attributed to the ν_1 mode of the $MgCl_4^{2-}$ ions while the ones resolved around ~ 220 and 300 cm^{-1} are attributed to the $Mg_2Cl_7^{3-}$ ions. The polarized peak resolved at 137 cm^{-1} in $KCl:MgCl_2$ (0.5:1) melt corresponds to the counterparts resolved at 161 and 145 cm^{-1} in $MgCl_2$ and $CsCl:MgCl_2$ (0.5:1) melts and attributed to polynuclear species of positive or neutral ions. The Raman data suggest that the $KCl:MgCl_2$ (0.5:1) melt contains a mixture of $MgCl_4^{2-}$ ions, $Mg_2Cl_7^{3-}$ ions, and $Mg_2Cl_n^{4-n}$ species. The synthetic and experimental spectra are shown in figures 76, 77, 78 and 79, and the curve resolution data are shown in Table 27.

4.3.3. Effect of temperature on the spectra of $CsMgCl_3$ and K_2MgCl_4 Melts

It was reported¹⁴ that the intensity of the polarized peak, estimated at 225 cm^{-1} and attributed to polynuclear species, decreased by increasing the temperature i.e. the intensity ratio I_{225}/I_{250} is decreasing by increasing the temperature. This decrease in intensity ratio by increasing the temperature was attributed to the breaking of the polynuclear species and the formation of more $MgCl_4^{2-}$ species.

The spectra of $CsMgCl_3$ melt were obtained at 899, 1054 and 1153 K, and it appears that the intensity of the peak due to $Mg_2Cl_7^{3-}$ ions does decrease with increasing the temperature, see figures 80, 81 and 82, Table 28. The spectra of K_2MgCl_4 melt are studied at 973 and 1143 K. Again the data indicate the breaking of the polynuclear species and the formation of more $MgCl_4^{2-}$ ions. The spectra are shown in figures 83 and 84. The results of the curve resolution analysis for $CsMgCl_3$ and K_2MgCl_4 at different temperatures are shown in Table 28.

Table 27. Summary of results of curve resolution analysis for
MgCl₂-KCl Melts.

Compound	Frequency (cm ⁻¹)	Intensity	Half band width (cm ⁻¹)	Assignments
K ₂ MgCl ₄	219.4	132	50.1	(ν) Mg ₂ Cl ₇ ³⁻
	247.5	357	40.4	(ν ₁) MgCl ₄ ²⁻
	296.3	21	44.8	(ν) Mg ₂ Cl ₇ ³⁻
KCl:MgCl ₂ (1.5:1)	227.9	361	93.5	(ν) Mg ₂ Cl ₇ ³⁻
	248.5	194	46.4	(ν ₁) MgCl ₄ ²⁻
	299.4	33	61.9	(ν) Mg ₂ Cl ₇ ³⁻
KMgCl ₃	220.7	276	77.2	(ν) Mg ₂ Cl ₇ ³⁻
	249.4	123	44.9	(ν ₁) MgCl ₄ ²⁻
	293.1	24	81.7	(ν) Mg ₂ Cl ₇ ³⁻
KCl:MgCl ₂ (0.5:1)	137.8	96	236.7	(ν) polynuclear species
	212.9	216	60.6	(ν) Mg ₂ Cl ₇ ³⁻
	244.2	218	69.1	(ν ₁) MgCl ₄ ²⁻
	295.0	5	20.0	(ν) Mg ₂ Cl ₇ ³⁻

Figure 72. Raman spectra of molten K_2MgCl_4 at 1049 K,
 $I_{||}$ and I_{\perp} .

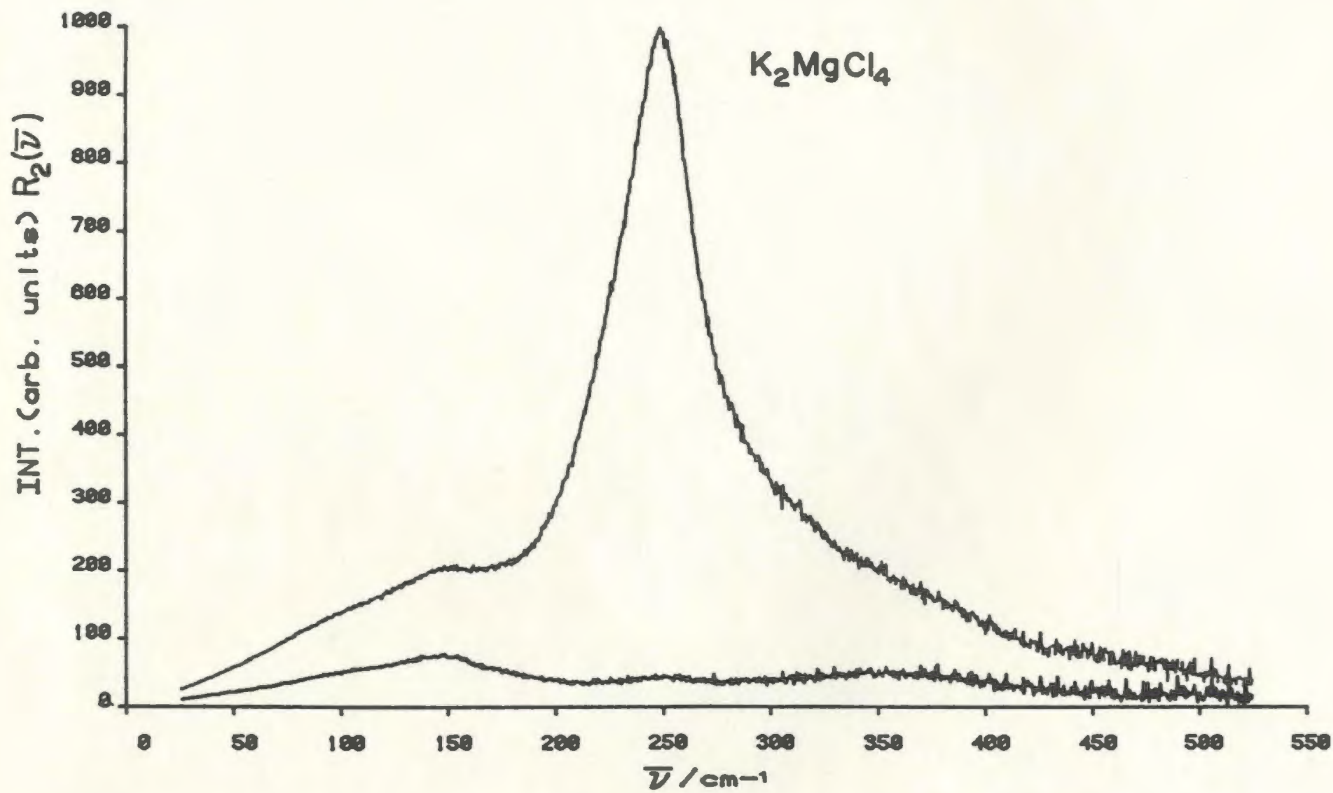
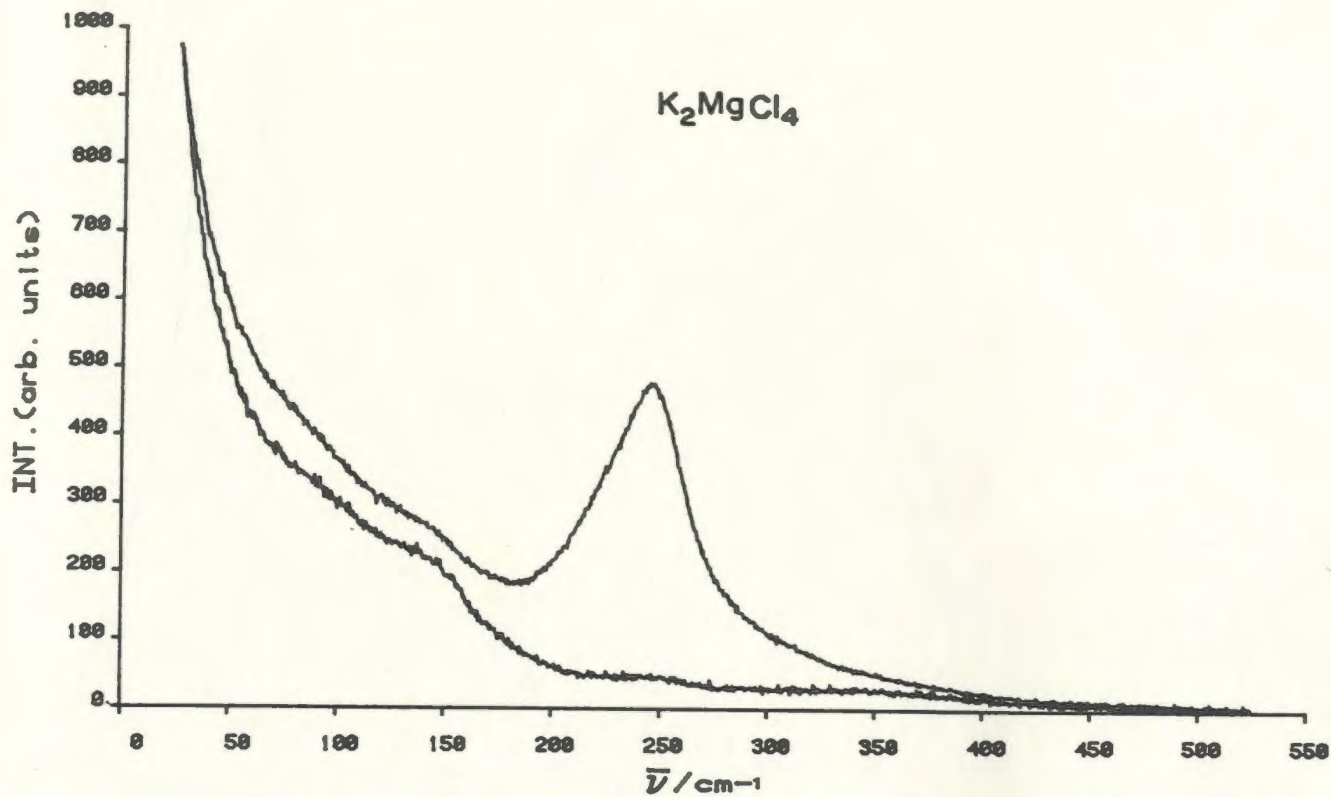


Figure 73. Raman spectra of molten KCl:MgCl_2 (1.5:1) at
1049 K, $I_{||}$ and I_{\perp} .

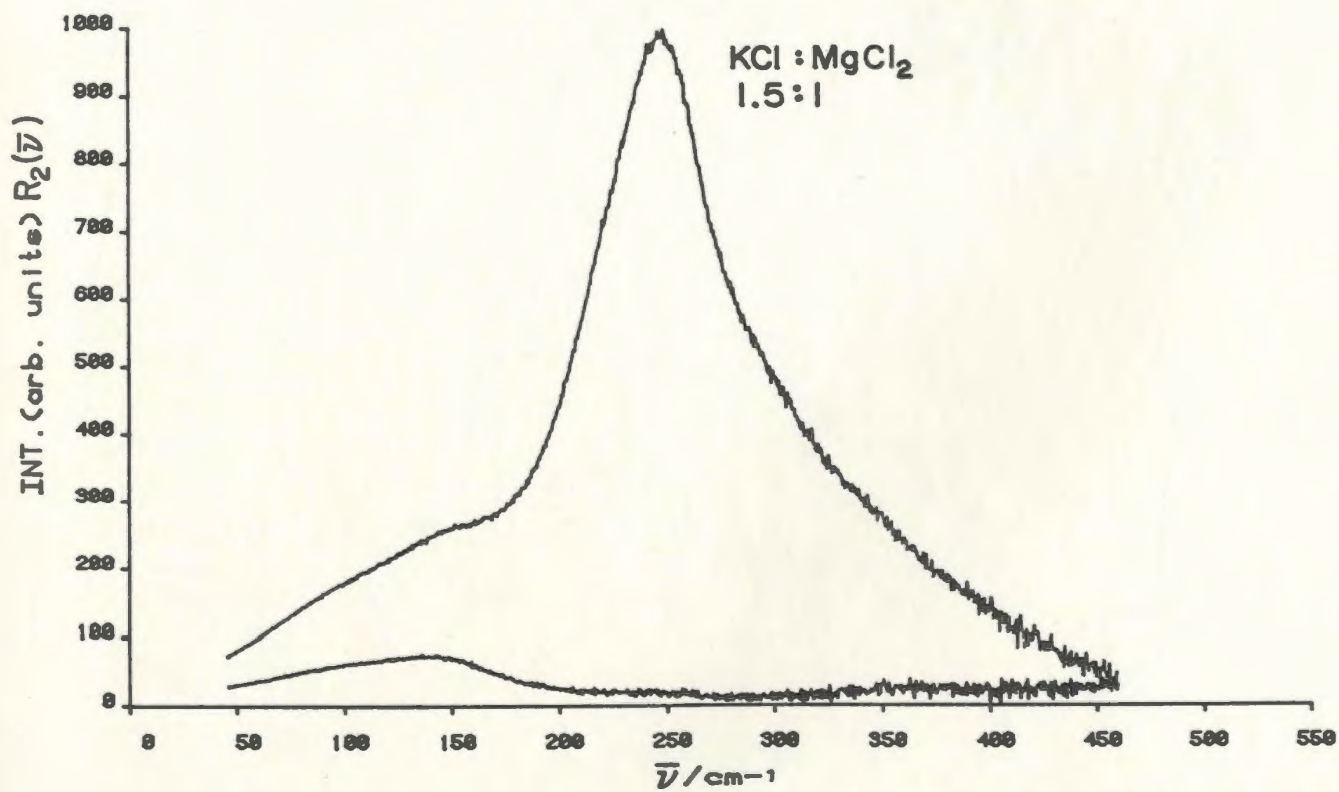
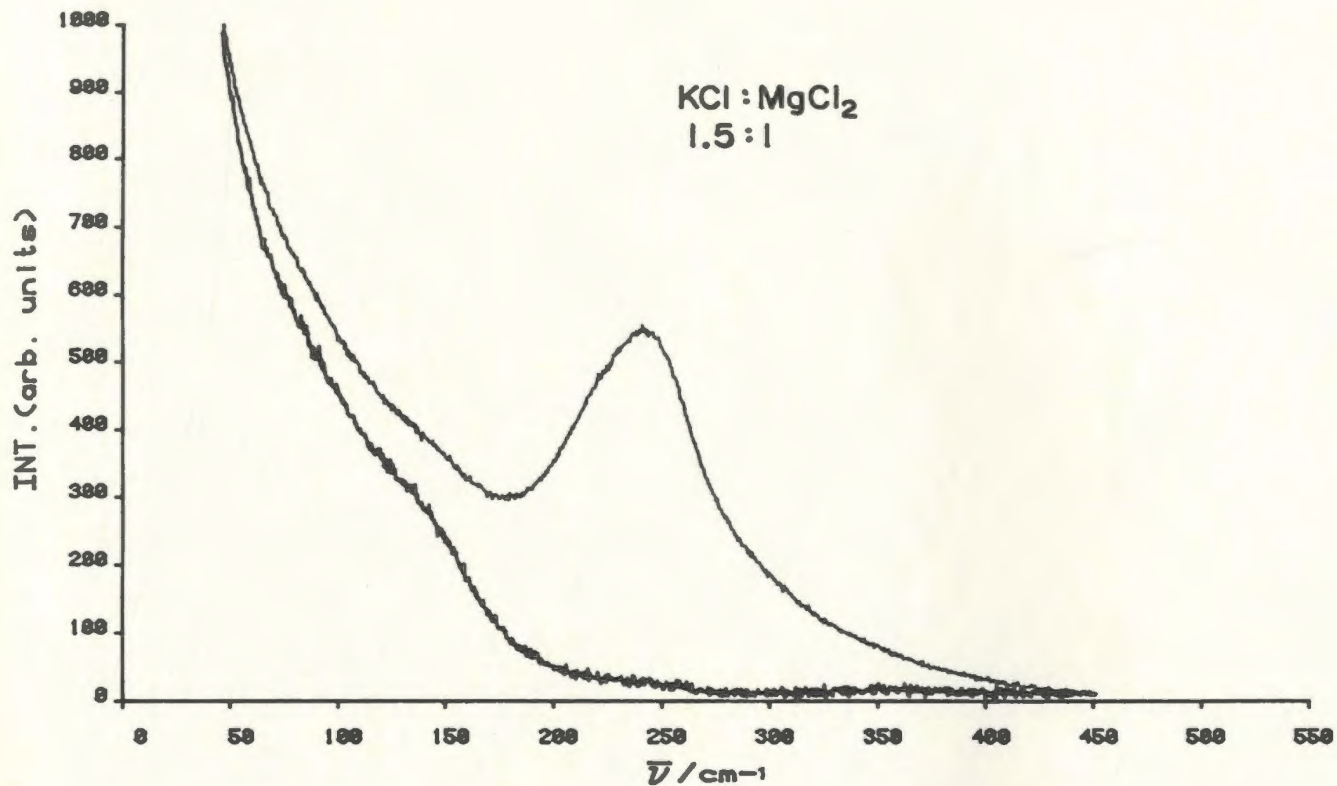


Figure 74. Raman spectra of molten KMgCl_3 at 1049 K,

$I_{||}$ and I_{\perp} .

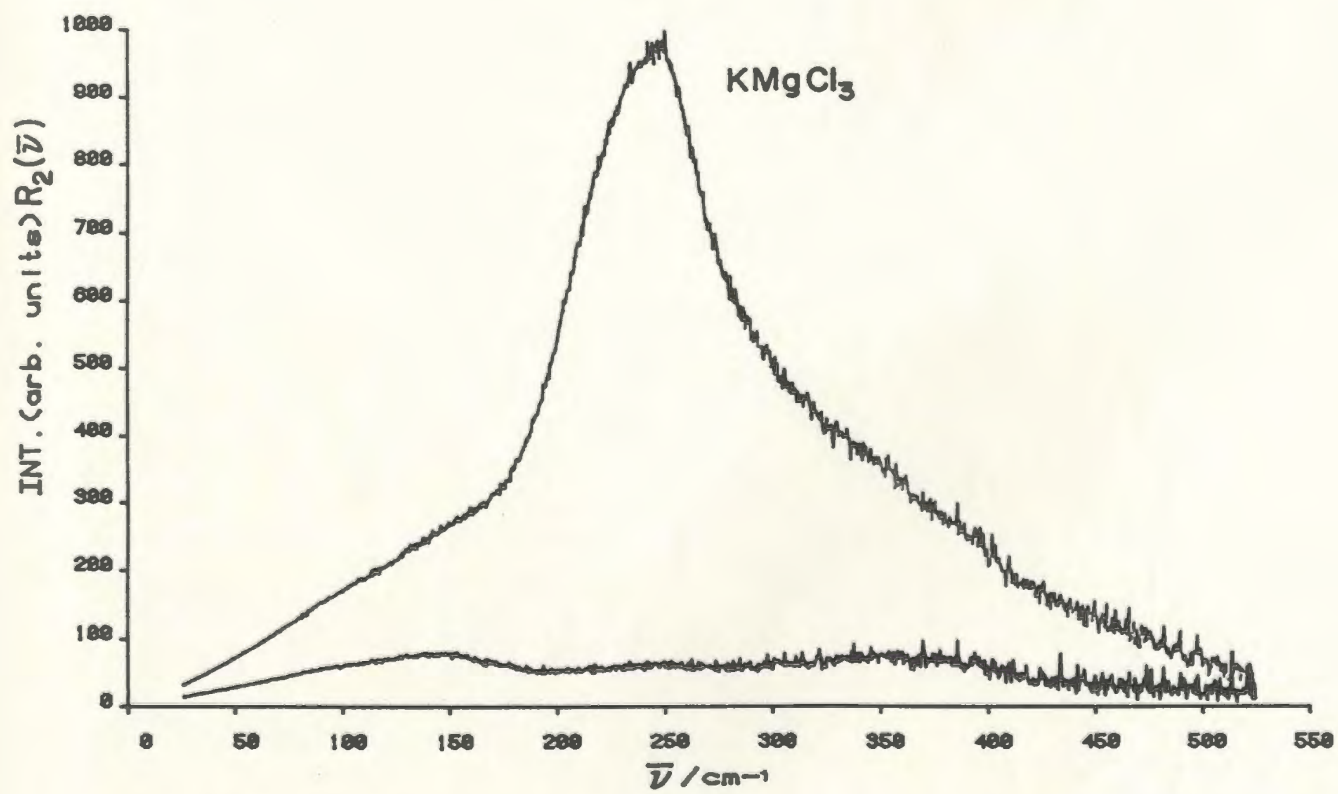
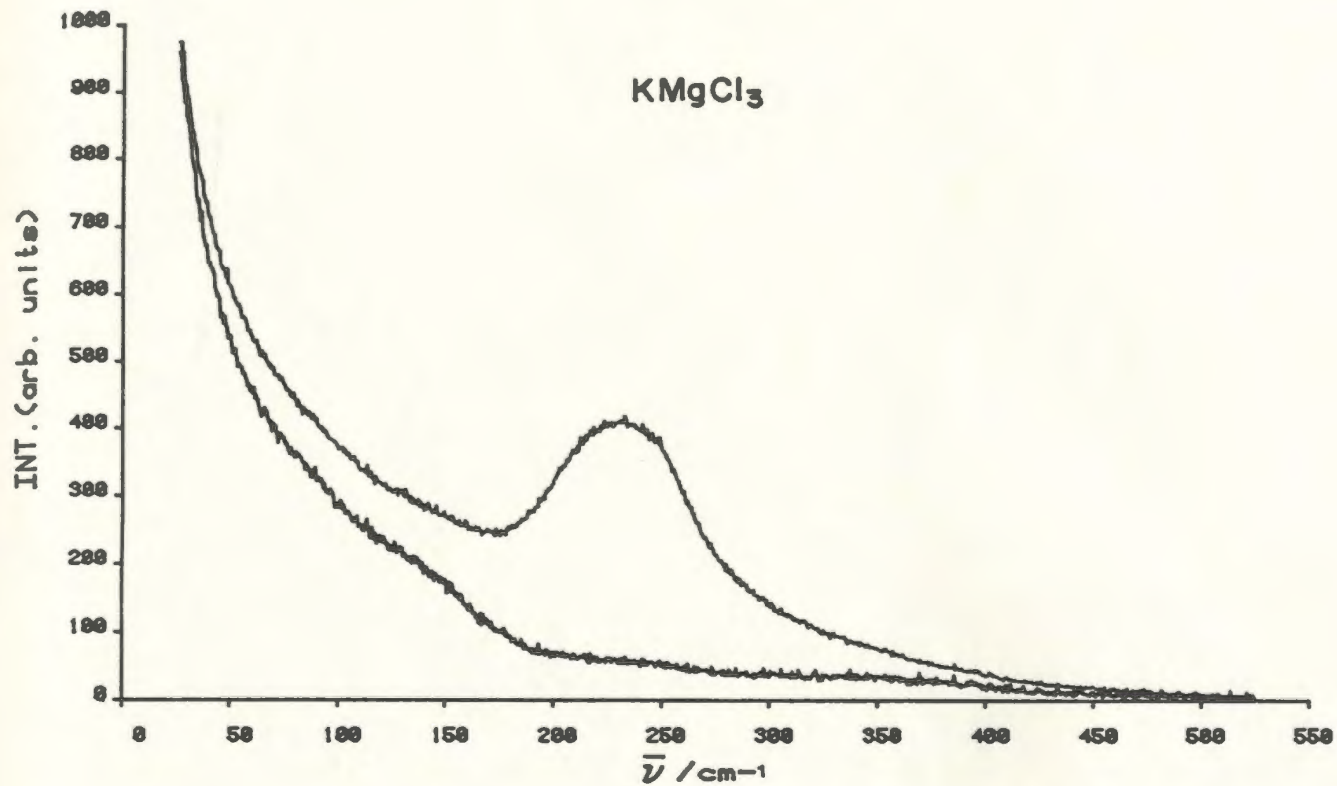


Figure 75. Raman spectra of molten KCl:MgCl_2 (0.5:1) at 1049 K, $I_{||}$ and I_{\perp} .

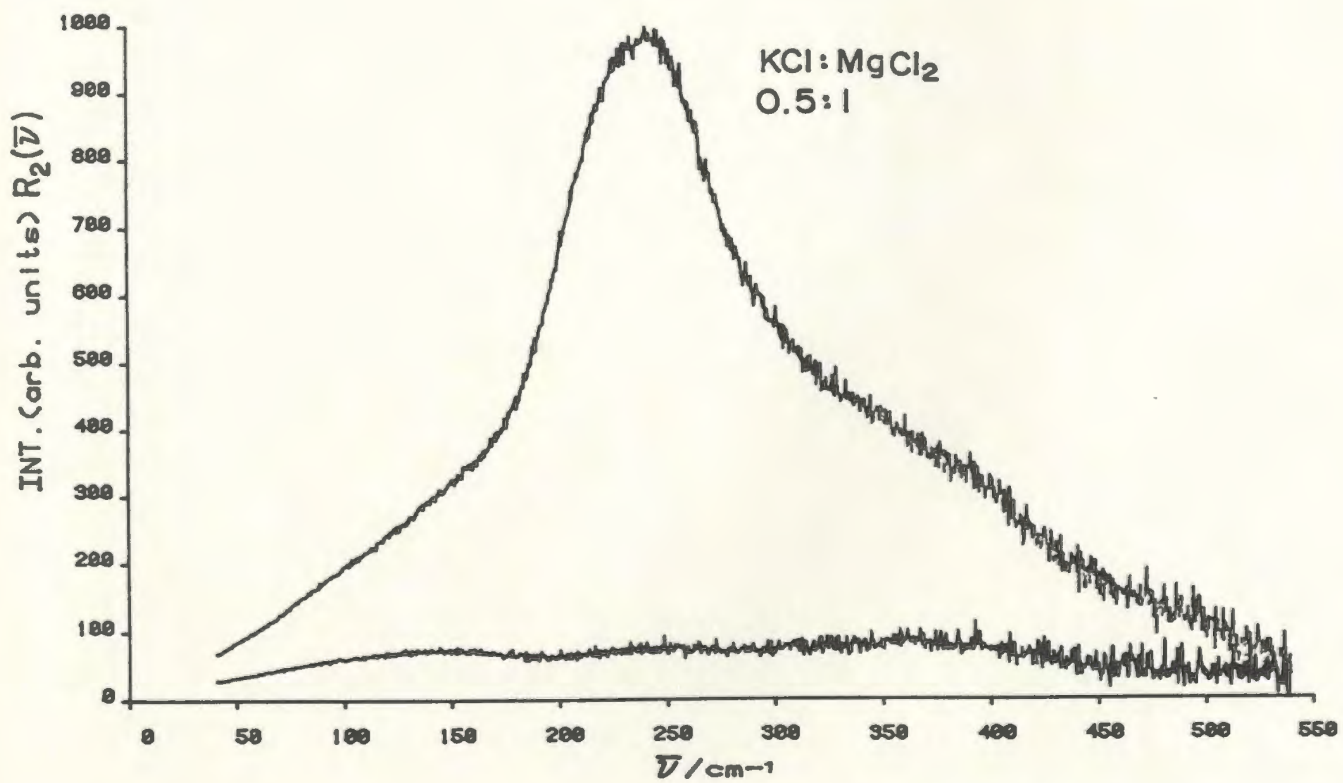
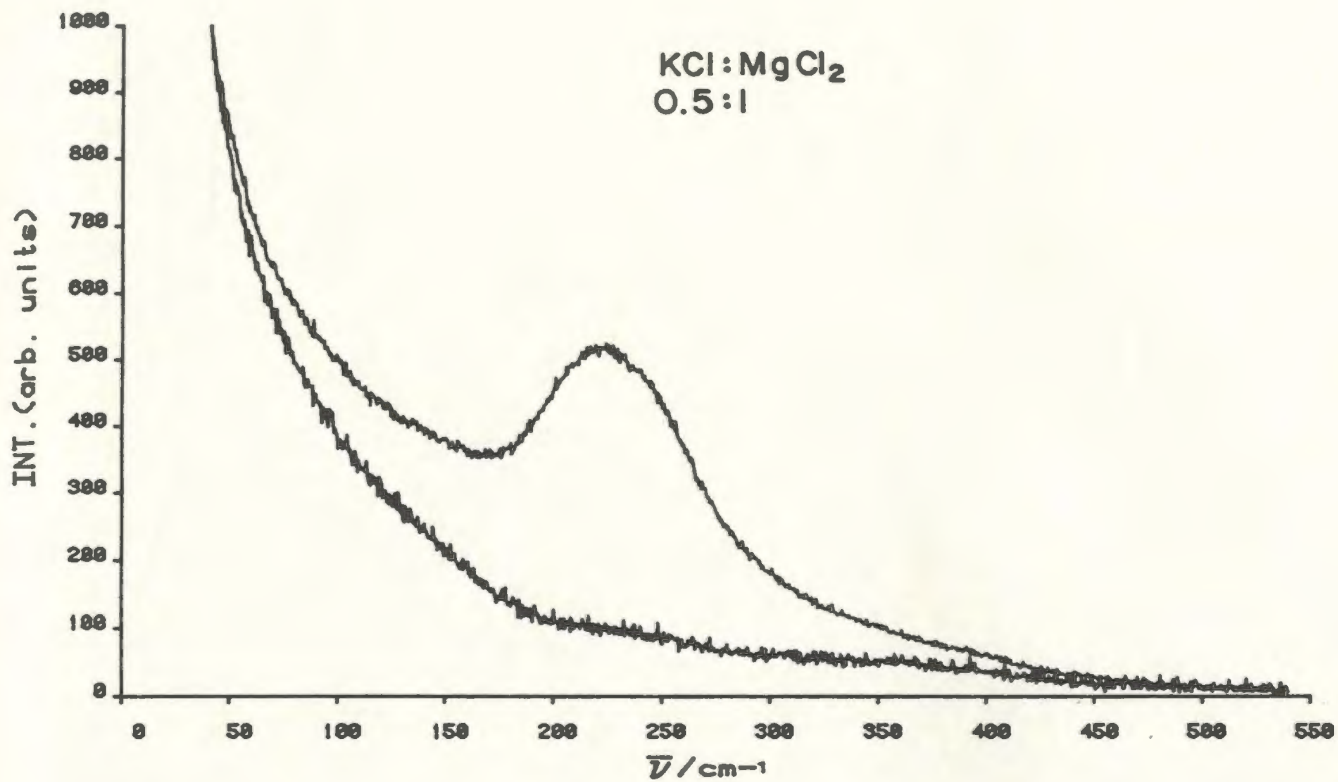


Figure 76. Isotropic Raman spectra of molten K_2MgCl_4 . The smooth line is the best-fit curve calculated as a sum of three Lorentzian functions.

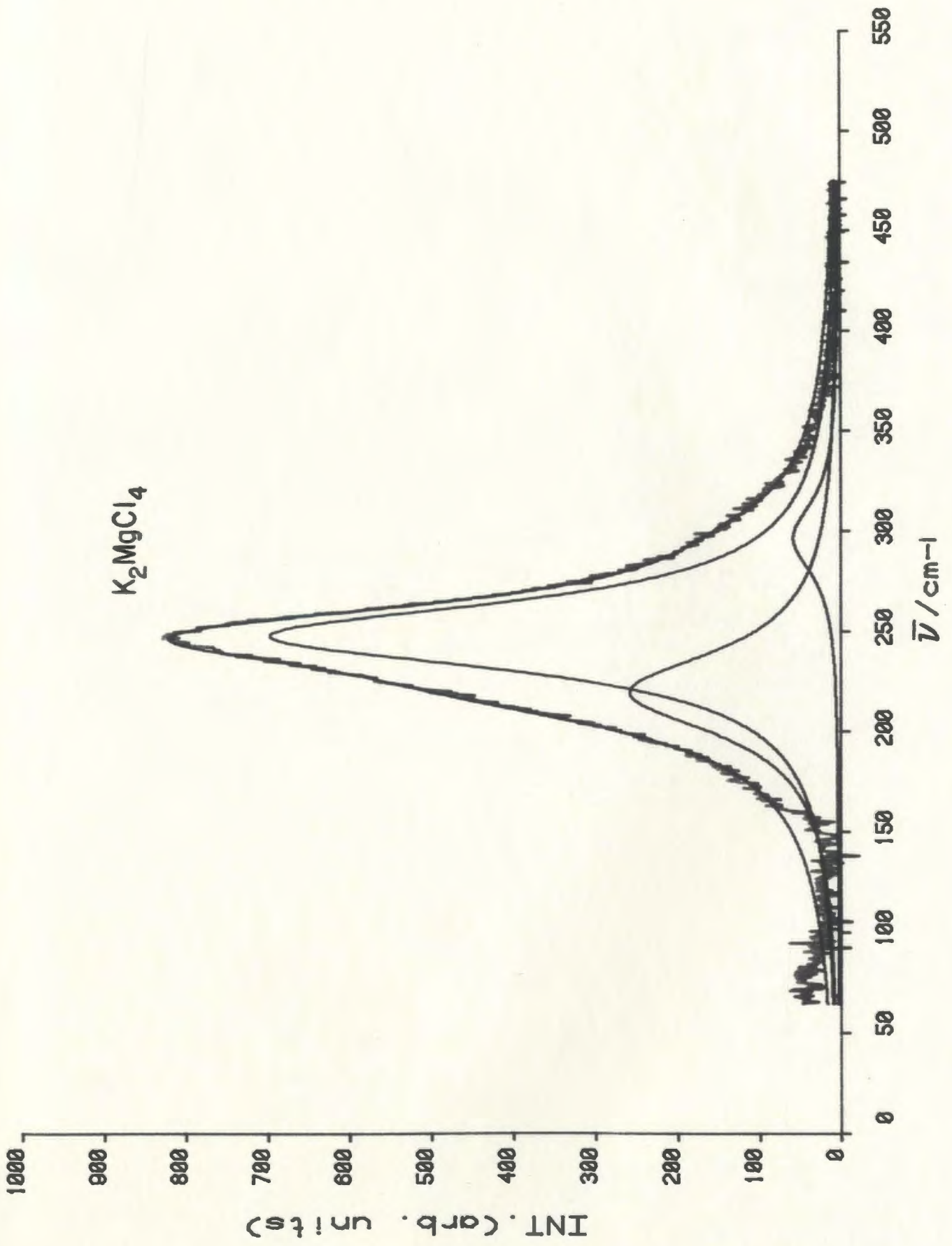


Figure 77. Isotropic Raman spectra of molten $\text{KCl}:\text{MgCl}_2$ (1.5:1).
The smooth line is the best-fit curve calculated as
a sum of three Lorentzian functions.

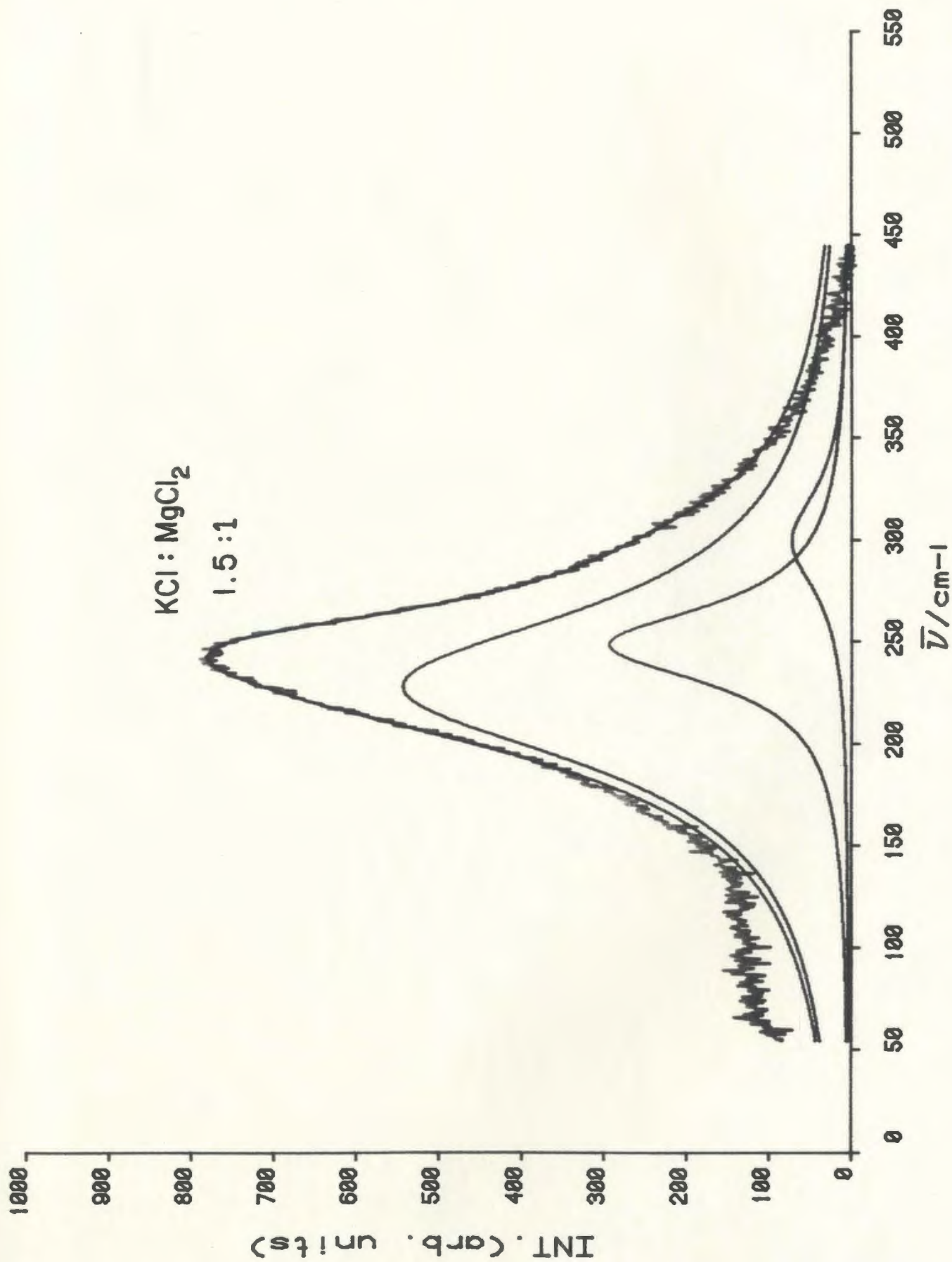


Figure 78. Isotropic Raman spectra of molten KMgCl_3 . The smooth line is the best-fit curve calculated as a sum of three Lorentzian functions.

KMgCl3

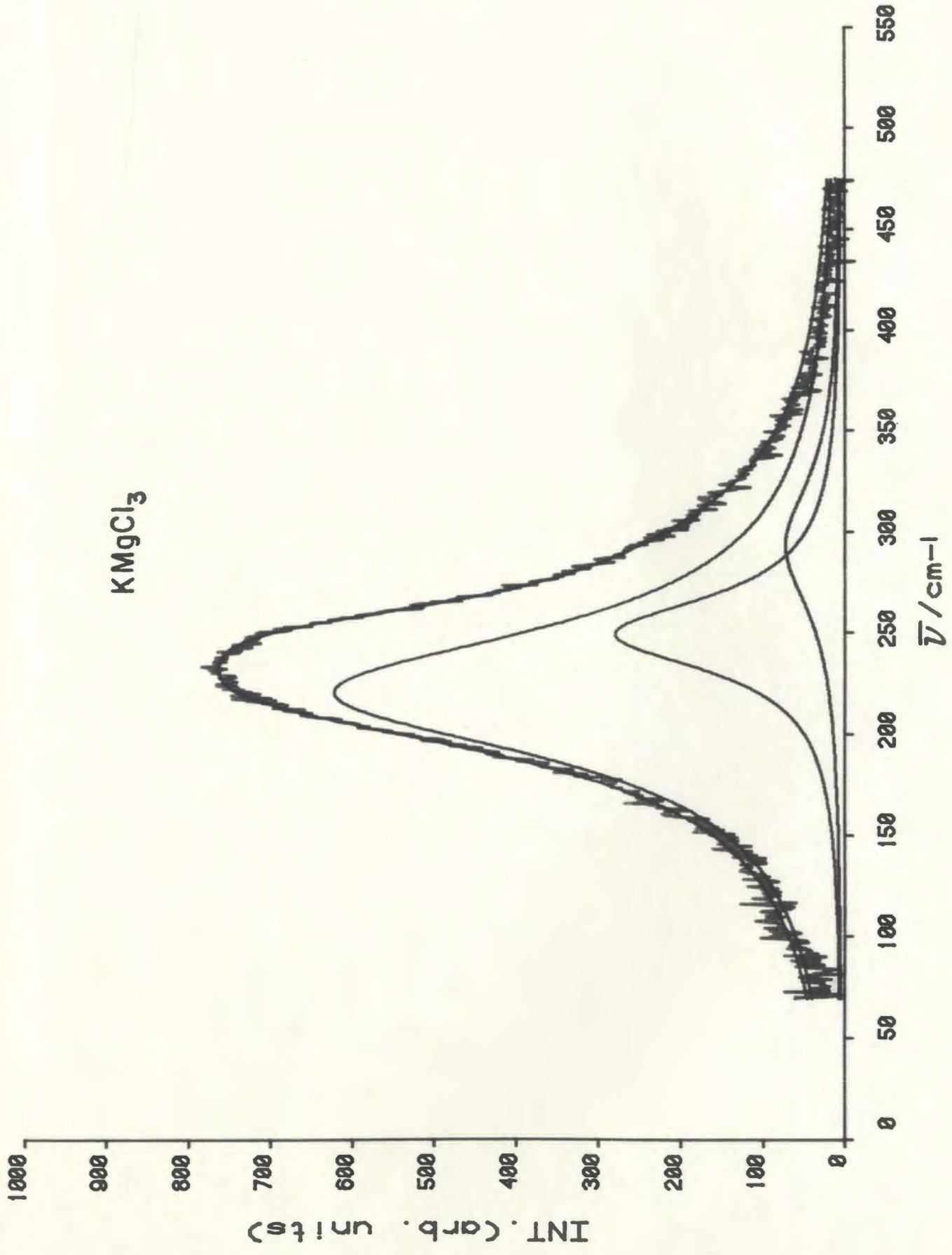


Figure 79. Isotropic Raman spectra of molten $\text{KCl}:\text{MgCl}_2$ (0.5:1).
The smooth line is the best-fit curve calculated as
a sum of four Lorentzian functions.

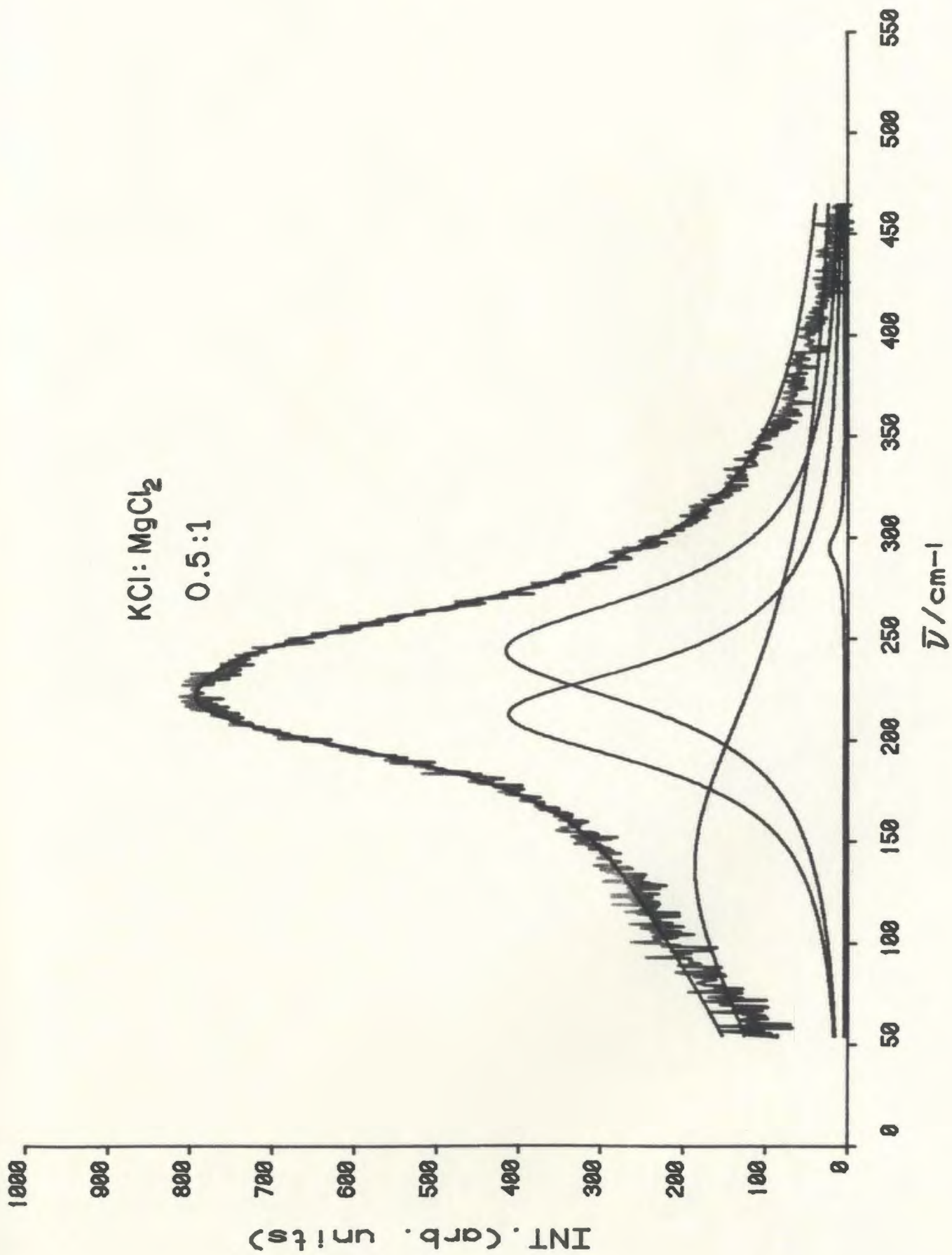


Table 28. Summary of results of curve resolution analysis for CsMgCl₃ and K₂MgCl₄ Melts.

Compound	Temperature (K)	Frequency (cm ⁻¹)	Intensity	Half band width (cm ⁻¹)	Intensity ratio
CsMgCl ₃	899	216.6	241	61.5	$\frac{I_{216} \times \Gamma_{216}}{I_{247} \times \Gamma_{247}}$ = 1.98
		247.7	178	42.1	
	1054	212.5	181	63.9	$\frac{I_{212} \times \Gamma_{212}}{I_{245} \times \Gamma_{245}}$ = 1.26
		245.5	178	51.5	
	1153	209.0	124	63.0	$\frac{I_{209} \times \Gamma_{209}}{I_{243} \times \Gamma_{243}}$ = 0.84
		243.3	161	58.1	
K ₂ MgCl ₄	973	225.3	146	54.7	$\frac{I_{225} \times \Gamma_{225}}{I_{249} \times \Gamma_{249}}$ = 0.72
		249.1	323	34.3	
	1143	218.7	54	69.1	$\frac{I_{218} \times \Gamma_{218}}{I_{246} \times \Gamma_{246}}$ = 0.68
		246.4	121	45.3	

Figure 80. Isotropic Raman spectra of molten CsMgCl_3 at 899 K. The smooth line is the best-fit curve calculated as a sum of three Lorentzian functions.

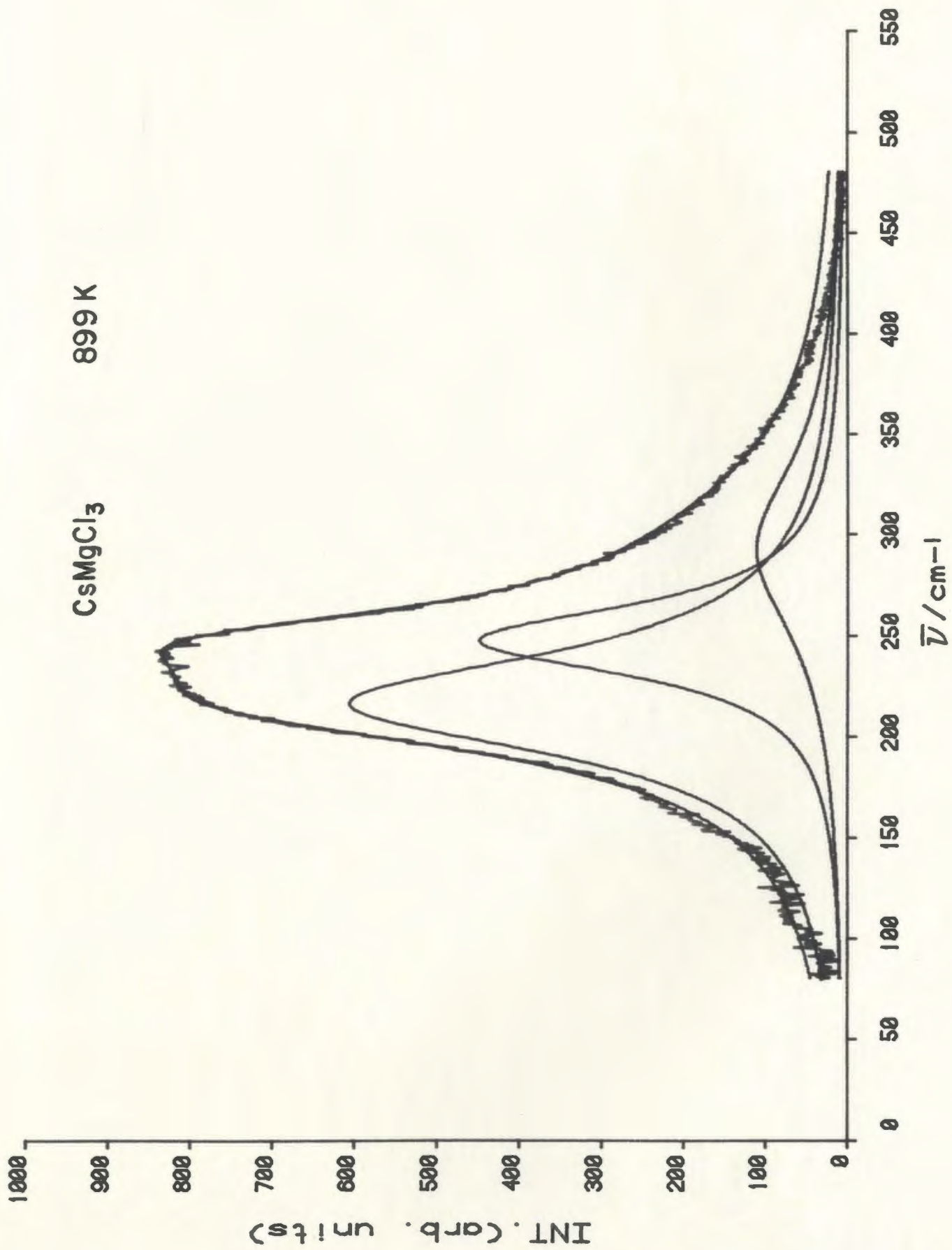


Figure 81. Isotropic Raman spectra of molten CsMgCl_3 at 1054 K. The smooth line is the best-fit curve calculated as a sum of three Lorentzian functions.

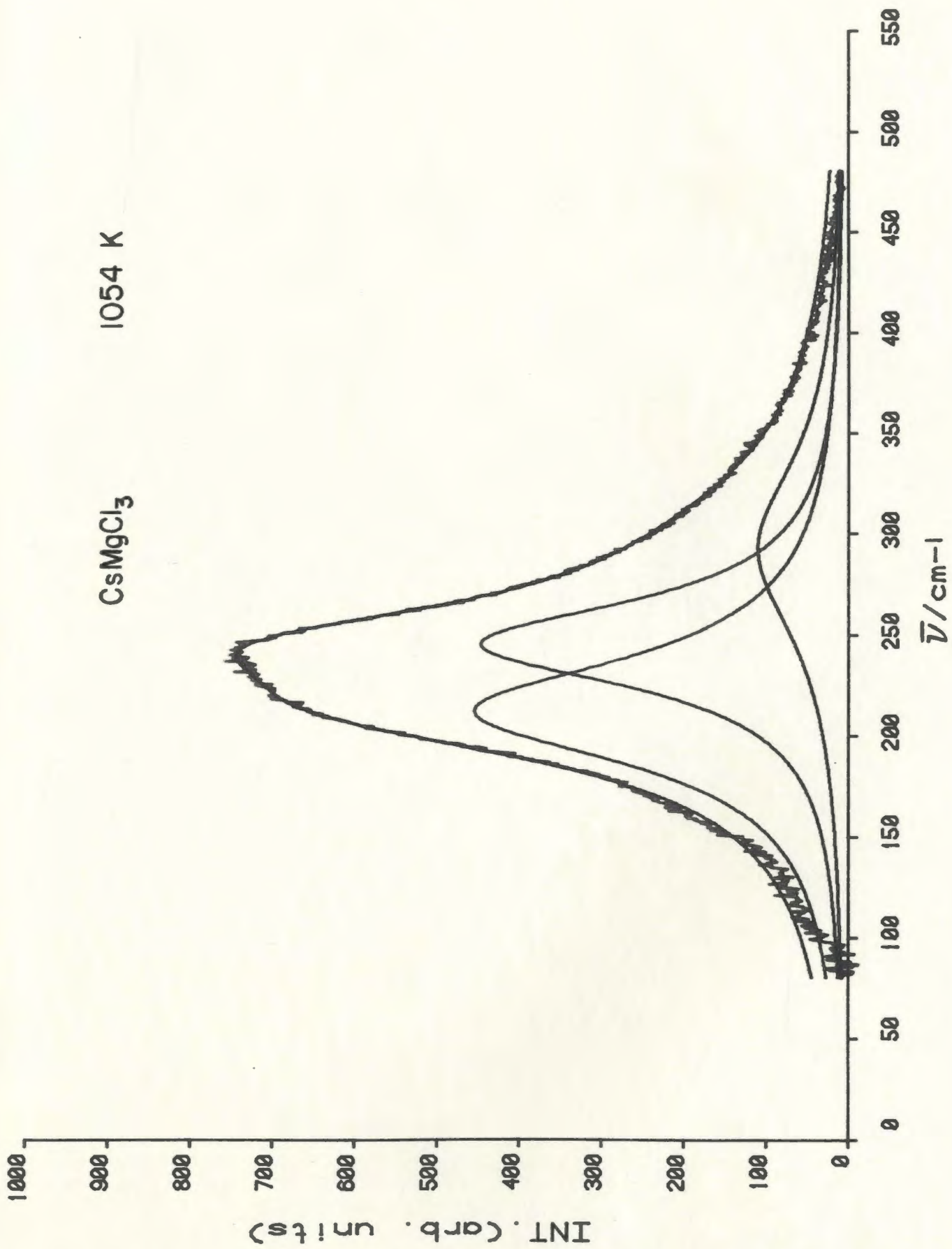


Figure 82. Isotropic Raman spectra of molten CsMgCl_3 at 1153 K. The smooth line is the best-fit curve calculated as a sum of three Lorentzian functions.

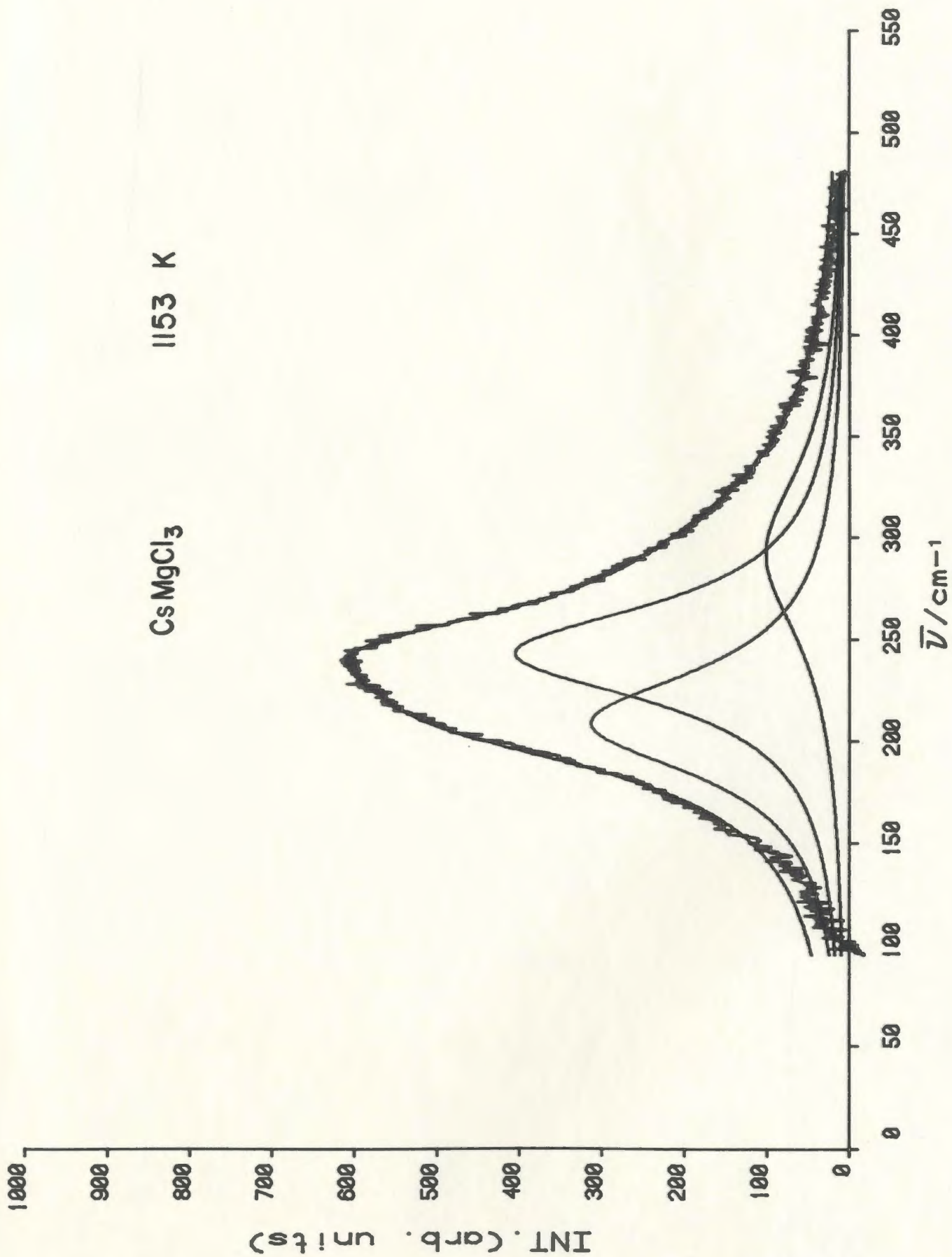


Figure 83. Isotropic Raman spectra of molten K_2MgCl_4 at 973 K.
The smooth line is the best-fit curve calculated as
a sum of three Lorentzian functions.

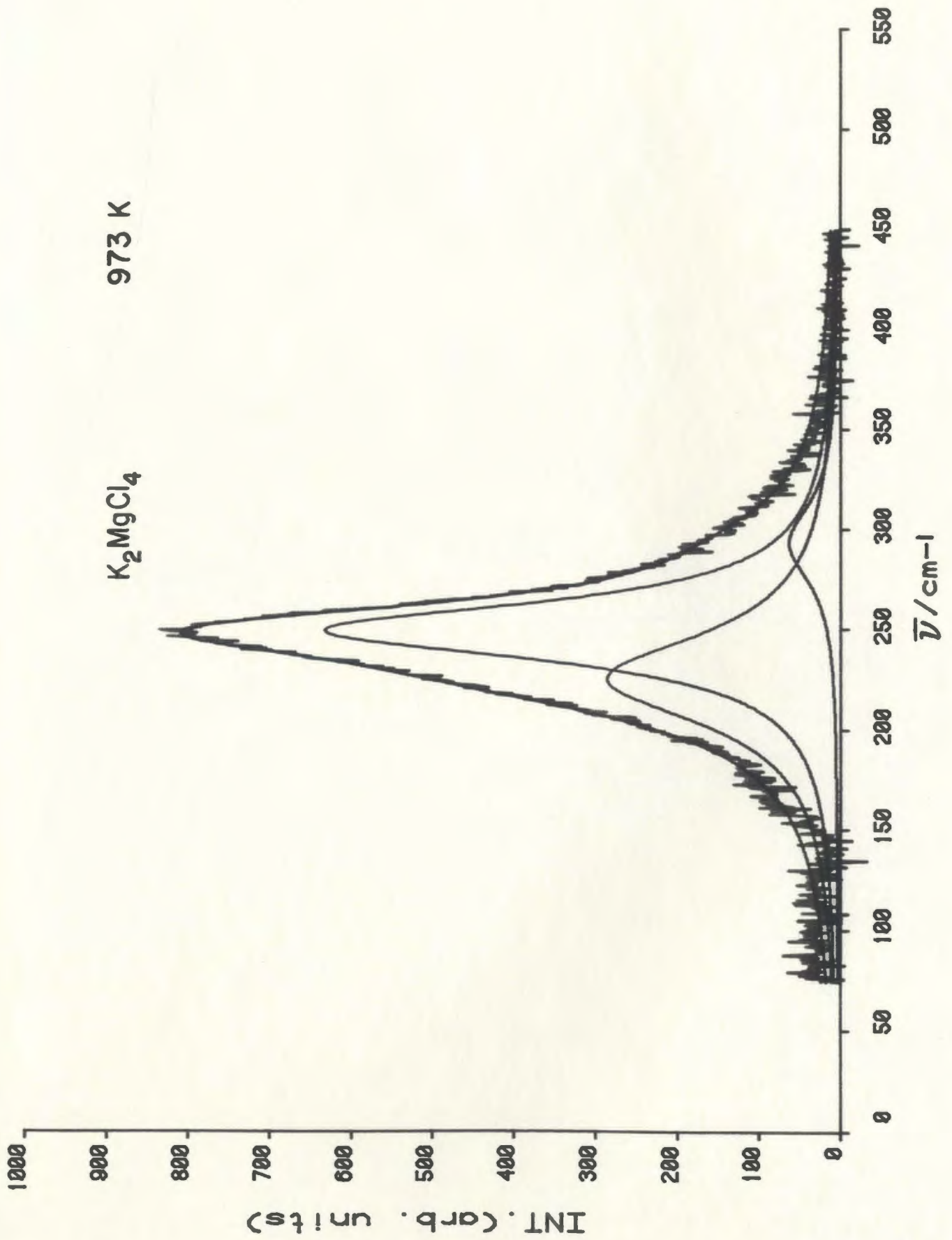
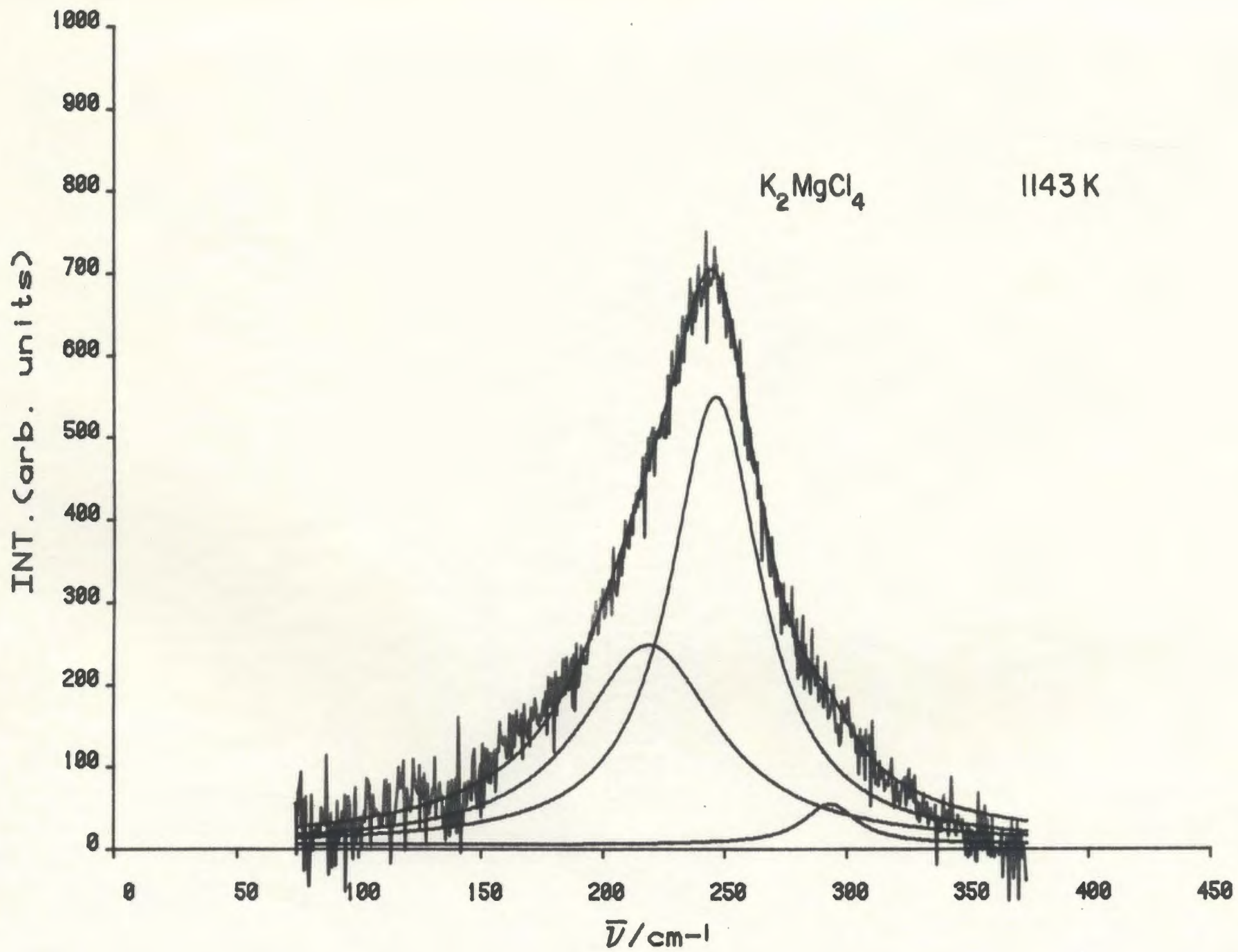


Figure 84. Isotropic Raman spectra of molten K_2MgCl_4 at 1143 K. The smooth line is the best-fit curve calculated as a sum of three Lorentzian functions.



4.3.4 Comparison of Results for MgCl₂ and MnCl₂ systems

The Raman spectra of MnCl₂ and MnCl₂-ACl melts indicated that the MnCl₄²⁻ species is the predominant species in melts of composition MnCl₂.nACl (n ≤ 2), and melts of higher MnCl₂ concentration most probably contain a rapid equilibrium between MnCl₄²⁻ and Mn₂Cl₇³⁻ and perhaps octahedral MnCl₆⁴⁻. The coordination number is not well defined because the exchange lifetime for Cl⁻ in the Mn²⁺ coordination sphere is short and near the Raman detection limit. Only one band was observed due to the Mn-Cl stretching vibration averaged over all coordinations and broadened by the wide range of environmental arrangements and Cl⁻ exchange. The Raman results of MgCl₂, MgCl₂-CsCl and MgCl₂-KCl melts indicate that the MgCl₄²⁻ ions are the predominant species in these melts. However, by increasing the concentration of MgCl₂ the polynuclear species Mg₂Cl₇³⁻ is formed, and for a further increment of MgCl₂ concentration a third species is detected and attributed to polynuclear Mg₂Cl_n⁴⁻ⁿ species. In contrast to the MnCl₂ system, the MgCl₂ system contains species that are long-lived enough to distinguish spectroscopically.

4.4 Visible Spectra of $MnCl_2 \cdot nACl$

The ground state^{78,79} of Mn^{+2} ion has five unpaired d-electrons, so the multiplicity for the ground level $2S + 1 = 2(\frac{5}{2}) + 1 = 6$ i.e. the ground state has spin sextuplet. The ground state of the free ion has no spacial degeneracy and it has the symbol 6S . Besides the ground state 6S , Mn^{+2} ion has excited states, four quartet terms 4G , 4P , 4D and 4F , and a number of doublet terms. The doublet states are of high energy and transition to them from the sextuplet ground state can only be observed at very low temperature in very thick crystals. The terms of the free ion and the splitting terms for Mn^{+2} ion in octahedral field are shown (Table 29). These terms can be applied in a tetrahedral field if the g subscripts are dropped, because T_d symmetry has no center of inversion and so the electronic states have no longer g or u character⁸⁶.

The spectrum of $Mn(H_2O)_6^{2+}$ has been measured by Heidt et. al.⁸⁰, Jorgensen⁸¹ and Orgel⁸². The characteristic band positions and assignments of Heidt et. al. are shown in Table 30. Compounds which contain the octahedrally coordinated Mn^{2+} exhibit a characteristic pale red color as a consequence of weak absorption in the 17000 to 20000 cm^{-1} region. Studies⁸³⁻⁸⁵ of the absorption spectra of solid manganese halide crystals indicated the presence of octahedrally coordinated Mn^{2+} . The diffuse reflectance spectrum of $MnCl_2$ has been reported by Clark⁸³ and assignments were similar to those proposed by Stout^{84,85} for manganese halides.

The absorption spectra of tetrahalogenomanganate (II) salts of onium cations have been studied⁸⁶ in nonaqueous polar solvents. It was noted that when these salts dissolved in polar solvents, a slightly yellow color was observed which is due to the anion $[MnX_4]^{2-}$. The

Table 29. Splitting of the sextet and quartet terms of a d^5 ion in octahedral field.

$6S$	$6A_{1g}$			
$4P$	$4T_{1g}$			
$4D$	$4E_g$	$4T_{2g}$		
$4F$	$4A_{2g}$	$4T_{1g}$	$4T_{2g}$	
$4G$	$4A_{1g}$	$4E_g$	$4T_{1g}$	$4T_{2g}$

Table 30. Absorption spectrum of $\text{Mn}(\text{H}_2\text{O})_6^{2+}$.

Band positions (cm^{-1})	Assignments
18870	${}^6\text{A}_{1g}({}^6\text{S}) \rightarrow {}^4\text{T}_{1g}({}^4\text{G})$
23120	$\rightarrow {}^4\text{T}_{2g}({}^4\text{G})$
24960	$\rightarrow {}^4\text{E}_g, {}^4\text{A}_{1g}({}^4\text{G})$
25275	
27980	$\rightarrow {}^4\text{T}_{2g}({}^4\text{D})$
29750	$\rightarrow {}^4\text{E}_g({}^4\text{D})$
32960	$\rightarrow {}^4\text{T}_{1g}({}^4\text{P})$
40810	$\rightarrow {}^4\text{A}_{2g}({}^4\text{F})$

observed spectra of the solutions were identical in all solvents and independent of the cation and similar to the reflexion spectra of the solid salts. Three distinct absorption regions were observed in the range 20000 to 38000 cm^{-1} , where ten transitions are expected.

Tetrahedral coordination of Mn^{2+} ion was proposed.

The absorption spectra⁸⁷ of tetrahalomanganate (II) ions $[\text{MnX}_4]^{2-}$, $\text{X} = \text{Cl}, \text{Br}, \text{I}$ have been studied in the solid state and in various solvents at 25°C. It was reported that the tetrahedral manganese (II) complex has a pale green, yellow or yellow-green color, and the larger crystals have a marked color while the very fine powders often appear practically colorless. Three absorption patterns were observed in the spectra of $[\text{MnBr}_4]^{2-}$ ion in the region 20000 to 38000 cm^{-1} . Three absorption bands were observed in the range 20000 to 25000 cm^{-1} and attributed to transitions to the states originating from the ^4G term of the free ion. A group of three absorptions was found in the range 25000 to 28000 cm^{-1} arising from the ^4D and ^4P terms. A third set of three bands was expected in the region 36000 to 38000 cm^{-1} due to transitions to the states arising from the ^4F term, but these transitions were less easily observed than the two previous patterns because they appear in a region where solvent absorption and absorption due to some organic groups of the cation. The peak positions and assignments for $[\text{MnCl}_4]^{2-}$ and $[\text{MnBr}_4]^{2-}$ are shown in Table 31.

The absorption spectra of MnCl_2 in LiCl-KCl eutectic at 436°C and MnBr_2 in LiBr-KBr eutectic at 457°C have been investigated⁸⁸. Two peaks were observed in both spectra around 360 millimicrons (27777 cm^{-1}) and 440 millimicrons (22727 cm^{-1}). It was concluded that Mn(II) ion in both the chloride and bromide melts is tetrahedrally coordinated. A

Table 31. Absorption spectra of $[\text{MnBr}_4]^{2-}$ and $[\text{MnCl}_4]^{2-}$.

Band positions (cm^{-1})		Assignments
$[\text{MnBr}_4]^{2-}$	$[\text{MnCl}_4]^{2-}$	
21350	21200	${}^6\text{A}_1({}^6\text{S}) \rightarrow {}^4\text{T}_1({}^4\text{G})$
22180	22400	$\rightarrow {}^4\text{T}_2({}^4\text{G})$
23000	23200	$\rightarrow {}^4\text{E}, {}^4\text{A}_1({}^4\text{G})$
25900	26300	$\rightarrow {}^4\text{T}_2({}^4\text{D})$
26750	27100	$\rightarrow {}^4\text{E}({}^4\text{D})$
27700	27900	$\rightarrow {}^4\text{T}_1({}^4\text{P})$
36150	38000	$\rightarrow {}^4\text{A}_2({}^4\text{F})$
36150		$\rightarrow {}^4\text{T}_1({}^4\text{F})$
37400		$\rightarrow {}^4\text{T}_2({}^4\text{F})$

further investigation⁸⁹ of the absorption spectra of Mn^{2+} ion in LiCl-KCl eutectic at 400 and 1000°C was done by Gruen and McBeth. The spectra were characterized by two absorption bands at ~ 22000 and 28000 cm^{-1} , and attributed to transitions from the 6S ground state to upper 4G , 4P and 4D states. The spectra were in good agreement with the previous work⁸⁸. The results favoured the tetrahedral $MnCl_4^{2-}$ species.

The optical spectra of $[MnX_4]^{2-}$, $X = Cl, Br, I$, were studied⁹⁰ at $160^\circ C$ in the molten state for low melting organic salts. The spectra were similar to the spectra obtained at room temperature by previous authors^{86,87}. The results indicated that the tetrahedral Mn^{2+} ion persisted into the fused salts. Islam⁹¹ investigated the optical spectra of $MnBr_2$ in molten tetra-n-Butyl phosphonium bromide at $112^\circ C$. The solution had a yellowish-green color. The spectra showed two sets of weak resolved peaks in the visible region between 18870 and 28990 cm^{-1} and assigned to $^6S \rightarrow ^4G$, and $^6S \rightarrow ^4P + ^4D$ transitions. A third band was observed in the ultraviolet region and attributed to $^6S \rightarrow ^4F$ transitions. It was suggested that the manganese (II) in molten tetra-n-Butyl phosphonium bromide forms a tetrahedral complex $MnBr_4^{2-}$.

The absorption spectra of $MnCl_2-AlCl_3$ and $MnCl_2-CsCl$ mixtures have been studied²³. The spectra of $MnCl_2$ with $CsCl$ in the concentration range $0 < X_{MnCl_2} \leq 0.33$ were less structured, but the Raman data indicated that the tetrahedral $MnCl_4^{2-}$ was the dominate species. However, the spectra of Mn^{+2} in $MnCl_2-AlCl_3$ melts, $X_{MnCl_2} \leq 0.30$, were attributed to octahedral coordination of Mn^{+2} ion.

The diffuse reflectance spectra⁹² of a number of Manganese (II) compounds in which the metal is surrounded by octahedral and tetrahedral arrangements of halogen atoms have been studied. The compounds included

MnX_2 , $X = Cl, Br, I$, $(MeNH_3)_2MnCl_4$, $\alpha-Cs_2MnCl_4$, K_4MnCl_6 , $KMnCl_3$, Me_4NMnCl_3 and Me_4NMnBr_3 . Also the spectrum of single crystal $MnCl_2$ has been investigated⁹³ at 77°K. Band assignments for $MnCl_2$ are shown in Table 32.

The optical spectra^{94,95} of Mn^{2+} ions in NaCl and KCl single crystals using impurity concentration in the range 0.1 to 15 mole % have been studied at room temperature and at 77°K. The formation of K_4MnCl_6 and $NaMnCl_3$ complexes was thought to be probable at high concentrations, but direct evidence was not presented. Recently^{96,97,98} the optical spectra of Mn^{2+} ions in the Suzuki-phase ($6NaCl:MnCl_2$) have been studied in NaCl. The results indicated that an intense band at 231 nm is characteristic of the Suzuki phase.

4.4.1 Solid state

(i) Cs_2MnCl_4 and Cs_3MnCl_5

The visible spectra of Cs_2MnCl_4 and Cs_3MnCl_5 at room temperature and at 681 K are shown in figures 85,86,87 and 88 respectively. These two compounds exhibit greenish-yellow color at room temperature and at 681 K. The X-ray studies^{64,43} indicated the presence of discrete $MnCl_4^{2-}$ tetrahedral species and Raman studies strongly confirmed the X-ray results.

It has been reported⁹² that the absorption spectra of $\alpha-Cs_2MnCl_4$ is identical in appearance to the spectra of $(CH_3NH_3)_2MnCl_4$ which is pink, and this implicitly suggest that the manganese has an octahedral environment. The Raman results indicate that the red low temperature form of this solid and referred to as $\alpha-Cs_2MnCl_4$ is really a hydrated solid $Cs_2MnCl_4 \cdot 0.16H_2O$. The so called high temperature form referred

Table 32. Electronic spectra of MnCl₂.

Band positions (cm ⁻¹)		Assignments
MnCl ₂ ⁹²	MnCl ₂ ⁹³	
18900	18500	${}^6A_1({}^6S) \rightarrow {}^4T_1({}^4G)$
22220	22000	$\rightarrow {}^4T_2({}^4G)$
23870	23574	$\rightarrow {}^4A_1, {}^4E({}^4G)$
	23800	
27030	27000	$\rightarrow {}^4T_2({}^4D)$
28250	28066	$\rightarrow {}^4E({}^4D)$
30490	30500	$\rightarrow {}^4T_1({}^4P)$
	38400	$\rightarrow {}^4A_2, {}^4T_1({}^4F)$
	40700	$\rightarrow {}^4T_2({}^4F)$

to as $\beta\text{-Cs}_2\text{MnCl}_4$ is the true anhydrous form and has a greenish yellow color.

One absorption pattern was observed at room temperature in both Cs_2MnCl_4 and Cs_3MnCl_5 . The observed peaks are close to the first three bands observed in the reflectance spectra⁸⁷ of $[\text{MnCl}_4]^{2-}$ compounds. One peak is observed at 681 K for both samples, and slightly shifted to lower frequency on comparison to the counterpart observed at room temperature. Both compounds remained greenish-yellow until they melted and there was no evidence to suggest a phase transition. There is a weak peak observed at $\sim 16000 \text{ cm}^{-1}$, and it is most probably due to the presence of Manganese oxide^{99,100} as a slight impurity in the sample. Band positions and assignments are shown in Table 33.

(ii) MnCl_2 , NaMn_4Cl_9 and $\text{Na}_2\text{Mn}_3\text{Cl}_8$

The visible spectra of MnCl_2 , NaMn_4Cl_9 and $\text{Na}_2\text{Mn}_3\text{Cl}_8$ at room temperature are shown in figures 89, 90 and 91 respectively. These compounds exhibit a pink color, and this suggests that they have octahedral environment^{71,68}.

The peak observed in the spectrum of MnCl_2 at $\sim 18089 \text{ cm}^{-1}$ is due to ${}^6\text{A}_{1g}({}^6\text{S}) \rightarrow {}^4\text{T}_{1g}({}^4\text{G})$ transition. A transition from the ground state ${}^6\text{A}_{1g}({}^6\text{S})$ to the excited state ${}^4\text{T}_{2g}({}^4\text{G})$ was reported^{83,84,92,93} to appear around $\sim 22000 \text{ cm}^{-1}$, so this indicate that the shoulder observed at $\sim 19826 \text{ cm}^{-1}$ is probably not real peak. The peak observed at $\sim 16000 \text{ cm}^{-1}$ in the spectrum of $\text{Na}_2\text{Mn}_3\text{Cl}_8$ is most probably attributed to Manganese oxide^{99,100}. Band positions and assignments are shown in Table 34.

Figure 85. A. Upper spectrum is the projection lamp spectrum.
Lower spectrum is the projection lamp plus
sample spectrum.

B. The subtracted spectrum represents the visible
spectrum of Cs_2MnCl_4 at room temperature.

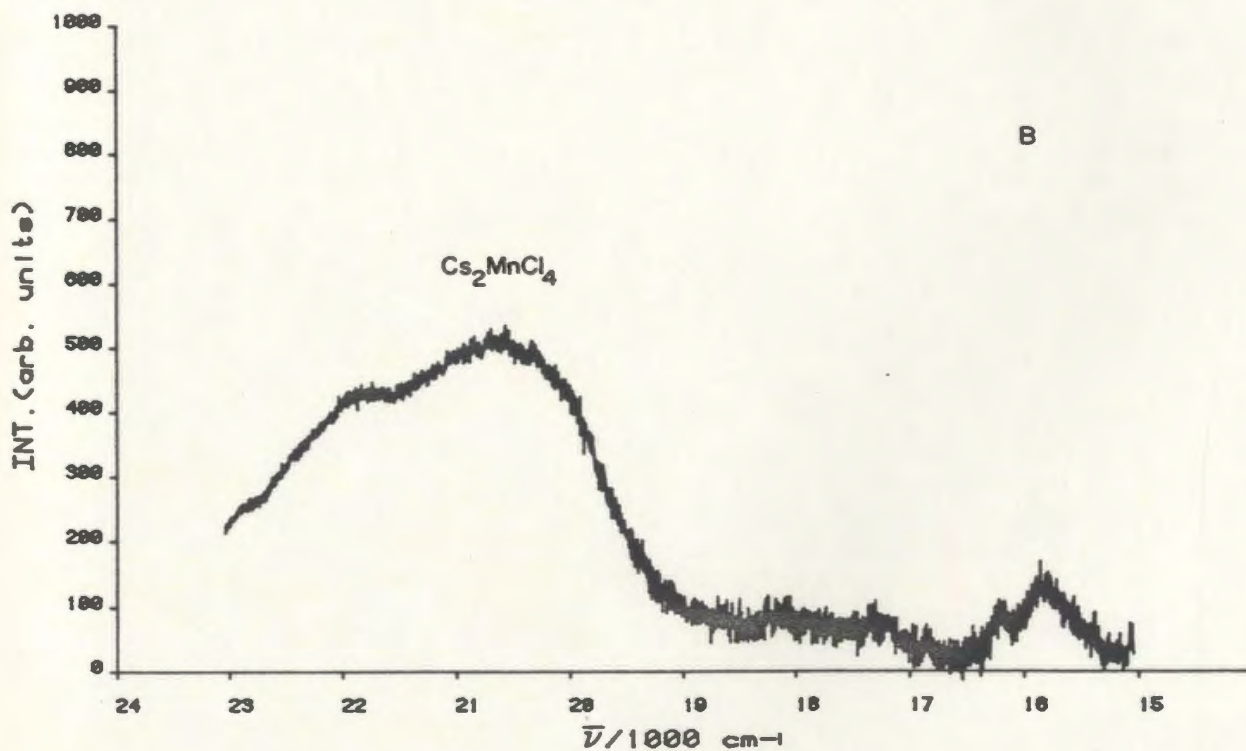
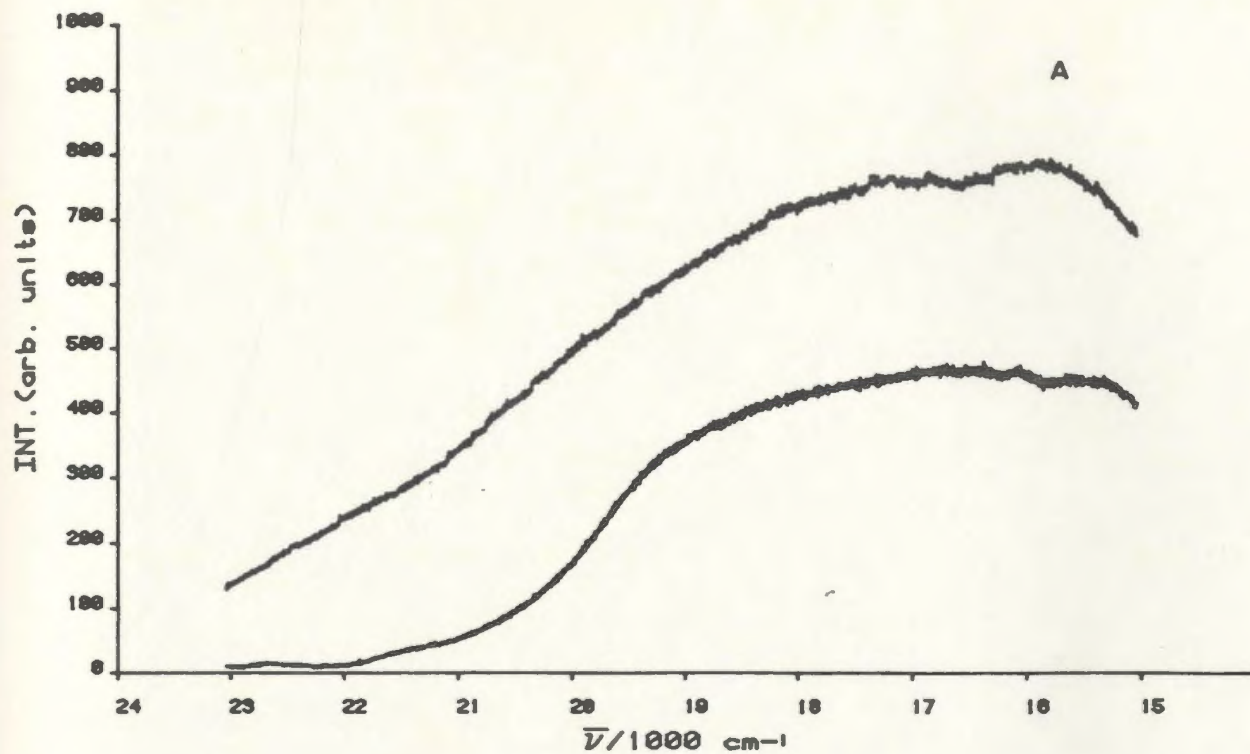


Figure 86. Visible spectrum of Cs_2MnCl_4 at 681 K.

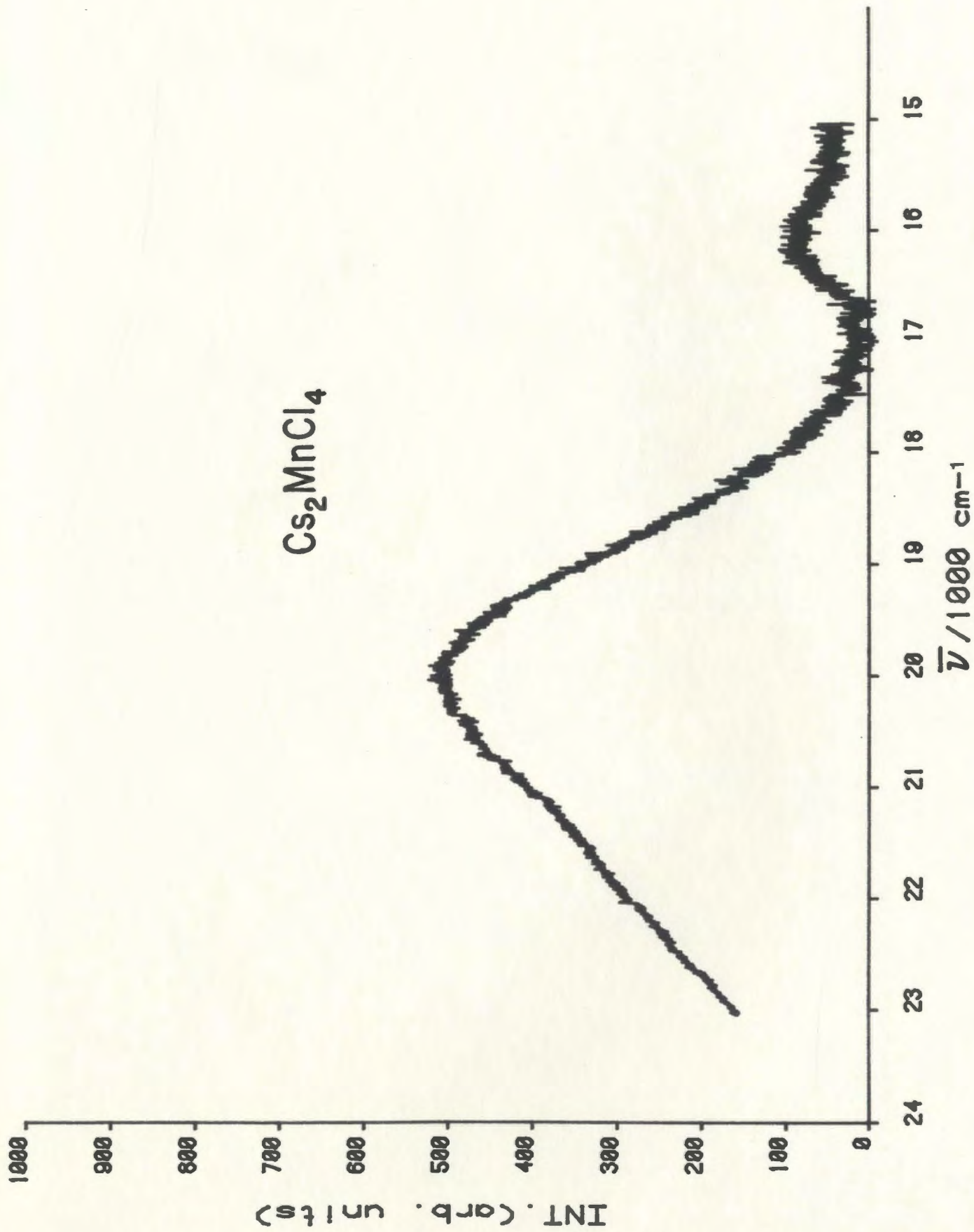


Figure 87. Visible spectrum of Cs_3MnCl_5 at room temperature.

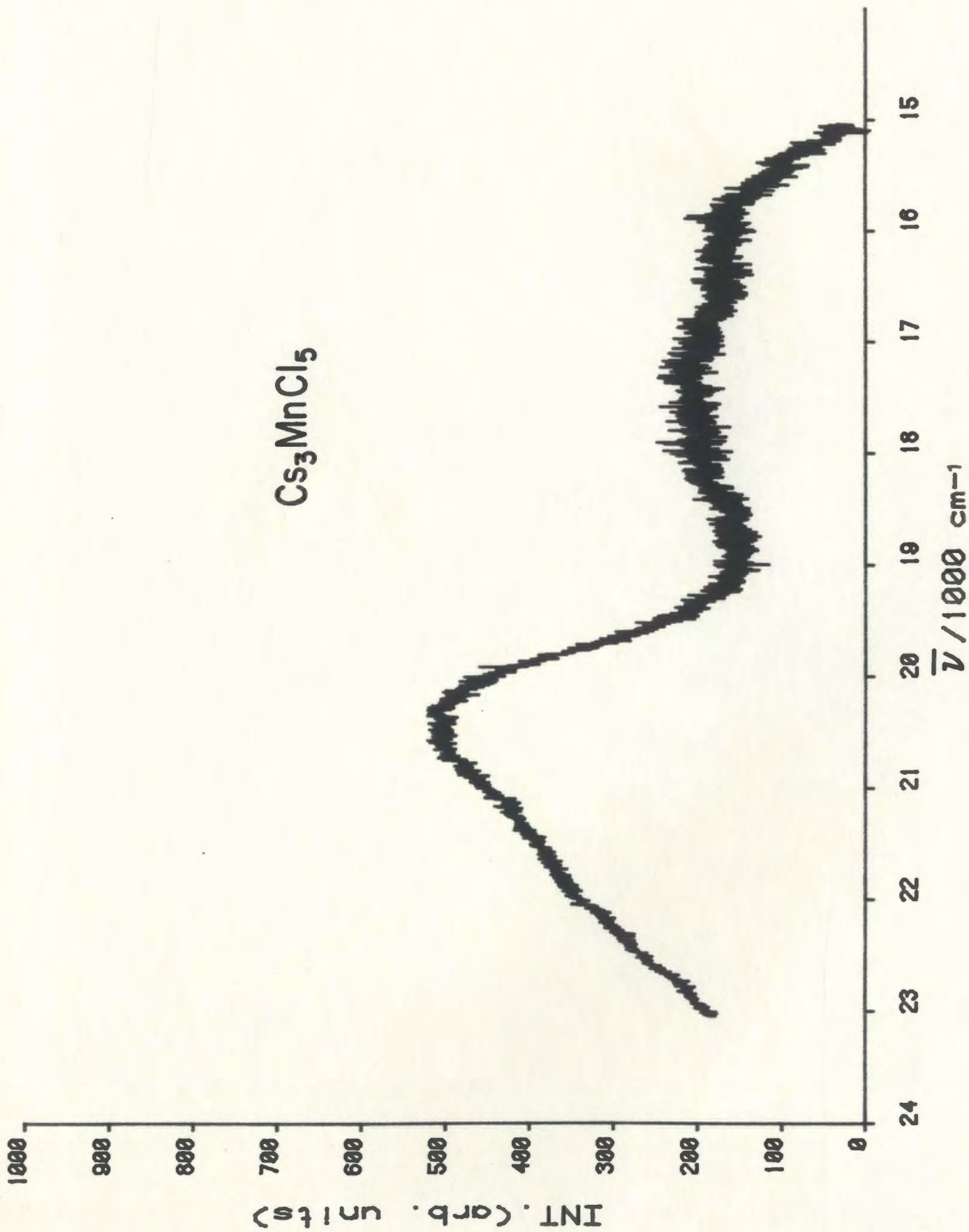


Figure 88. Visible spectrum of Cs_3MnCl_5 at 681 K.

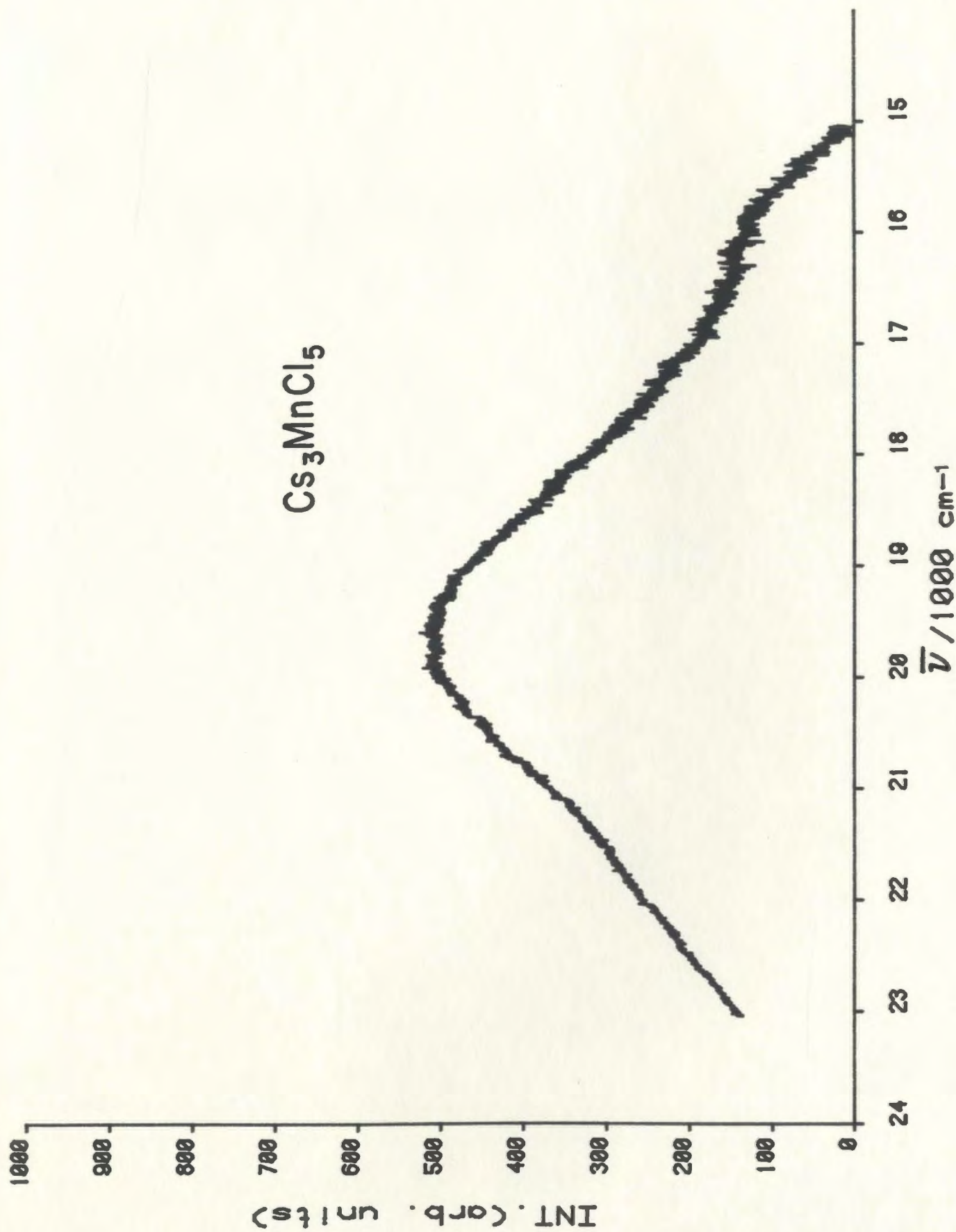


Table 33. Band positions in cm^{-1} and assignments for solid Cs_2MnCl_4 and Cs_3MnCl_5 .

Assignments	Cs_2MnCl_4 at Room Temp.	Cs_2MnCl_4 at 681 K	Cs_3MnCl_5 at Room Temp.	Cs_3MnCl_5 at 681 K	$[\text{MnCl}_4]^{2-}$ ions ⁸⁷
${}^6\text{A}_1({}^6\text{S}) \rightarrow {}^4\text{T}_1({}^4\text{G})$	20542	20042	20542	19742	21050
$\rightarrow {}^4\text{T}_2({}^4\text{G})$	21802		21802		22000
$\rightarrow {}^4\text{E}, {}^4\text{A}_1({}^4\text{G})$	22802		22802		23000

Figure 89. Visible spectrum of MnCl_2 at room temperature.

MnCl₂

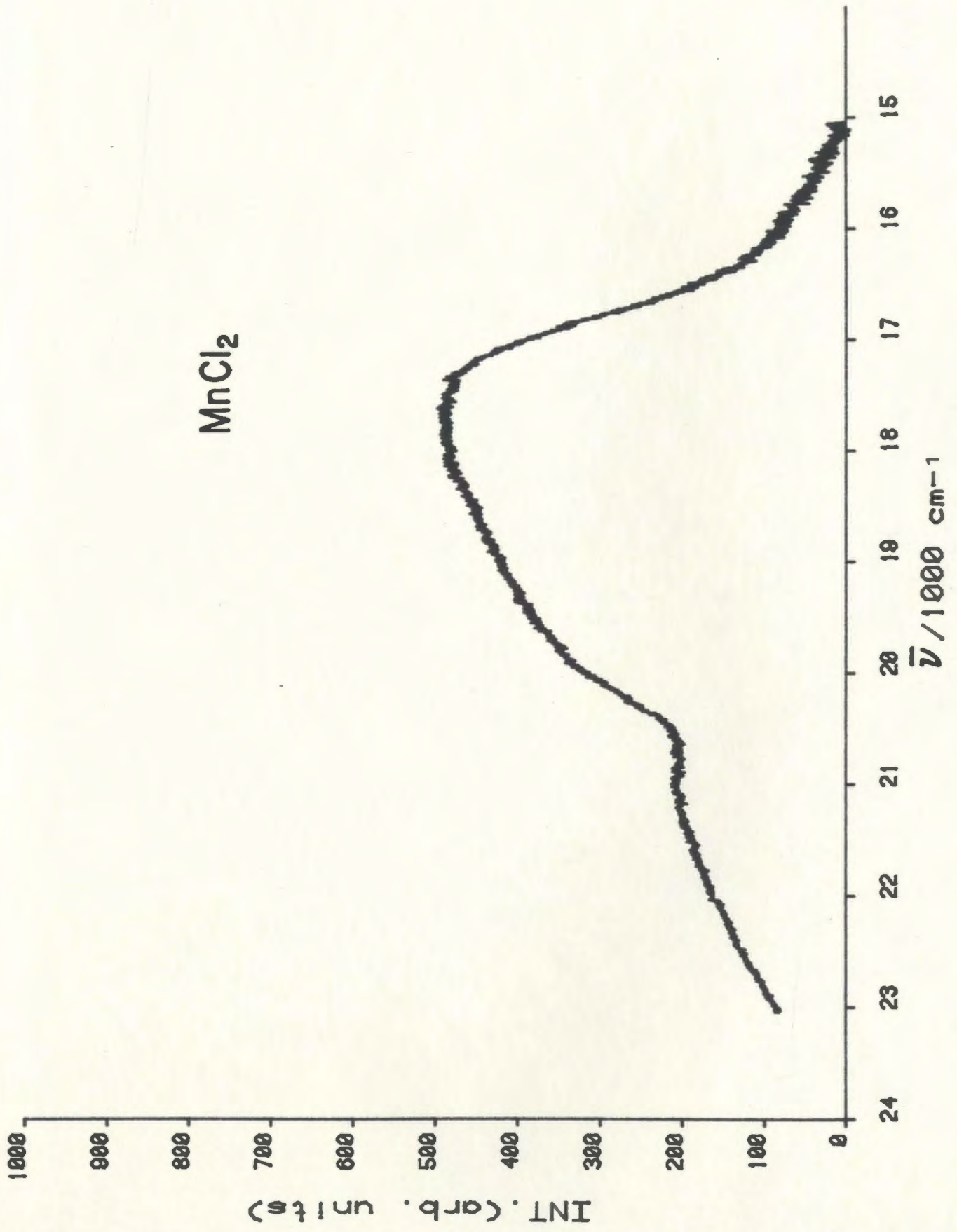


Figure 90. Visible spectrum of NaMn_4Cl_9 at room temperature.

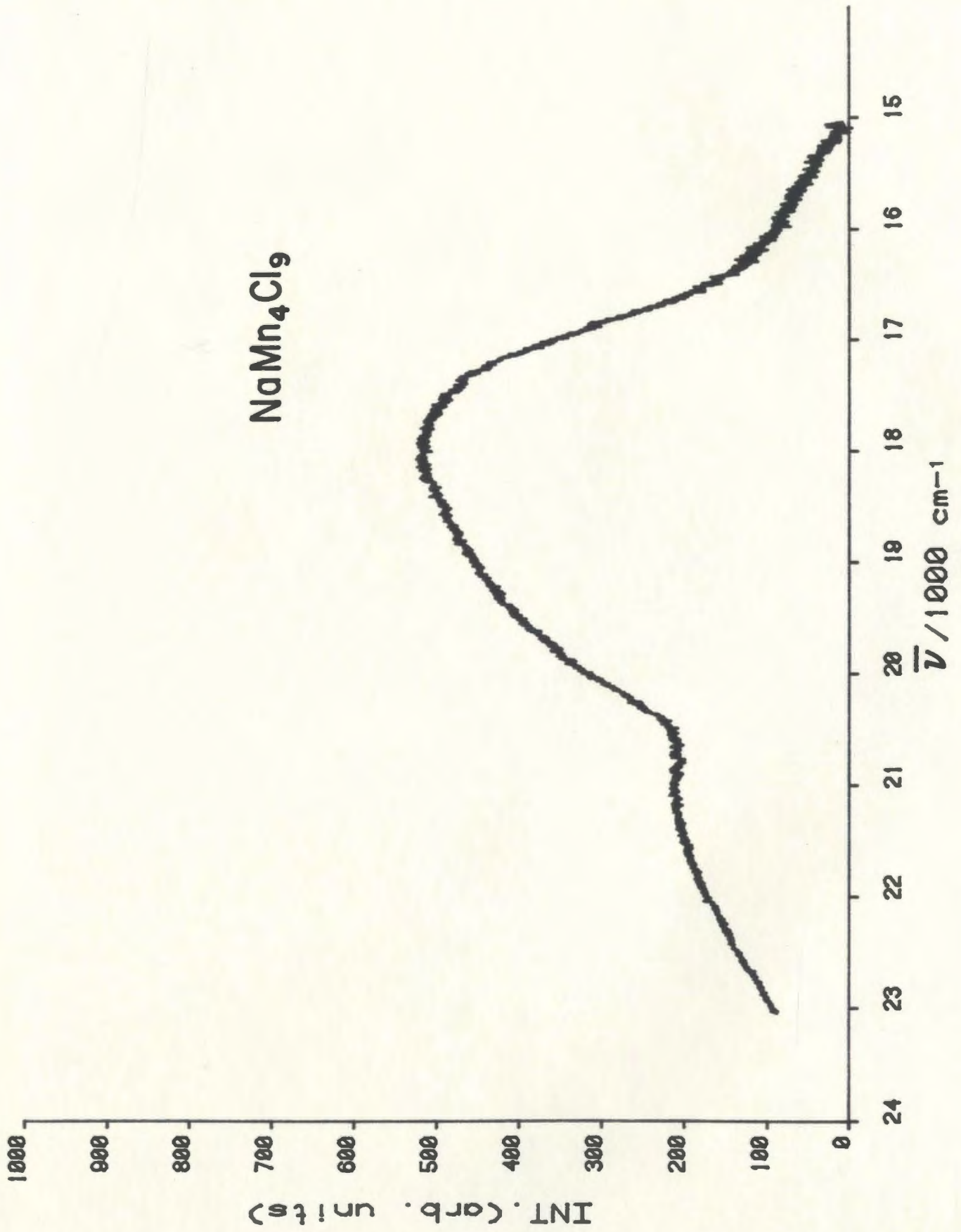


Figure 91. Visible spectrum of $\text{Na}_2\text{Mn}_3\text{Cl}_8$ at room temperature.

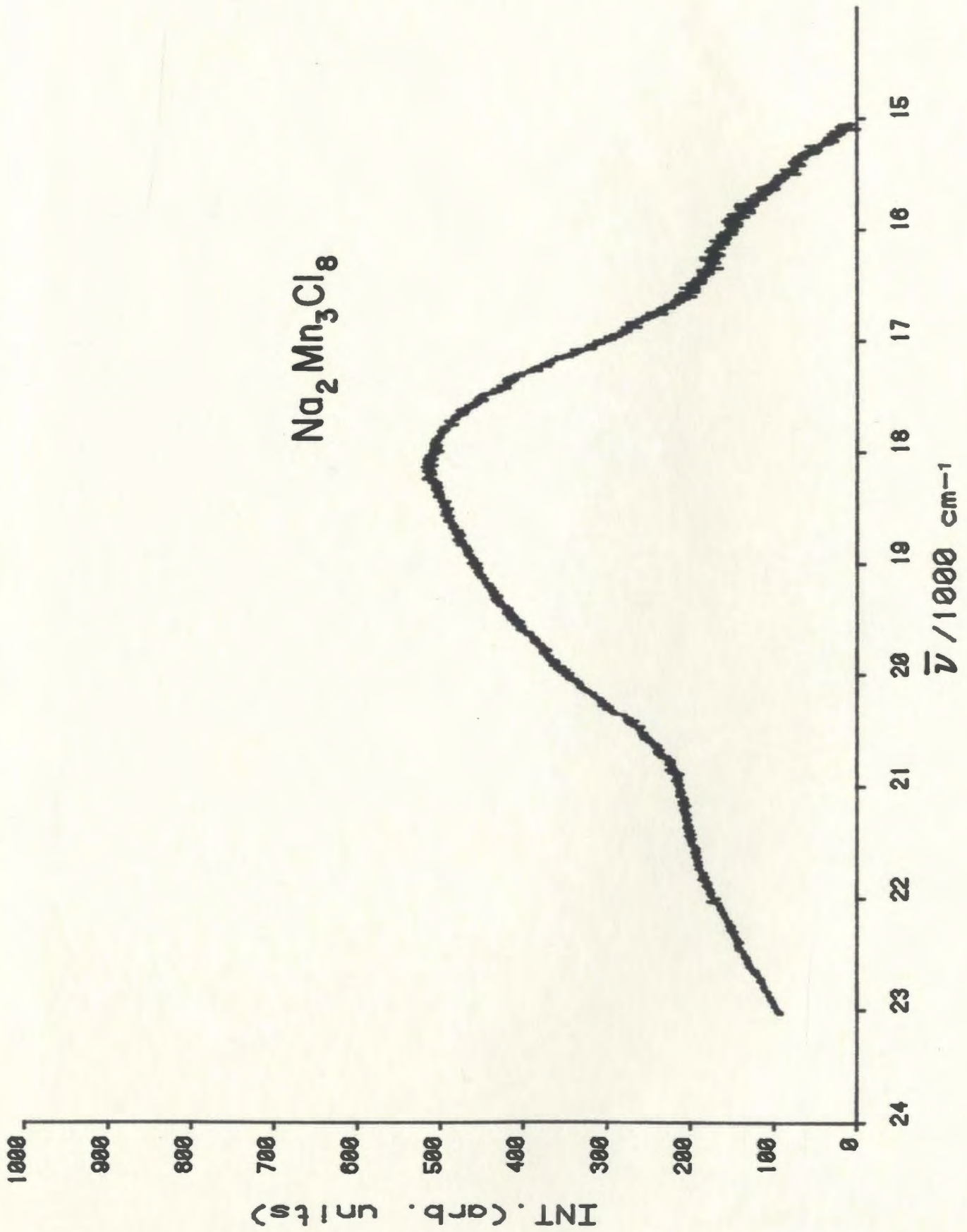


Table 34. Peak frequencies in cm^{-1} and assignments for solid MnCl_2 , NaMn_4Cl_9 and $\text{Na}_2\text{Mn}_3\text{Cl}_8$ at room temperature.

Assignments	MnCl_2	MnCl_2^{83}	NaMn_4Cl_9	$\text{Na}_2\text{Mn}_3\text{Cl}_8$
${}^6\text{A}_{1g}({}^6\text{S}) \rightarrow {}^4\text{T}_{1g}({}^4\text{G})$	18089	18650	18159	18259
$\rightarrow {}^4\text{T}_{2g}({}^4\text{G})$	21099	22100	21099	21099

(iii) CsMnCl₃ and CsMn₄Cl₉

The visible spectra of CsMnCl₃ and CsMn₄Cl₉ at room temperature and at 681 K are shown in figures 92, 93, 94 and 95 respectively. These compounds are pink at room temperature and at 681 K. It was reported that the Mn²⁺ ion has an octahedral environment in CsMnCl₃⁵² and CsMn₄Cl₉³⁹. The shoulder observed at ~ 16000 cm⁻¹ in the spectrum of CsMn₄Cl₉ at room temperature is probably due to Manganese oxide^{99,100}. Band assignments are shown in Table 35.

(iv) RbMnCl₃, Rb₂MnCl₄ and Rb₃Mn₂Cl₇

The visible spectra of RbMnCl₃, Rb₂MnCl₄, and Rb₃Mn₂Cl₇ at room temperature are shown in figures 96, 97 and 98 respectively. RbMnCl₃ has an orange-slight red color, while Rb₂MnCl₄ and Rb₃Mn₂Cl₇ exhibit bright orange color. So it is noted that the peak observed at ~ 18709 cm⁻¹ in RbMnCl₃ is slightly shifted to lower frequency in comparison to its counterpart observed in Rb₂MnCl₄ and Rb₃Mn₂Cl₇.

The X-ray study⁵⁶ of RbMnCl₃ indicated that the manganese has an octahedral environment. It was reported⁴³ that Rb₂MnCl₄ is isomorphous with K₂MgCl₄⁴² in which the magnesium is octahedrally coordinated by Cl atoms. Seifert⁴³ reported that Rb₃Mn₂Cl₇ is isostructural with Sr₃Ti₂O₇ which has a tetragonal structure⁶¹ in which the titanium is surrounded by six oxygen atoms, so this implicitly indicates that the manganese is octahedrally coordinated by Cl atoms. Band positions in cm⁻¹ and assignments are shown in Table 36.

(v) KMnCl₃, K₄MnCl₆ and K₃Mn₂Cl₇

The visible spectra of KMnCl₃, K₄MnCl₆ and K₃Mn₂Cl₇ at room

Figure 92. Visible spectrum of CsMnCl_3 at room temperature.

CsMnCl₃

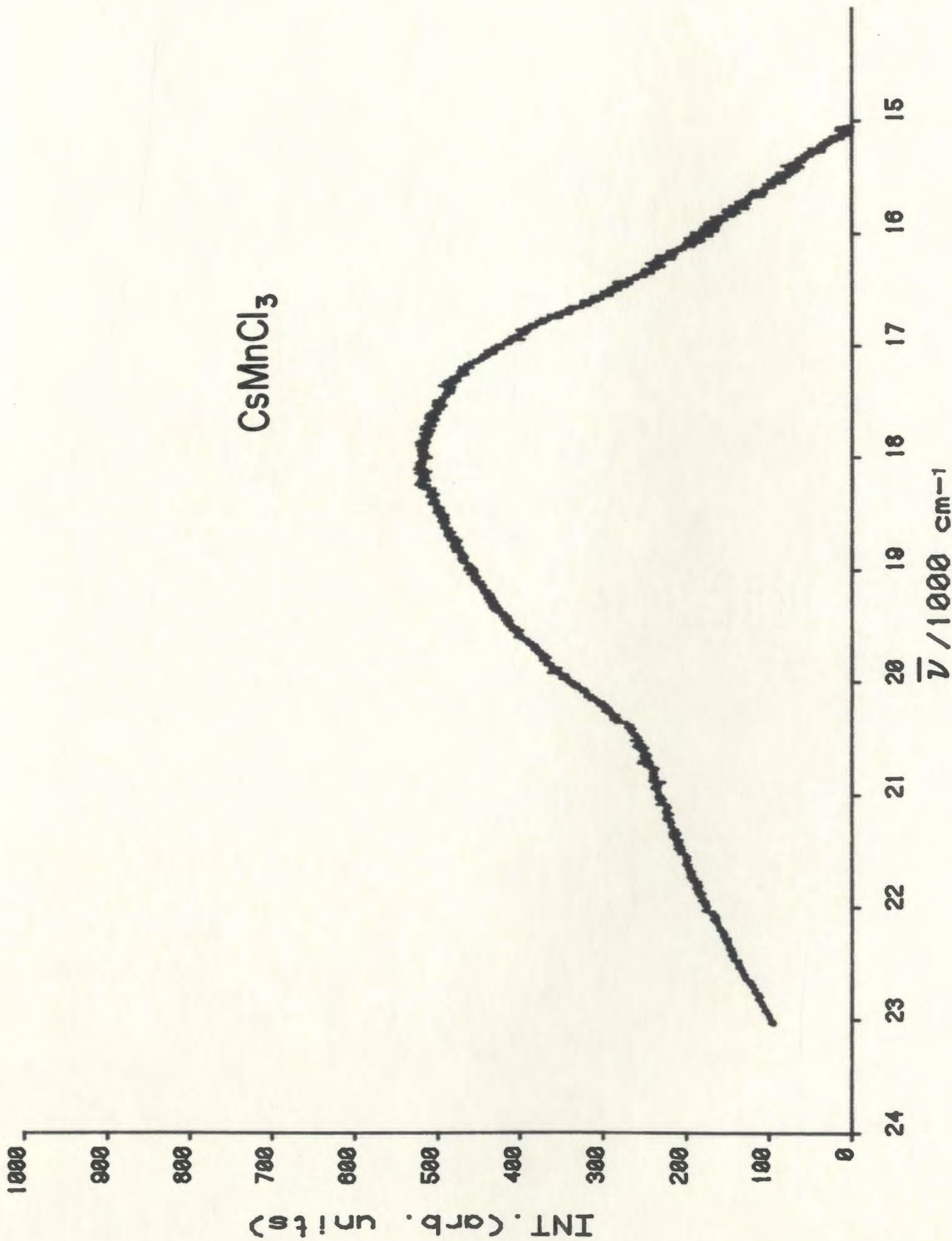


Figure 93. Visible spectrum of CsMnCl_3 at 681 K.

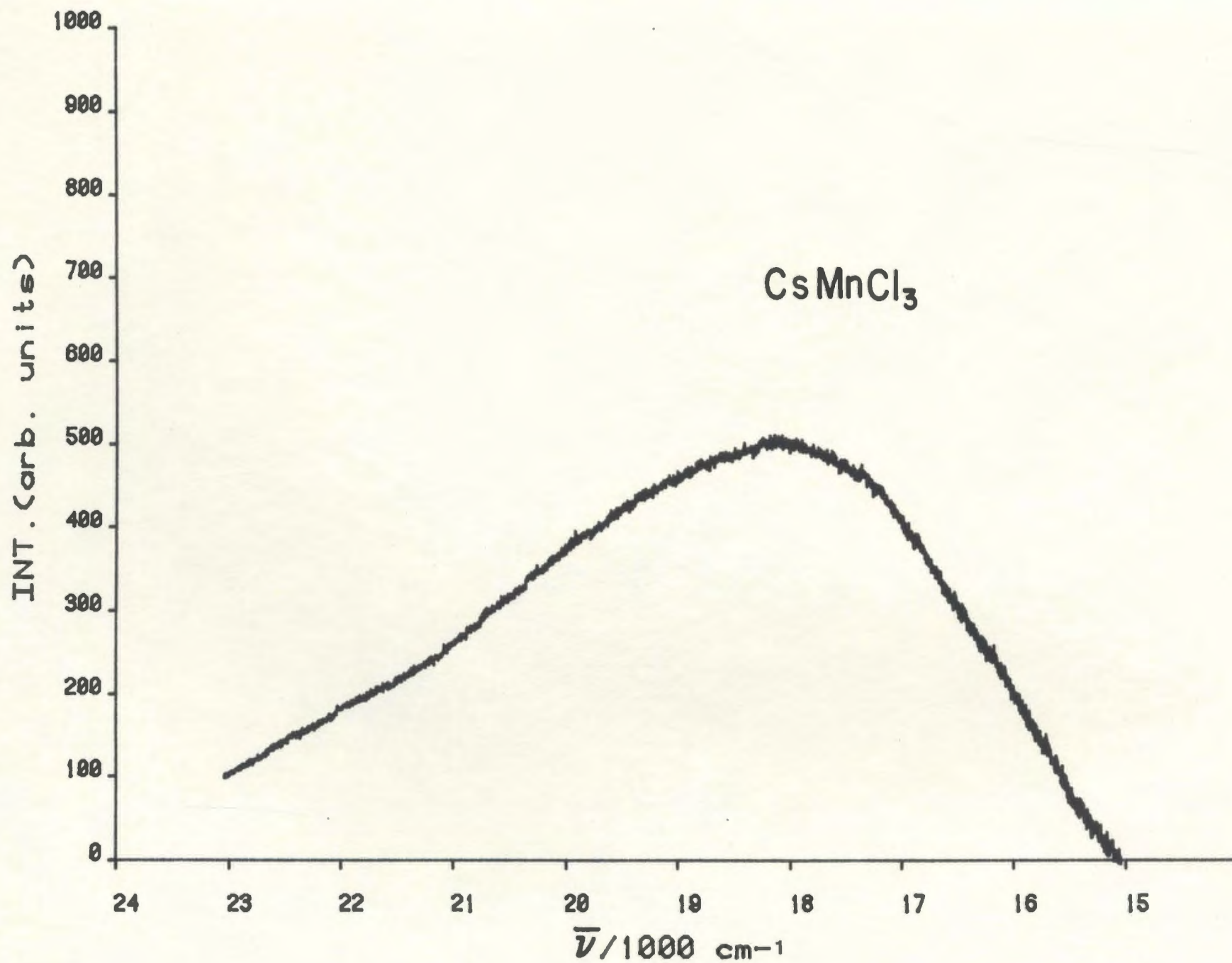


Figure 94. Visible spectrum of CsMn_4Cl_9 at room temperature.

CsMn4Cl9

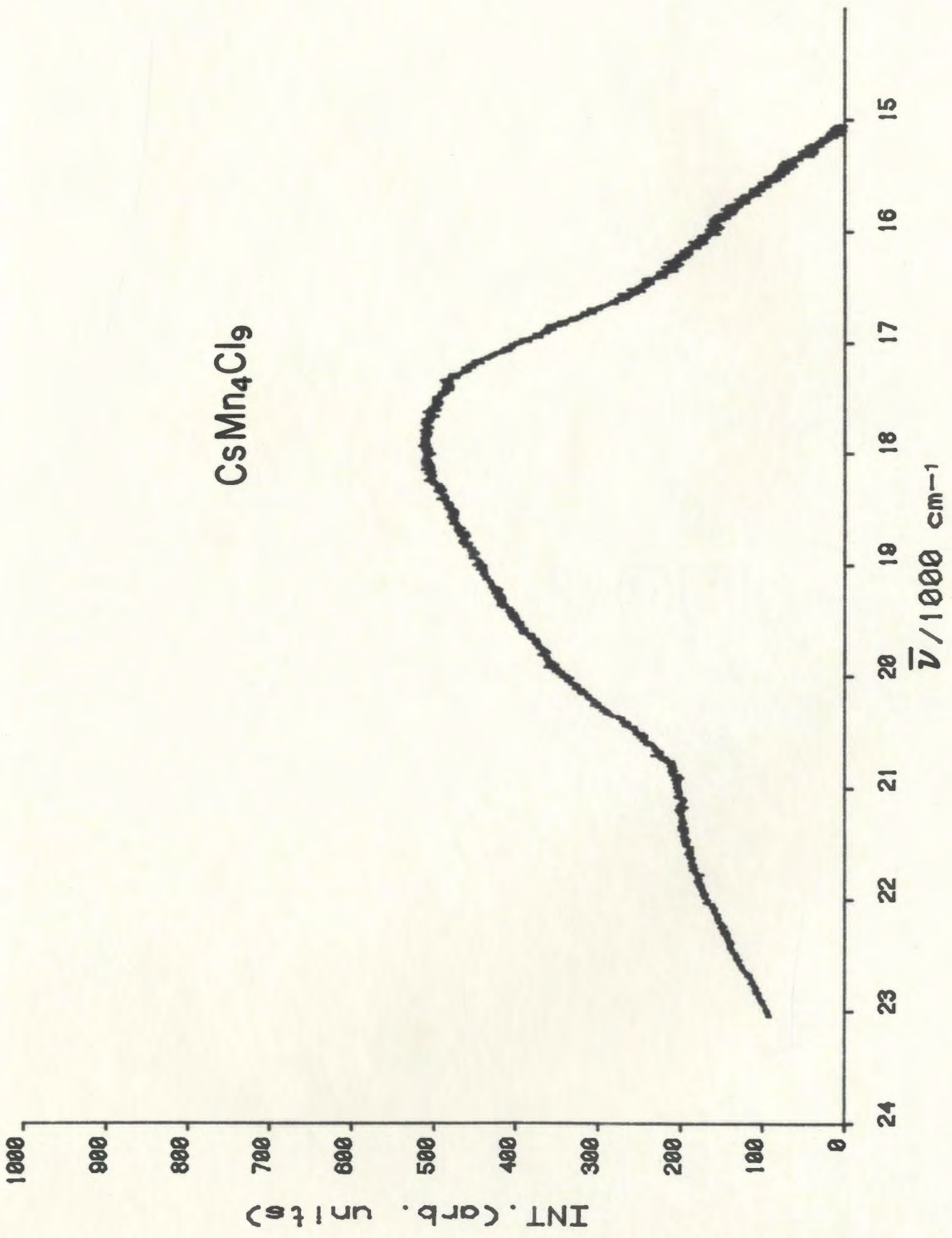


Figure 95. Visible spectrum of CsMn_4Cl_9 at 681 K.

CsMn₄Cl₉

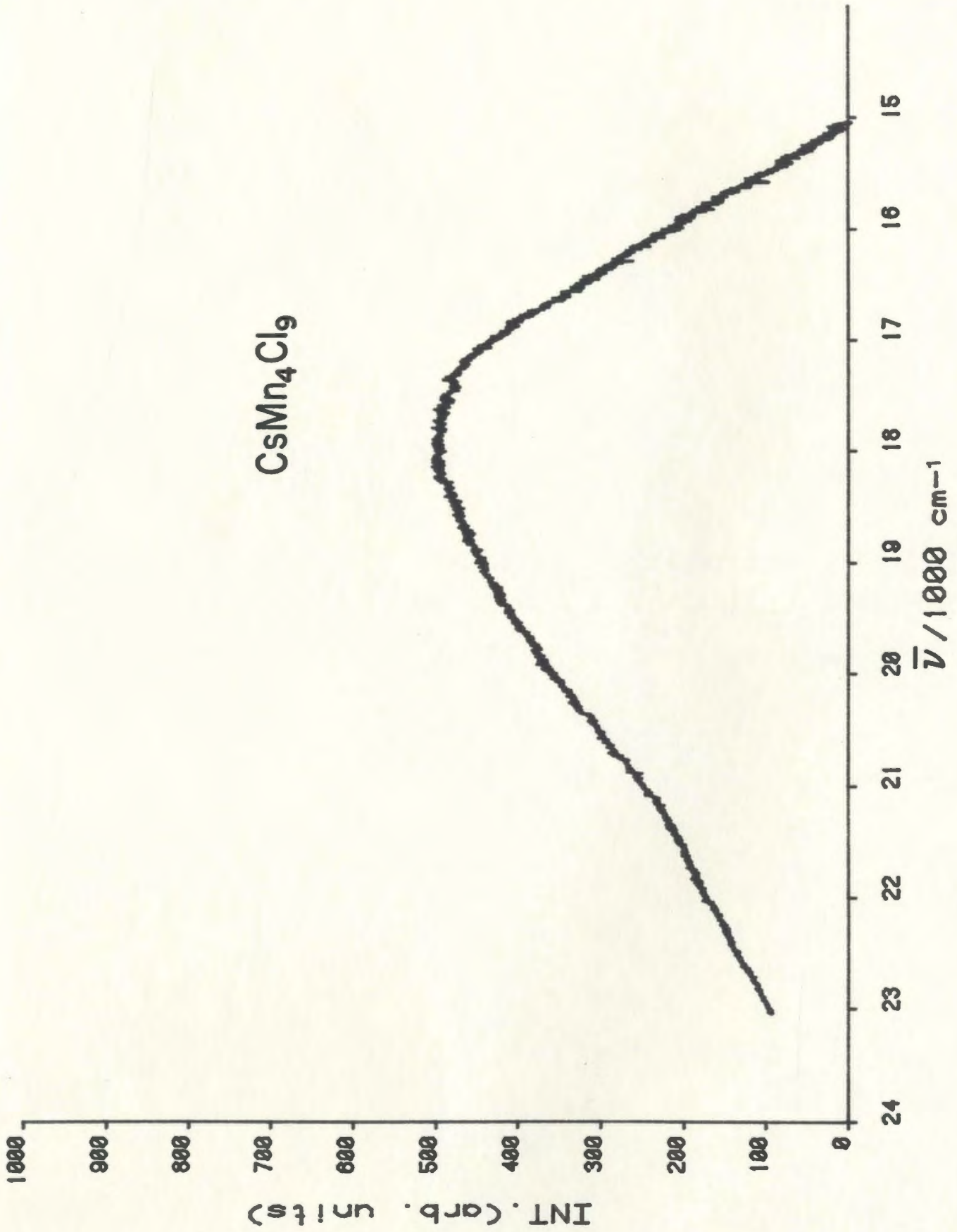


Table 35. Peak positions in cm^{-1} and assignments for solid CsMnCl_3 , CsMn_4Cl_9 and $(\text{CH}_3)_4\text{NMnCl}_3$.

Assignments	CsMnCl_3 at Room Temp.	CsMnCl_3 at 681 K	CsMn_4Cl_9 at Room Temp.	CsMn_4Cl_9 at 681 K	$(\text{CH}_3)_4\text{NMnCl}_3$ ⁹²
${}^6\text{A}_{1g}({}^6\text{S}) \rightarrow {}^4\text{T}_{1g}({}^4\text{G})$	18042	18042	18042	18042	18840
$\rightarrow {}^4\text{T}_{2g}({}^4\text{G})$	21000		21099		22560

Figure 96. Visible spectrum of RbMnCl_3 at room temperature.

RbMnCl₃

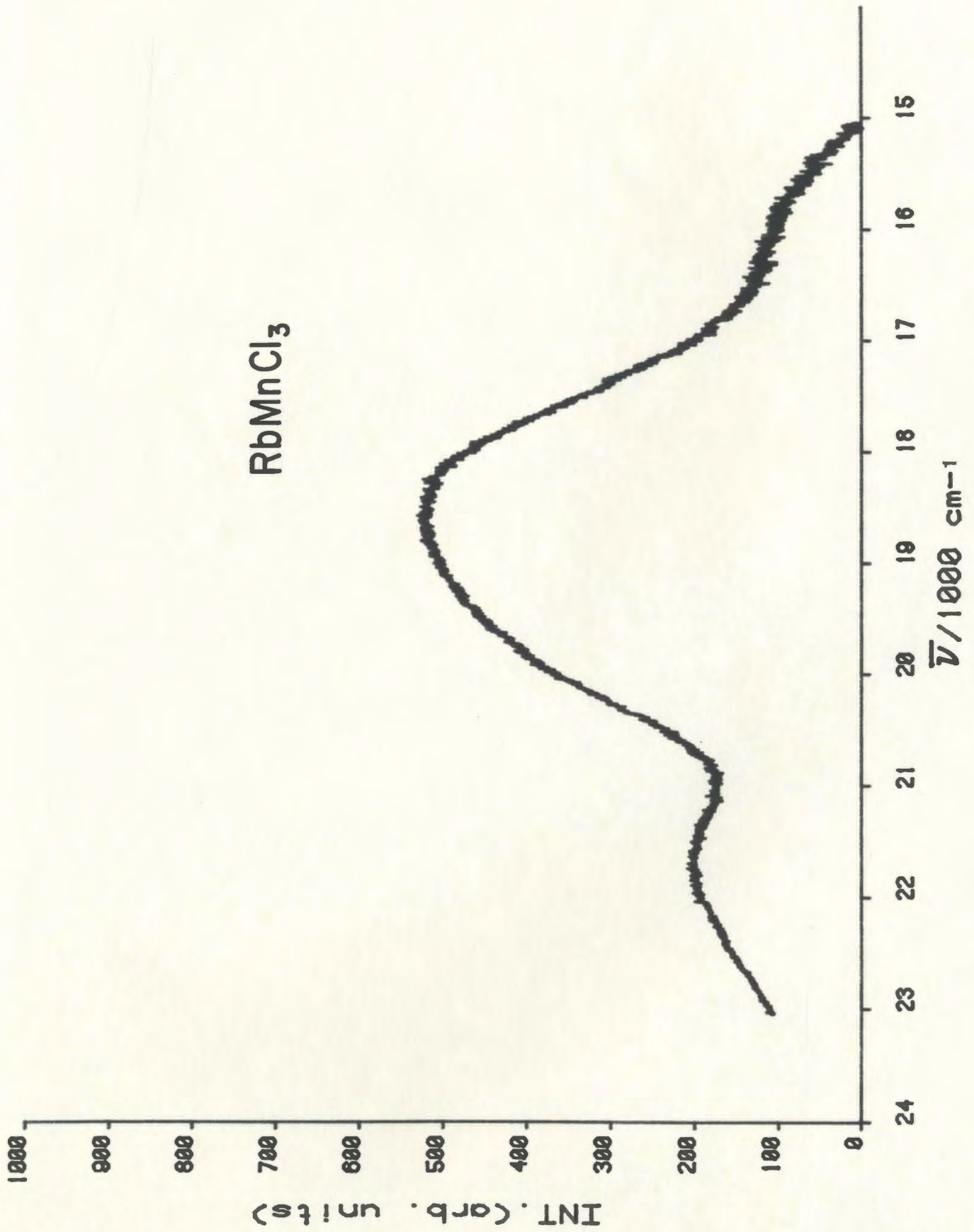


Figure 97. Visible spectrum of Rb_2MnCl_4 at room temperature.

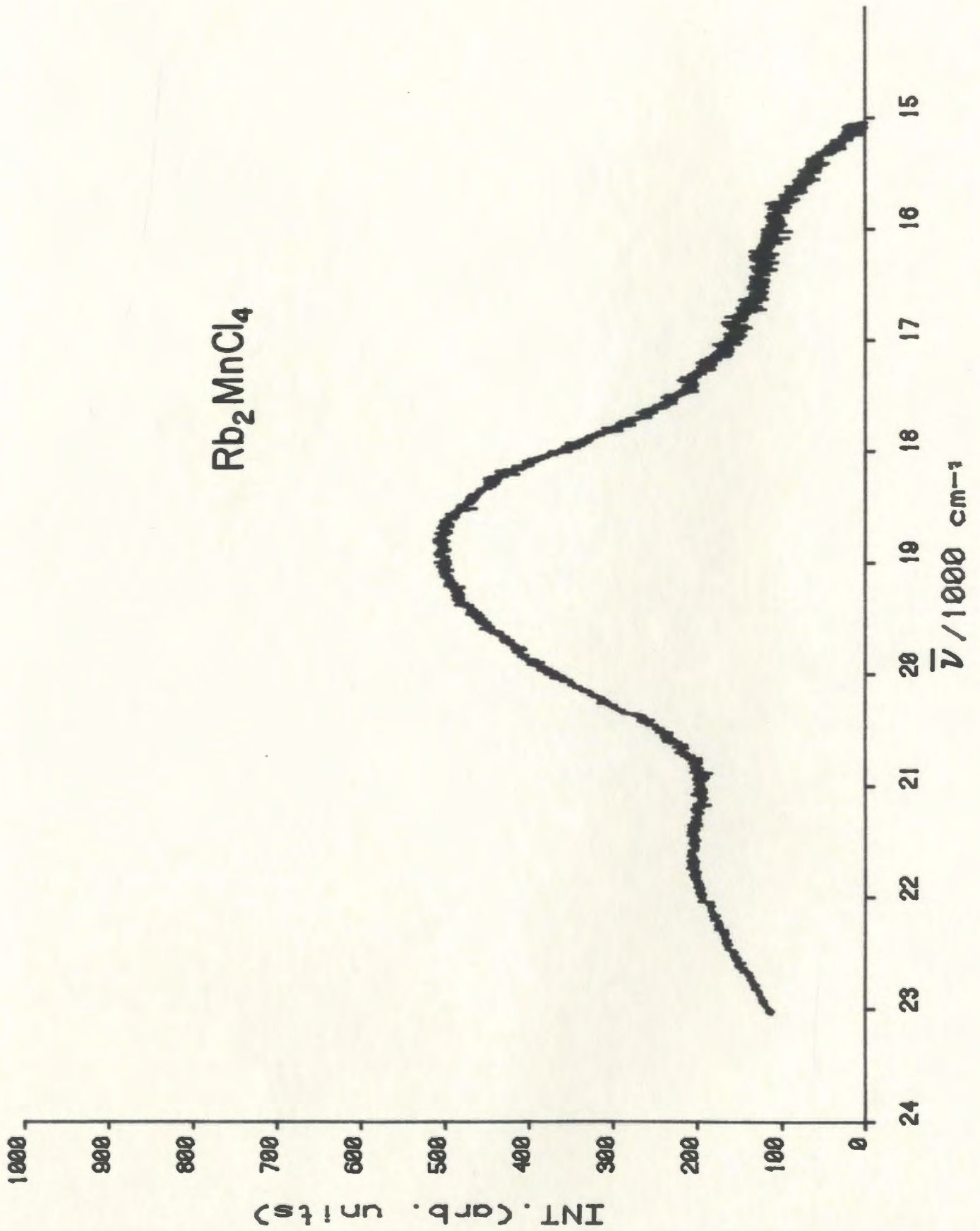


Figure 98. Visible spectrum of $\text{Rb}_3\text{Mn}_2\text{Cl}_7$ at room temperature.

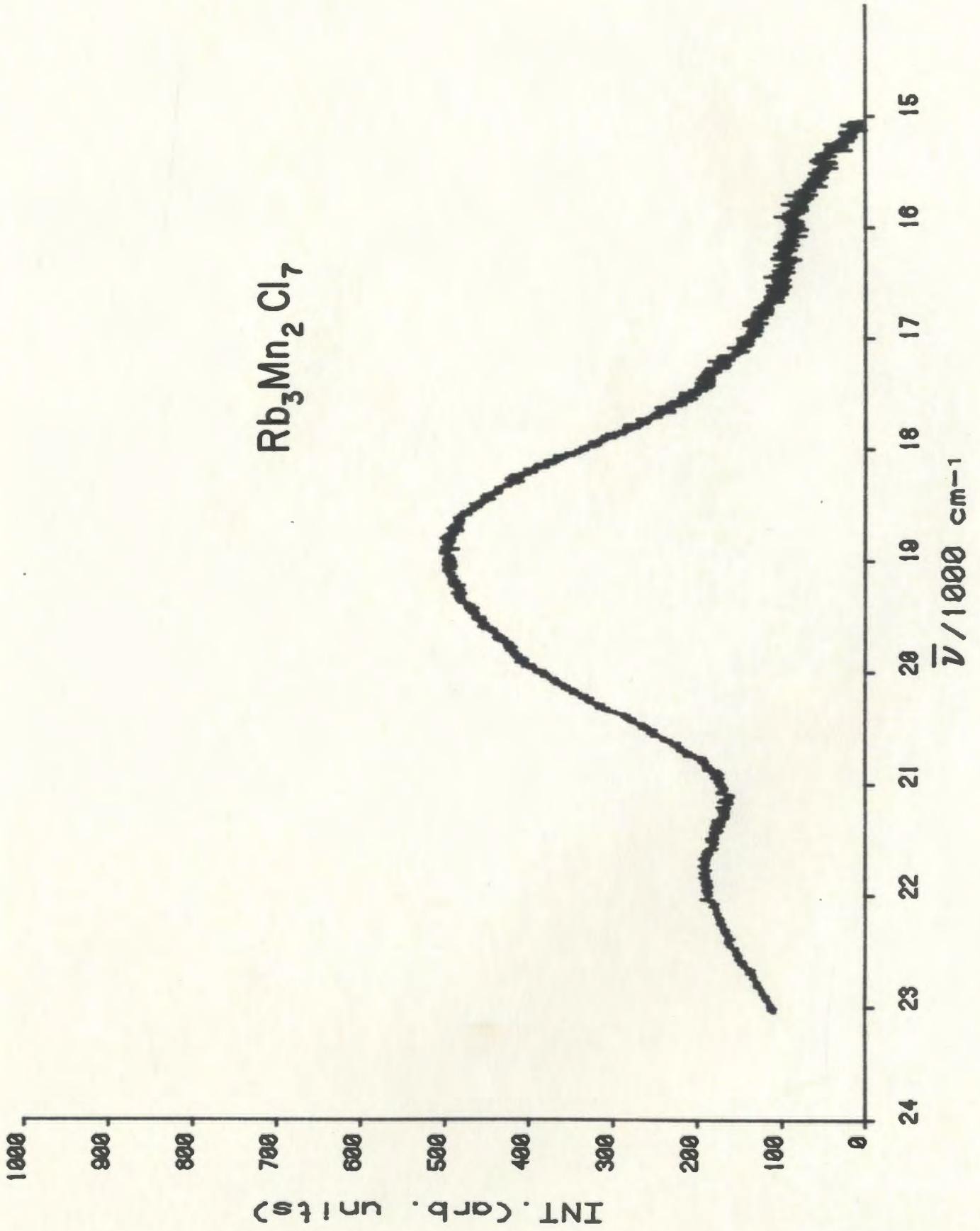


Table 36. Peak frequencies in cm^{-1} and assignments for solid RbMnCl_3 , Rb_2MnCl_4 and $\text{Rb}_3\text{Mn}_2\text{Cl}_7$ at room temperature.

Assignments	RbMnCl_3	Rb_2MnCl_4	$\text{Rb}_3\text{Mn}_2\text{Cl}_7$
${}^6\text{A}_{1g}({}^6\text{S}) \rightarrow {}^4\text{T}_{1g}({}^4\text{G})$	18709	18942	18942
$\rightarrow {}^4\text{T}_{2g}({}^4\text{G})$	21788	21788	21788

temperature are shown in figures 99, 100 and 101 respectively. These compounds exhibit orange color.

Seifert⁶⁴ reported that Mn^{2+} ions occupy octahedral holes in compounds of the formula $AMnX_3$, so the Mn^{2+} ions in $KMnCl_3$ have an octahedral arrangement. Also⁶⁴ he suggested that compounds of the formula A_4MnX_6 contain isolated MnX_6 octahedra, so this indicate that the Mn atom in K_4MnCl_6 is octahedrally coordinated by Cl atoms. $K_3Mn_2Cl_7$ ⁴³ is isostructural with $Rb_3Mn_2Cl_7$, in which the Mn atom has an octahedral environment.

The spectrum of K_4MnCl_6 is similar in appearance to the reflectance spectrum reported by Foster and Gill⁹². The peaks observed in the reflectance spectrum⁹² of $KMnCl_3$ at ~ 19700 and at ~ 22960 were assigned to ${}^6S \rightarrow {}^4G$ transitions, so the shoulder observed at $\sim 20542\text{ cm}^{-1}$ in the spectrum of $KMnCl_3$ is probably not real peak. Assignments and peak positions in cm^{-1} are shown in Table 37.

(vi) $NaMnCl_3$, Na_2MnCl_4 and Na_6MnCl_8

The visible spectra of $NaMnCl_3$, Na_2MnCl_4 and Na_6MnCl_8 at room temperature are shown in figures 102, 103 and 104. $NaMnCl_3$ and Na_2MnCl_4 have an orange color while Na_6MnCl_8 is colorless.

The manganese has an octahedral environment in $NaMnCl_3$ ⁶⁵ and Na_2MnCl_4 ⁶⁷. It was reported⁶⁸ that the Mn in Na_6MnCl_8 has an octahedral arrangement.

The peak observed at 19256 cm^{-1} in the spectrum of Na_6MnCl_8 is close to its counterpart observed in the Suzuki phase spectrum^{96,97,98}. Band assignments and frequency in cm^{-1} are shown in Table 38.

Figure 99. Visible spectrum of KMnCl_3 at room temperature.

KMnCl₃

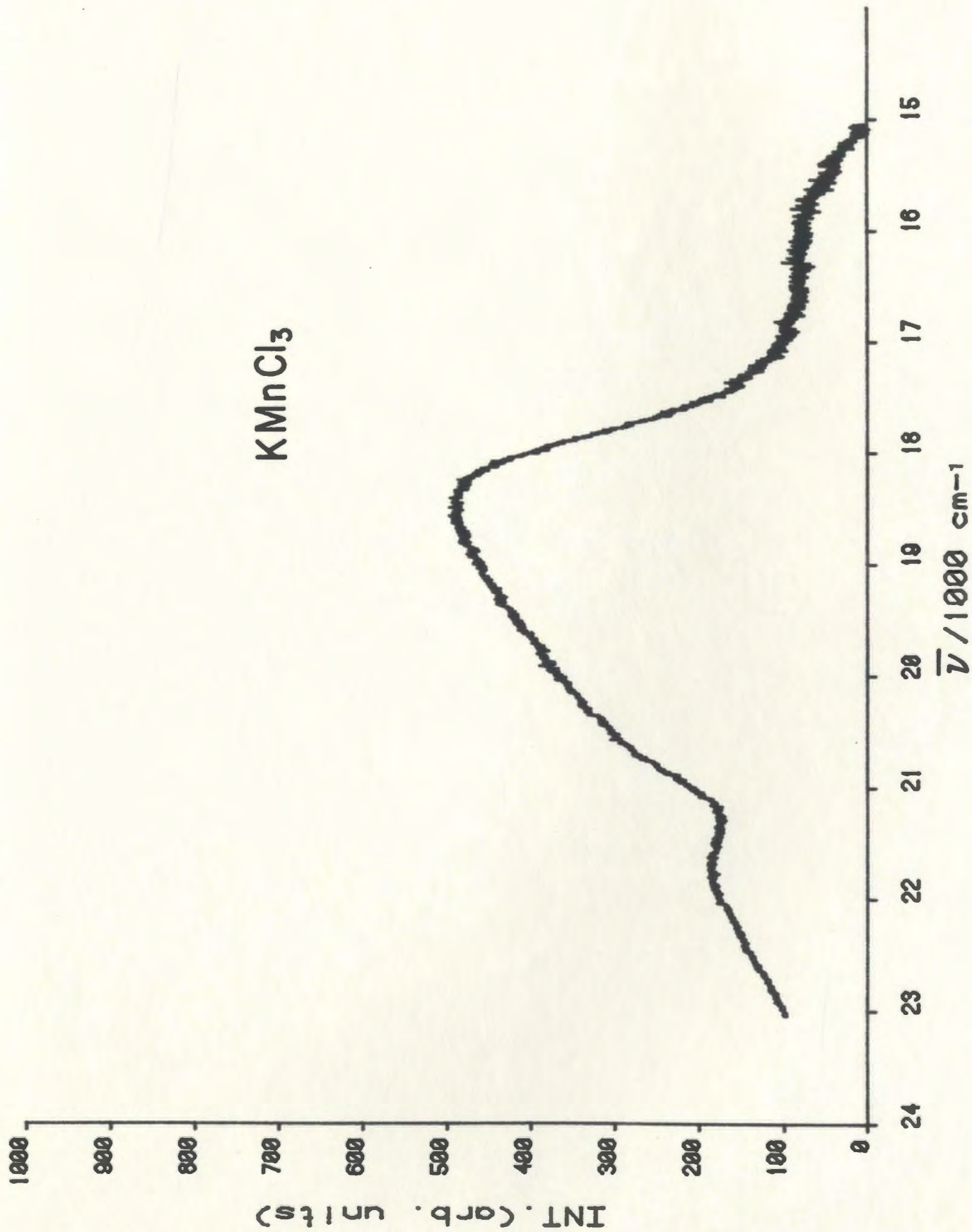


Figure 100. Visible spectrum of K_4MnCl_6 at room temperature.

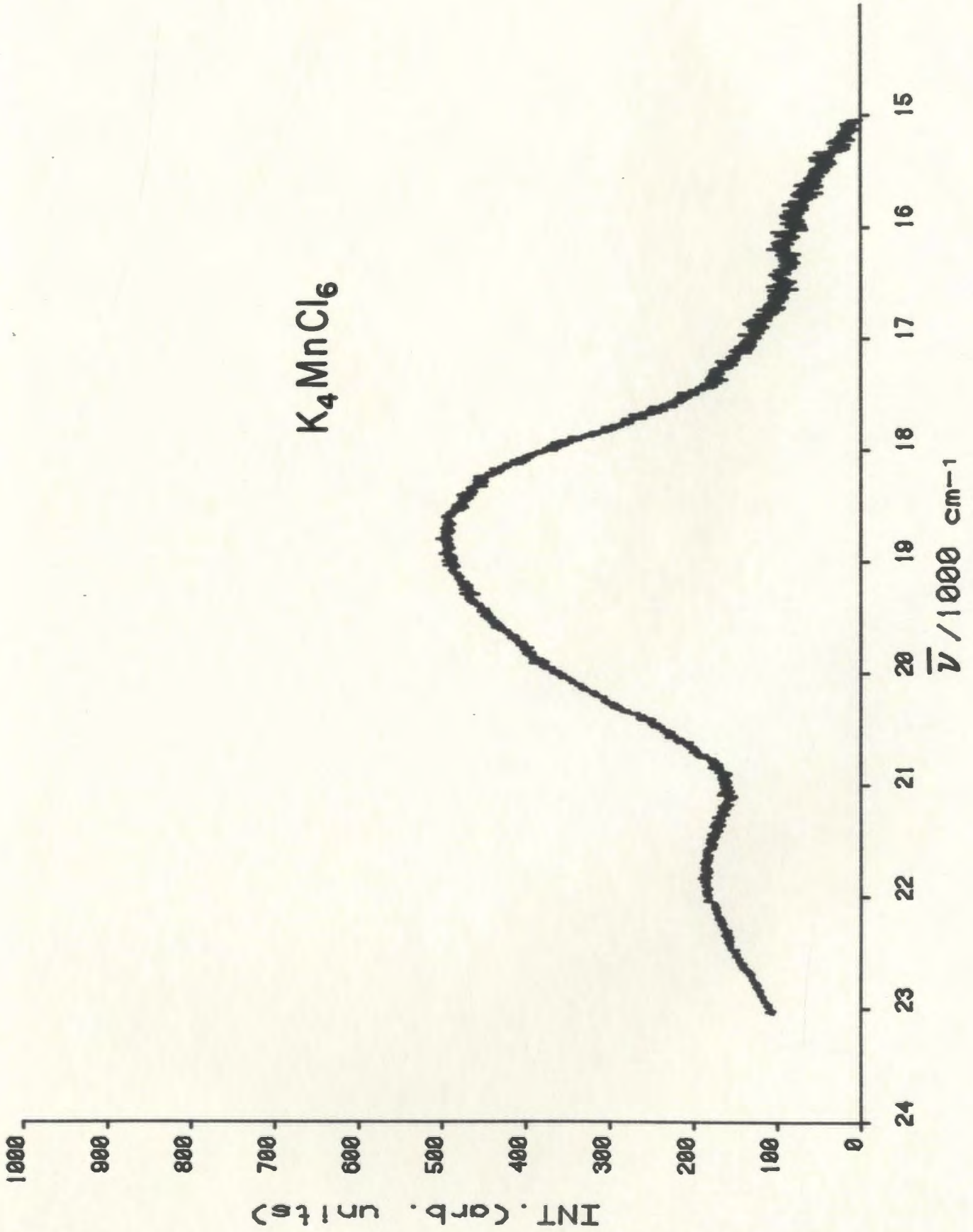


Figure 101. Visible spectrum of $K_3Mn_2Cl_7$ at room temperature.

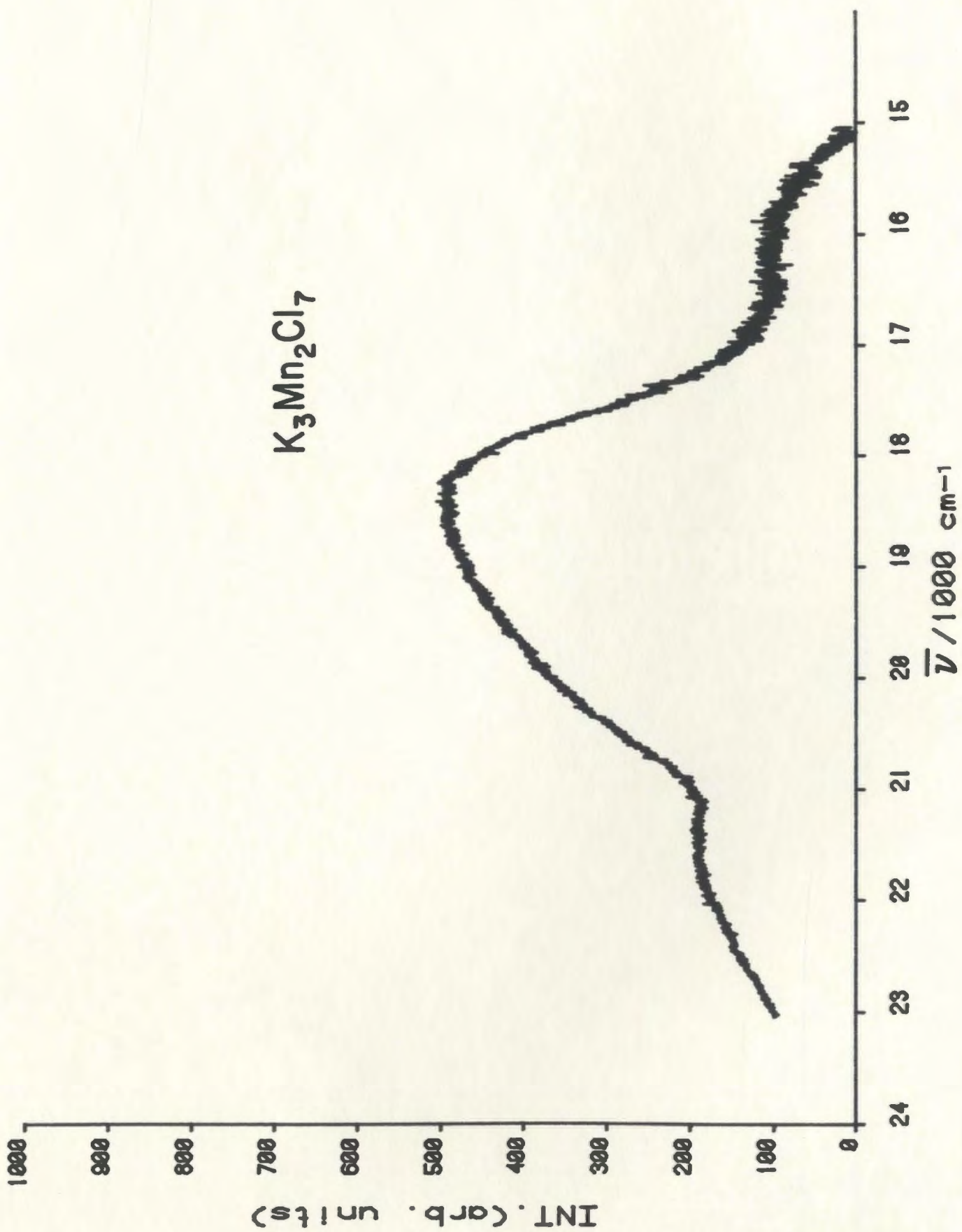


Table 37. Peak positions in cm^{-1} and assignments for solid KMnCl_3 , K_4MnCl_6 and $\text{K}_3\text{Mn}_2\text{Cl}_7$ at room temperature.

Assignments	KMnCl_3	KMnCl_3^{92}	K_4MnCl_6	$\text{K}_4\text{MnCl}_6^{92}$	$\text{K}_3\text{Mn}_2\text{Cl}_7$
${}^6\text{A}_{1g}({}^6\text{S}) \rightarrow {}^4\text{T}_{1g}({}^4\text{G})$	18729	19700	18885	19460	18709
$\rightarrow {}^4\text{T}_{2g}({}^4\text{G})$	21788	22960	21788	22900	21788

Figure 102. Visible spectrum of NaMnCl_3 at room temperature.

NaMnCl₃

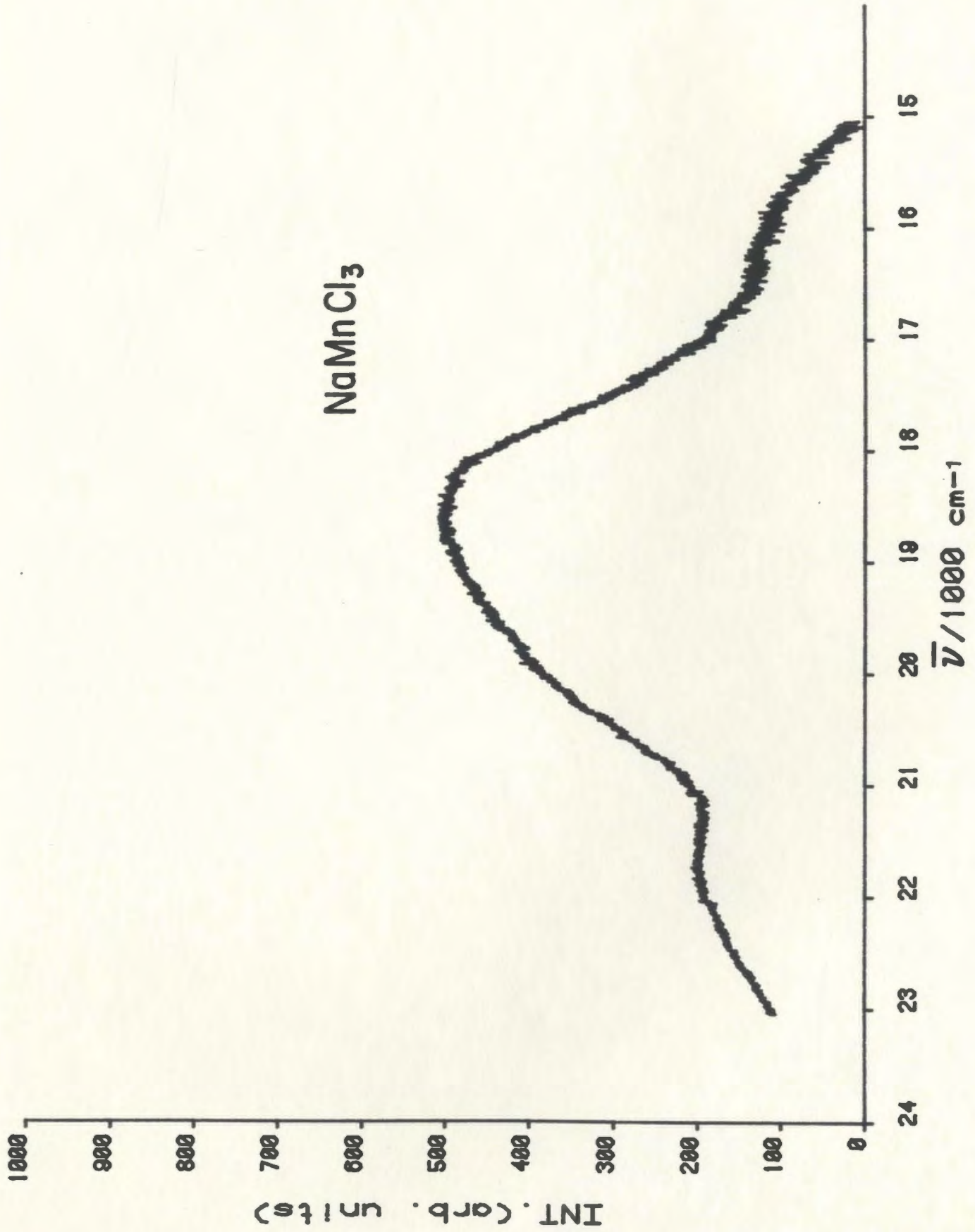


Figure 103. Visible spectrum of Na_2MnCl_4 at room temperature.

Na2MnCl4

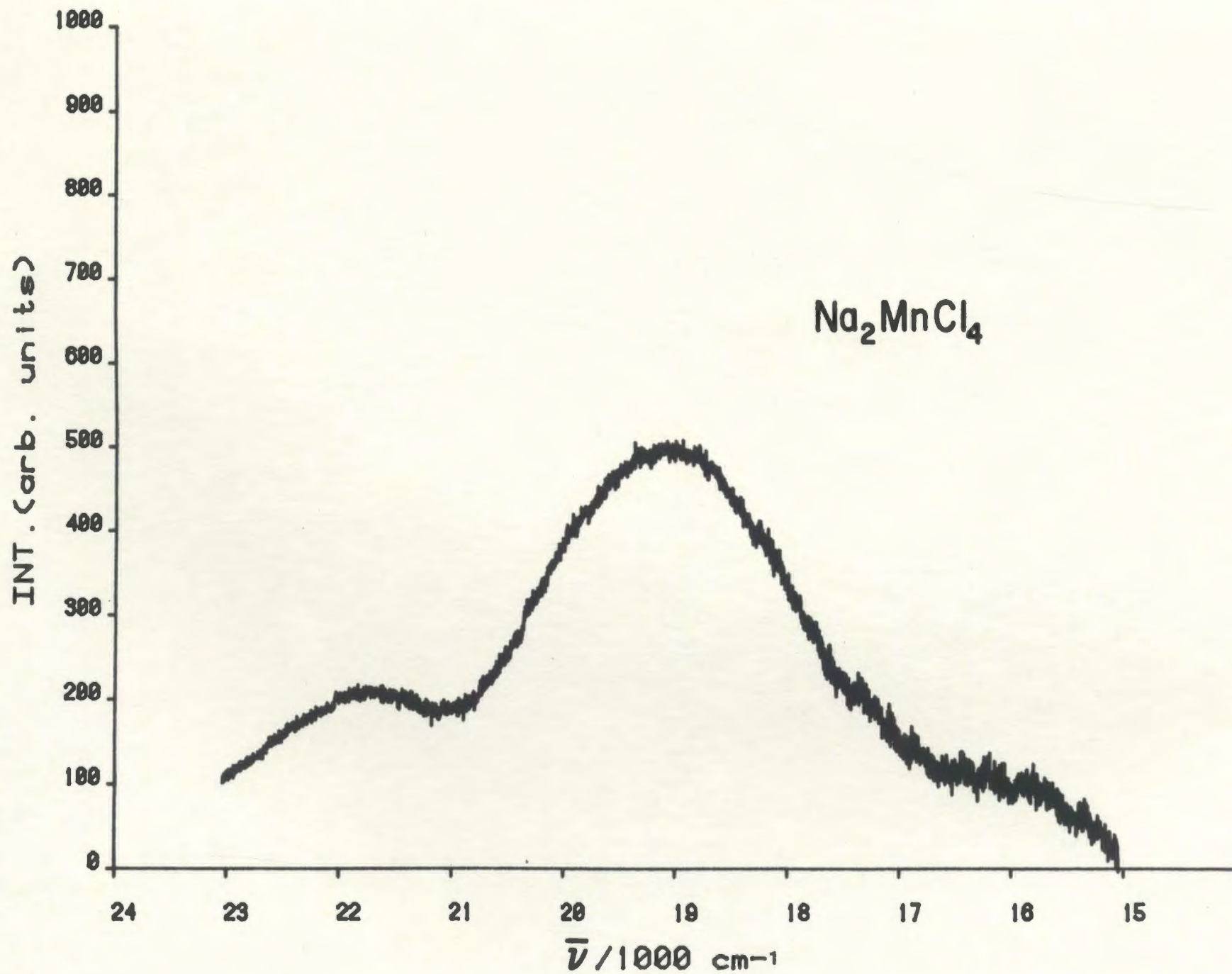


Figure 104. Visible spectrum of Na_6MnCl_8 at room temperature.

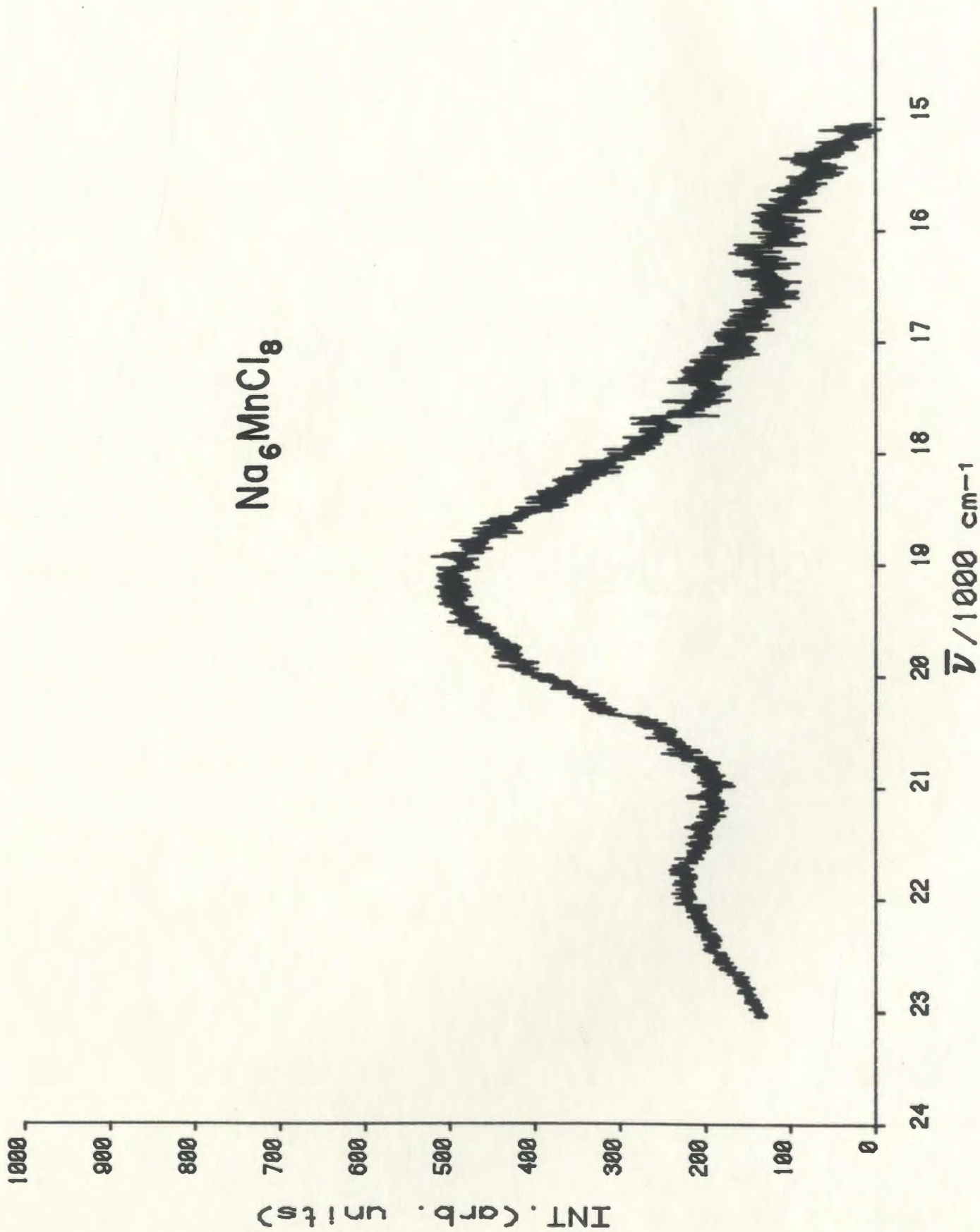


Table 38. Assignments and peak positions in cm^{-1} for solid NaMnCl_3 , Na_2MnCl_4 and Na_6MnCl_8 at room temperature.

Assignments	NaMnCl_3	Na_2MnCl_4	Na_6MnCl_8	Suzuki phase ⁹⁶
${}^6A_{1g}({}^6S) \rightarrow {}^4T_{1g}({}^4G)$	18786	19042	19256	19242
$\rightarrow {}^4T_{2g}({}^4G)$	21788	21788	21788	22878

4.4.2 Molten State

(i) Cs₂MnCl₄, Cs₃MnCl₅, K₄MnCl₆ and Na₆MnCl₈

The visible spectra of Cs₂MnCl₄, Cs₃MnCl₅, K₄MnCl₆ and Na₆MnCl₈ melts are shown in figures 105, 106, 107 and 108. These compounds have yellow color in the melt and exhibit similar spectra. The peak observed at ~ 20142 cm⁻¹ in Cs₂MnCl₄, Cs₃MnCl₅ and K₄MnCl₆ melts is attributed to ⁶A₁(⁶S) → ⁴T₁(⁴G) transition. This peak is slightly shifted to lower frequency and observed at ~ 20042 cm⁻¹ in Na₆MnCl₈ melt. This peak was observed in the spectra of melt MnCl₂-CsCl mixtures²³ at ≈ 20000 cm⁻¹. The peak observed at ~15892 cm⁻¹ in the melts is most probably due to Manganese oxide^{99,100} impurity in the samples. Since there is no peak reported below 19000 cm⁻¹ in the optical spectra of MnCl₂-CsCl melts²³, [MnX₄]²⁻ melts⁹⁰, [MnCl₄]²⁻ melt^{88,89}, and [MnX₄]²⁻ solutions⁸⁶, then the peak observed at ~ 17392 cm⁻¹ in Cs₂MnCl₄, Cs₃MnCl₅ and K₄MnCl₆ melts, and the peaks observed at ~ 16842, 17542 and 18142 cm⁻¹ in Na₆MnCl₈ melt are attributed to artifacts or to unknown impurity in the melts.

Cs₂MnCl₄ is isostructural with Cs₂MgCl₄ which melts¹⁴ with the retention of the discrete tetrahedral MgCl₄²⁻ ions. Also, Cs₃MnCl₅ is isomorphous with Cs₃MgCl₅ which contains¹⁷ the discrete tetrahedral MgCl₄²⁻ ion in the molten state. Since Raman studies of Cs₂MnCl₄ and Cs₃MnCl₅ melts indicated the presence of MnCl₄²⁻ tetrahedral species, and most probably these species are present in these melts as a discrete entities because there is enough chloride to facilitate this kind of isolated species.

By comparing the spectra of K₄MnCl₆ and Na₆MnCl₈ melts with the spectra of Cs₂MnCl₄ and Cs₃MnCl₅ melts, the presence of MnCl₄²⁻ tetra-

hedral species in both melts is suggested. Band positions in cm^{-1} and assignments are shown in Table 39.

(ii) $\text{Rb}_3\text{Mn}_2\text{Cl}_7$, $\text{K}_3\text{Mn}_2\text{Cl}_7$, Na_2MnCl_4 and Rb_2MnCl_4

The visible spectra of $\text{Rb}_3\text{Mn}_2\text{Cl}_7$, $\text{K}_3\text{Mn}_2\text{Cl}_7$, Na_2MnCl_4 and Rb_2MnCl_4 melts are shown in figures 109, 110, 111 and 112. These melts have a bright yellow color. In the case of Na_2MnCl_4 and Rb_2MnCl_4 melts, an isolated tetrahedral MnCl_4^{2-} species is expected because there is enough chloride, but for $\text{Rb}_3\text{Mn}_2\text{Cl}_7$ and $\text{K}_3\text{Mn}_2\text{Cl}_7$ melts, a tetrahedral species with corner sharing is the most probable structure because the spectra and the yellow color suggest that tetrahedral coordination is retained. The peak observed at $\sim 15892 \text{ cm}^{-1}$ in the melts is most probably due to Manganese oxide^{99,100}. Peak positions in cm^{-1} and assignments are shown in Table 40.

(iii) CsMnCl_3 , NaMnCl_3 , KMnCl_3 and RbMnCl_3

The visible spectra of CsMnCl_3 , NaMnCl_3 , KMnCl_3 and RbMnCl_3 melts are shown in figures 113, 114, 115 and 116. These melts exhibit dark yellow color. Since these melts have yellow color, then a tetrahedral MnCl_4^{2-} species with corner sharing is expected because there is not enough chloride to form an isolated MnCl_4^{2-} entity. The peak observed at $\sim 16000 \text{ cm}^{-1}$ in the melts is due to Manganese oxide^{99,100}. Band positions and assignments are shown in Table 41.

(iv) MnCl_2 , CsMn_4Cl_9 , NaMn_4Cl_9 and $\text{Na}_2\text{Mn}_3\text{Cl}_8$

The visible spectra of MnCl_2 , CsMn_4Cl_9 , NaMn_4Cl_9 and $\text{Na}_2\text{Mn}_3\text{Cl}_8$ melts are shown in figures 117, 118, 119 and 120. MnCl_2 , CsMn_4Cl_9 and NaMn_4Cl_9

Figure 105. Visible spectrum of molten Cs_2MnCl_4 at 906 K.

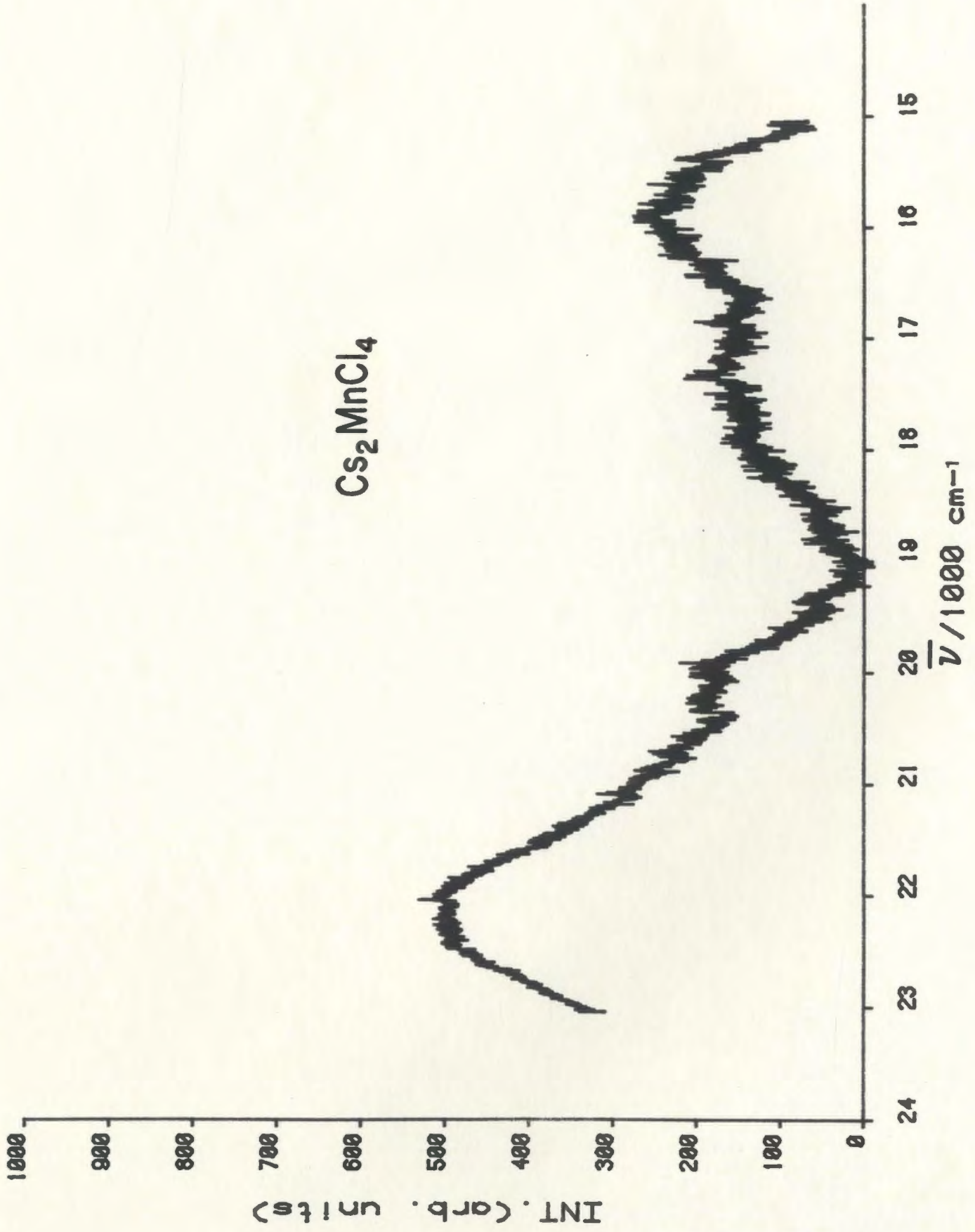


Figure 106. Visible spectrum of molten Cs_3MnCl_5 at 906 K.

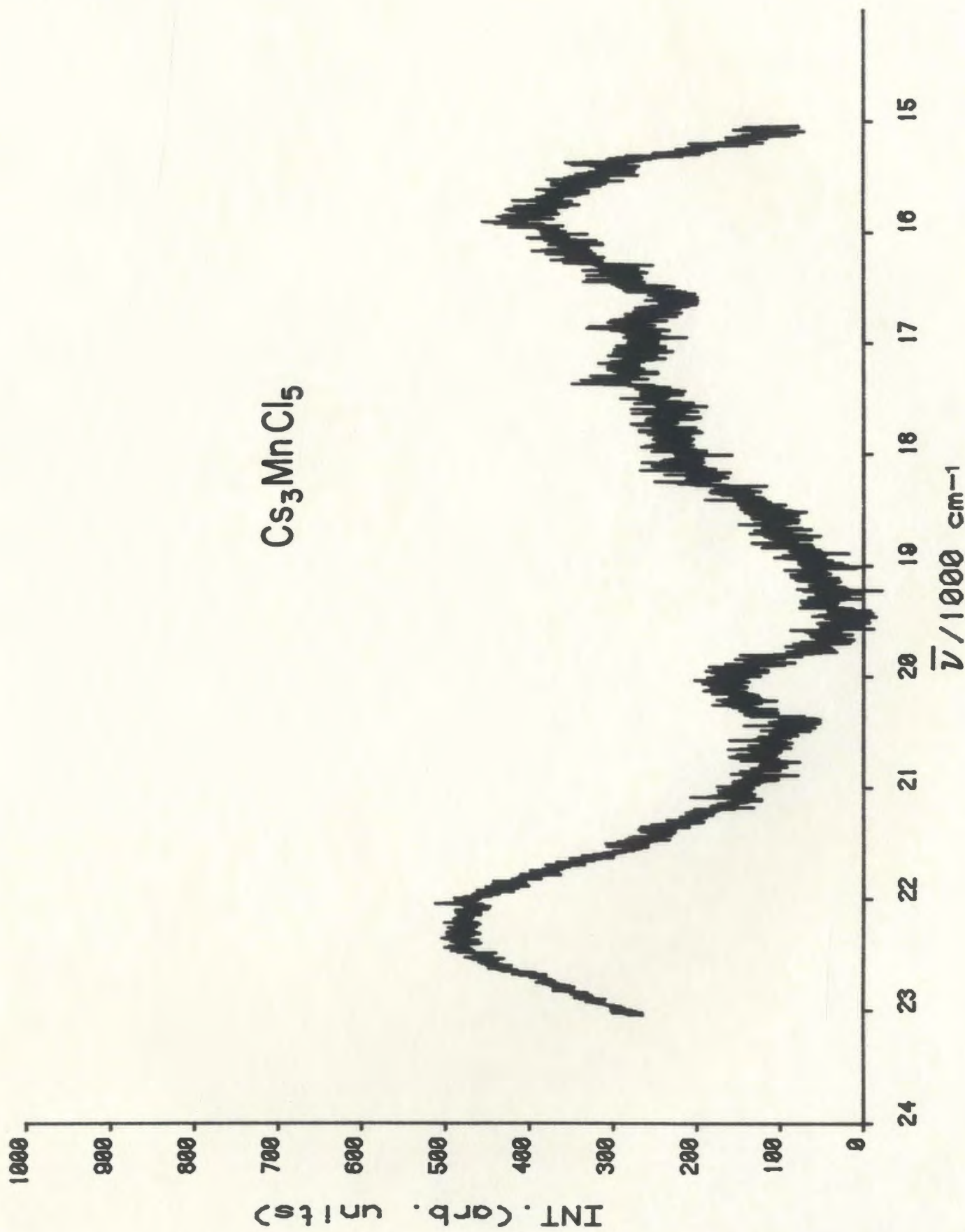


Figure 107. Visible spectrum of molten K_4MnCl_6 at 906 K.

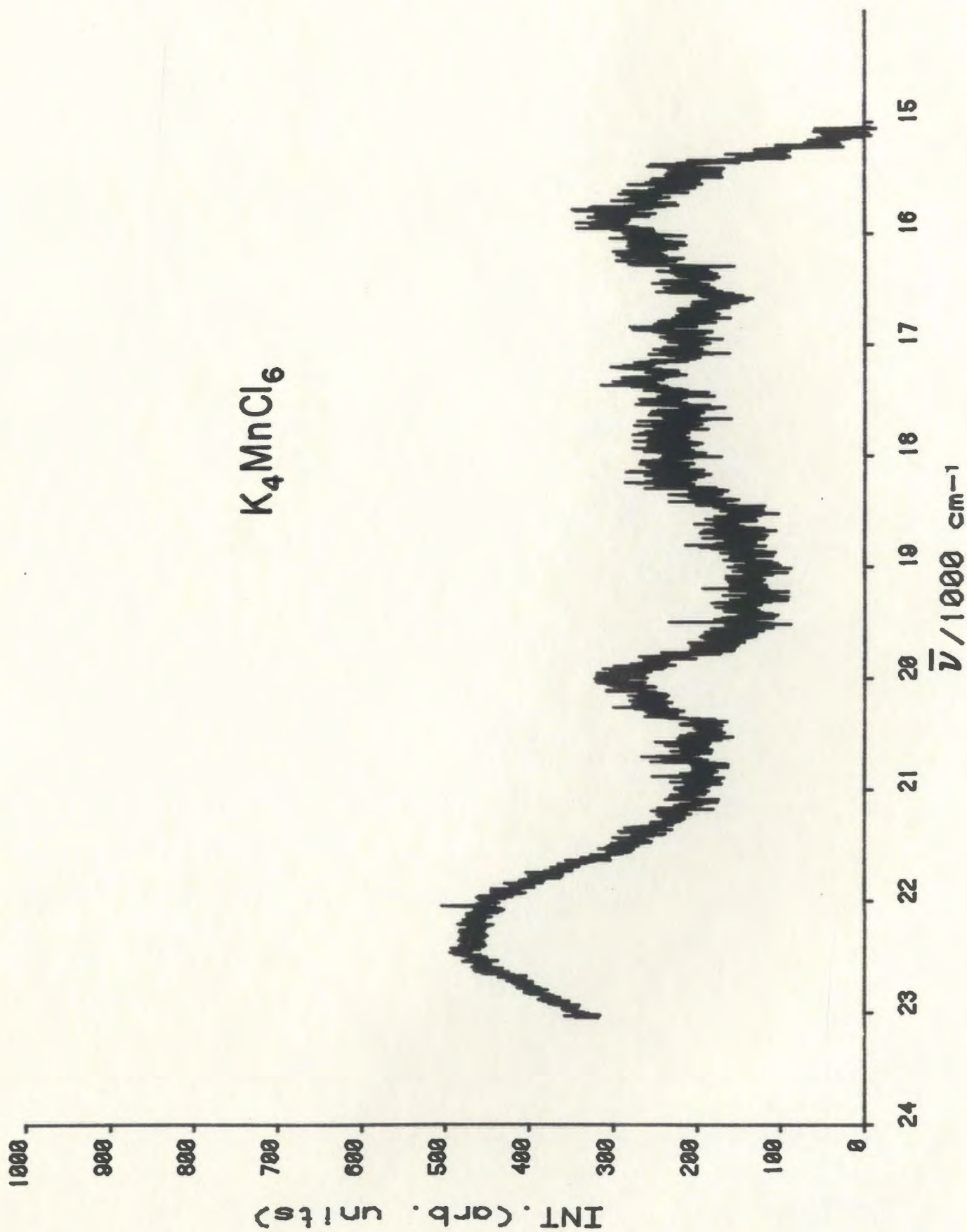


Figure 108. Visible spectrum of molten Na_6MnCl_8 at 922 K.

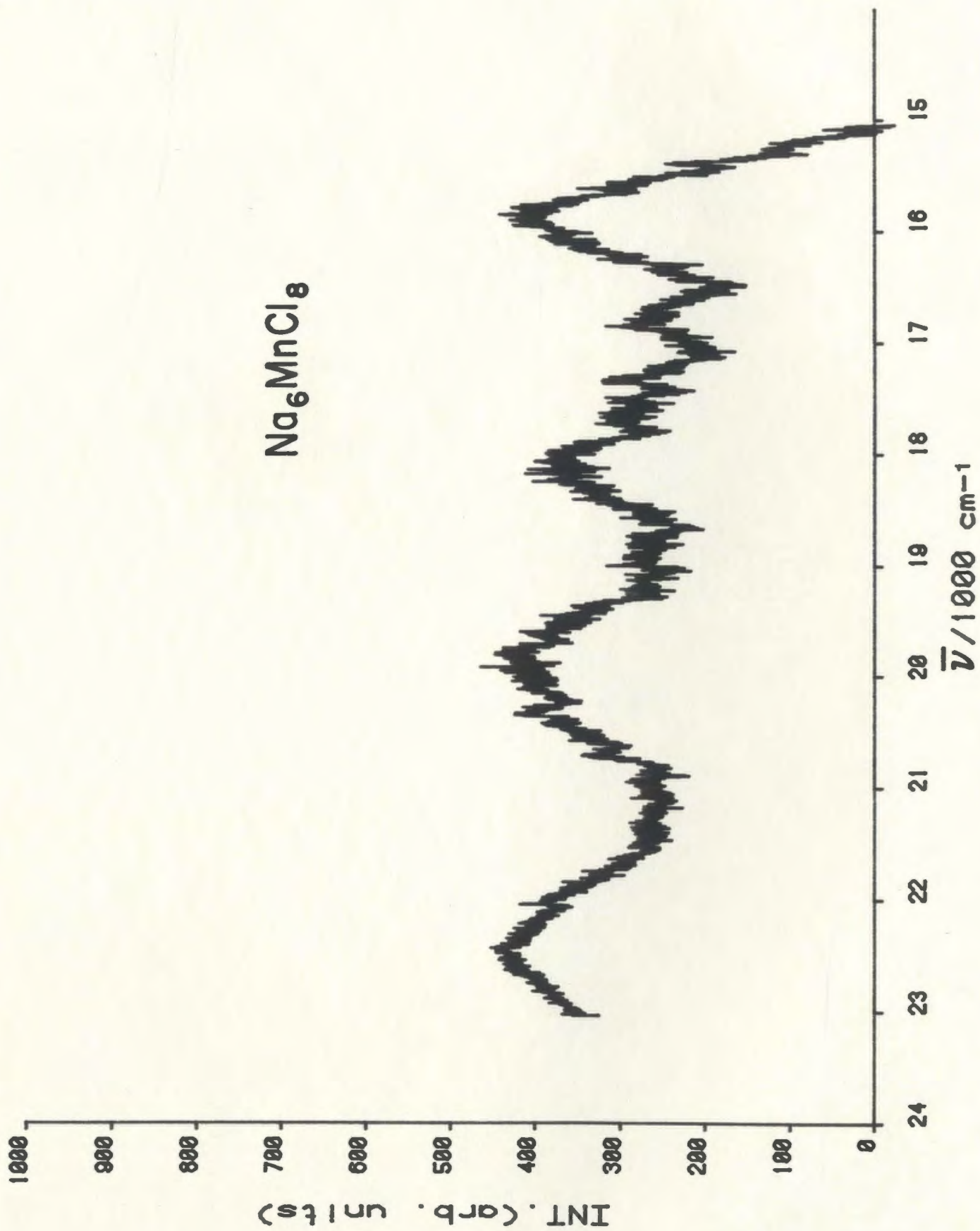


Table 39. Assignments and peak positions in cm^{-1} for Cs_2MnCl_4 , Cs_3MnCl_5 , K_4MnCl_6 , Na_6MnCl_8 and $\text{MnCl}_2\text{-CsCl}$ melts.

Assignments	Cs_2MnCl_4	Cs_3MnCl_5	K_4MnCl_6	Na_6MnCl_8	$\text{MnCl}_2\text{-CsCl}^{23}$ (0.33-0.67)
${}^6\text{A}_1({}^6\text{S}) \rightarrow {}^4\text{T}_1({}^4\text{G})$	20142	20142	20142	20042	20000
$\rightarrow {}^4\text{T}_2({}^4\text{G})$	22292	22292	22292	22492	22750

Figure 109. Visible spectrum of molten $\text{Rb}_3\text{Mn}_2\text{Cl}_7$ at 900 K.

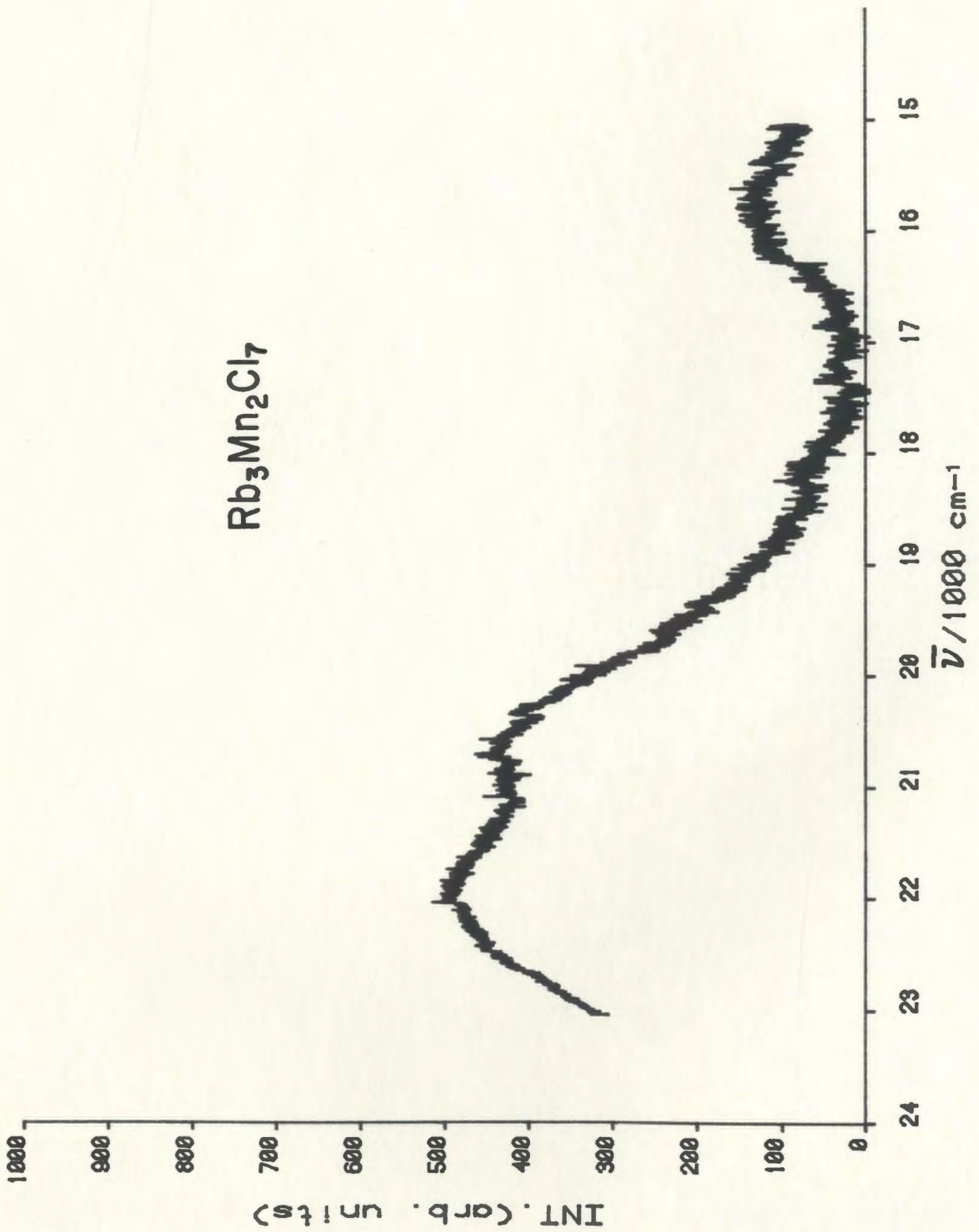


Figure 110. Visible spectrum of molten $K_3Mn_2Cl_7$ at
900 K.

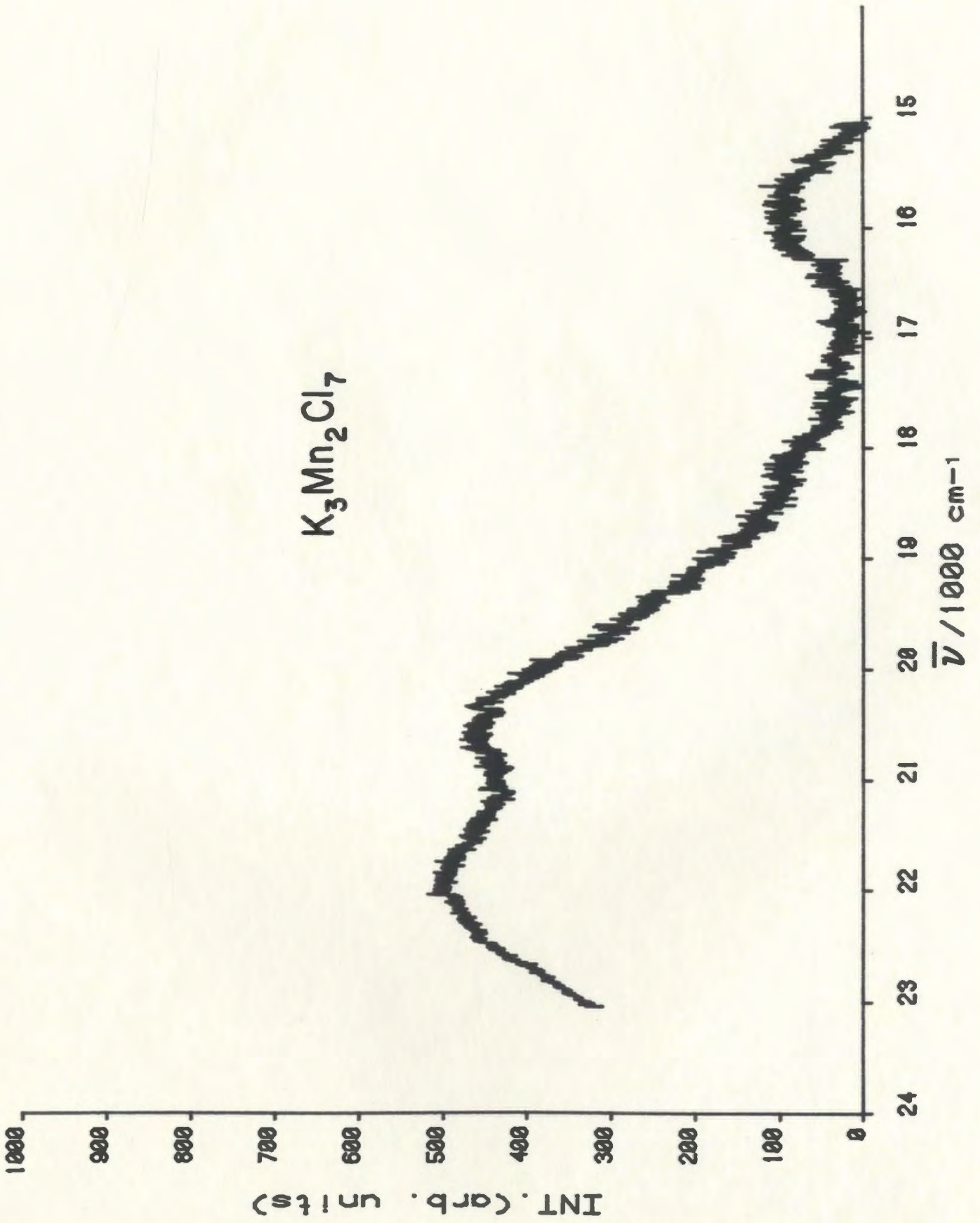


Figure 111. Visible spectrum of molten Na_2MnCl_4 at
900 K.

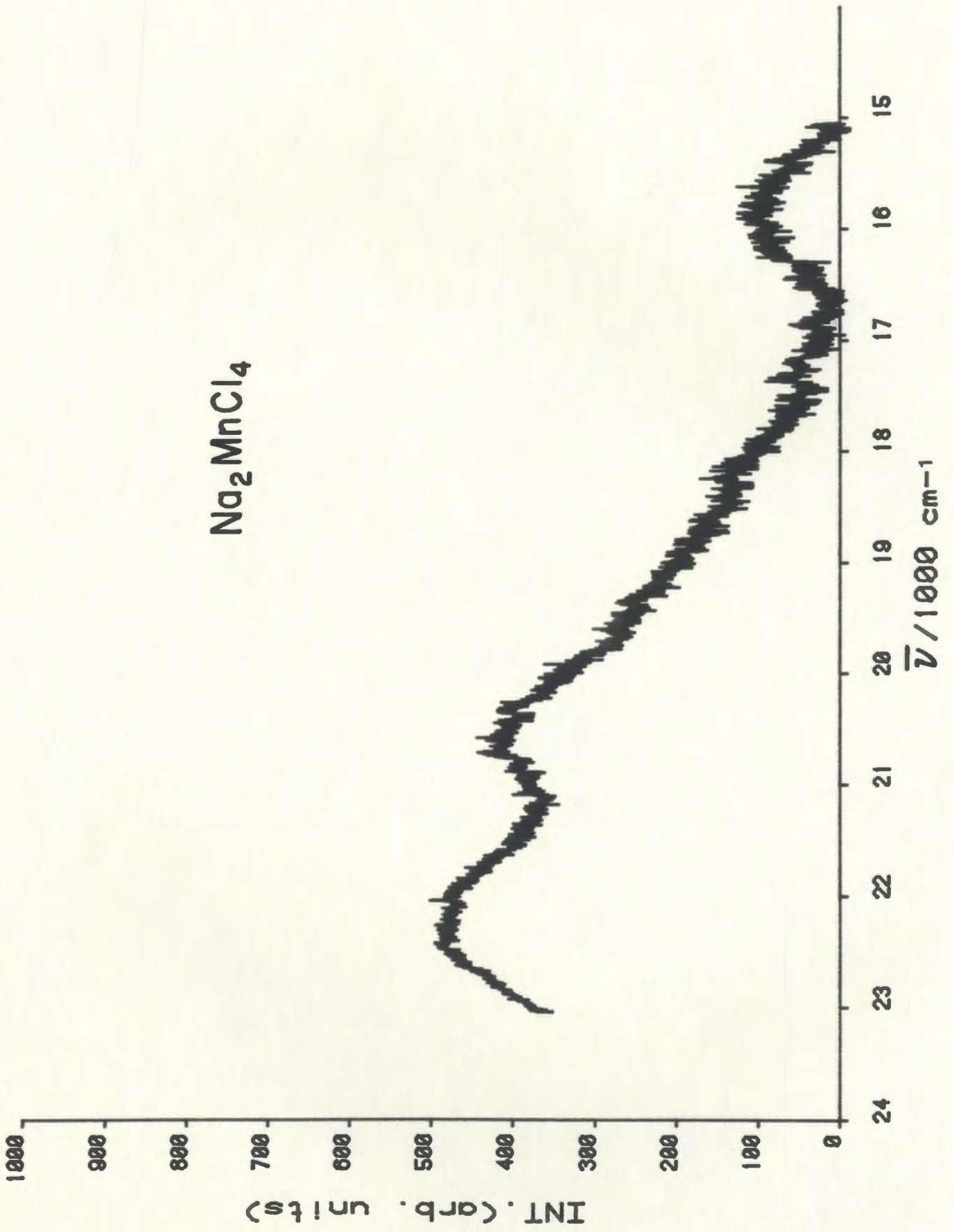


Figure 112. Visible spectrum of molten Rb_2MnCl_4 at 916 K.

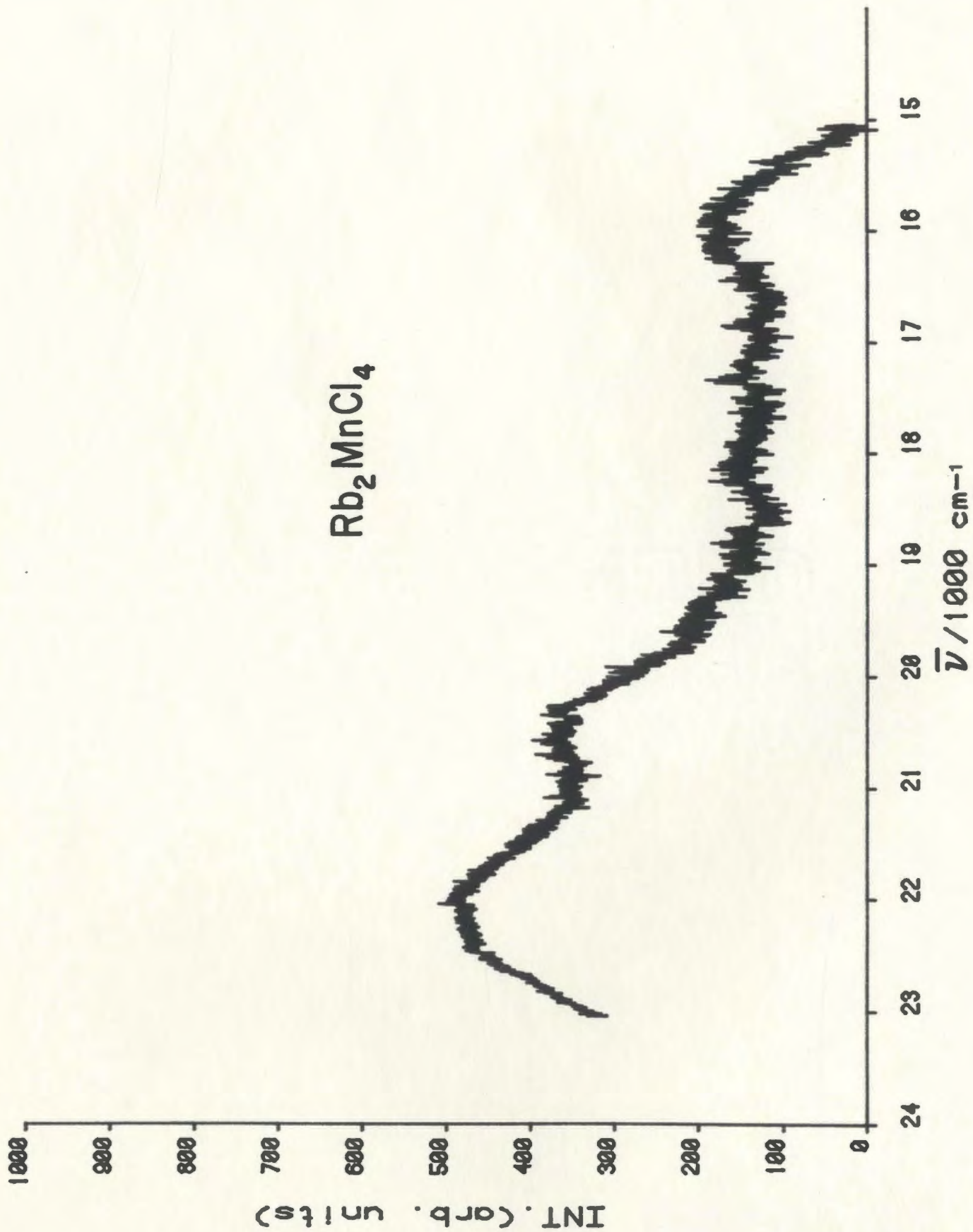


Table 40. Peak positions in cm^{-1} and assignments for $\text{Rb}_3\text{Mn}_2\text{Cl}_7$, $\text{K}_3\text{Mn}_2\text{Cl}_7$, Na_2MnCl_4 , Rb_2MnCl_4 melts and $[\text{MnCl}_4]^{2-}$ solution⁸⁶.

Assignments	$\text{Rb}_3\text{Mn}_2\text{Cl}_7$	$\text{K}_3\text{Mn}_2\text{Cl}_7$	Na_2MnCl_4	Rb_2MnCl_4	$[\text{MnCl}_4]^{2-}$ 86
${}^6\text{A}_1({}^6\text{S}) \rightarrow {}^4\text{T}_1({}^4\text{G})$	20692	20692	20692	20692	21300
$\rightarrow {}^4\text{T}_2({}^4\text{G})$	22062	22062	22292	22292	22530

Figure 113. Visible spectrum of molten CsMnCl_3 at 906 K.

CsMnCl₃

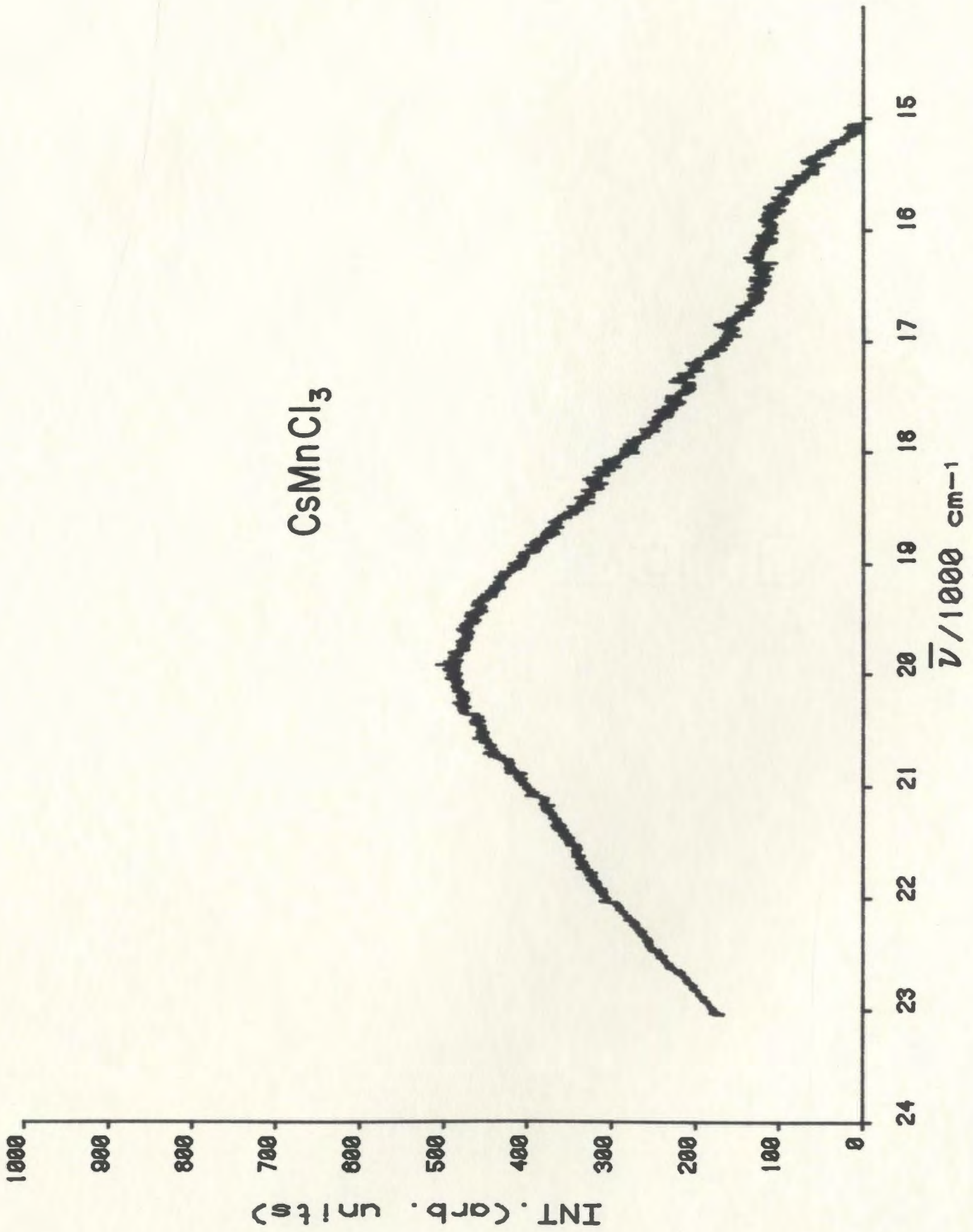


Figure 114. Visible spectrum of molten NaMnCl_3 at
900 K.

NaMnCl₃

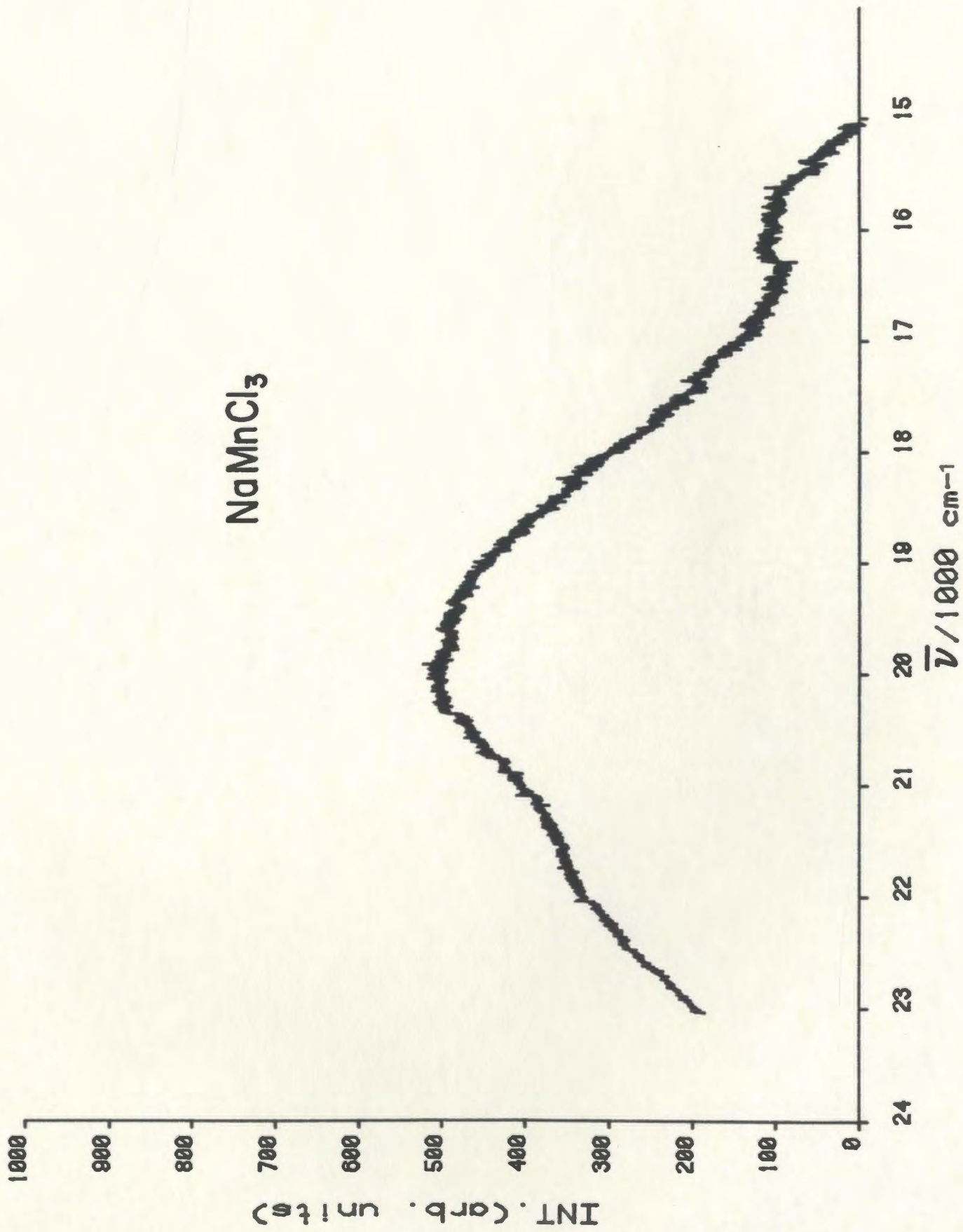


Figure 115. Visible spectrum of molten KMnCl_3 at 906 K.

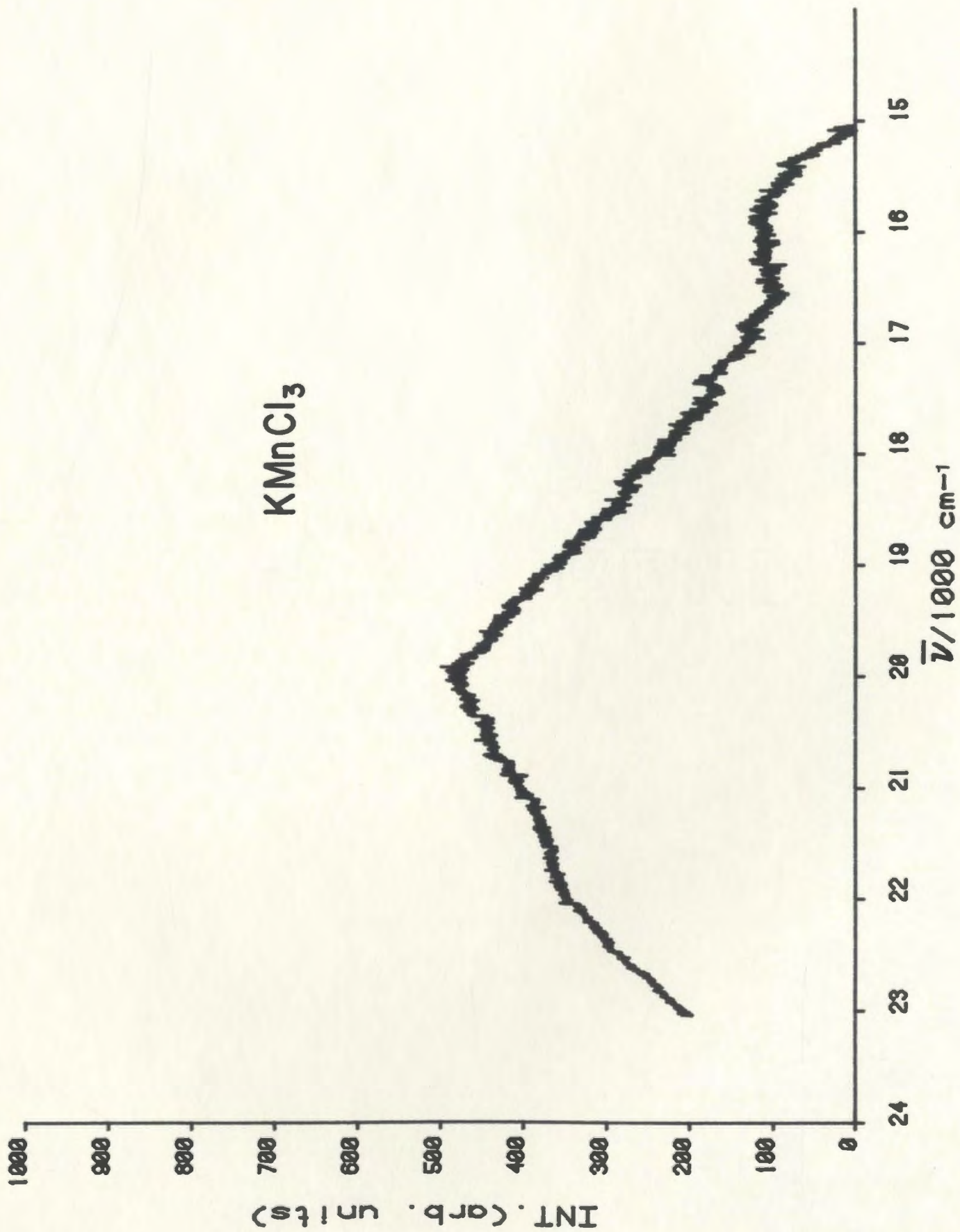


Figure 116. Visible spectrum of molten RbMnCl_3 at 906 K.

RbMnCl₃

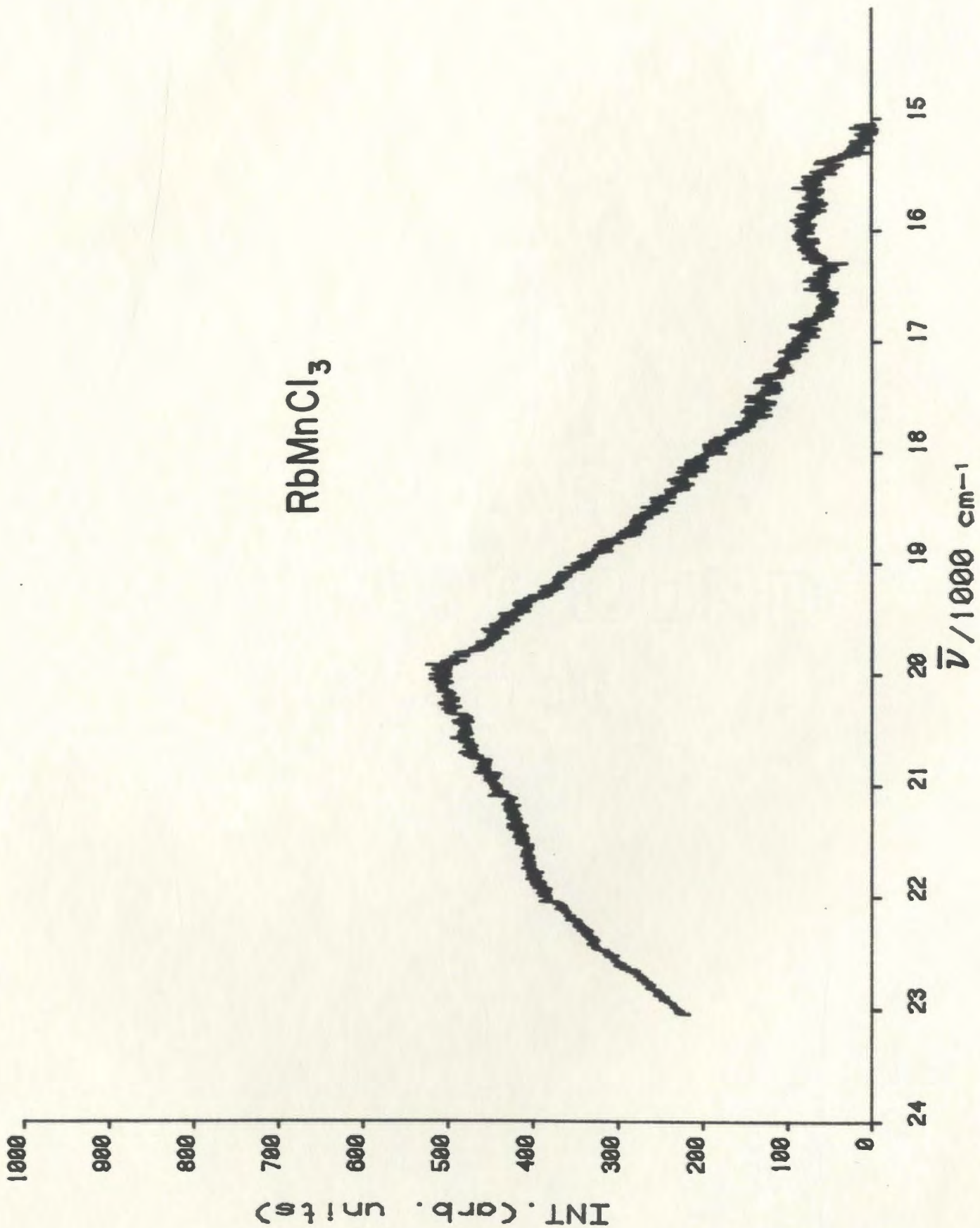
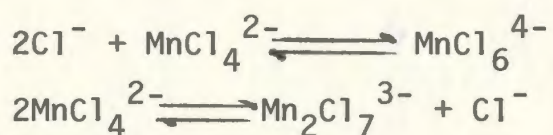


Table 41. Assignments and peak positions in cm^{-1} for CsMnCl_3 , NaMnCl_3 , KMnCl_3 , RbMnCl_3 and MnCl_2 - CsCl melts.

Assignments	CsMnCl_3	NaMnCl_3	KMnCl_3	RbMnCl_3	MnCl_2 - CsCl ²³ (0.5:0.5)
${}^6\text{A}_1({}^6\text{S}) \rightarrow {}^4\text{T}_1({}^4\text{G})$	19942	19942	19975	19975	20000
$\rightarrow {}^4\text{T}_2({}^4\text{G})$	21739	21739	21739	21739	23050

melts have orange-slightly red color, while $\text{Na}_2\text{Mn}_3\text{Cl}_8$ melt exhibit a yellow-orange color. The slight red color and the band positions in the visible spectra for melts of high MnCl_2 content suggest the presence of a small amount of octahedrally coordinated Mn^{2+} . The results suggest that Mn remains mostly tetrahedral coordination but octahedral coordination may be present. However Raman studies indicated that the coordination of Mn is ill-defined due to rapid exchange of ligands:



The formation of these ions take place through corners sharing. The peak observed at $\sim 16000 \text{ cm}^{-1}$ in NaMn_4Cl_9 and $\text{Na}_2\text{Mn}_3\text{Cl}_8$ melts is attributed to Manganese oxide^{99,100}. Band positions in cm^{-1} and assignments are shown in Table 42.

It was possible to differentiate between the compounds which have tetrahedral manganese from the ones in which the manganese is octahedrally coordinated by chlorine atoms on the basis of their visible spectra. In the molten state, the tetrahedral MnCl_4^{2-} species as an isolated entities or through corners sharing are the predominant species in the melts.

Figure 117. Visible spectrum of molten MnCl_2 at 974 K.

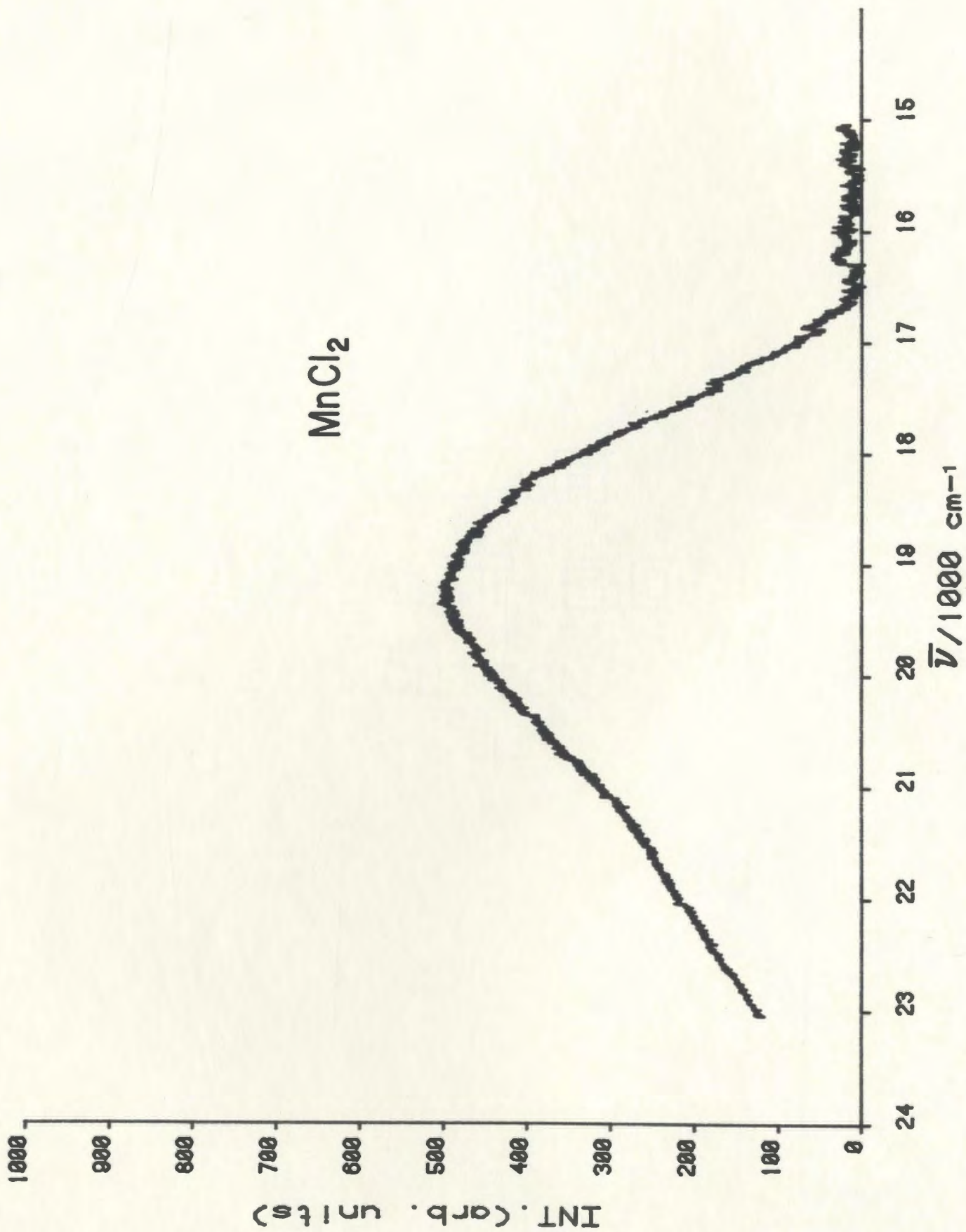
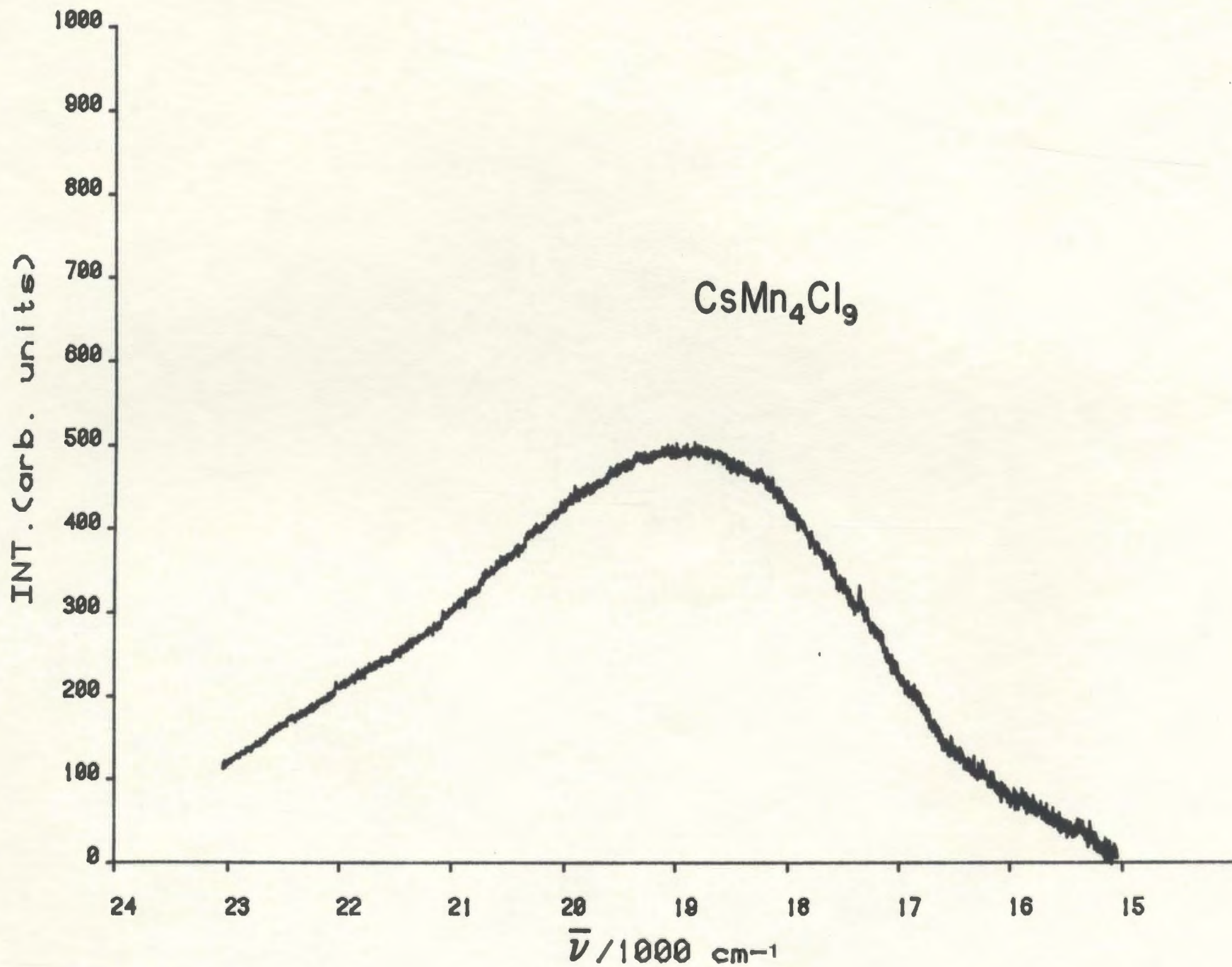


Figure 118. Visible spectrum of molten CsMn_4Cl_9 at
925 K.



CsMn_4Cl_9

Figure 119. Visible spectrum of molten NaMn_4Cl_9 at 916 K.

NaMn4Cl9

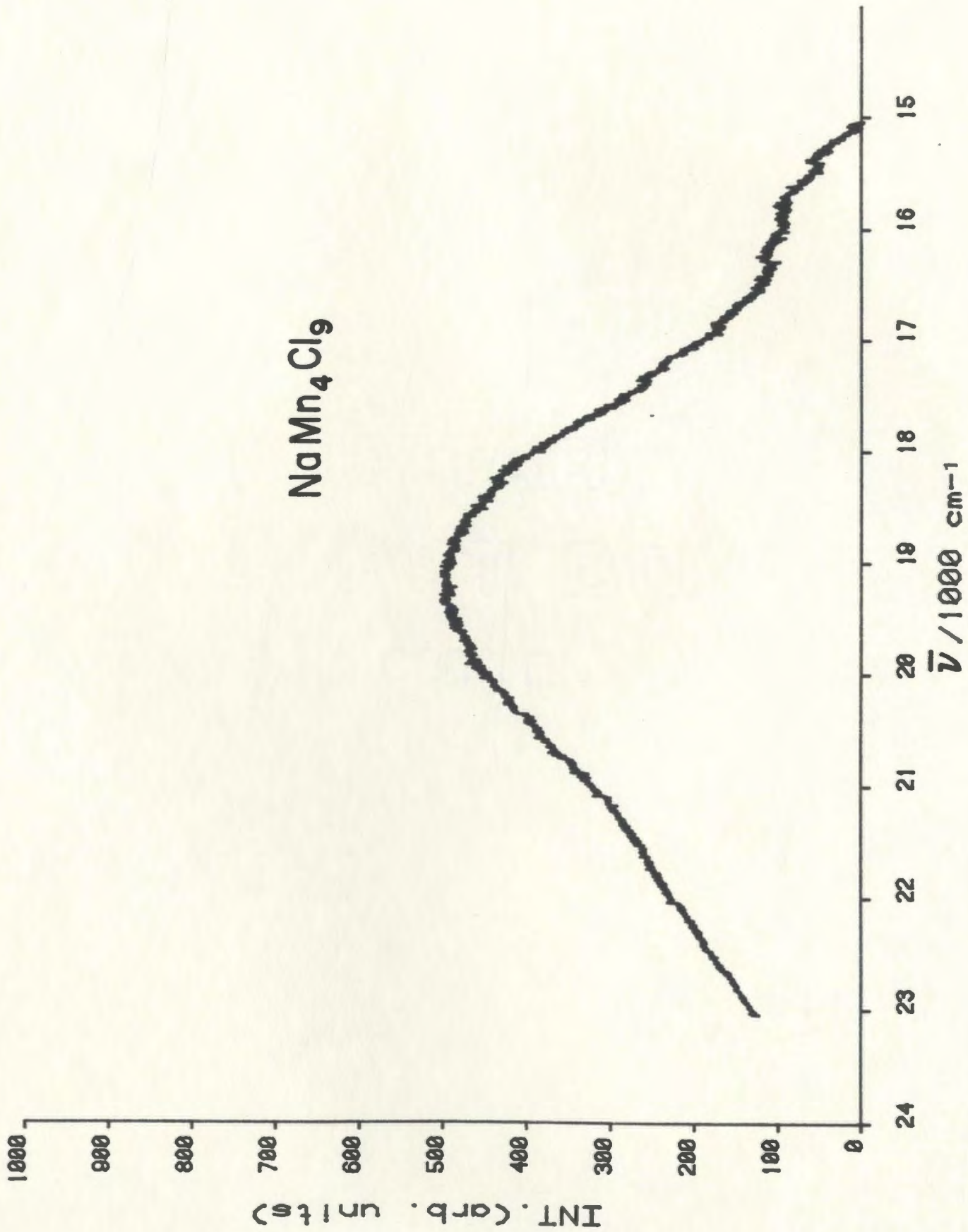


Figure 120. Visible spectrum of molten $\text{Na}_2\text{Mn}_3\text{Cl}_8$ at 901 K.

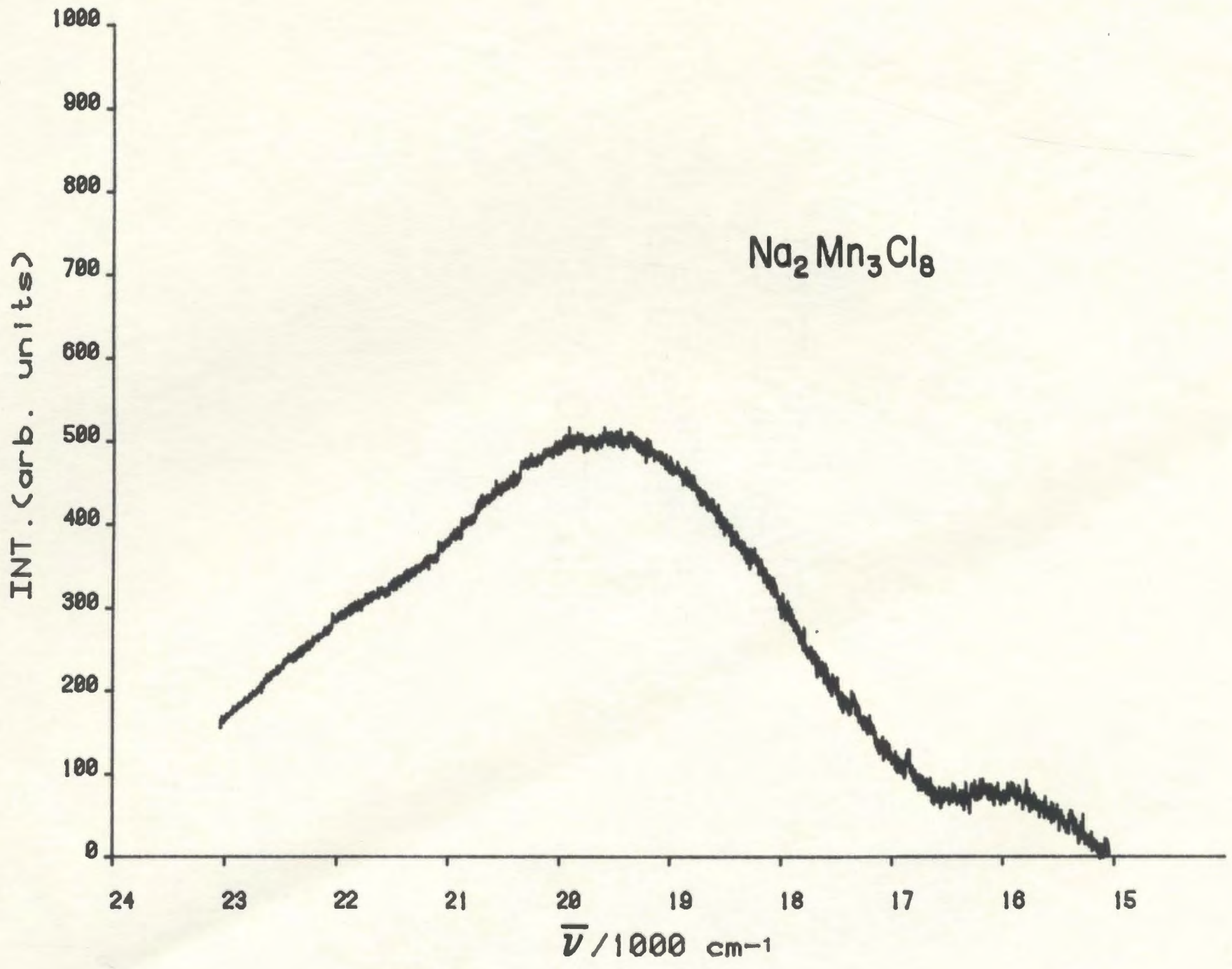


Table 42. Assignments and peak positions in cm^{-1} for MnCl_2 , CsMn_4Cl_9 , NaMn_4Cl_9 , $\text{Na}_2\text{Mn}_3\text{Cl}_8$ and MnCl_2 - CsCl melts.

Assignments	MnCl_2	MnCl_2 - CsCl ²³ (1.0:0.0)	CsMn_4Cl_9	MnCl_2 - CsCl ²³ (0.8:0.2)	NaMn_4Cl_9	$\text{Na}_2\text{Mn}_3\text{Cl}_8$
${}^6\text{A}_1({}^6\text{S}) \rightarrow {}^4\text{T}_1({}^4\text{G})$	19300	20000	19042	20000	19042	19542
$\rightarrow {}^4\text{T}_2({}^4\text{G})$		23300		23260		21739

5. Conclusion

The Raman and visible results indicate the presence of MnCl_4^{2-} ions as the predominant species for $\text{MnCl}_2 \cdot n\text{ACl}$ melts. However for melts of high MnCl_2 concentration, the Raman results suggest the presence of MnCl_4^{2-} ions as the predominant species in addition to the very short-lived species such as, $\text{Mn}_2\text{Cl}_7^{3-}$. The visible results for the melts suggest the presence of a small fraction of MnCl_6^{4-} ions in addition to the predominant MnCl_4^{2-} ions.

The Raman results for $\text{MgCl}_2 \cdot n\text{ACl}$ melts indicate the presence of equilibrium concentrations of MgCl_4^{2-} and $\text{Mg}_2\text{Cl}_7^{3-}$ ions as the predominant species in melts of moderate MgCl_2 content. A third species $\text{Mg}_2\text{Cl}_n^{4-n}$ was detected by further increment of MgCl_2 concentration but the short lifetimes of the higher polymeric species makes it difficult to fully characterize their spectra.

Absorption spectra of the solid compounds in the visible range has lead to identification of tetrahedral and octahedral coordination but could not differentiate between extended array structures and discrete species. The combined visible and Raman spectra can be used to characterize the many solids formed in the ACl-MnCl_2 systems.

6. References

1. B. Gilbert, G. Mamantov and G.M. Begun, J. Chem. Phys., 62, 950 (1975).
2. E. Rytter, H.A. Øye, S.J. Cyvin, B.N. Cyvin and P. Klæboe, J. Inorg. Nucl. Chem., 35, 1185 (1973).
3. J.L. Gray and G.E. Maciel, J. Am. Chem. Soc., 103, 7147 (1981).
4. L.M. Toth and G.E. Boyd, J. Phys. Chem., 77, 2654 (1973).
5. L.M. Toth, A.S. Quist and G.E. Boyd, J. Phys. Chem., 77, 1384 (1973).
6. Encyclopedia of Electrochemistry of Elements vol. VI, VIII by: Allen J. Bard, M. Dekker, New York, 1973.
7. K. Balasubrahmanyam, J. Chem. Phys., 44, 3270 (1966).
8. V.A. Maroni, E.J. Hathaway and E.J. Cairns, J. Phys. Chem., 75, 155 (1971).
9. V.A. Maroni, J. Chem. Phys., 55, 4789 (1971).
10. R.J. Capwell, Chem. Phys. Letters, 12, 443 (1972).
11. E.J. Hathaway and V.A. Maroni, J. Phys. Chem., 76, 2796 (1972).
12. G.M. Begun, J. Brynstad, K.W. Fung and G. Mamantov, Inorg. Nucl. Chem. Lett., 8, 79 (1972).
13. J.E.D. Davies, J. Inorg. Nucl. Chem., 36, 1711 (1974).
14. M.H. Brooker, J. Chem. Phys., 63, 3054 (1975).
15. C.-H. Huang and M.H. Brooker, Chem. Phys. Letters, 43, 180 (1976).
16. M.H. Brooker and C.-H. Huang, Mat. Res. Bull., 15, 9 (1980).
17. M.H. Brooker and C.-H. Huang, Can. J. Chem., 58, 168 (1980).
18. D.J. Lockwood, J. Opt. Soc. Am., 63, 374 (1973).
19. K. Tanemoto and T. Nakamura, Chem. Letters, 351 (1975).
20. S.V. Volkov, N.P. Evtushenko and K.B. Yatsimirskii, Theor. Exp. Chem., 12, 85 (1976).
21. R. G. Synder and J.R. Scherer, J. Polym. Sci. Phys. Ed., 18, 421 (1980).

22. M.H. Brooker and G.N. Papatheodorou in "Advances in Molten Salt Chemistry", Vol. 5, G. Mamantov, Editor, Elsevier, 1983, p. 26.
23. W. Bues, L. El-Sayed and H.A. Øye, Acta Chem. Scand., 31A, 461 (1977).
24. K. Tanemoto and T. Nakamura, Japan. J. Appl. Phys., 17, 2161 (1978).
25. W. Bues, Z. Anorg. Allgem. Chem., 279, 104 (1955).
26. M. Tanaka, K. Balasubrahmanyam and J.O'M. Bockris, Electrochim. Acta, 8, 621 (1963).
27. V.A. Maroni and E.J. Hathaway, Electrochim. Acta, 15, 1837 (1970).
28. J.H.R. Clarke, P.J. Hartley and Y. Kuroda, J. Phys. Chem., 76, 1831 (1972).
29. H. Ohno et. al., J. Chem. Soc. Faraday I, 74, 804 (1978), and private communication.
30. H. Ohno et. al., J. Chem. Soc. Faraday I, 75, 1161 (1979).
31. O.J. Kleppa and F.G. McCarty, J. Phys. Chem., 70, 1249 (1966).
32. H. Flood and S. Urnes, Z. Elektrochem., 59, 834 (1955).
33. T. Østvold, Acta Chem. Scand., 23, 688 (1969).
34. G.N. Papatheodorou and O.J. Kleppa, J. Inorg. Nucl. Chem., 33, 1249 (1971).
35. A.S. Kucharski and S.N. Flengas, J. Electrochem. Soc., 119, 1170 (1972).
36. H.J. Borchardt and F. Daniels, J. Phys. Chem., 61, 917 (1957).
37. P. Ehrlich, F.W. Koknat and H.J. Seifert, Z. Anorg. Allg. Chem., 341, 281 (1965).
38. B.F. Markov and R.V. Chernov, Ukr. Khim. Zh., 24, 139 (1958).
39. J. Goodyear and D.J. Kennedy, Acta Cryst., B29, 2677 (1973).
40. J. Goodyear, G.A. Steigmann and D.J. Kennedy, Acta Cryst., B28, 1231 (1972).
41. G.N. Papatheodorou, J. Inorg. Nucl. Chem., 35, 465 (1973).
42. C.S. Gibbons, V.C. Reinsborough and W.A. Whittle, Can. J. Chem., 53, 114 (1975).

43. H.J. Seifert and G. Flohr, Z. Anorg. Allg. Chem., 436, 244 (1977).
44. H.J. Seifert, private communication.
45. A. Epstein, E. Gurewitz, J. Makovsky and H. Shaked, Phys. Review, 2B, 3703 (1970).
46. Symmetry and Spectroscopy
by: Daniel C. Harris and Michael D. Bertolucci, Oxford University Press, 1978.
47. Infrared and Raman Spectroscopy
by: Norman B. Colthup, Lawrence H. Daly and Stephen E. Wiberley, Academic Press, 2nd Edition, 1975.
48. K.R. Loos, V.A. Campanile and C.T. Goetschel, Spectrochim. Acta, 26A, 365 (1970).
49. J.S. Avery, C.D. Burbridge and D.M.L. Goodgame, Spectrochim. Acta, 24A, 1721 (1968).
50. A. Sabatini and L. Sacconi, J. Am. Chem. Soc., 86, 17 (1964).
51. J. Goodyear and D.J. Kennedy, Acta Cryst., B32, 631 (1976).
52. Ting-I Li, G.D. Stucky and G.L. McPherson, Acta Cryst., B29, 1330 (1973).
53. M. Melamud, J. Makovsky and H. Shaked, Phys. Review, 3B, 3873 (1971).
54. B. Morosin and E.J. Graeber, Acta Cryst., 23, 766 (1967).
55. D.M. Adams and R.R. Smardzewski, Inorg. Chem., 10, 1127 (1971).
56. J. Goodyear, G.A. Steigmann and E.M. Ali, Acta Cryst., B33, 256 (1977).
57. H.J. Seifert and F.W. Koknat, Z. Anorg. Allgem. Chem., 341, 269 (1965).
58. A.S. Kuzmenko, E.N. Ryabov and R.A. Sandler, Russ. J. Inorg. Chem., 19, 1392 (1974).
59. H. Bürger, K. Strobel, R. Geick and W. Müller-Lierheim, J. Phys. C: Solid State Phys., 9, 4213 (1976).
60. B. Briat, A. Vervoitte, J.C. Canit and E. Francke, Solid State Commun., 50, 229 (1984).
61. S.N. Ruddlesden and P. Popper, Acta Cryst., 11, 54 (1958).
62. R. Bellanca, Periodica Mineral. (Rome), 16, 73 (1947).

63. A. Horowitz, D. Gazit and J. Makovsky, *J. Crystal Growth*, 51, 489 (1981).
64. H.J. Seifert and K.H. Kischka, *Thermochim. Acta*, 27, 85 (1978).
65. C.J.J. Van Loon and G.C. Verschoor, *Acta Cryst.*, B29, 1224 (1973).
66. T.F.W. Barth and E. Posnjak, *Z. Kristallogr.*, 88, 265 (1934).
67. J. Goodyear, S.A.D. Ali and G.A. Steigmann, *Acta Cryst.*, B27, 1672 (1971).
68. C.J.J. Van Loon and D.J.W. Ijdo, *Acta Cryst.*, B31, 770 (1975).
69. J.M. Calleja, A. Ruiz, F. Flores, V.R. Velasco and E. Lilley, *J. Phys. Chem. Solids*, 41, 1367 (1980).
70. E. Fjaer and E.J. Samuelsen, *Ferroelectrics*, 36, 459 (1981).
71. Crystal structures
by: Ralph W.G. Wyckoff, Vol. 1, Second Edition, John Wiley & Sons, 1963.
72. G.J. Janz et. al., *J. Phys. Chem. Ref. Data*, 4, 871 (1975).
73. C.J.J. Van Loon and J. Dejong, *Acta Cryst.*, B31, 2549 (1975).
74. H.D. Lutz, W. Schmidt and H. Haeuseler, *Z. Anorg. Allg. Chem.*, 453, 121 (1979).
75. P. Andersen, *Nordiske Kemikermode*, 9th Aarhus, August 1956.
76. J. Goodyear and D.J. Kennedy, *Acta Cryst.*, B29, 744 (1973).
77. J. Brynstad, H.L. Yake1 and G.P. Smith, *J. Chem. Phys.*, 45, 4652 (1966).
78. Ligand Field Theory
by: Hans L. Schläfer and Günter Gliemann
English Translation by: David F. Ilten, Wiley-Interscience, 1969.
79. J. Ferguson, *Prog. Inorg. Chem.*, 12, 159 (1970).
80. L.J. Heidt, G.F. Koster and A.M. Johnson, *J. Am. Chem. Soc.*, 80, 6471 (1959).
81. C.K. Jorgensen, *Acta Chem. Scand.*, 11, 53 (1957).
82. L.E. Orgel, *J. Chem. Phys.*, 23, 1824 (1955).
83. R.J.H. Clark, *J. Chem. Soc.*, 417 (1964).

84. J.W. Stout, J. Chem. Phys., 33, 303 (1960).
85. J.W. Stout, J. Chem. Phys., 31, 709 (1959).
86. C. Furlani and A. Furlani, J. Inorg. Nucl. Chem., 19, 51 (1961).
87. F.A. Cotton, D.M.L. Goodgame and M. Goodgame, J. Am. Chem. Soc., 84, 167 (1962).
88. B.R. Sundheim and M. Kukk, Discussions Faraday Soc., 32, 49 (1961).
89. D.M. Gruen and R.L. McBeth, Pure and Appl. Chem., 6-7, 23 (1963).
90. B.R. Sundheim, E. Levy and B. Howard, J. Chem. Phys., 57, 4492 (1972).
91. N. Islam, Appl. Spectrosc., 29, 266 (1975).
92. J.J. Foster and N.S. Gill, J. Chem. Soc., A, 2625 (1968).
93. A. Mehra, J. Chem. Phys., 48, 1871 (1968).
94. A. Mehra and P. Venkateswarlu, J. Chem. Phys., 45, 3381 (1966).
95. A. Mehra, Phys. Stat. Sol., 29, 847 (1968).
96. F. Rodriguez, M. Moreno, F. Jaque and F.J. Lopez, J. Chem. Phys., 78, 73 (1983).
97. A. DE Andrés, J.M. Calleja, F.J. López and F. Jaque, Radiation Effects, 75, 241 (1983).
98. F. Jaque, F.J. López, F. Cussó, F. Meseguer, F. Aguiló-López and M. Moreno, Solid State Commun., 47, 103 (1983).
99. D.R. Huffman, R.L. Wild and M. Shinmei, J. Chem. Phys., 50, 4092 (1969).
100. G.W. Pratt and R. Coelho, Phys. Rev., 116, 281 (1959).

84. U.M. Stobur, *J. Chem. Phys.*, 33, 203 (1960).

85. U.M. Stobur, *J. Chem. Phys.*, 31, 709 (1959).

86. C. Furlani and A. Furlani, *J. Inorg. Nucl. Chem.*, 19, 21 (1967).

87. F.A. Cotton, D.W.L. Goodgame and M. Goodgame, *J. Am. Chem. Soc.*, 84, 167 (1962).

88. B.R. Sundheim and W. Kirk, *Discussion Faraday Soc.*, 32, 49 (1967).

89. B.M. Gryn and K.L. McKeith, *Pure and Appl. Chem.*, 6-7, 23 (1963).

90. B.R. Sundheim, E. Levy and B. Howard, *J. Chem. Phys.*, 51, 688 (1972).

91. N. Isler, *Appl. Spectrosc.*, 29, 206 (1975).

92. G.J. Foster and H.S. Giff, *J. Chem. Soc.*, A, 2632 (1968).

93. A. Mohr, *J. Chem. Phys.*, 58, 1871 (1968).

94. A. Mohr and F. Vankovskovic, *J. Chem. Phys.*, 52, 3381 (1966).

95. A. Mohr, *Phys. Stat. Sol.*, 28, 847 (1967).

96. F. Rodriguez, R. Moreno, F. Jague and F.L. Lopez, *J. Chem. Phys.*, 78, 73 (1963).

97. A. De Andrade, G.M. Caljeira, F.L. Lopez and F. Jague, *Radiation Effects*, 78, 241 (1963).

98. F. Jague, F.L. Lopez, F. Gussé, F. Messager, F. Aguilé-López and M. Moreno, *Solid State Commun.*, 52, 103 (1963).

99. D.R. Huffman, R.C. Wild and R. Shinnar, *J. Chem. Phys.*, 50, 4032 (1969).

100. E.W. Pratt and R. Collins, *Phys. Rev.*, 110, 281 (1958).

①
6906316

